EMPLOYING INSECT ANTENNAL LOBE OLFACTORY NEURAL SIGNALS FOR NON-INVASIVE DISEASE DETECTION

By

Alexander J. Farnum

A DISSERTATION

Submitted to
Michigan State University
in partial fulfillment of the requirements
for the degree of

Biomedical Engineering — Doctor of Philosophy

2023

ABSTRACT

Gas-based chemical sensors have proven invaluable for investigating the underlying chemical configuration of a particular odorant. Technologies such as gas chromatography-mass spectrometry and hyphenated ion mobility spectrometry have elucidated numerous causal factors and biochemical pathways contributing to a variety of healthy and pathologic conditions. Nevertheless, these technologies face innate challenges that have precluded their adoption and implementation in the clinical environment. As a result, a considerable amount of research and development has been geared towards fabricating cheap, easy-to-use, and highly portable electronic noses. These devices have demonstrated excellent potential for applications such as environmental monitoring, food analysis, and forensic science. Moreover, innovations in nanotechnology and other materials science fields have spurred the ideation and creation of highly efficient electronic noses. However, the broad range and low concentrations of chemical metabolites observed in breath profiles, hinders their use as medical diagnostics for complex diseases. Here, this work proposes a novel technology utilizing biologically based chemical biosensors to accurately characterize the volatile profiles associated with pathological disease states, especially that of cancer. The development of this powerful and efficient gas-sensing system has the potential for use in a variety of real-world contexts, including homeland security, law enforcement, and medicine.

It is well known that the presence of disease alters underlying biochemical processes, thereby influencing metabolic byproducts and the volatile chemicals excreted via the breath. Existing manmade chemical sensors as medical diagnostics lack the ability to differentiate the breath profiles of healthy individuals from those with complex diseases. Chapter 1 investigates

the field of volatolomics as a whole, including the gas-based identification of ‘simple’ diseases and the application of state-of-the-art sensor technologies to diagnose complex pathologies. In chapter 2, the methodology for all experiments involving this novel gas-based biosensor in the context of disease diagnosis is discussed. Chapters 3, 4, and 5 detail applied research which validates the biosensors’ powerful abilities to differentiate chemicals and chemical profiles. This work serves to establish its potential as a non-invasive medical diagnostic using biological matrices, such as breath profiles. Finally, chapter 6 discusses the current limitations of the proof-of-concept technology as well as modifications that will mitigate such limitations and aid in the creation of an effective state-of-the-art breath-based medical diagnostic.

TABLE OF CONTENTS

CHAPTER 1 | INTRODUCTION

Volatolomics

Chemical molecules are the building blocks of the material world. Depending on their physical properties and environmental conditions, molecules can exist in solid, liquid, or gaseous forms. For example, a sufficient increase in temperature can break the covalent bonds of H_2O molecules, evaporating the hydrogen and oxygen atoms into their respective gases. The resultant volatile chemicals can convey a considerable amount of information about the underlying chemical composition of the stimulus itself. Since atoms in the gaseous state can diffuse more freely than those of solids or liquids, gas-based sensing offers a method for non-invasive chemical analysis, particularly important for toxic, delicate, or otherwise inaccessible stimuli. Today, such gas sensors exist in a litany of fields, from law enforcement to environmental monitoring to medicine. However, given the millions of known chemicals and minute conformational differences between individual species, accurately characterizing a volatile requires exceptionally high precision. This task is made even more difficult when one considers that the vast majority of stimuli are constructed of heterogeneous molecular matrices, significantly complicating the associated volatile profiles. These demands have led to the development and progression of a number of disparate scientific domains. Volatolomics, one such field still in its infancy, seeks to apply chemical sensing technologies intended to aid in the identification of the unique volatile organic compounds (VOCs) emitted by biological organisms[1]. Volatolomics has direct implications for a wide variety of societal sectors. In food science, the VOC profiles of specific foodstuffs have been observed to indicate overall quality and possible nutritional deterioration[2]. In environmental

Disease	Source	Smell
Diabetic Ketoacidosis	Breath	Rotting apples, acetone
Renal Failure	Breath	Stale urine
Intestinal Obstruction	Breath	Feculent, foul
Liver failure	Breath	Musty fish, raw liver, feculent
Fetor hepaticus	Breath	Newly mown clover, sweet
Pneumonia	Breath	Putrid
Typhoid	Skin	Freshly baked brown bread
Yellow Fever	Skin	Butcher's shop
Squamous-cell carcinoma	Skin	Offensive odor
Diphtheria	Sweat	Sweet
Rubella	Sweat	Freshly plucked feathers
Schizophrenia	Sweat	Mildly acetic
Bladder Infection	Urine	Ammonia

Table 1.1 | Characteristic Odors of Disease. Patient odor has long been used by physicians as a diagnostic element. A large number of diseases have been documented to elicit stereotypical odors, perceivable even with the human nose, which displays relatively poor olfactory capabilities relative to other animals. Adapted from [3, 4].

maintenance, the growing number of densely populated cities has led to an increased demand to actively monitor air pollution levels via IoT (Internet of Things) devices[5]. In homeland security, detecting and differentiating between the volatile profiles of various explosive precursors could allow means for highly accurate, non-destructive sampling and safer public spaces[6].

Certain diseases have been known to exude particular odors since antiquity[4, 7-11] and physicians were taught to consider smell as a key factor for assessing a patient's health until relatively recently (**Table 1.1**) [12-14]. Nevertheless, this subjective olfactory-based diagnostic fell into disuse with the advent of objective technologically based diagnostics. In fact, gas-sensors as medical devices are just now becoming standard tools in research laboratories and clinical practice. Capnography, the monitoring of CO_2 levels in patients' exhaled breath, has enabled

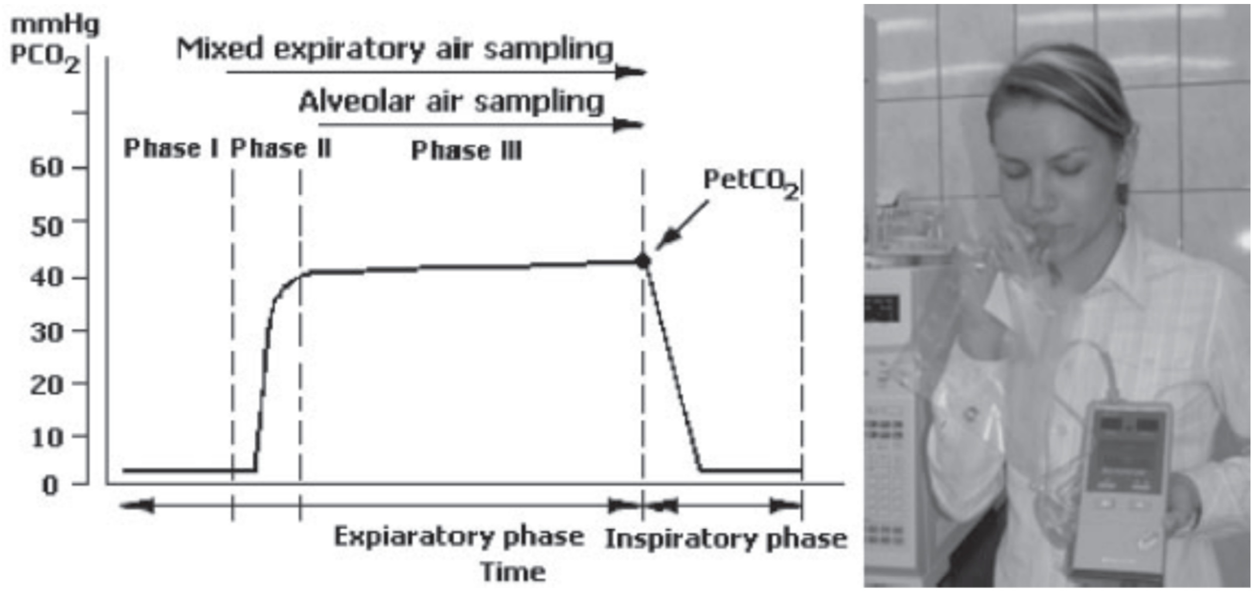

Figure 1.1 | Real time monitoring of CO_2 using a handheld capnograph device. Capnography provides insight into the amount of expired carbon dioxide in exhaled breath. As such, it can aid in breath sampling protocols by standardizing collection procedures using chemically derived information. Reproduced from [15].

anesthesiologists to significantly mitigate hypoxia induction and is useful for enhancing the quality of breath samples **(Figure 1.1)** [16, 17]. For individuals with suspected bronchial asthma

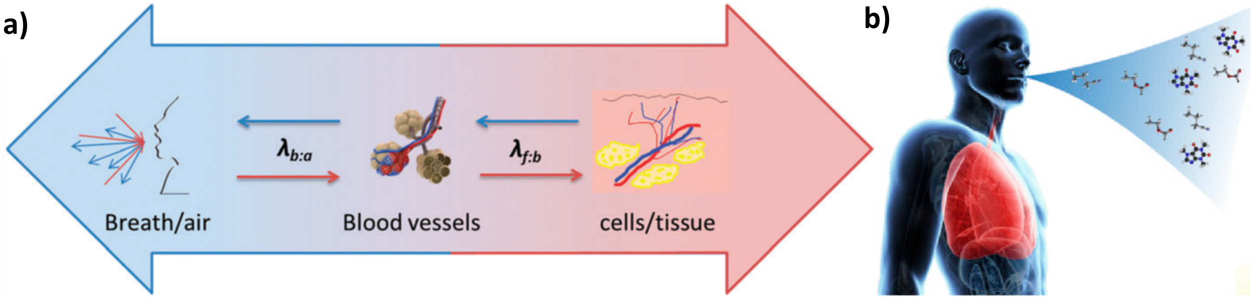

Figure 1.2 | Breath profiles include various volatile metabolites useful for disease diagnosis. Exhaled breath contains a myriad chemical information pertaining to underlying biochemical processes. Analysis of breath profile constituents can aid in non-invasive disease diagnosis. **a)** Metabolic byproducts from cells and tissues are passed into the blood stream based on the partition coefficient between fat and blood ($\lambda_{f:b}$). As the pulmonary circulatory system transports blood and metabolic byproducts to the lungs, molecules diffuse into the alveoli of the lungs based on the partition coefficient between blood and air ($\lambda_{b:a}$). Reproduced from [18]. **b)** These volatile biomarkers are excreted via the breath in trace-level concentrations, which can aid in identifying underlying metabolic processes. Reproduced from [19].

or other inflammatory airway diseases, fractional exhaled nitric oxide (F_ENO) measurements are commonplace[20-22] and may even be superior to conventional diagnostic approaches[23]. Exhaled levels of acetone have been shown to increase significantly in those with type I diabetes, especially during bouts of ketoacidosis[24-29]. Even nonpathogenic, yet suboptimal cellular processes, such as free radical formation and systemic oxidative stress can be determined by elevated concentrations of ethane, pentane, and other unbranched hydrocarbons **(Figure 1.2)** [30-33].

Selective Gaseous Sensors

Independent of the specific analytical technology, all gaseous chemical sensors operate according to two basic principles: chemical recognition and signal transduction. Initially, the device must incorporate methods for interacting with the analytes of interest, oftentimes separating out individual chemicals based on one or more physicochemical molecular properties. Thereafter, a readout signal is generated permitting direct stimulus classification or subsequent analysis designed to aid in stimulus classification. Two approaches to gas sensing have been realized due to the implementation of novel technologies and new knowledge acquisition. Targeted bottom-up approaches first identify volatile biomarkers corresponding to a disease of interest and subsequently look to fabricate gas sensing devices most equipped to separate out and identify these chemicals. Conversely, untargeted top-down strategies utilize broad-scale sensors that aim to characterize highly informative features present within a sample with no preconception of potential biomarker identities[1].

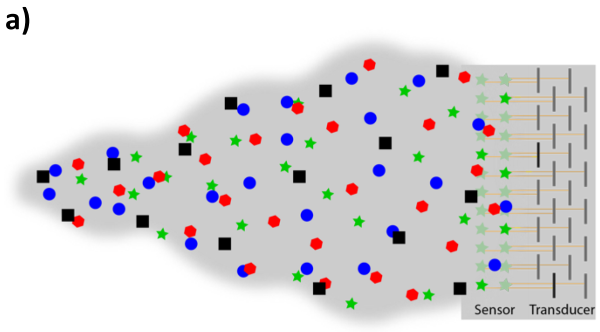

Figure 1.3 | Single and multi-component sensor schematics. a) Sensors highly specific to individual chemicals can provide exceptional sensitivity owing to the sheer number of integrated sensors. Higher sensor concentrations enable a higher rate of analyte-sensor chemical reactions, capable of eliciting high signal-to-noise ratios. **b)** Multi-component sensors are necessary for highly heterogeneous gaseous stimuli. Although these sensors do not display the fine detection limits of single-component sensors, they can be made responsive to a range of chemical species whose identity is dependent on incorporated sensor materials.

For pathophysiological conditions well characterized by an individual chemical species, targeted sensors can be highly effective for classification **(Figure 1.3a)**. These selective sensor technologies ought to be able to detect the volatile marker of interest at the appropriate concentration. Since exhaled breath aerosol consists predominantly of a mixture of nitrogen, oxygen, carbon dioxide, water vapor and inert gases, devices such as capnographs do not face significantly high sensitivity requirements[7]. However, in addition to these main breath constituents, more than 3400 other volatile biomarker species have been found at trace levels, though some of these are likely of exogeneous origin[34-36]. Selective sensors are constructed according to a lock-and-key type model, in which an individual chemical species and corresponding sensor interface are highly specific for one another. This ligand specificity enables high degrees of sensitivity, capable of achieving the necessary parts-per-million and parts-per-billion detection thresholds for some of these compounds. Nitric oxide, for example, is routinely present at low parts-per-billion levels in healthy individuals, yet average concentrations in those with bronchial asthma are increased three-fold[37-41]. Innovative functional transducer surface modifications, such as electrode platinization and electrochemical film layering, have been found to heighten nitric oxide sensitivity and selectivity, culminating in more robust patient classification[42-45]. Alternatively, exhaled acetone concentrations for healthy individuals have been noted to be between 300 and 900 parts-per-billion, whereas diabetics' levels often exceed 1.8 parts-per-million[46, 47]. During bouts of diabetic ketoacidosis, acetone concentrations can reach a thousand parts-per-million or higher **(Figure 1.4)**. Novel selective sensor designs have continued to improve device sensitivity reaching low parts-per-billion ranges[48-54]. Such highly selective sensors are simple, robust, and provide adequate discriminability for some diseases[55]. However, they do not offer sufficient diagnostic power for all, or even most pathophysiological conditions[45, 47]. The presence of confounding factors (i.e. concomitant disease, smoking

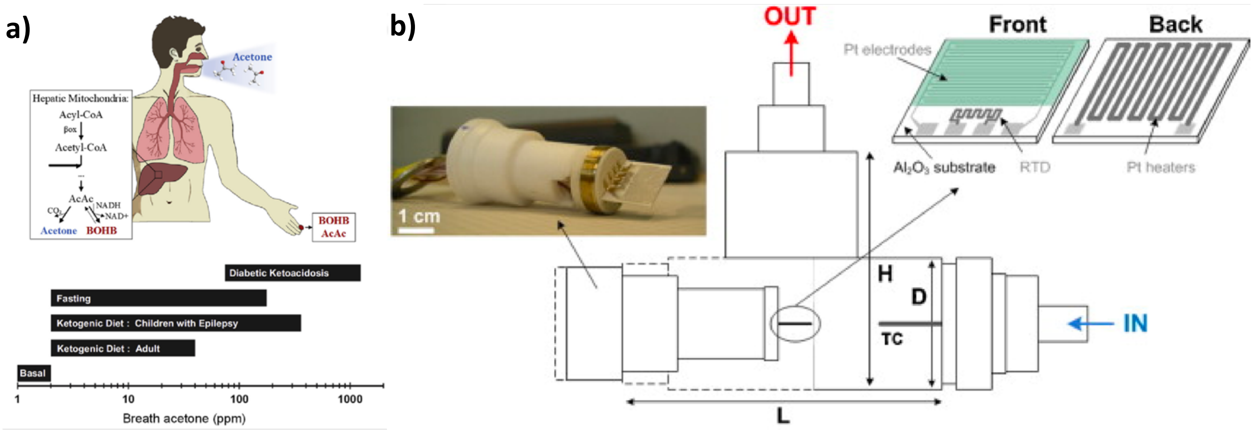

Figure 1.4 | Exhaled acetone concentrations are indicative of underlying ketogenic conditions. a) The overproduction of ketone bodies induces changes in blood chemistry. Elevated levels of breath-based acetone correspond to blood serum concentrations and have been observed for those experiencing ketogenetic conditions and diabetics at large. Reproduced from [1]. **b)** A portable chemo-resistive acetone sensor incorporating interdigitated platinum electrodes with a resistance temperature detector (RTD) is shown. Back-heating by the platinum electrode increases the sensitivity of silicon-doped tungsten oxide nanoparticles on the electrode surface with detection limits of 20 parts-per-billion. Reproduced from [50].

status, etc.) or large variations in individual breath-based VOCs, can complicate real-world diagnostic implementation[39, 41, 56-60]. The majority of diseases are complex phenomena that have multifaceted consequences on cells, tissues, and entire organs. As such, the immediate effects of a specific disorder can elicit downstream signaling cascades, increasing or decreasing levels of various primary as well as secondary metabolites. Devices that aim for high chemical specificity with narrowly tuned sensors are effective for a handful of diseases but are generally not well-suited for multi-component identification.

Instead of relying on single-component sensing methods for disease detection and classification, the majority of diseases have been found to be associated with altered levels of a host of disparate VOCs[15]. This suggests that multi-component discrimination techniques may offer superior diagnostic potential, especially for heterogeneous samples[61] **(Figure 1.3b)**. The breath profile of a particular individual is a snapshot in time reflecting a unique combination of genetic, dietary, environmental and lifestyle influences. As such, there may not be a linear correlation between any single biomarker and an underlying pathological state. That is, the concentration of a particular VOC found in a healthy individual may be the same as that found in a diseased patient. Even two patients expressing the same pathology will have some degree of variability in VOC concentrations, based on the resolution of the analytical technology. Multi-component sensors approach this challenge by integrating various sensor measurements to glean relevant stimulus information from a large proportion of the constituent volatile chemicals. Such systems are characterized by more degrees of freedom and superior discriminatory power than selective systems. Even for diseases well-characterized by individual chemical species, broad spectrum chemical analyses can offer superior diagnostic precision due to the idiosyncratic nature of breath samples[36, 62]. A number of multi-component gas sensing technologies have undergone rigorous laboratory testing with the goal of demonstrating sufficient discriminability to warrant clinical implementation.

Gas Chromatography-Mass Spectrometry (GC-MS)

One untargeted technology that has shown tremendous potential for analyzing breath samples is gas-chromatography mass spectrometry (GC-MS) (**Figure 1.5**). Gaseous samples are initially collected and concentrated onto an analyte trapping device, usually in the form of a sorbent tube or microextraction fiber. The matrix containing these adsorbed sample chemicals is then placed inside the injection port of a gas chromatograph. Here, an ultra-pure carrier gas is passed through the sample as the oven temperature is incrementally increased to facilitate analyte-sorbent desorption. With continual heating, chemicals are desorbed in accordance with their volatility before entering a capillary column—highly volatile components are desorbed at lower oven temperatures followed by the elution of those with lower volatilities at higher temperatures. Column- and molecule-specific properties determine the state phase probability and rate of transmission through the column. The larger and less volatile components will display longer column retention times and will elute later than smaller, highly volatile chemicals (**Figure 1.5b**). Prior to pairing with mass spectrometers, detectors such as flame-ionization and thermal conductivity detectors, were incorporated to measure the elution time of each molecule. However, similar retention times for compounds, such as pentane and isoprene, have been observed, confounding readout accuracy[63, 64]. The spatiotemporally stratified gas molecules are depressurized at the GC-MS interface before entering the mass spectrometer. Once the

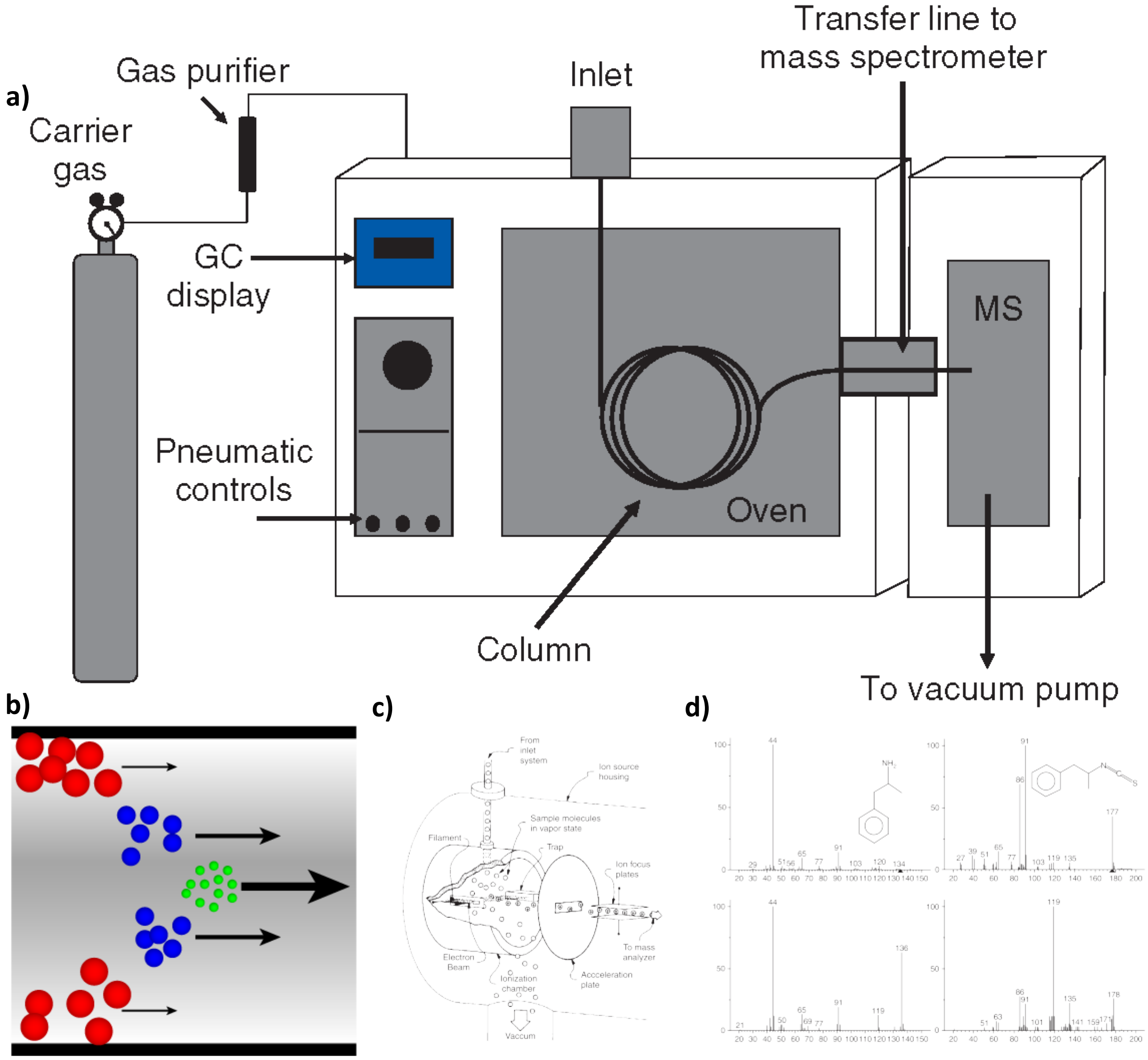

Figure 1.5 | GC-MS. a) GC-MS schematic illustrating separate components. Carrier gas is purified and passes over the heated sample at the sample inlet/injection port. Molecular separation occurs along the length of the capillary column. Spatiotemporally segregated analytes are ionized, fragmented, and separated by mass-charge ratio in the mass spectrometer (MS). **b)** Gas chromatography separates ions based on size and volatility, or gaseous vs. liquid state phase probability. **c)** Electron ionization schematic. An electron beam interacts with molecules of a low-pressure gas cloud. Proximal electrons energize the analyte molecule, cueing electron release and formation of a positively charged ion. **d)** Different ionization techniques can result in completely different fragmentation patterns, eliciting contrasting mass spectra. Amphetamine (*left*) and a derivative of amphetamine (*right*) were both observed to exhibit variability in fragmentation patterns based on the ionization technique. Reproduced from [65].

eluted chemicals have entered the mass spectrometer, they are bombarded with 70-eV electrons, ionized, and, with sufficient energy, rapidly fragment to smaller ions. The low-pressure environment of the mass spectrometer enables ion flow trajectories to be dictated purely by electromagnetic properties, with little to no influence from ambient air particles. The stream of ions travels along the mass-to-charge analyzer until striking a detector. An overall sample chromatogram indicates the relative quantity of unique molecules separated by their retention time. At each time step, a unique mass spectrum is constructed, detailing an analyte-specific molecular configuration. The unique separation techniques utilized by gas chromatography and mass spectrometry serves to significantly enhance molecular discriminability than using either one as standalone sensors[66, 67].

A decade after the first GC-MS publication in 1959, Jansson demonstrated the potential use of GC-MS for breath analysis by identifying a few breathborne VOCs, including methane, acetone, and isoprene[68, 69]. While experiments utilizing urine headspace vapors were analyzed to generate metabolic profiles[70-73], Pauling's successful identification of 250 compounds from exhaled breath first hinted at the power of gas sensors for medical volatolomics[74]. A subsequent experiment sought to link increased levels of sulfuric compounds to liver cirrhosis[75]. Research by Gordon and O'Neill facilitated the incorporation of whole-sample mass spectral matching algorithms to a public database to successfully distinguish lung cancer patients from healthy controls based solely on expired breath[76, 77]. Further work utilizing breath-based sensors as disease diagnostics by Phillips in the 1990s supported the notion that altered breath profiles were indicative of cancer[78] and also revealed a correlation with schizophrenia[79, 80]. The positive results garnered from these early studies spurred the development of novel sampling technologies[81-88] and protocols[7, 33, 82, 89-91], as well as a plethora of research into the VOCs involved in various pathogenic conditions[63, 92-115], with particular emphasis on lung cancer[19, 87, 88, 116-133]. Experimental findings by Barash et al., suggest that breath-based GC-MS analysis is even powerful enough to differentiate between disease subtypes caused by genetic mutations[134].

The resolution of GC-MS and related technologies has improved tremendously since their inceptions, with current day systems able to extract over 500 biomarkers from individual breath samples[36, 78, 134]. Owing to their high information content, GC-MS and other mass spectrometry techniques have been integral research tools for identifying novel compounds contained within heterogeneous samples. The elucidation of key compounds indicative of a particular stimuli or associated with a disease has enabled the fabrication of highly efficient application-specific targeted sensors. Moreover, VOCs common to both in vivo and in vitro experiments have supported the possibility of utilizing cell culture headspace as a proxy for exhaled breath under specific environmental conditions[135, 136]. This finding has facilitated proof-of-concept research on a broad range of novel gas-sensing devices for pathogenic and nonpathogenic VOC-profile analysis without the need for animal or human subjects[137-156]. GC-MS has shown comparable performance to standard diagnostic imaging techniques, such as CT and PET scans, while avoiding patient exposure to doses of ionizing radiation[157-161] and potentially reducing the associated high rates of false positive diagnoses[162, 163].

However, GC-MS remains largely sequestered to research laboratories owing to a host of undesirable attributes for a clinical diagnostic. The operation of such instruments especially for highly complex samples, such as breath, requires expert personnel. For any given sample, the technician must consider a myriad variables such as the operation mode (split vs. splitless), column oven temperature, type and velocity of carrier gas, thickness of the stationary phase, column length and diameter, etc.[65]. Additionally, the resolution and signal-to-noise ratio are positively correlated with the length of the capillary column. This necessitates longer sample processing times for heterogeneous samples in order to attain minimally separable chromatographic peaks[19]. Though GC-MS is touted as a highly sensitive analytical technology, sample pre-concentration is necessary for breath-based VOCs. This is due, in part, to the low concentration of biomarkers in the breath as well as the inefficiency of the mass spectrometer's electron ionization process, which only ionizes 0.01-0.001% of the total analyte molecules[65]. Furthermore, the high oven temperatures restricts GC-MS to analyzing compounds that can sustain thermal vaporization without chemical decomposition[65, 164]. While GC-MS is not likely to be of particular use as a point-of-care clinical diagnostic, it has conclusively demonstrated that breath-based biomarkers, potentially indicative of an underlying pathophysiological condition, are well within detectable ranges. As related instrument technology continues to mature, greater degrees of sensitivity will be possible, unveiling novel chemical species that may aid in our understanding of the underpinnings of a variety of disease states[65].

Ion Mobility Spectrometry (IMS) & High-Field Asymmetric Waveform Ion Mobility Spectrometry (FAIMS)

Another type of untargeted gas-sensing technology, ion mobility spectrometry (IMS), has also proven useful for disease detection and differentiation by using volatiles from exhaled breath samples (**Figure 1.6**)[165-167]. As the name suggests, this technology initially ionizes sample molecules, which allows for analyte separability based on the different mobility constants unique

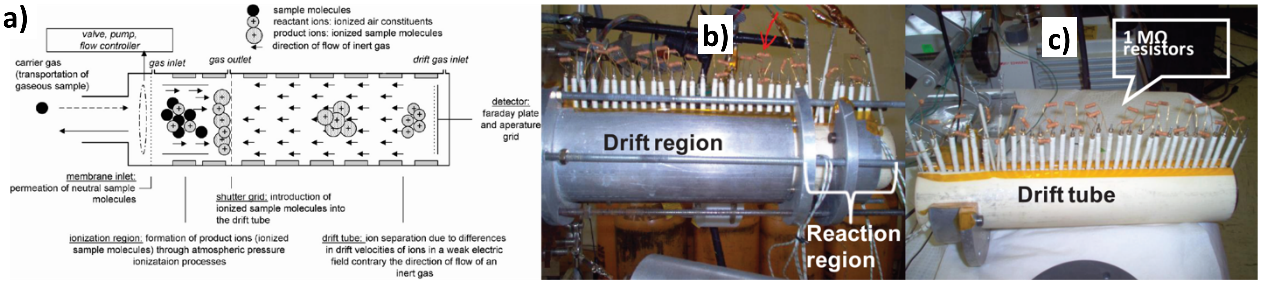

Figure 1.6 | Ion mobility spectrometry (IMS). a) Schematic illustrated IMS principles. Molecules are ionized in the ionization region before being intermittently passed to the drift tube. A carrier gas is applied in the opposite direction of ion flow, whose molecules collide with sample ions at differential rates based on cross-sectional area. Reproduced from [168]. **b)** Image of IMS drift region housing drift tube attached to reaction region housing faraday plate for ion detection is also depicted. **c)** Internal drift tube shown with attached electrical resistors to augment injected current in ring electrodes. Reproduced from [169].

to each type of ion. Most commonly, these ions pass into a trapping region where packets of them are intermittently released into the drift tube (**Figure 1.6a**). Within the drift tube, ions are exposed to a homogeneous electric field, permitting a higher drift velocity in ions with higher charges. Simultaneously an inert drift gas is propelled in the opposite direction of the electric field and ion trajectories. Larger ions tend to engage in more collisions with neutral drift gas molecules lowering their velocity relative to smaller ions. Therefore, once the ion gate is opened, the ion's overall mass and charge will determine the overall rate of migration and arrival time at the end of the drift tube. Here, spatiotemporally stratified ions can be detected to form a mobility spectrum or undergo additional analysis via the incorporation of tools like mass spectrometers. IMS has two important similarities to gas chromatography: the device can be operated at atmospheric pressures and the drift tube length determines spectral resolution. This latter feature constrains the miniaturization of drift tube-based IMS systems, especially for complex sample analysis (**Figure 1.6b**). While systems with circular drift tubes can be constructed to mitigate the resolution-size tradeoff[170], other variants of IMS, such as high-field asymmetric waveform ion mobility spectrometry (FAIMS), are more amenable to device miniaturization (**Figure 1.7**) [168]. In FAIMS, molecules of a carrier gas are ionized to form reactant ions, which collide with and bind to analyte molecules. These cluster ions are pulled into the filter region by

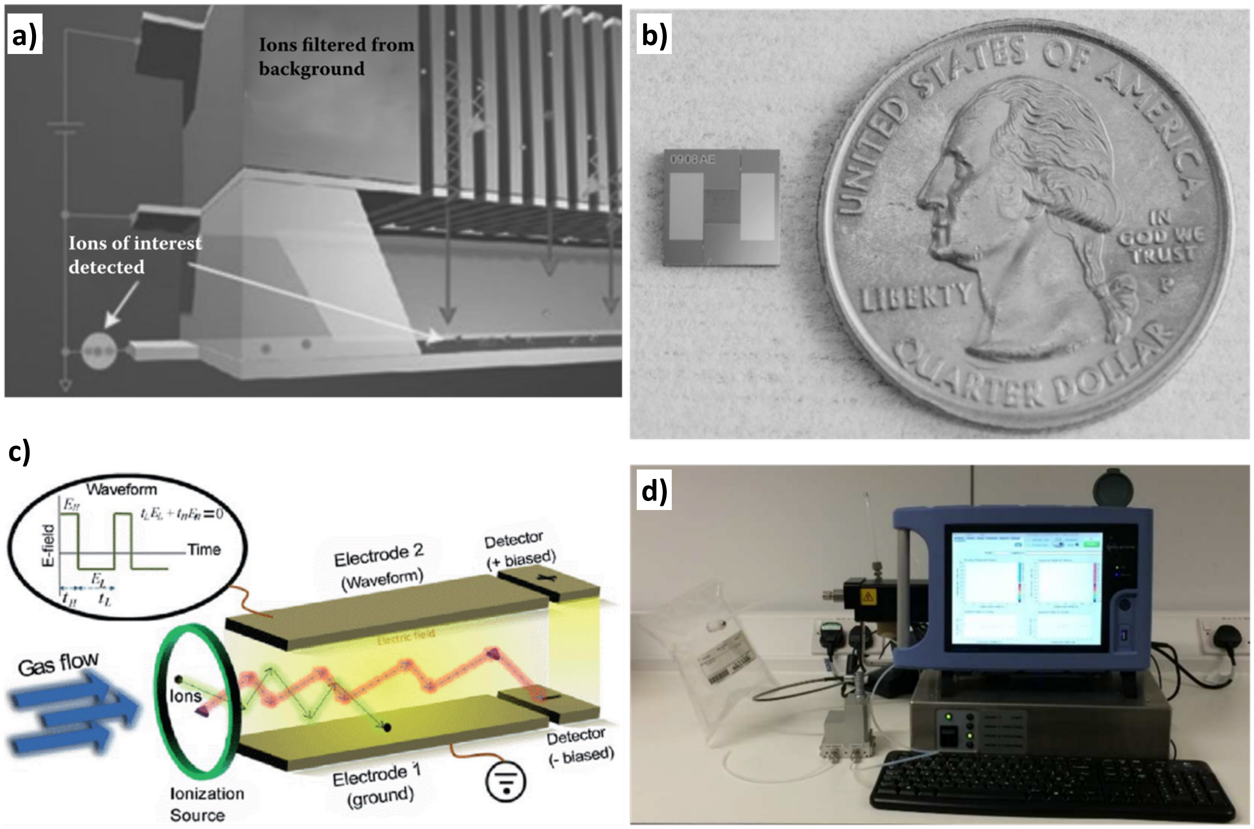

Figure 1.7 | High field asymmetric waveform mobility spectrometry (FAIMS). FAIMS technology is related to IMS but removes the need for an elongated drift tube and shutter, promoting device miniaturization and continuous stream injection. **a)** Schematic of FAIMS-based operation inside Owlstone Nanotech's μFAIMS analyzer. Molecules are ionized in the ionization region (not shown) and are transmitted through the FAIMS filter. The ions that follow stable flight trajectories and reach the detector electrode are determined by the radio frequency input as well as the compensation voltage. Ionization region and detector electrode are separated by a 300 μm gap. Individual electrode columns are 30 μm in width. Reproduced from [171]. **b)** Image of Owlstone Nanotech's μFAIMS analyzer. Reproduced from [171]. **c)** FAIMS working principle relies on the differential mobility of various ion species. Those with similar mobilities will pass to the detector electrode at the same compensation voltage. A full sample mixture can be analyzed by sweeping through a range of compensation voltages. Reproduced from [172]. **d)** Owlstone Nanotech's Lonestar with Atlas sampling system incorporating the μFAIMS analyzer for sample testing. Reproduced from [173].

the electrical field between the top and bottom electrode[174]. FAIMS-based sensors incorporate strong oscillatory radio frequency fields which alters the flight trajectory of the cluster ions. Simultaneously, a low-strength direct current compensation voltage is applied between the top and bottom electrode. By changing the compensation voltage, different types of ions will follow sufficiently stable flight trajectories to traverse the filter region and measured at the detector. Ions that follow unstable flight trajectories collide with and are neutralized by one of the electrodes. Sweeping this value through a preselected or experimentally determined range can produce a plot of ion current intensity as a function of the compensation voltage.

IMS-based devices are relatively new in the field of diagnostic volatolomics. Traditional applications of IMS were predominantly concerned with drug detection, explosive detection, and environmental monitoring[168]. One of the earliest studies applying an IMS sensor as a diagnostic tool demonstrated significant differences between the chromatograms of healthy individuals and those with lung infections[175]. Subsequently a number of studies have sought to provide support for IMS as a clinical diagnostics for a range of pneumological and nephrological conditions as well as those common in critical care[176]. Mobility spectrum chromatograms from healthy individuals were shown to be differentiable from those of individuals with lung cancer[177-180] and other diseases[166, 181-187]. Some evidence suggests that IMS devices can also be used to differentiate between disease subtypes due to genetic mutations[188]. As of late, FAIMS devices have been investigated owing to their attraction as point-of-care devices. They have proven effective in identifying various cancers from breath samples and urine headspace[97, 173, 189-191]. A number of commercial products have been developed, some of which are currently being tested in clinical trials (Owlstone, Thermo Fischer, Chemring, Bahia 21).

Having been routinely utilized for field-based applications, IMS and FAIMS sensors are quite robust and operable in a variety of environmental conditions. Additionally, the processing time for IMS and FAIMS devices is on the order of seconds to minutes, offering online or quasi-online sample analysis[168, 171, 192-196]. GC-MS requires sample pre-concentration on trapping materials before offline analysis. In contrast, IMS devices avoid this requirement as their detection limits can progress into the parts-per-trillion ranges[168]. Hyphenated IMS techniques with in-line pre-concentrators can even offer sensitivities in the parts-per-quintillion range[197]. A common struggle for breath-based gas sensing technologies is the high levels of moisture present in exhaled breath, capable of decreasing device sensitivity by more than 40%[198-200]. The incorporation of multi-capillary columns increases water retention time, enabling a gas chromatographic-like form of molecular pre-separation[175, 195, 198]. However, the removal of humidity from a breath sample can wash out many organic compounds and shift peak positions, significantly decreasing analyte identification accuracy[176, 201].

IMS and FAIMS technologies are powerful tools for analyzing gaseous stimuli, yet they are not without their drawbacks. These systems are restricted to only ionizable compounds and, unlike GC-MS, there is no general database against which to compare mobility spectrum chromatograms. Sample ionization often introduces radiation hazards[168, 197] and readouts for such technologies are rather complex, requiring skilled operational personnel. However, the largest concern when employing IMS and FAIMS devices is their limited resolution. Ions can cluster and interact in the ionization region (and drift tube if present) leading to overlapping chromatographic peaks[172, 197]. High resolution is likely critical for highly complex breath samples that can contain well over 500 compounds while only minute differences in a fraction may be relevant for diagnostic purposes. Novel ultra-high-resolution ion mobility spectrometers[202] and the selective use of hyphenated techniques can aid in analyzing specific chemicals present in complex mixtures, yet whether this will lead to a preference for IMS over GC-MS remains to be seen[172].

Electronic Noses

Untargeted chemical sensors such as GC-MS and hyphenated IMS/FAIMS can provide excellent insight into the underlying biochemical structure of a gaseous sample. Stand-alone IMS/FAIMS, while sacrificing specific analyte identification, permits portability, lower power requirements and a considerable degree of separation strength. Such technologies are sensitive enough to detect a large number of trace level chemicals present in exhaled breath, sometimes even without sample preconcentration. However, for complex diseases involving subtle concentration changes of numerous VOCs, these component-wise methods may not offer sufficient whole sample discriminability. Electronic noses, or enoses, strive to generate a qualitative readout of sample gaseous stimuli in its totality. Originally inspired by biological olfaction, they seek to incorporate numerous cross-reactive sensors and sophisticated signal compression algorithms, thereby generating stimulus-specific fingerprints. These “breathprints” can be conceptualized as a point in high-dimensional space, in which the number of dimensions is a function of the number of sensors[203]. The system design and combinatorial selectivity eliminates the necessity for high sensor specificity and engenders an immense encoding hyperspace, capable of classifying highly heterogeneous stimuli[204].

The introduction of cross-reactive sensors reduces the impact of confounding factors, such as inter-individual variability in breath profiles[205], since alterations of one or a few VOCs will have a negligible effect on the overall compound signal[36, 102, 206, 207]. Importantly, enose sensitivity and specificity correspond to the total amount of nonredundant information procurable by each individual sensor. As such, simply incorporating a higher sensor concentration density without diversifying response characteristics serves to increase overall system noise[208, 209]. This critical need for targeted application specificity in sensor design in conjunction with significant improvements in nanotechnology, microfabrication and materials sciences have fueled the development of novel enose systems.

The first enose, constructed by Persaud and Dodd in 1982, consisted of two tin oxide semiconductors that elicited a conductance change once analyte molecules interacted with ambient oxygen atoms on the metallic surface[210]. This metal-oxide semiconductor-based sensor encouraged future metal-oxide enose iterations to incorporate a variety of doped metals to alter analyte specificity. In these devices, combustion reactions occurring on the surface of the metal oxide particles, oxidize or reduce the host material and issue a change of electrical resistance (**Figure 1.8d**) [211]. By operating these enose devices at temperatures ranging from 200-500°C, reaction rates are increased, thereby enhancing sensitivity and selectivity[211, 212] assuming VOC breakdown is avoided[207]. Metal-oxide sensors have shown promising results for differentiating breath and urine samples of cancer patients and healthy controls[213-227]. Additional studies demonstrated metal-oxide sensors were effective in identifying conditions such as diabetes[228, 229] and renal failure[228, 230]. Yet such systems suffer from specificity limitations and are sensitive to environmental conditions[208, 211, 231].

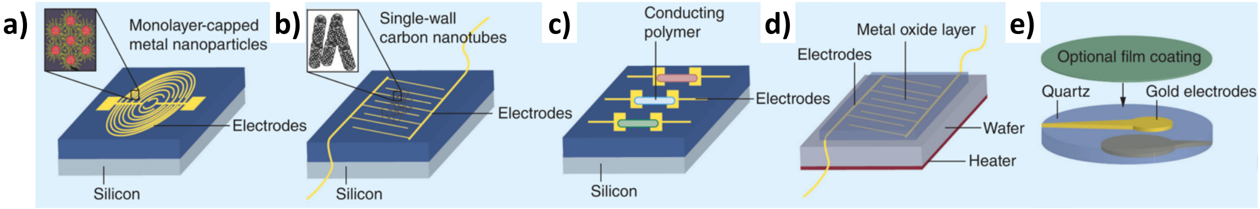

Figure 1.8 | Design schematics for various electronic nose technologies. a) Chemiresistor based on monolayer-capped metal nanoparticles. **b)** Chemiresistor based on single-wall carbon nanotubes **c)** Chemiresistor based on conducting polymers. **d)** Chemiresistor or chemicapacitor based on metal oxide film **e)** Quartz microbalance with selective coating. Reproduced from [27].

Devices incorporating conductive organic polymers offer an alternative to metal-oxide based enoses **(Figure 1.8c)**. Here, the conducting polymers serve as the analyte sensing and signal transduction element, with a pair of electrodes and a substrate material providing signal transmission and structural stability, respectively[232]. These systems pass a voltage across their electrode pair, eliciting current flow in the attached conducting polymer[233]. Adsorption of gas molecules to the polymer surface alters the electron flow, imparting a measurable change of electrical resistance[234]. As a medical diagnostic, conductive polymer-based enoses have been used to differentiate cancer patients from healthy controls[118, 235-241], though it is important to consider patient history prior to sampling as confounding factors could potentially skew breath profiles[242-244]. Such devices have also been investigated as a diagnostic for diabetes[245], asthma, and other conditions[246-248]. Enoses based on conductive polymers have been shown to be highly susceptible to water vapor, thus complicating online, point-of-care sampling[234].

Another common enose design is based on quartz-microbalance technology, which incorporates organometallic compounds for chemical adsorption **(Figure 1.8e)**. Upon adsorption, the gas molecules alter the mass and therefore the fundamental oscillating frequency of a quartz crystal. Chemical modifications to the associated organometallic material can adjust the selectivity of individual microbalance sensors. Such enose devices were among the first to demonstrate breath-based discriminability between cancer patients and healthy controls[249]. Subsequent studies indicated that quartz microbalances conjugated with sensitive metalloporphyrins can differentiate between cancer samples, healthy samples, and those of other non-cancer diseases[118, 249-260]. Interestingly, early stage classification was superior to that of later stages, suggesting unsuitability as a stage invariant disease diagnostic[252].

More recently, sensors based on various nanomaterials, such as nanocrystals, nanoparticles, or nanowires, have been incorporated into enose devices. The nanoscale dimensions not only promote device miniaturization, but the increased surface-to-volume ratio increases the rate of sensor—analyte chemical interactions[261, 262]. While individual devices vary in design specifics, all nanomaterial-based enoses consist of organic films or functional groups that coat the exterior of inorganic conductive nanomaterials to provide VOC adsorption sites. However, the manner of signal transduction can provide select system designs with unique sensing qualities, which may be advantageous in analyzing samples of a particular nature. For example, chemiresistive sensors utilize nanoparticles **(Figure 1.8a)**, carbon nanotubes **(Figure 1.8b)**, semiconducting nanowires, or a combination of such nanomaterials. Whereas carbon nanotubes and semiconducting nanowires display high sensitivity for polar compounds, they show little affinity for nonpolar molecules. In pre-clinical testing, devices incorporating these nanomaterials have demonstrated an ability to distinguish healthy individuals from those with various cancers[19, 101, 102, 106, 109, 114, 116, 134, 138, 263-273] as well as non-cancer diseases[274-277].

While the majority of preliminary enose volatolomics research was geared towards identifying volatile signatures of many common microbial pathogens[273, 278-310], recent research has focused on the utilization of enose devices as diagnostics for a variety of noncommunicable diseases. Enoses have a number of advantages inherent to their unique system design. Cheap costs, operation simplicity and real-time readouts offer a more ubiquitous appeal as point-of-care devices in primary and secondary clinical care. The multitude of e-nose designs offers significant flexibility. Yet, it may be difficult to determine the best sensor for a given task. Prior identification of key volatiles, through technologies such as GC-MS, can guide system design, increasing sensitivity and specificity to the molecules of interest. A single breath sample can contain hundreds of types of analytes with wildly differing chemical attributes. As such, a complementary approach by combining various bulk and nanomaterials may aid in

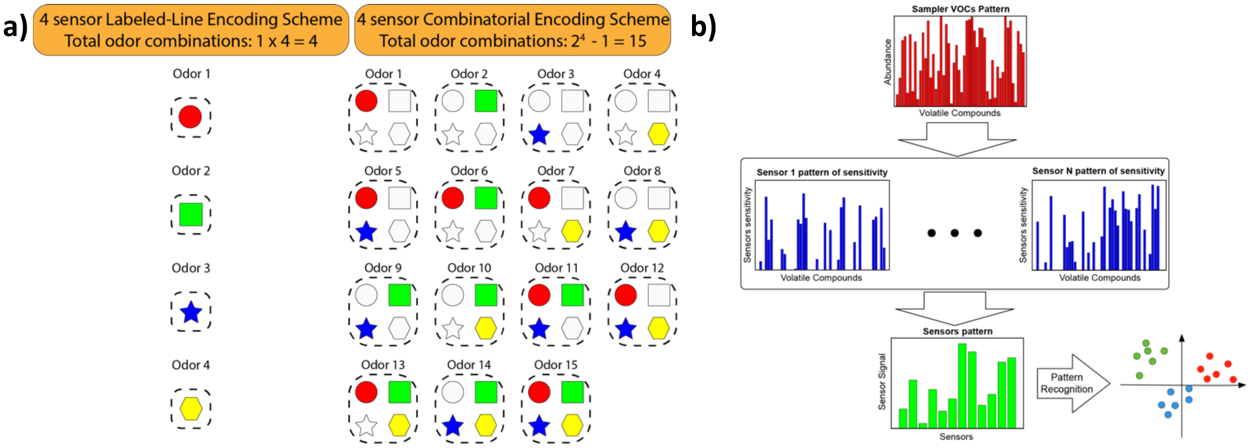

Figure 1.9 | Cross-reactive sensors enables a highly efficient combinatorial encoding scheme. **a)** *Left*, four sensors can encode a maximum of four stimuli in a labeled-line approach. *Right*, the same four sensors, working as a group and implementing different activation (ON-OFF) combinations, can encode a maximum of 15 stimuli. Adapted from [311]. **b)** Cross-reactivity of sensors enables sophisticated pattern recognition algorithms to map stimuli to unique parts of a high dimensional encoding hyperspace. Dimensionality reduction techniques can be utilized to reduce hyperspace dimensionality and enable response visualizations in an algorithm-specific subspace. Adapted from [1].

improved feature extraction and sample identification[312]. E-noses replace the intricate molecular separation techniques seen in more conventional technologies with cross-reactive sensors **(Figure 1.9)**, promoting device miniaturization and portability. The inclusion of sensors capable of responding to numerous analytes also endows e-noses with a robustness to environmental variability and background interferants. This feature is critical for applications such as breath analysis, in which the concentrations of volatile metabolites can be highly codependent. Enoses target the relative abundance of various biomarkers, which may be much more indicative of an underlying pathology than exact concentration changes.

The low-profile nature of enoses makes them an attractive gas-based diagnostic but enforces limitations. For the ideal point-of-care medical diagnostic, no pre-processing steps, such as the concentration of volatiles onto a sorbent material, will be necessary. Sensitivity is of particular concern when analyzing trace-level VOCs present in breath samples with any technological intervention. The majority of enose devices exhibit sensitivities in the parts per million and upper parts per billion ranges[313]. High relative humidity is a challenge for many technologies and enoses are no exception. Varying degrees of water vapor in each breath sample complicates system calibration and can induce variation in sensor responsivity[204, 209, 312]. The struggle to achieve high sensitivity as well as process humid samples can lead to significant losses of potentially useful chemical information. Moreover, sensor drift, characterized by a gradual change in output despite no change in input, can corrupt signals and accurate stimulus classification[231, 314, 315].

When designing an effective gaseous chemical sensor, it is essential to integrate technologies from discrete scientific domains. In order to optimize performance, the component limiting device efficacy must be identified and improved[316]. The sensor material interacts with the volatile molecules and, thus, serves as the first and most significant bottleneck for stimulus-related information. Moreover, the sensitive materials seem to exhibit an inherent tradeoff: high levels of specificity correspond to high levels of irreversibility[312]. Enoses attempt to find an optimal balance between the two so as to enhance device stability and longevity. However, this approach seems to significantly limit their chemical resolvability. Biological olfaction, from which enoses are inspired, has seemed to favor the latter, given the fact that human receptor cells only have a lifetime of a few weeks[317]. Olfactory receptors have also been shown to be more broadly tuned than the synthetic sensors of enoses, relying to a greater degree on their population-wide activity for odorant processing[318]. Apart from encoding stimuli as a single entity, these critical distinctions suggest that enoses bear little resemblance to biological olfaction[211]. Considering that living organisms are the ultimate sensing machines, it reasons that the demanding conditions of stimulus discrimination in the natural world have imposed stringent constraints on effective chemical sensors[319] that human manufacturing has yet to match.

Biological Olfaction

Olfactory-based chemical sensing is an inordinately difficult task, mandating precise detection and efficient encoding of millions of different odorants with strikingly disparate molecular configurations[320]. Yet, it can provide critical information about the surrounding chemical environment, including the presence and location of food, predators, and potential mates. For example, animals must differentiate between vegetation of different genotypes and growth stages to determine if they contain a sufficient nutritional payload. Foraging insects identify flowers that have already been visited to maximize the probability of reward procurement while minimizing energy expenditure[321-324]. More extremely, all organisms must differentiate between toxic and innocuous stimuli for proper growth and development[319]. In fact, the benefits of chemical sensing are so valuable that olfaction was one of the earliest senses to evolve and striking commonalities are seen between genetically dissimilar organisms[325].

In vertebrates, hydrophobic odorant molecules initially enter the nasal epithelium where they are bound and solubilized by odorant binding proteins. These proteins transport the molecules to the superficially located cilia of olfactory receptor neurons (ORNs). Here, binding affinity is dictated by the underlying chemical configuration of the odorant molecule as well as the receptor expressed on the cilia. The number and diversity of functional odorant receptors (ORs) permits substantial specificity to a broad range of chemicals and is thought to be indicative of overall olfactory ability[326]. Humans, for example, possess 388 functional OR genes (802 in total), enabling olfactory-based discrimination of up to more than one trillion stimuli[1, 327-329]. Canines, whose olfactory sensitivity is 100,000 times stronger than that of humans, display 713 functional OR genes (971 in total)[326]. Each ORN expresses only a single type of OR, however ORs can exhibit significantly different tuning curves, from acutely specific to very broad. One theory posits that ORs recognize particular features of odorants, with some being more ubiquitous than others, to allow for variable chemical recognition specificity. The axonal processes of all ORNs expressing a particular receptor innervate olfactory bulb neurons within one of many glomeruli, producing a topographically-specific epitope map[330, 331]. Owing to a dense network of inhibitory granule and periglomerular cells, glomeruli function as highly efficient information processors, providing a 100-fold decrease in the number of neurons necessary for signal transmission[332, 333]. This is accomplished by incorporating an oscillatory-based temporal component to the spatially distinct glomeruli, dramatically expanding the odorant encoding hyperspace **(Figure 1.10)** [334-336]. Extrinsic neurons, mitral and tufted cells, propagate action potentials to higher order brain areas that further interpret the incoming electrical signal[337].

The skeletal system offers immense structural stability, ultimately permitting vertebrates unique developmental adaptations and ways in which to interact with the physical environment[338]. Alternatively, insects utilize an exoskeleton, limiting growth potential and

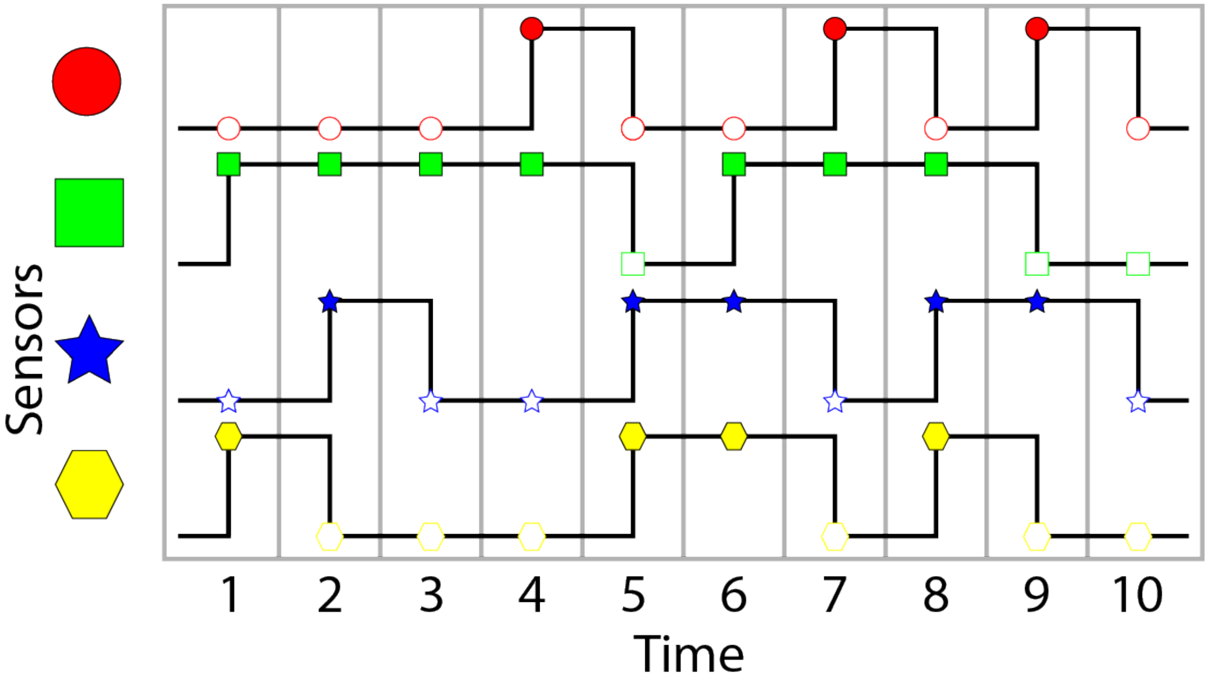

Figure 1.10 | Temporal encoding rapidly expands odor state space. The use of multiple sensors enhances the encoding state space in an exponential manner. Adding a dynamic temporal component, increases the encoding space even further. For example, using a set of only four sensors, each with two possible states (ON-OFF), and 10 time points, allows for over a trillion possible spatiotemporal signals ($2^4 = 16$, $16^{10}-1 = 1,099,511,627,775$).

total lifespan. As a result, insects have developed highly acute chemosensory abilities due to their reliance on olfaction for nearly all tasks, from food source localization to predator and prey detection to identifying potential mates. While many fundamental chemosensory mechanisms remain consistent with those of vertebrates, insects have evolved a number of adaptations that are well-suited to their ecological niches[339-341]. Odor perception in insects originates in microscopic hairlike structures, known as sensilla, that coat the surface of the antennae **(Figure 1.11c)**. Similar to the nasal epithelium in vertebrates, these sensilla house ORN dendrites that interact directly with odorant molecules. Once an odorant molecule is encountered, it enters a

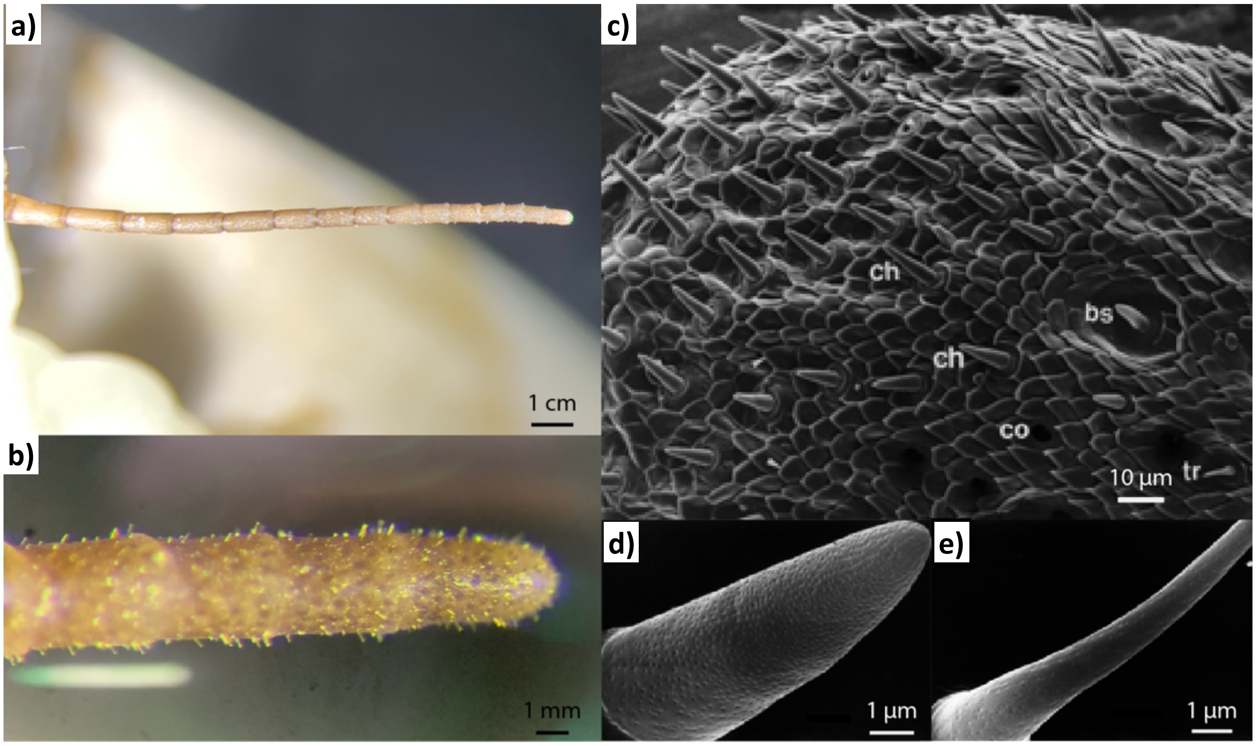

Figure 1.11 | Sensilla coat the locust antennal surface. a) Antenna depicting individual antennal segments. **b)** Antennal segments housing microscopic sensilla. **c)** Electron micrograph of distal antennal segment depicting various types of sensilla: ch- chaetica, bs- basiconica, co- coeloconica, tr- trichodea. **d)** Individual basiconic sensillum. Tiny pores along the cuticular surface allow molecule entry and subsequent ORN-analyte binding. **e)** Individual trichoid sensillum. Note the slender morphology of the trichoid sensillum vs. the basiconic sensillum in **d**. Reproduced from [342].

sensillum through tiny cuticular pores or spoke channels, where it is solubilized and transported to ORNs by odorant binding proteins. ORNs are the site for chemical reception and signal transduction and, as such, are of particular importance for chemical sensing. Structural studies

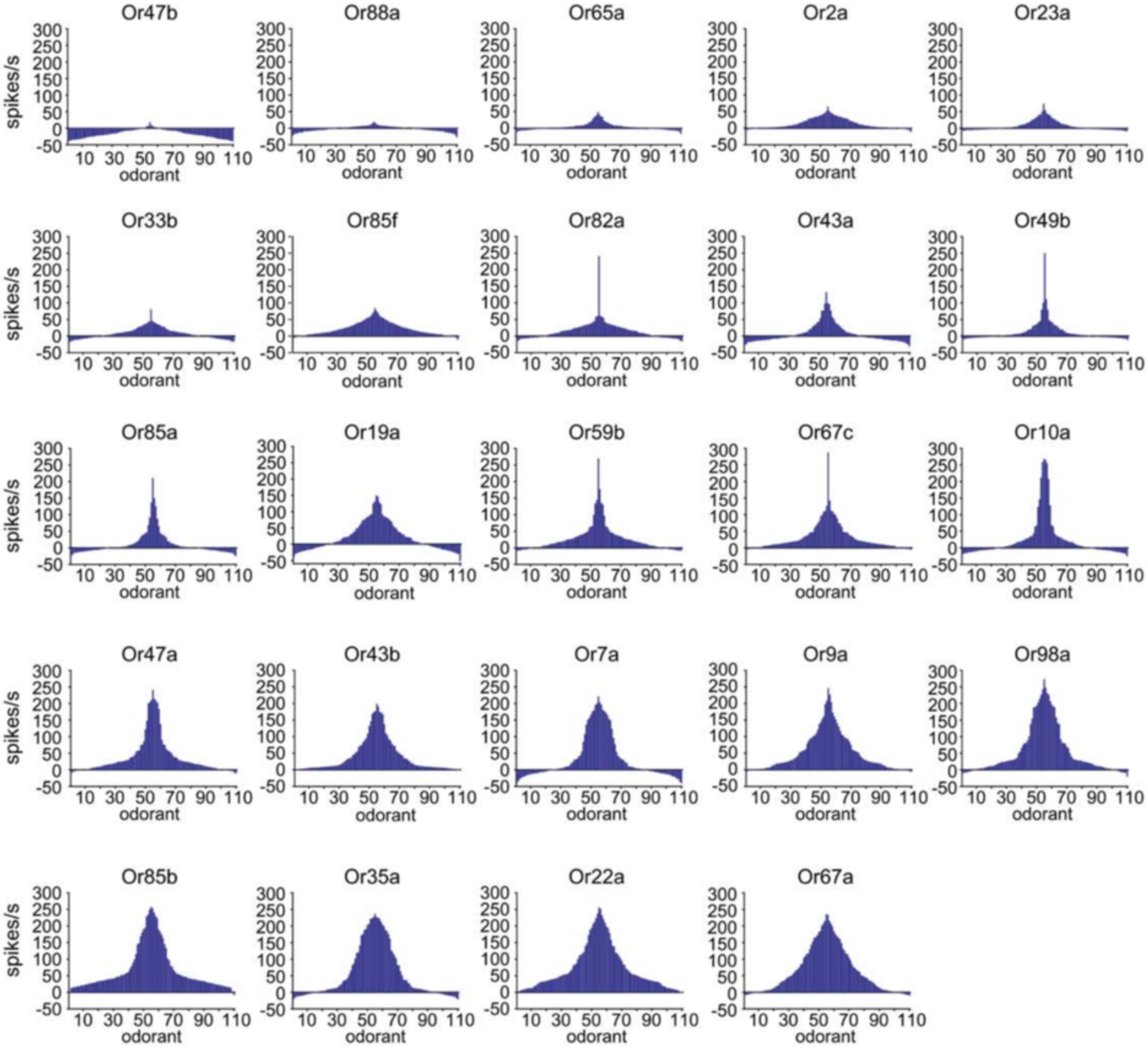

Figure 1.12 | Olfactory receptors display significant variability in chemical specificity. Functional responses of twenty-four olfactory receptors to a panel of 110 different odorants is shown for Drosophila melanogaster. Each panel indicates tuning properties of an individual olfactory receptor. The tuning curves are ordered according to the number of odorants eliciting a strong response. Through combinatorial coding, variable tuning properties allow for discrimination of a large number of diverse odorants at low concentrations. Reproduced from [343].

have demonstrated that densities of olfactory receptor sites can reach 30,000 per μm^2[344]. ORN response properties are dictated by the expressed olfactory receptor and can exhibit broad molecular specificity, responding to hundreds of different analytes, or very high selectivity with strong binding affinities for one or a select few **(Figure 1.12)**. Insects display a number of morphologically and functionally disparate olfactory sensilla. Sensilla basiconica, the most abundant type, contain a high density of pores, whereas sensilla trichodea contain far fewer, thereby limiting the rate at which molecules can enter and bind to ORNs. Moreover, the internal configuration of sensilla appears to be species-specific. Whereas sensilla basiconica house either two or four ORNs in *Drosophila melanogaster*[345], in locusts they can house anywhere between 20 and 50[342]. The presence of more neurons within an individual sensillum introduces a competitive ligand binding environment subsequently altering the ionic concentration gradient experienced by any one neuron. Unlike the metabotropic OR receptors found in vertebrates, evidence suggests that invertebrate ORs form heteromeric ionotropic transmembrane channels that allow direct ion influx upon ligand binding[346, 347]. This theory has been corroborated by molecular studies[347, 348] as well as the low-latency of odorant-based electrophysiological and behavioral responses observed in a variety of insect species[349-351]. ORNs exhibit low levels of spontaneous activity, but upon ligand binding, response dynamics of individual neurons and entire neural ensembles shift dramatically. The spontaneous baseline activity presents an ingenious method for increasing the chemical encoding state space. Not only can odorant binding cause unique upregulations in spiking activity, but others, oftentimes aversive odorants, can significantly reduce firing rates. While at the cost of a slight increase in energetic output necessary for the spontaneous activity of these neurons, an individual neuron can demonstrate additional unique firing patterns to incoming stimuli. Efferent signals are transmitted along the ORN axons into glomeruli of the antennal lobe[352]. Most insects, including *Drosophila melanogaster* and *Apis mellifera*, project receptor-specific ORN axons to one or two glomeruli within the antennal lobe, closely resembling the uniglomerular branching patterns observed in the olfactory bulb of vertebrates[353-358]. However, the antennal lobe of most insects contains an order of magnitude fewer neurons and glomeruli than are found the vertebrate olfactory bulb. Here, a complex network of inhibitory local neurons induces 20-30 Hz oscillatory cycles that are essential for odor recognition[359, 360]. Additionally, the signal processing within the antennal lobe has been shown to amplify weaker signals as well as mitigate undesirable chemical noise[361, 362]. This oscillatory behavior not only synchronizes the activity of efferent projection neurons to transmit action potentials to higher-order processing regions, but also increases the total number of encodable stimuli. Inclusion of a temporal component seems to be essential for providing organisms with high olfactory resolution, necessary for interpreting complex stimuli and differentiating similar odorants[363, 364]. Afferent signals become increasingly sparse in higher order brain regions as neuronal divergence occurs and neuronal tuning curves show very high signal specificity[360, 365-367].

While the low number of neurons in the insect olfactory system seemingly ought to endue gross detection limits and poor chemical differentiation relative to vertebrates, insects are equally or more potent in their sensitivity and discrimination capabilities[368]. Separate studies have found moths to elicit an observable physiological response to a single or tens of chemical molecules[369, 370]. Exactly how such low detection limits are achieved is an active area of

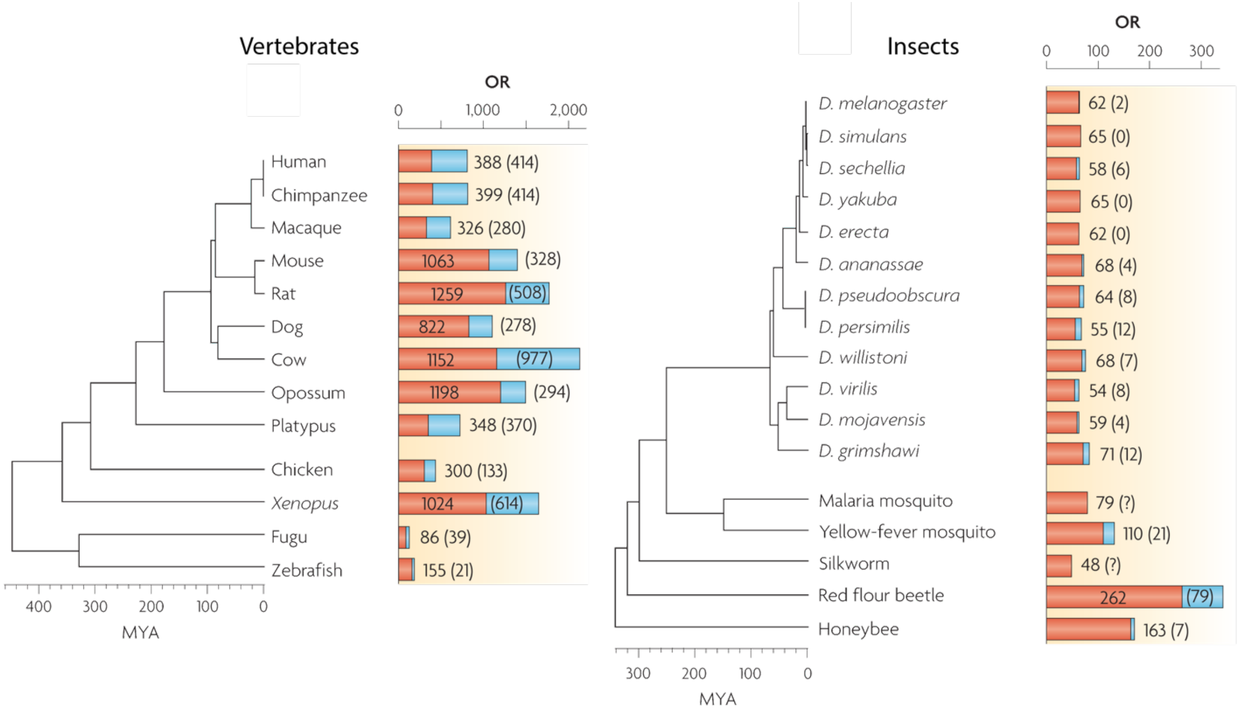

Figure 1.13 | Olfactory receptors display significant variability in chemical specificity. The red and blue bars represent the number of active and pseudogenes, respectively. Vertebrates exhibit significantly more olfactory receptors (OR) than insects. Moreover, they have a larger portion of disrupted pseudogenes that no longer encode for functional olfactory receptors. This suggests the development of and heavy reliance on sensory abilities other than olfaction. While insects display approximately an order of magnitude fewer olfactory receptors than vertebrates, they exhibit alternate coding schemes enabling highly acute chemosensation. Reproduced from [371].

research. The heavy reliance on olfaction has caused insects to retain many more functionally active ORs than their vertebrate counterparts **(Figure 1.13)**. The limitation of expressing a low number of neurons for sensory processing is likely also significantly mitigated by the intricate network dynamics observed in the antennal lobe. One key anatomical difference is that ORN axons within the olfactory bulb primarily innervate extrinsic neurons directly as well as indirectly via interneurons, such as granule cells[372]. In the antennal lobe, however, ORNs only form polysynaptic connections to projection neurons by way of local neurons, with no direct input[368]. Additionally, extraglomeruluar synapses are present in the olfactory bulb, whereas none have been observed in the antennal lobe[333, 368]. Exactly how these anatomical disparities alter functional aspects of olfactory encoding remains to be seen, yet insects have been found to display exceptionally high levels of olfactory acuity based on a significantly reduced neural network.

Biosensors & Bioelectronic Noses

The prowess of animal olfaction has been long recognized by humans. The domestication of dogs, for example, first allowed humans to take advantage of the canine olfactory system and behavioral responses for prey localization during hunting or fumes indicative of dangerous environments. The sensitivity, selectivity, generalizability and response rapidity of canine olfaction cannot be matched by current state-of-the-art manmade sensors[233]. Understandably, canines have proven highly effective for a number of applications from the detection of explosive compounds[373-378] to identification of human disease states[379-386]. Since the first anecdotal reports of canines' abilities to recognize various forms of cancers in their owners[387-390], research utilizing sniffer dogs as medical diagnostics has shown promising findings. Though results vary due to lack of standard training and testing regimens, canines have demonstrated impressive discriminatory power in identifying samples associated with lung, breast, and skin cancer, among others[225, 391-406].

In addition to expressing more ORs than humans, dogs' enhanced olfactory abilities stem from a substantial increase in nasal epithelium surface area, permitting a higher density and 20-40 fold more total ORNs **(Figure 1.14)** [355, 407]. As a result, the sensitivity and specificity of canine olfaction, especially among variable background interferants, is exceptional, with detection levels at 1-2 parts-per-trillion[391, 399, 408-410]. Thus, it is understandable that the

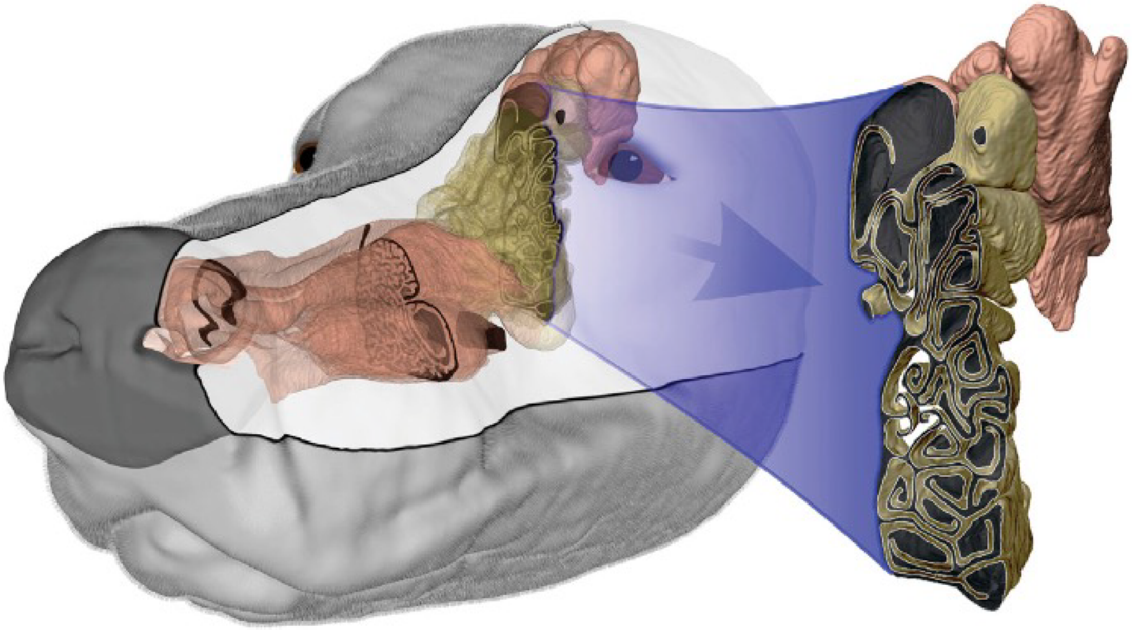

Figure 1.14 | The highly convoluted nasal epithelium of canines enables impressive olfactory abilities. The structural adaptation of a enables a significant increase in ORN density. In conjunction with the wide variety of ORNs, canines can detect a broad range of chemical stimuli with sensitivities as low as 1-2 parts-per-trillion. Reproduced from [411].

sensitivity of artificial systems pales in comparison to biological olfaction, given that most devices contain a maximum of a few dozen sensors. Furthermore, the high water vapor concentration present within biological samples, while a significant concern for analytical devices, actually enhances canine olfactory abilities[412]. Nevertheless, sniffer dogs for disease detection are not without their limitations. Since canine chemical reception is inherently linked with respiration, only approximately 12-13% of inspired air reaches the olfactory neuroepithelium, thus wasting a fair amount of otherwise useful chemical information[411]. Highly standardized training protocols that often last weeks or months must be adopted for a particular stimulus[413, 414]. Furthermore, easily interpretable binary behavioral responses limit readout intricacies and the amount of stimulus-related information. Other models utilizing rodents to detect tuberculosis via sputum samples have elicited positive results with minimal testing time relative to canines[415-419]. While rodents express even more ORs than canines and are not easily influenced by a specific handler, they face similar sampling and readout challenges. Animal models mitigate the sensing limitations seen in manmade technologies, however reliance on behavioral readouts significantly hinders signal saliency.

To bypass many of the limitations of using current animal models as chemical sensors, researchers have looked to invertebrates, which exhibit a much wider dynamic range than that of their vertebrate counterparts[420]. A few studies have determined that the nematode, *Caenorhabditis elegans*, can be genetically modified to reliably exhibit stereotypical chemotactic behaviors when presented with explosives[421], prominent tuberculosis biomarkers[422], and cancer urine samples[423-428]. The parasitic wasp, *Microplitis croceipes*, has been explored for its use as a gaseous sensor for a variety of VOCs[429-431]. Detection limits were found to be 10-fold lower than those for a common electronic nose[432]. While displaying very high sensitivity, the wasps did not respond to some standard alcohols[429, 433], suggesting a limited range of chemical specificity.

The chemical sensing abilities of higher order insect species exhibiting more complex olfactory circuitry and discriminatory power have also been investigated. Field studies with honeybees, *Apis mellifera*, have shown them capable of detecting explosive vapors at parts-per-billion and parts-per-trillion concentrations, surpassing state-of-the-art devices based on IMS/FAIMS technologies[434-437]. For medical purposes, sniffer bees can be taught to elicit a proboscis-extension behavioral response when presented with various compounds associated with tuberculosis[438]. A prototype breath sampling device has been developed intended to screen patients for various diseases based on the behavioral responses of pre-conditioned honeybees[439, 440]. Like canines, bees have evolved in naturalistic conditions, permitting excellent detection sensitivity for humid samples or samples among humid environments[434]. In the moth, *Manuduca* sexta, King et al. showed that olfactory-induced electromyographic signals could be used as an electrical proxy for a behavioral readout[441]. The technological application allowed for a finer level of discrimination than binary behavioral responses, however, the insect still necessitated a training period to associate muscular activation with the processed neuronal signals. While insects do not require significant training times (hours-days)[442], basing stimulus identity on behavioral readouts, whether vertebrate or invertebrate, requires that they be preconditioned to associate a reward with the intended stimulus.

In an effort to remove this bottleneck, biohybrid chemical sensors have predominantly sought to incorporate low-level neural correlates, such as specific olfactory receptors and even entire insect antennae. Antennal-based electronic noses target either neural activity from a large number of ORN axonal processes across the antennal flagellum or a more select group of ORN dendrites located within individual sensilla. For whole-antennae electroantennography (EAG), the electrical potentials of ORN axons are recorded by metal or saline-filled glass electrodes. Despite reflecting the aggregate activity of a large neural population, resulting readout amplitudes and shapes roughly correspond to the concentration and identity of the presented odorant stimulus[443-445]. A number of EAG technologies have been developed since its inception, including portable antenna-on-a-chip devices[444, 446-448], multi-antennae arrays[449-452], and hyphenated GC-EAG systems[449, 453-456]. EAGs have largely been used to investigate insect response profiles to a variety of pheromone components, given their strong attunement to pheromone blends[457]. Other EAG devices have also shown promise for more general chemical-sensing applications[458-463], detecting parts-per-trillion concentrations for some odorant species with the incorporation of signal amplification technologies[464-468]. In addition to chemosensation, various types of sensilla respond to a variety of input modalities, such as temperature, humidity, and mechanical stimulation. The non-specific recording technique employed by EAGs necessitates stringent environmental controls to mitigate the influence of such non-chemical signals. The longevity of such devices has also been of concern. Whereas antennae-only setups enable device miniaturization, satisfactory readings last for approximately 30 minutes[446]. Whole animal EAG recordings, in contrast, can be continued for several days and are ultimately limited by the total lifetime of the incorporated organism[443]. The main limitation of electroantennogram technology stems from the fact that the electrical potentials represent the summation of activity of a large population of ORNs. This reduces the overall chemical specificity as individual ORN responses, which may contain feature-specific information, likely only minorly contribute to the aggregate population-wide signal. As such, information from sparsely firing or smaller populations of narrowly tuned neurons that would otherwise transmit critical stimulus features to the antennal lobe may be irresolvable[449].

Alternatively, sharp metal or glass electrodes can be inserted into individual sensilla to record electrochemical alterations within the extracellular lymphatic solution surrounding ORN dendrites to enhance chemical specificity. These sensilla-specific recordings (SSRs) offer lower detection thresholds and effective neuron differentiation via spike amplitudes[449, 455, 469-473]. Recordings from diverse odor panels have demonstrated rich temporal response dynamics based on stimulus identity, with each neuron responding to a limited subset of odors[457, 474-

482]. SSRs even elicit clear responses to a number of natural stimuli as well as biologically irrelevant odorants, such as those from explosives and illicit drugs[483, 484].

Whereas EAG recordings are characterized by their gross neural population-wide resolution, SSRs occupy the alternate end of the spectrum. The high spatiotemporal precision enables intricate analyses of fine-scale biochemical processes occurring within individual sensilla; however, it also significantly restricts scaling up associated recording systems to attain a broad response profile from disparate sensilla. Moreover, the small profiles and high impedances of SSR electrodes make them vulnerable to signal contamination via electrical interference.

In addition to electrode-based recordings, transgenic organisms and fluorescent dyes can be used to visualize intracellular calcium concentrations that are indicative of underlying neural activity. In vivo calcium imaging of the antennae of fruit flies bypasses the challenge of simultaneously targeting multiple disparate sensilla by incorporating a relatively wide field of view. This sensillar-ensemble technique has been used to successfully discriminate between various odorants[485-487] as well as the volatiles associated with cancerous and healthy cell cultures[488]. However, most imaging techniques for odorant encoding in insects have targeted second-order neurons within the antennal lobe. Projection neurons, the efferent cells of the antennal lobe, exhibit a number of key features elevating their ability for stimulus encoding and candidacy for bioelectronic interfacing. Relative to ORNs, PN responses show superior reliability and are more broadly tuned, increasing the stimulus related information attainable from any one cell over time[489-491]. This is in large part due to the intricate inhibitory network of local neurons as well as reciprocal PN-LN interactions, which are responsible for sublinear signal transformations between ORNs and PNs[491-496]. Calcium imaging of antennal lobe PNs has shown odor-specific glomerular activation in multiple invertebrate species, including locusts[497], honeybees[498-503], and others[485, 504-507]. However, the reliance on optical methods restricts neuronal analysis to visible glomeruli and the temporal resolution of such technologies is too low to reveal fast dynamic effects[499-501]. While calcium imaging permits the differentiation of various stimuli, the lack of high temporal resolution likely impairs discriminating between complex, similar odorant mixtures. Since 20-30 Hz oscillations are essential for efficient signal transmittal by projection neurons, technologies with courser sampling rates will promote information loss. Calcium signals are not always correlated with neuronal action potentials and increases in fluorescence can be observed due to subthreshold activity[497]. Alternatively, electrode-based recordings are not restricted by the relatively slow kinetics of calcium indicators or limiting optical parameters, such as tissue-induced light diffraction[508-510]. Numerous studies have shown that odorant-induced projection neuron activity can be used to discriminate between a plethora of natural stimuli using electrode-based technology[360, 362, 491, 511-522]. Taking this approach a step further, Saha et al. demonstrated the efficacy of an insect biosensor for identifying varying concentrations of explosive compounds, which have played no part in guiding olfactory sensory evolution[523].

Forward Engineering Novel Insect Biosensors

Our forward-engineering approach for chemical gas sensing combines a highly sensitive sensor with broad-ranging specificity and an efficient functional processing scheme optimized to elicit highly discriminable spatiotemporal response patterns. The decoupling of olfactory receptors and/or antennae from the dense network of the antennal lobe would not be a significant bottleneck if the inner dynamics of biological olfactory systems had been sufficiently elucidated.

Even more extreme, researchers pursuing gas-sensing devices based on cross-reactive sensor materials, exclude biological sensors and, therefore, any downstream circuitry. This has contributed to the inability of enoses, for example, to process natural stimuli as rapidly and efficiently as the biological olfactory system it aims to emulate. By tapping into the extrinsic neural signals of the antennal lobe, we posit that we can interpret the intricate spatiotemporal response patterns as encoding for key volatile biomarkers seen in the exhaled breath of diseased patients. Moreover, we suspect that the massive encoding state space affiliated with such processing schemes is powerful enough to differentiate between small, few-component variations in highly heterogeneous mixtures. Our rationale for intervening at the point of the antennal lobe is rooted in functional neurobiology. The substantial convergence of chemical signals to a relatively small number of extrinsic neurons permits maximal information extraction by a finite number of microelectrodes. The spatiotemporal response patterns are amenable to high-level, time-based signal processing analyses and ultimately may underly a gas sensing system with discriminatory power superior to that of current state-of-the-art manmade technologies.

CHAPTER 2 | METHODOLOGY

In order to record precisely timed stimulus-evoked neuronal signals, a number of independent technologies were integrated.

Odorant Delivery

A cylinder of purified zero-contaminant air provided all supply air to a commercial olfactometer (Aurora Scientific, 220A). The olfactometer can deliver highly controlled concentrations of gaseous odorant stimuli with precise timing. Upon sequence initiation, a stream of clean supply air equal to that of the experimenter-determined total air flow rate flowed through mass flow controller three (fresh air line) via a 1/16” diameter polytetrafluoroethylene (PTFE) tube to a final solenoid valve. Another stream of clean air was sent through the other two mass flow controllers via similar PTFE tubing. Mass flow controller two (odor line) passed a percentage of the total air flow rate predetermined by the experimenter. The remaining air flow equal to that of the total air flow rate minus the odor line air flow rate was directed through mass flow controller one (dilution line). The odor line and dilution line joined as air streams from each line mixed together upstream of the final valve. The final valve directed the incoming air lines one of two ways: to an exhaust line or to a thirty-centimeter-long stimulus flow line, the end of which was positioned approximately two to three centimeters from the most distal antennal segment. During interstimulus intervals, the vial inlet and outlet valves remained closed. Clean air from the odor line continued through the mixing valve where it mixed with clean air from the dilution line. Air from the fresh air flow line was directed via the final valve towards the insect antenna, while combined dilution-odor line air was directed via the final valve towards exhaust. Five seconds prior to stimulus delivery, vial inlet and outlet valves opened while the mixing valve closed. The clean air from the odor line carried the vial headspace contents through the vial outlet valves until combining with the clean air from the dilution line. The final valve remained in the unactuated state, directing clean air to the insect and odor-laden air to exhaust (**Figure 2.1a**). After receiving a stimulus delivery signal, the final valve was actuated, directing clean air to exhaust and odor-laden air to the insect (**Figure 2.1b**). Stimulus periods lasted four seconds in duration, at which point, the final valve returned to the unactuated state. One second after returning to the unactuated state, the vial/flask inlet and outlet valves were closed to ensure the

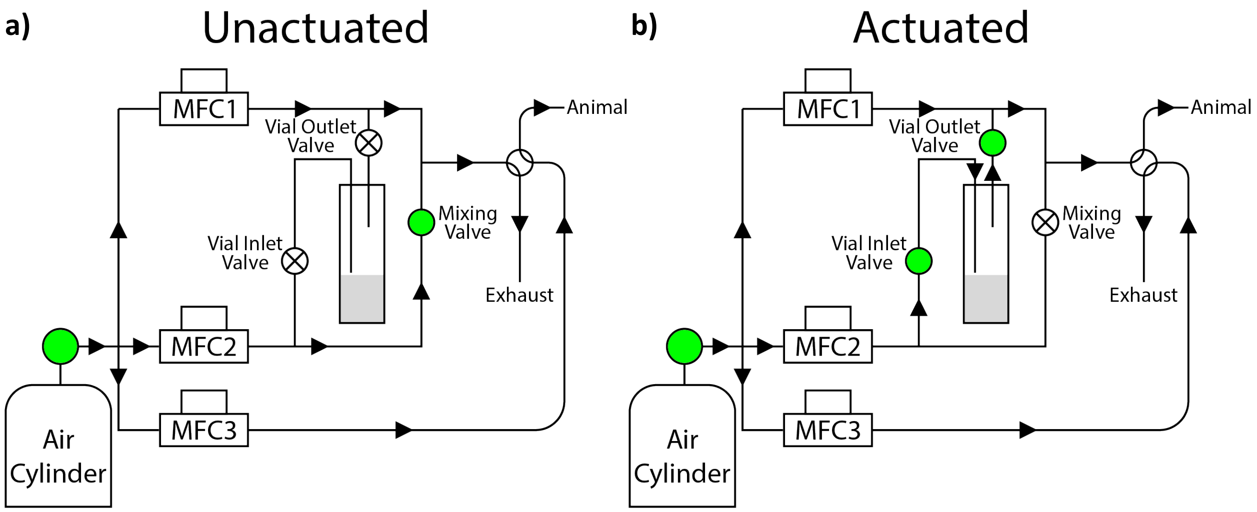

Figure 2.1 | Olfactometer flow design schematic (adapted from Aurora Scientific). Mass flow controller 3 (MFC3) passes the total flow rate of clean air to the final valve via the clean air flow line. An additional allotment of clean air equal to that of the total flow rate is split between mass flow controller 1 (MFC1) and 2 (MFC2), the dilution and odor lines, respectively. The path of the air travelling through MFC2 is dependent on the state of the olfactometer. **a)** Olfactometer configuration in the unactuated state. The vial inlet and outlet valves remain closed while the mixing valve is open. Clean air from the odor line combines with that of the dilution line to achieve the total flow rate. The final valve directs this portion of clean air to exhaust, while directing the clean air from MFC3 to the insect antenna. **b)** Olfactometer configuration in the actuated state. The vial inlet and outlet valves open while the mixing valve remains closed. Clean air from the odor line travels into the vial, disrupting the sample headspace, and recombines the odor-laden air with clean air from the dilution line. The final valve directs this portion of clean air to the insect antenna, while directing the clean air from MFC3 to exhaust.

headspace sufficiently repopulated with odorant volatiles prior to successive stimulus deliveries. This protocol was designed to maintain a constant flow rate through the stimulus flow line, thereby eliminating any potentially confounding neuronal responses due to a change in air pressure. A six-inch diameter funnel pulling a slight vacuum was placed immediately behind the

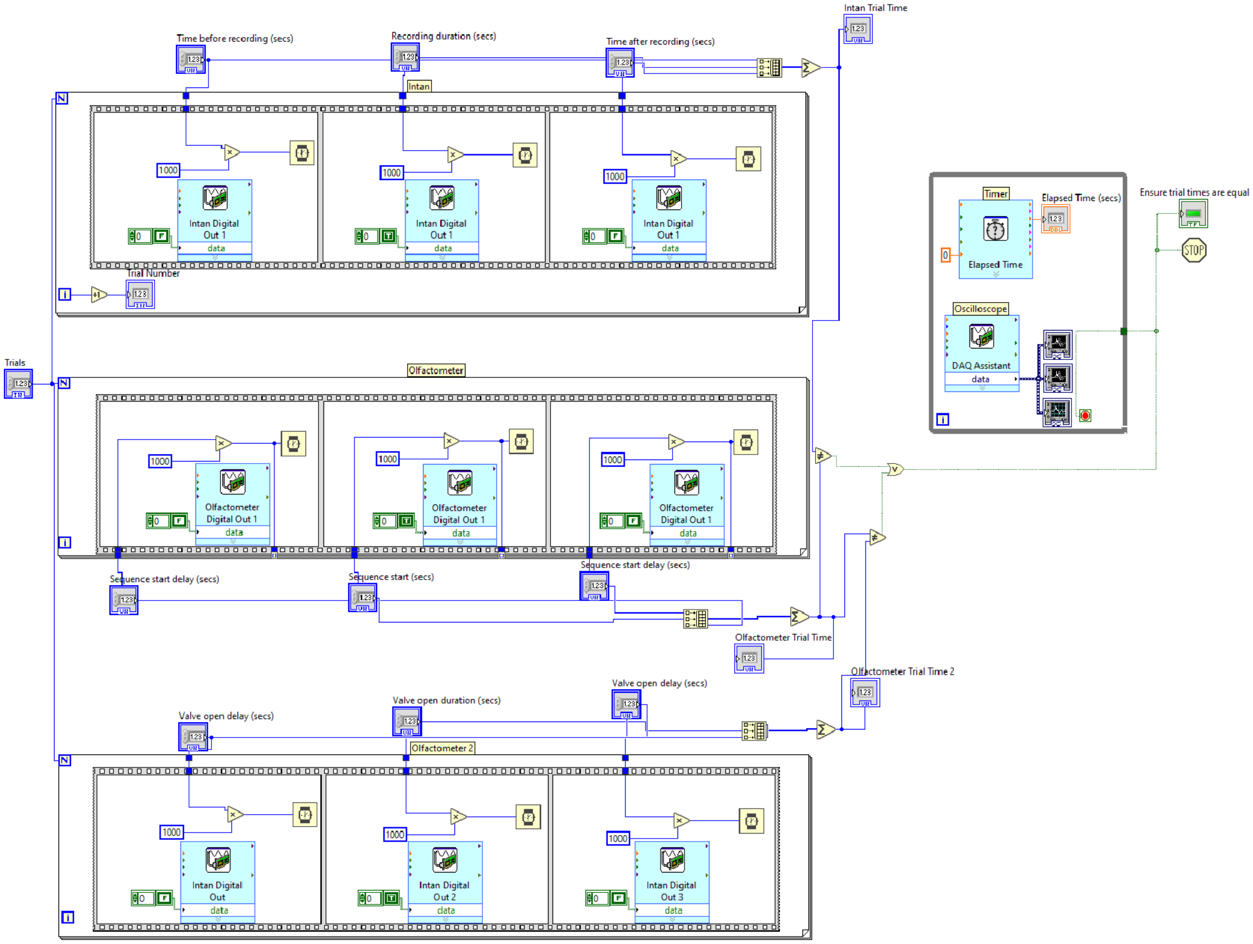

Figure 2.2 | Odor Delivery Program. Labview (National Instruments) block diagram depicting clock synchronization controller schematic. The three sequences depict three independent clocks. The top row corresponds to the clock determining the absolute times to record and save neural signals. The middle row determines the timing of the TTL pulse to begin the olfactometer challenger sequence. The bottom row guards the triggering of the final valve on the olfactometer. Users selected the number of trials to run. Electronic feedback loops were installed to the accompanying DAQ assistant. The right-hand side of the block diagram displays plots for the outgoing signals to ensure timing of each clock occurred as expected. If the total time selected for any of the clocks was not equal, the program would not execute and throw a warning.

insect to ensure swift removal of odorants. Each stimulus was repeated five times with an interstimulus interval of one minute. The order of stimuli was pseudorandomized for each experiment.

A multifunction I/O device was installed into the computer and connected via a multifunction cable to a terminal block. This hardware installation allowed for signal transmission to and from external electrical devices. Custom Labview code was written (**Figure 2.2**) along with a corresponding GUI (**Figure 2.3**). The program allowed for user-defined stimulus presentation

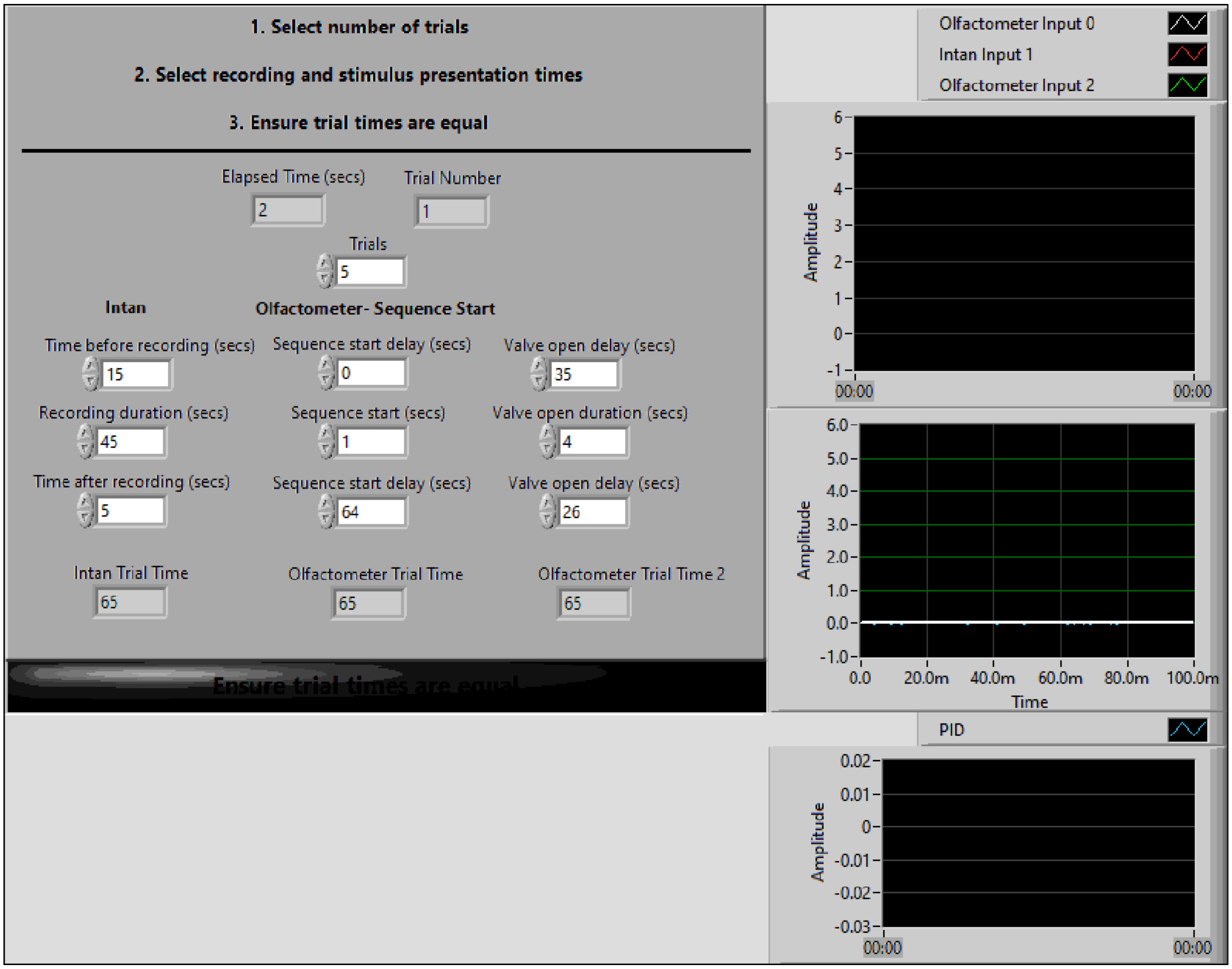
1. Select number of trials

2. Select recording and stimulus presentation times

3. Ensure trial times are equal

Elapsed Time (secs): 2
Trial Number: 1
Trials: 5

Intan
Time before recording (secs): 15
Recording duration (secs): 45
Time after recording (secs): 5

Olfactometer- Sequence Start
Sequence start delay (secs): 0
Sequence start (secs): 1
Sequence start delay (secs): 64
Valve open delay (secs): 35
Valve open duration (secs): 4
Valve open delay (secs): 26

Intan Trial Time: 65
Olfactometer Trial Time: 65
Olfactometer Trial Time 2: 65

Figure 2.3 | Odor Delivery GUI. Labview (National Instruments) front panel depicting GUI for selecting experimental timing parameters and initiating the sequence. Data recording times and stimulus presentation times are customizable based on experiment. If trial times are unequal, the program will trigger an error and will not execute. Plots on the right-hand side provide visual feedback for signal transmission and clock synchronization.

periods and neuronal recording times. A high TTL output pulse served to initiate the challenger sequence within the olfactometer software. A subsequent high TTL output pulse opened the final valve of the olfactometer, prompting odorant delivery to the insect antenna.

Signal Recording & Electrode Preparation

A USB interface board software was used to visualize and record all neuronal signals and an RHD USB interface board (Intan Technologies, LLC, **Figure 2.4**) was used for acquisition of all neural signals. Either four or eight of the low-noise amplifier channels were active at any one time

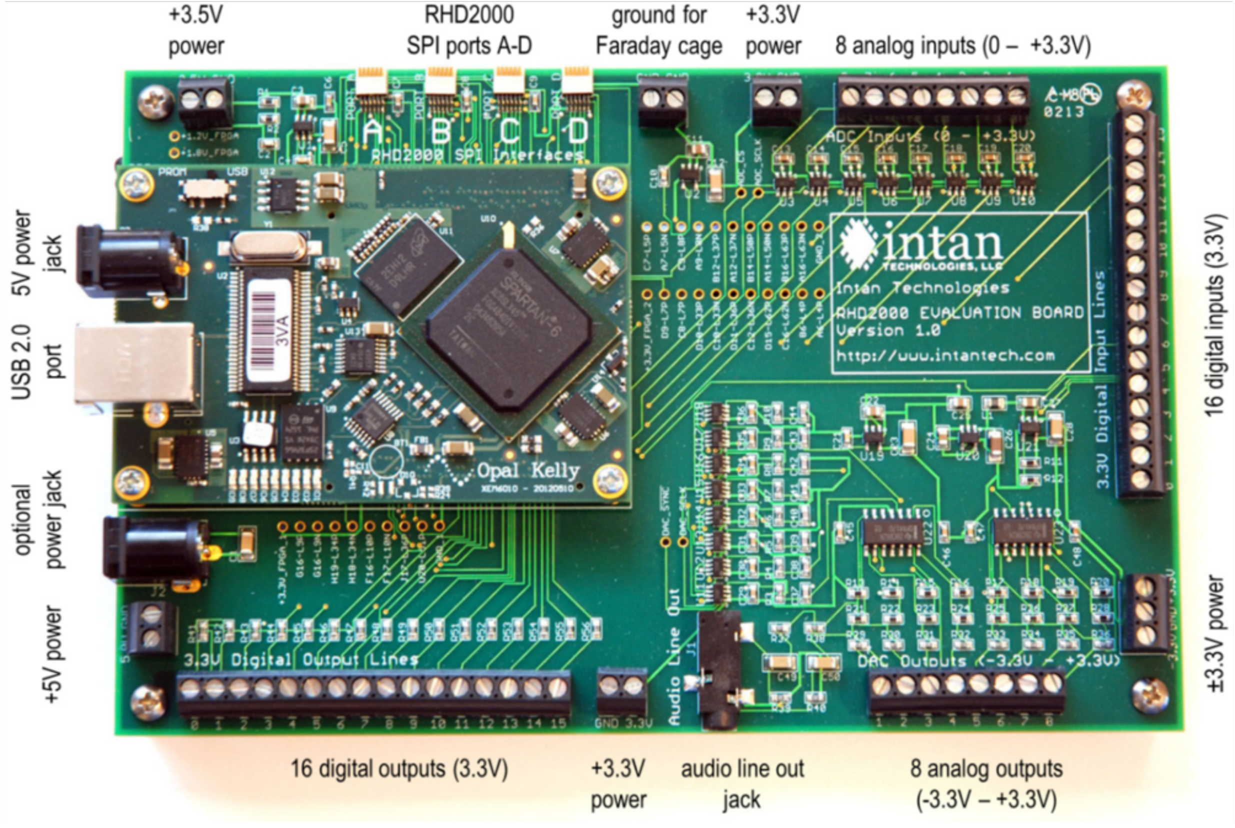

Figure 2.4 | RHD USB Interface Board (courtesy of Intan Technologies, LLC). Circuit board providing up to 256 amplifier channels (64 per SPI port). SPI cable extended to a small headstage (not shown), which digitized neuronal signals recorded from microelectrodes. Digital input channels received a high signal during the stimulus presentation period to record stimulus onset and offset times for subsequent analysis.

depending on microelectrode targeting and neuronal signal quality. The sampling rate of the board was set to 20 kHz for all experiments. Upon stimulus presentation, a TTL input pulse issued by the olfactometer was transmitted to the RHD USB interface board to record exact stimulus onset and offset times. The RHD USB interface board was connected to a 16-channel preamplifier headstage (RHD2132, Intan Technologies, LLC) via a serial peripheral interface cable. A wire adapter connected to a 16-channel DIP pin socket received neural signals via a microelectrode array.

For all locust-specific experiments, multi-electrode arrays (MEAs) were purchased from NeuroNexus Technologies (**Figure 2.5**). MEAs consisted of dual silicon shank probes with two sets of iridium tetrodes embedded into each shank. The lower two tetrodes were located 55-101 μm

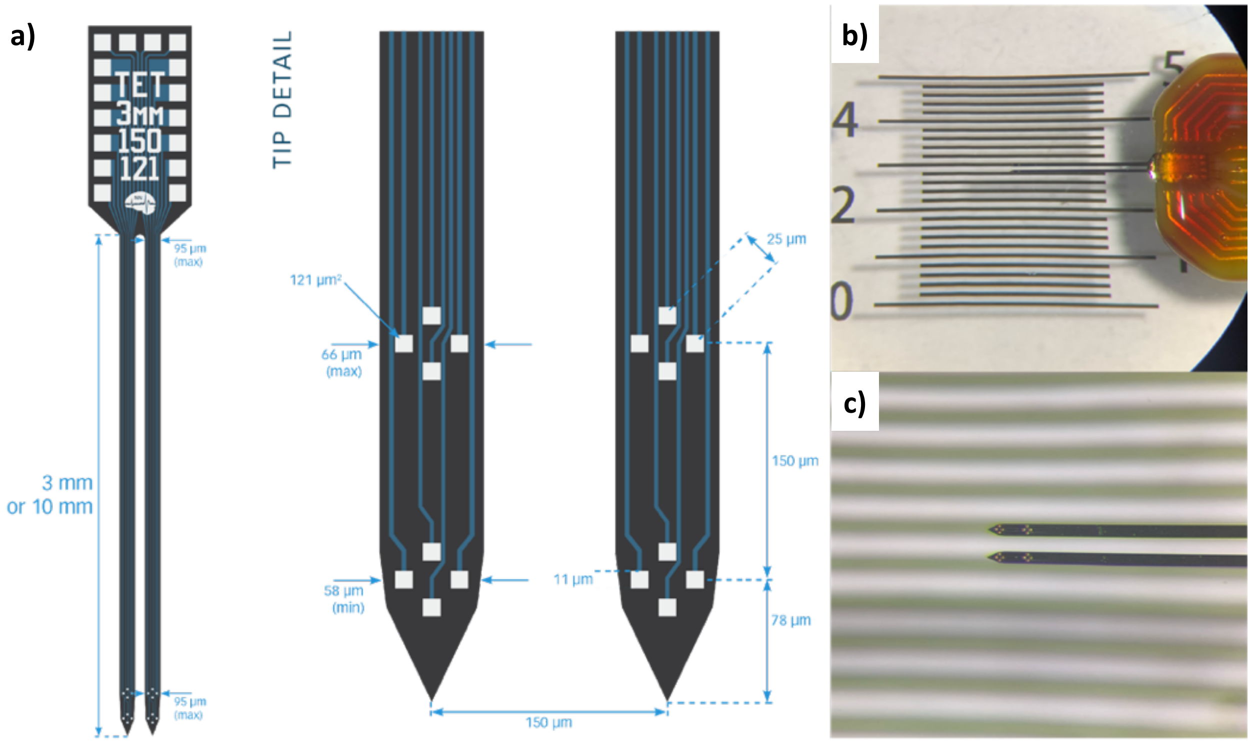

Figure 2.5 | Neuronexus Multi-Electrode Array. **a)** Schematic of dual shank multi-electrode array configuration. Figure reproduced from Neuronexus Technologies. **b)** and **c)** Magnified images of one probe used for locust neural recordings. Four individual tetrodes can be seen along the two shanks.

above the tip of the shank. The upper two tetrodes were located 121-177 μm above the lower and were not used as recordings only required minimal penetration depths. Electrodes pads had a surface area of 11 μm^2 and a center-to-center pitch of 25 μm within each tetrode.

Custom fabricated wire tetrodes were used for honeybee-specific neuronal recordings. Ultra-fine nickel-chromium 12.7 μm diameter wire with a ~0.254 um thick polyimide coating for insulation was used (Sandvik Technologies). A six-foot length of wire was drawn out and secured at both ends with lab tape. The taped ends were carefully brought together while avoiding the introduction of any kinks in the wire strands. Using tungsten-carbide scissors, the looped end

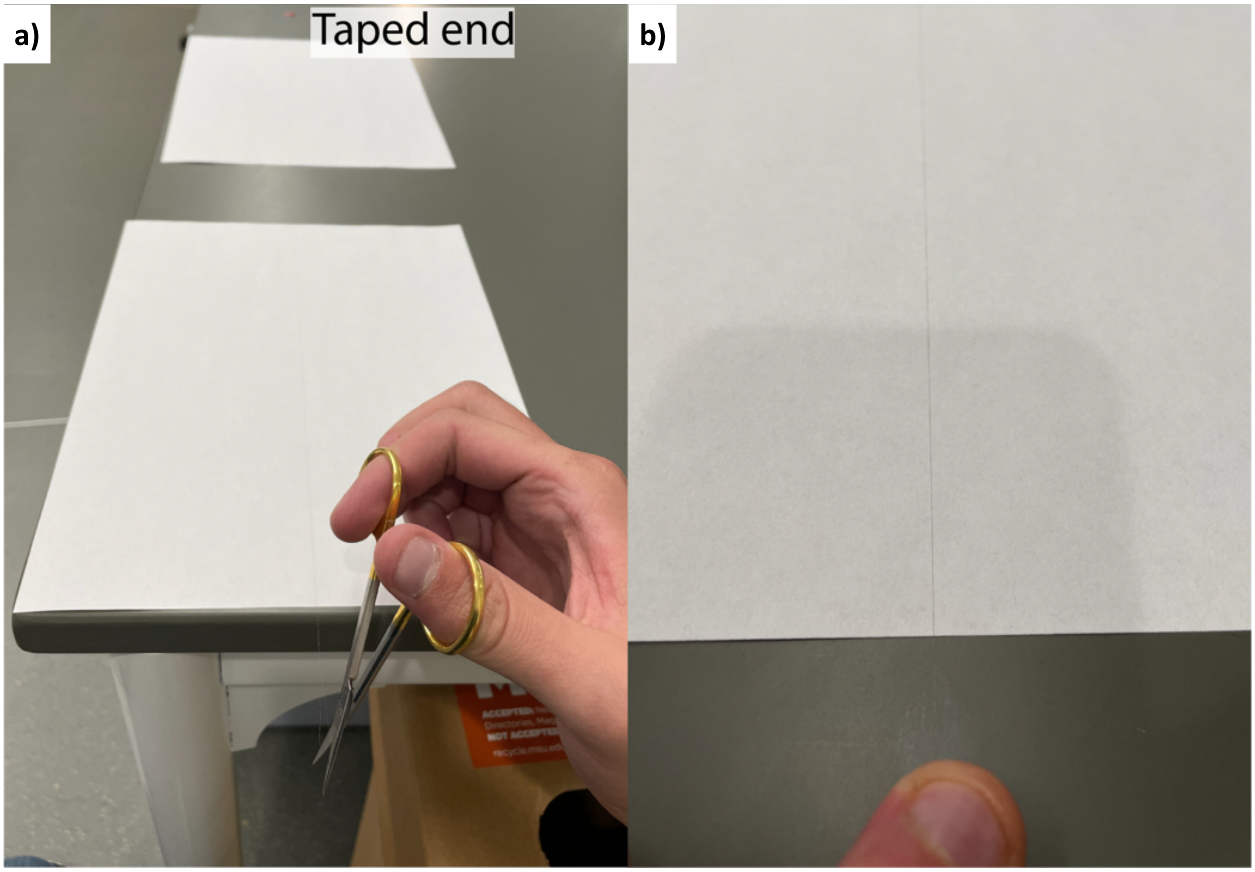

Figure 2.6 | Tetrode Wire Drawing. a) Tungsten-carbide scissors were used to cut the wire loop(s), creating strands of equal lengths. **b)** Strands were manually drawn out to ensure equal length prior to securing with tape. Image depicts two 12.5 μm wires.

distal to the tape was cut, ensuring the wire strands were of equal length (**Figure 2.6**). Another piece of lab tape was placed over the ends of the cut-wires and subsequently folded onto the existing taped end. The dual-loops were strewn over a lab retort stand bar and a binder clip was attached to the taped ends to stretch the wire strands and keep them in place overtop a magnetic stirrer. Wires were twisted in a clockwise fashion for approximately five minutes at 500 rpm. The twisted wire strands were then heated by running a heat gun up-and-down the length of the wire for ten passes lasting a total of ~45 seconds (**Figure 2.7**). After heating, wires were allowed 20 seconds to cool, then spun in a counterclockwise fashion for five to ten seconds to release any residual tension. Having stopped the spinning wires, another ten passes of a heat gun was applied to the wire strands. A piece of lab tape was applied to the top of the wire near the looped ends. Holding the tape, the loop was cut, and the wire was strewn across two elevated platforms

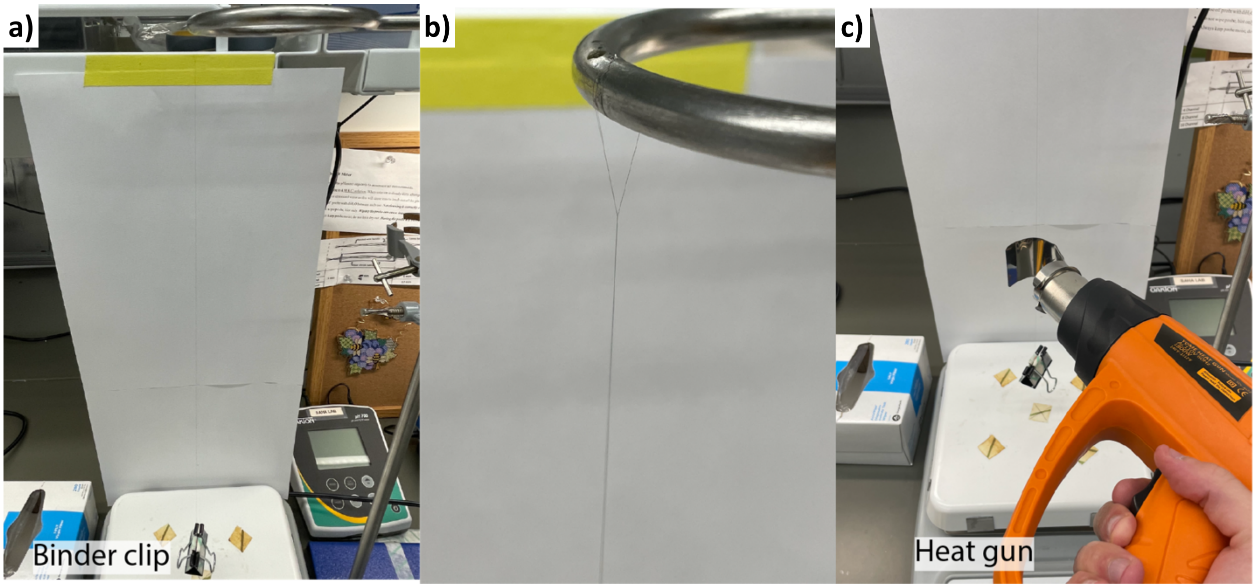

Figure 2.7 | Tetrode Spinning. Looped wire strands were strewn over metal retort stand atop a magnetic stirrer. Attached binder clip allowed free rotation of the lower end, spinning wires into a tetrode. The wires were heated to reduce residual tension and prevent wire recoiling once removed from the stand.

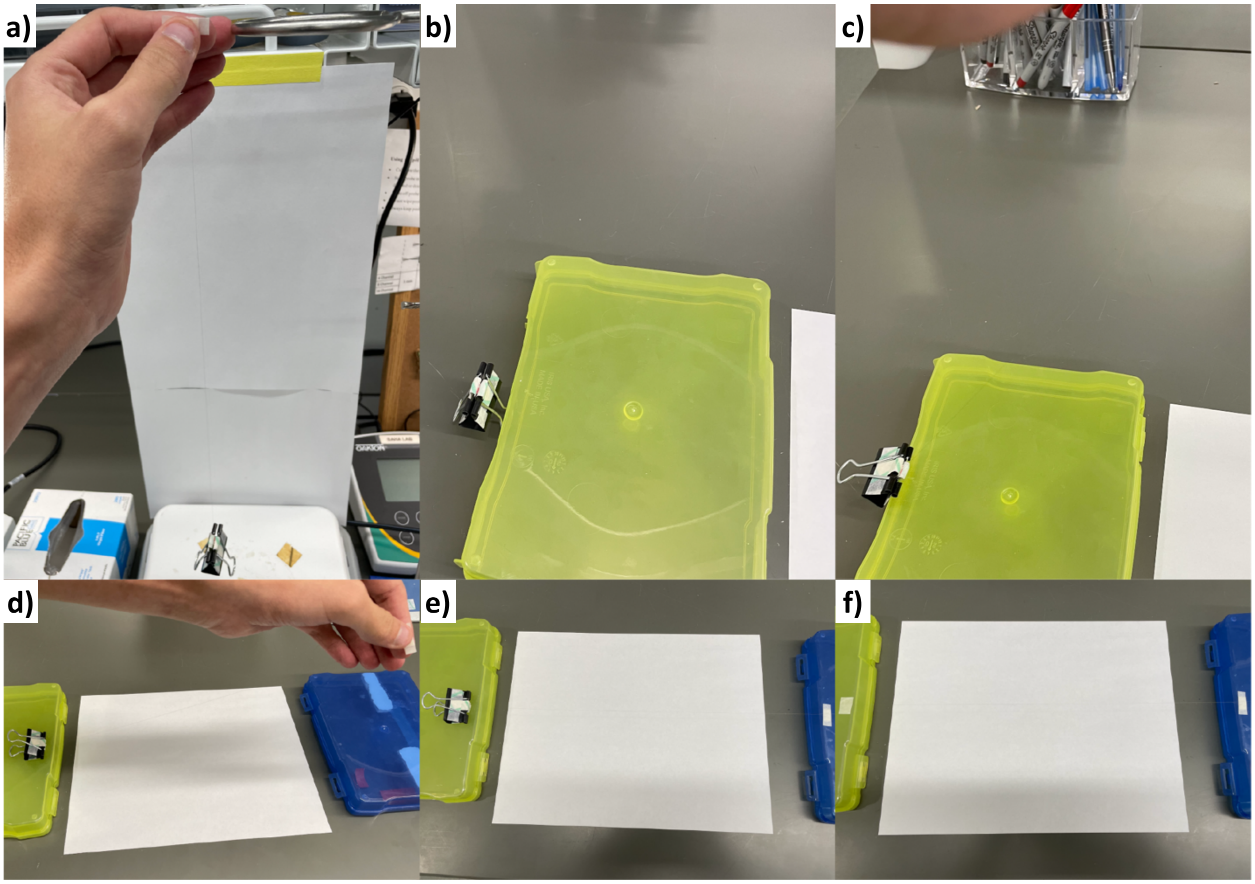

Figure 2.8 | Tetrode Wire Removal and Sectioning. While holding the wire between lab tape, the loop was cut, and the twisted wire was strewn across two elevated platforms. Special care was taken to ensure the wire was kept taught and did not exert any recoil. Both sides were secured using lab tape.

(**Figure 2.8**). Tape was applied to both ends to prevent any coils or kinks from forming. Five-minute epoxy was mixed in a small petri dish and applied at intervals along the length of the twisted wire tetrode strands. A ball of epoxy was placed two inches (51 mm) from the future brain insertion point of the tetrode wires. After another inch, a second ball of epoxy was positioned to section off the portions of the wires to be soldered. The process was repeated for the entire length of the twisted tetrode strands (**Figure 2.9**). The epoxy balls were left at room temperature overnight to ensure full curing occurred. The wire strands were cut immediately upstream of the sections to be soldered. A thin-walled PEEK tube was cut to size (**Figure 2.9**) and

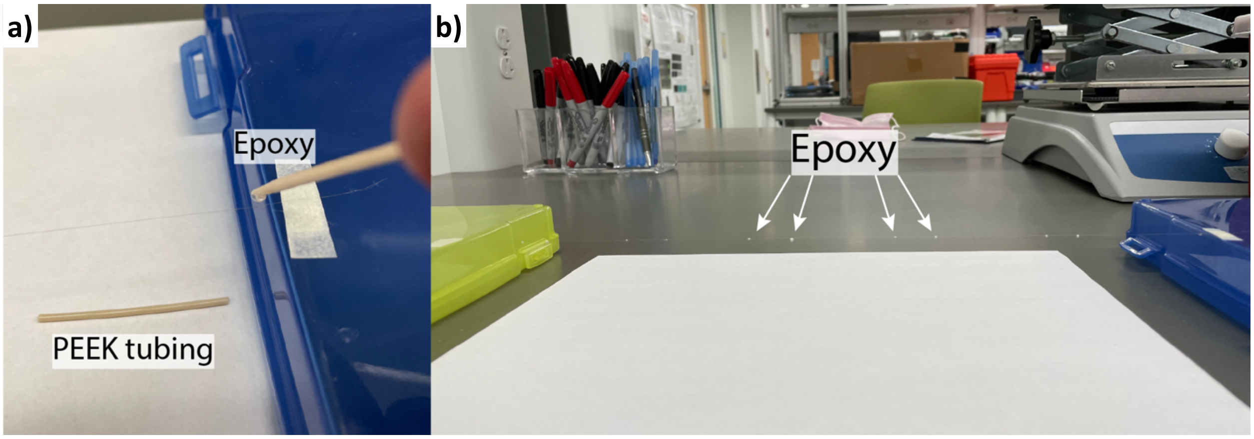

Figure 2.9 | Tetrode Epoxy Application. Equal parts of two-part epoxy were mixed, and droplets were applied along the length of the spun tetrode. One epoxy ball was placed at the end to be soldered and another was positioned at the junction point.

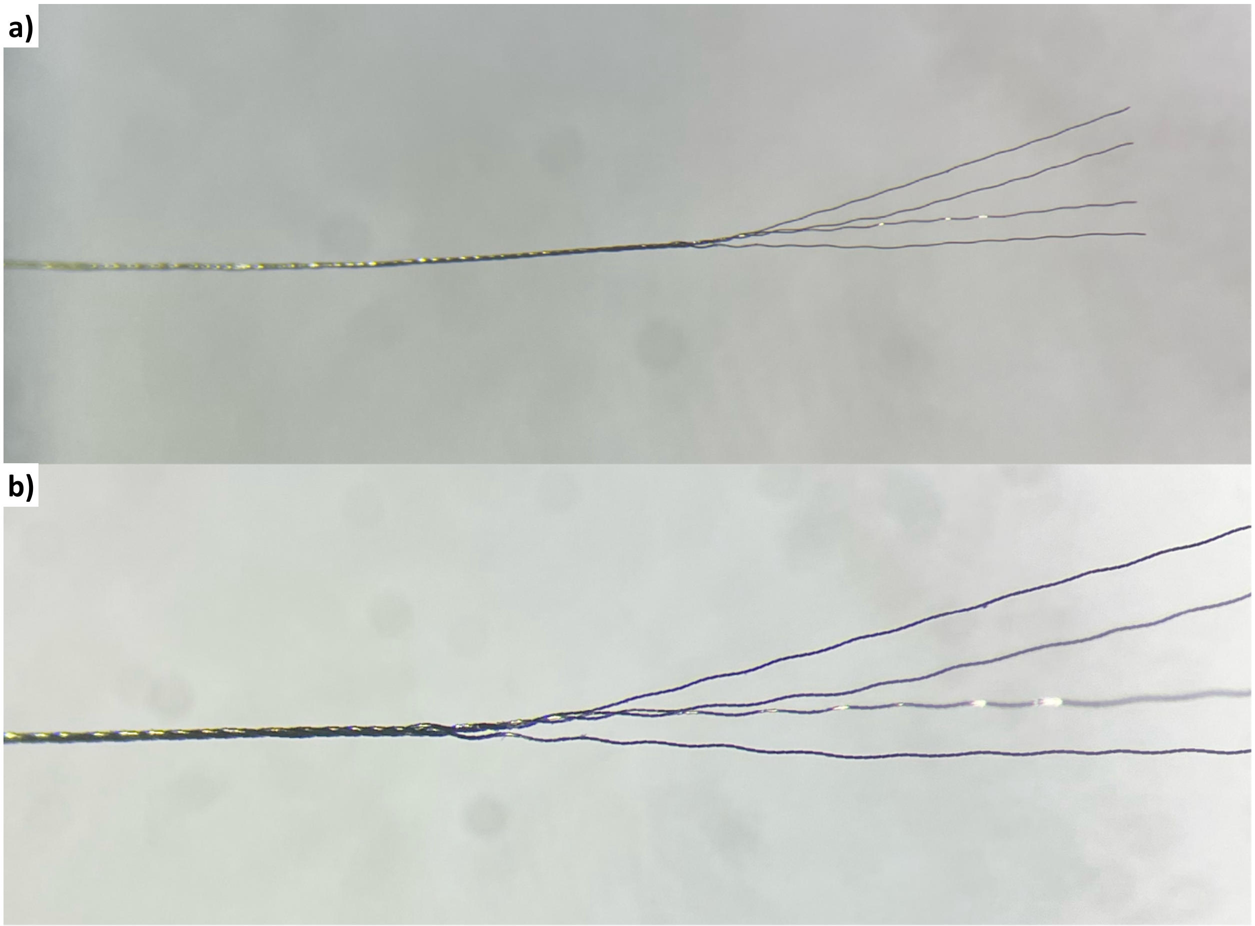

Figure 2.10 | Tetrode Splaying. Tetrodes were manually unwound under a stereomicroscope and the end epoxy ball was cut off. Note: here, no junction epoxy ball is depicted to aid in tetrode visualization. If needed, tweezers coated with a soft plastic were used to unwind individual wires until sufficiently separated.

the wire bundle was placed through the tube until the end touched the remaining epoxy ball. More epoxy was used to mechanically bond the existing epoxy ball and wire bundle to the PEEK tube. Under a stereomicroscope, the end epoxy ball was spun counterclockwise to unwind a portion of the wire bundle. The wire bundle was cut and any remaining wire twists were removed by clasping the tetrode strands with a Plasti Dip coated tweezer and repeatedly running the softened tool along the length of the wire until reaching the free end (**Figure 2.10**). A low-heat electric lighter was briefly touched to the free wires to remove the polyimide insulation, while allowing the metal wires to maintain mechanical strength and integrity. Solder flux was placed in

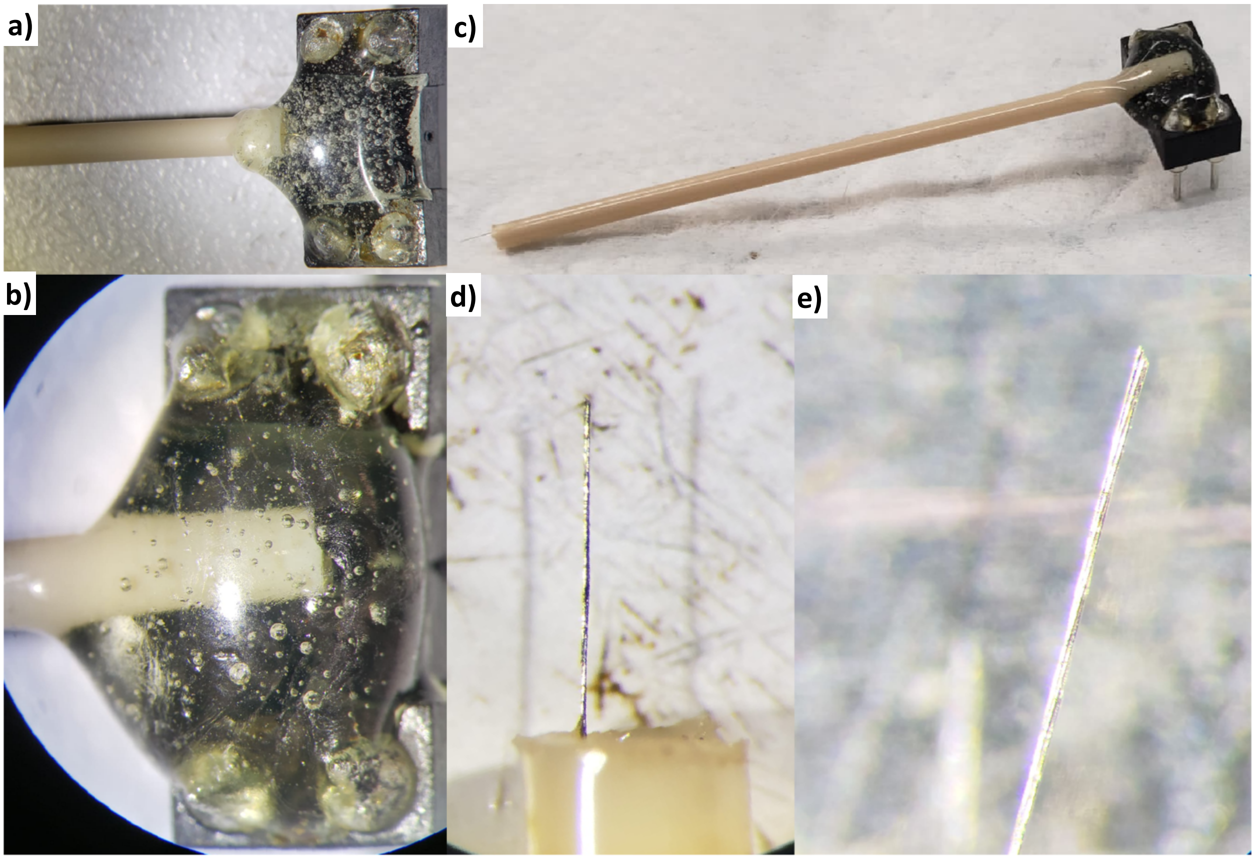

Figure 2.11 | Finished Tetrode. A finished tetrode is depicted having been appropriately soldered and finished with epoxy application for structural support and additional electrical insulation. **b)** Thin wires can be seen completing the electrical circuit from each wire tip to its respective pin channel. **d, e)** Brain insertion point.

each pin connector of a four pin DIP socket prior to filling each pin connector with a small amount of lead-free solder. Grasping each deinsulated wire strand, solder joints were remelted, and wires were individually pulled through channel-specific solder joints until taught. Any wire extruding beyond solder joints was trimmed. Two-part epoxy was placed over solder joints and the DIP socket body to provide effective channel insulation and structural support (**Figure 2.11**).

Both NeuroNexus probes and custom fabricated wire tetrodes were electroplated to achieve desired impedances and improve signal-to-noise ratio (**Figure 2.12**). A stainless-steel anode and either multi-electrode array or tetrode were submerged into a non-cyanide gold plating solution within a custom-designed, 3-D printed electroplating reservoir. A constant current stimulus isolator delivered a steady state current of 1.5 mA to an IMP-2A impedance tester, which gated the input to deliver square waves at a frequency of 3 Hz. The afferent voltage signal was transmitted via the impedance tester to an electroswitch, which was soldered to a 16

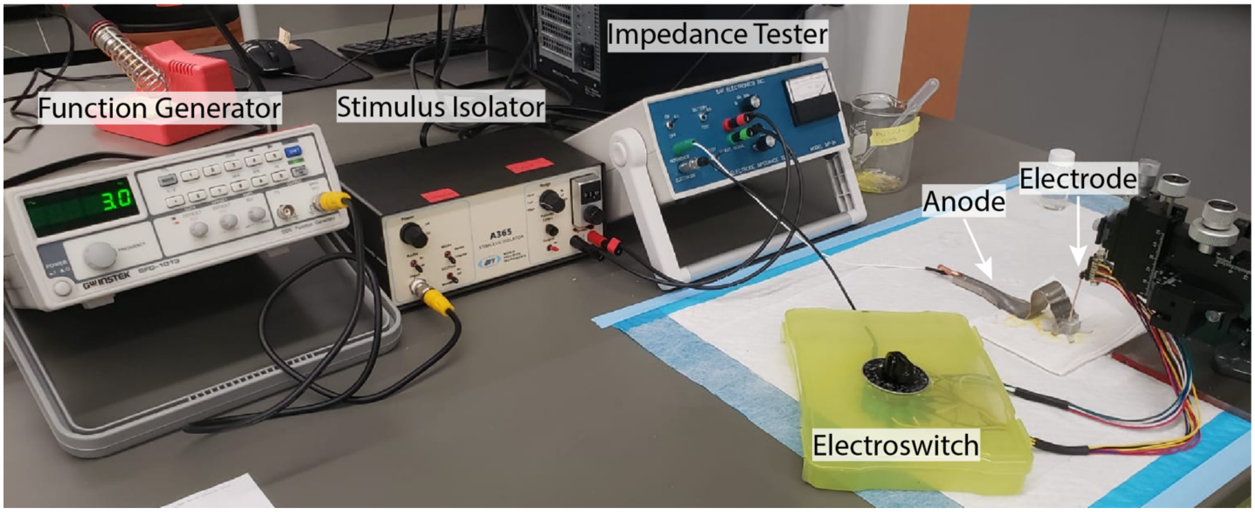

Figure 2.12 | Electroplating setup. Current from the stimulus isolator is gated according to input parameters on the function generator. The oscillating current is directed to the impedance tester, which can be selected to plate electrode channels with gold ions or test the impedance of individual channels.

pin DIP socket. By adjusting the channel on the electroswitch, the current was redirected to the appropriate pin connection and corresponding electrode channel. The stainless-steel anode was connected to the impedance tester and completed the electrical circuit. While in test mode, the externally derived current was directed towards ground and impedance measurements of each electrode channel were taken at 1 kHz. Upon switching to plating mode, the current stimulus isolator-derived current was passed through the electrode channel, into the plating solution and through the anode. Gold particles from within the solution were deposited onto the electrode, thereby decreasing overall channel impedance. Individual channels were plated to 200-300 kΩ for locust recordings and 300-400 kΩ for honeybee recordings.

Stimulus Creation

Odor Vials

All stimuli used for experiments were constructed within the same week to avoid volatile leakage or chemical breakdown. For 1% odorant experiments, 10 mL of mineral oil was placed into airtight 20 mL vials followed by the liquid chemical stimulus. For synthetic lung cancer mixtures, 10 mL of mineral oil was placed into airtight 20 mL vials with additional steps shown below. Micropipettes were used to achieve precise chemical concentrations in individual vials.

For those chemicals naturally found in lower concentrations within healthy and lung cancer breath samples, serial dilution was used. For simulated healthy breath samples, final desired chemical concentrations were as follows: 0.2 μL of decane, 0.09 μL of nonanal, 0.005 μL of 2-methylheptane, 0.0006 μL of 2,2,4,6,6-pentamethylheptane, and 0.00001 μL of pentanal

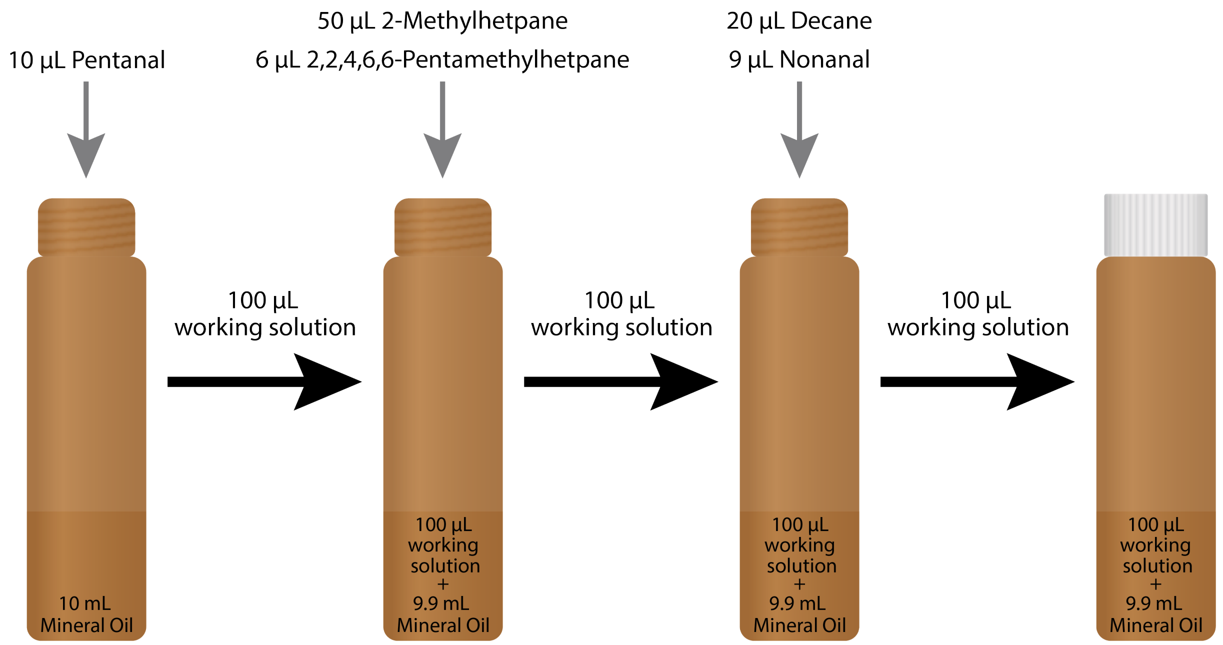

Figure 2.13 | Synthetic Healthy Breath Construction. Diagrammatic steps detailing the serial dilution protocol used to create synthetic healthy breath stimuli.

(**Figure 2.13**). Steps to achieve appropriate chemical concentrations within odorant mixtures were as follows:

1. 10 µL of pentanal added to 10 mL of mineral oil to make working solution
2. 100 µL of working solution added to 10 mL of mineral oil
3. 50 µL of 2-methylheptane and 6 µL of 2,2,4,6,6-pentamethylheptane added to working solution
4. 100 µL of working solution added to 10 mL of mineral oil
5. 9 µL of nonanal and 20 µL of decane added to working solution
6. 100 L of working solution added to 10 mL of mineral oil to make final stimulus solution

For synthetic lung cancer breath samples, final desired chemical concentrations were as follows: 0.7 µL of nonanal, 0.4 µL of decane, 0.02 µL of 2-methylheptane, 0.002 µL of 2,2,4,6,6-

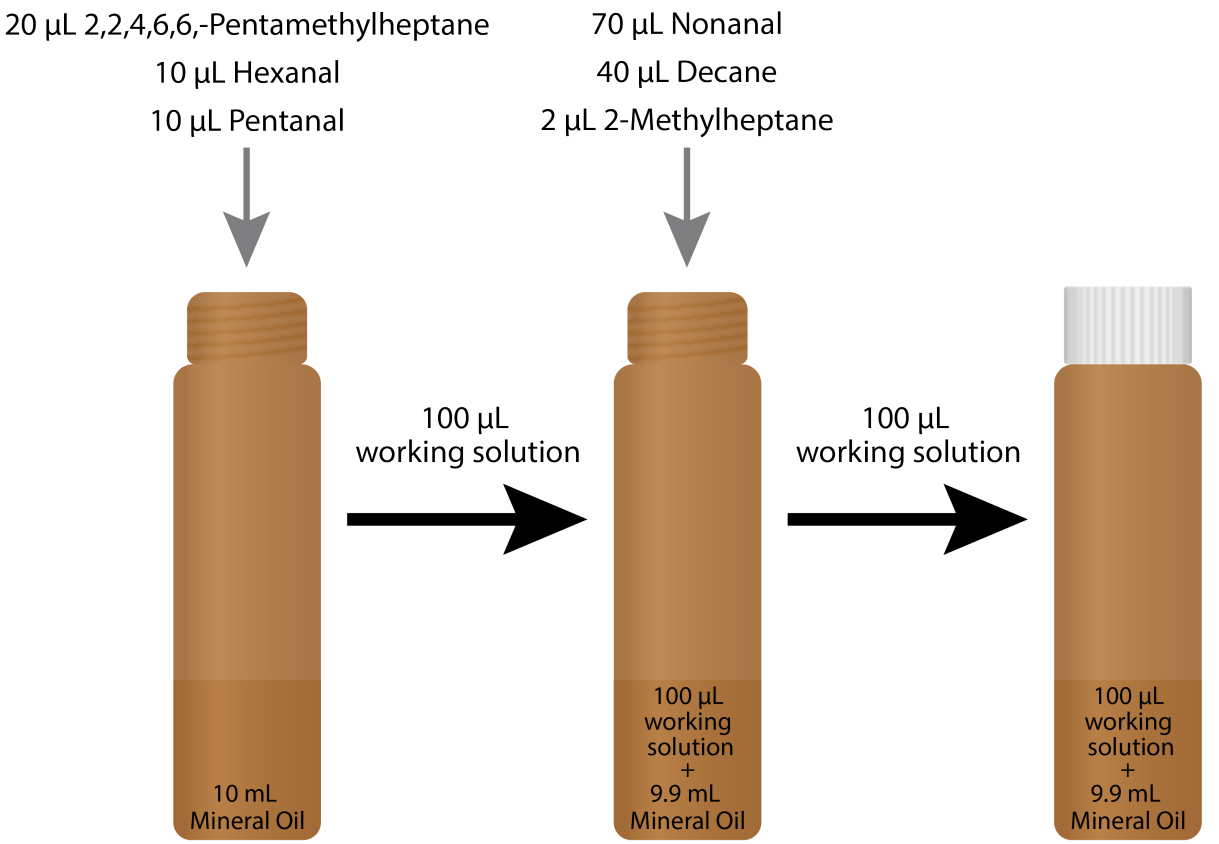

Figure 2.14 | Synthetic Lung Cancer Breath Construction. Diagrammatic steps detailing the serial dilution protocol used to create synthetic lung cancer breath stimuli.

pentamethylheptane, 0.001 µL of pentanal, and 0.001 µL of hexanal (**Figure 2.14**). Steps to achieve appropriate chemical concentrations within odorant mixtures were as follows:

1. 10 µL of pentanal, 10 µL of hexanal, and 20 µL of 2,2,4,6,6-pentamethylheptane added to 10 mL of mineral oil to make working solution
2. 100 µL of working solution added to 9.9 mL of mineral oil
3. 2 µL of 2-methylheptane, 70 µL of nonanal, and 40 µL of decane added to working solution
4. 100 µL of working solution added to 9.9 mL of mineral oil to make final stimulus solution

All 1% and synthetic lung cancer breath samples were rapidly sealed, vortexed for a total of 30 seconds to achieve sample homogeneity, and stored in a cool, dry location prior to conducting experiments.

Cell Culture Flasks

Modified airtight T25 flasks were used for all in vitro cell culture experiments. Initially holes were drilled using 19-gauge needles, one in the back right corner of the body and one in the cap. One 19-gauge needle was inserted through the flask body to serve as an inlet pin and another through the cap to serve as an outlet pin. Two successive layers of a low-volatile, two-part epoxy was applied to the flask and cap surface, hermetically sealing the flask—needle joints. Two 5-cm long PTFE tubes were sealed with the low-volatile epoxy, placed over both pins and stabilized via a small tube clamp (**Figure 2.15**). The incorporation of the needles allowed for a rapid and simple

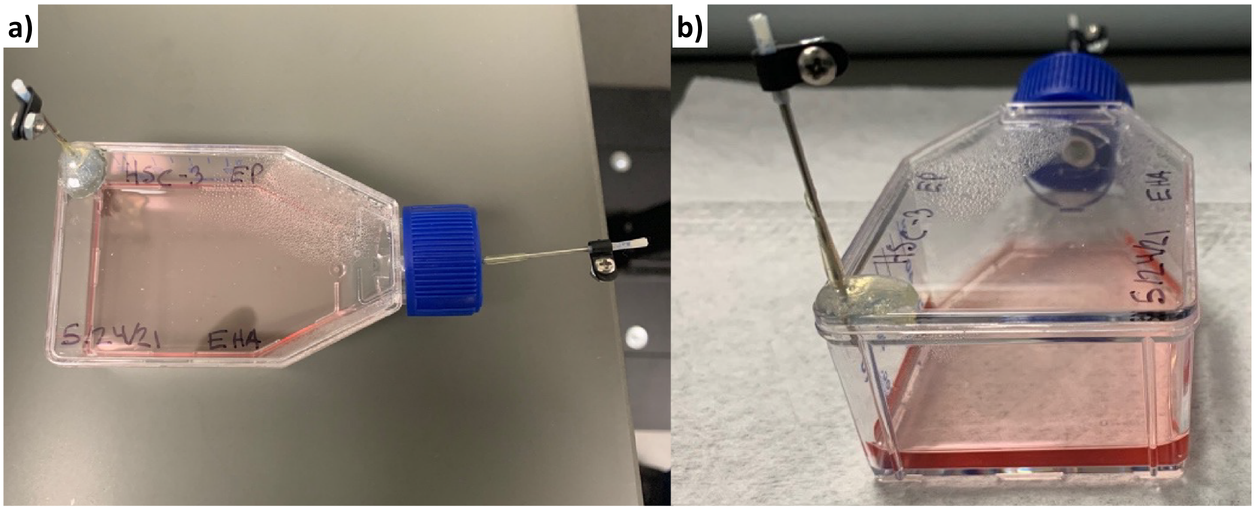

Figure 2.15 | Modified Flask Construction. Images depict fully constructed flasks with cell media and freshly seeded cells. Two layers of two-part epoxy was used to secure the 19-gauge pins to the polystyrene T25 flasks. Flasks were always capped other than during stimulus presentation to ensure sufficient cell culture volatiles within the flask headspace. Flasks were constructed at least 72 hours before cell seeding to allow epoxy to cure entirely.

connection to an airline through which headspace volatiles could be transmitted. Five stimuli were used in the current experiment, including three cancer cell lines, HSC-3, SAS, and Ca9-22, one non-cancer cell line, HaCaT, and one flask with solely cell media. These cell lines were selected due to the observed metabolic differences during longitudinal cell culture analysis (*unpublished data*). Cell media (Dulbecco's modified eagle media) was kept consistent for all stimuli in order to maintain consistency between cell line environments. A HEPES zwitterionic organic buffering agent was added to the flasks to promote cell growth while in a hypoxic environment. A total of one million cells for each cell line were initially seeded in the augmented flasks. Cell progression was monitored over the course of four days and experiments were repeated once every 24 hours. Electrophysiological experiments took place over a period of 8 weeks. Flasks were stored in an incubator set at 37° C and were only removed when in active use during an experiment.

Husbandry

Locusts

All locusts were housed within cages in an environmentally controlled incubator. Locust cages were adapted from commercially purchased reptile cages to include a plexiglass front screen with a 6" diameter hole and custom designed door covering (**Figure 2.16**). The locust incubator (Powers Scientific, Inc.) operated according to a 18-6-hour light-dark cycle at a daytime temperature of 35.5°C and nighttime temperature of 25°C. All locusts were fed a diet of organic, hydroponically grown wheat grass once a day with supplementary organic wheat germ available

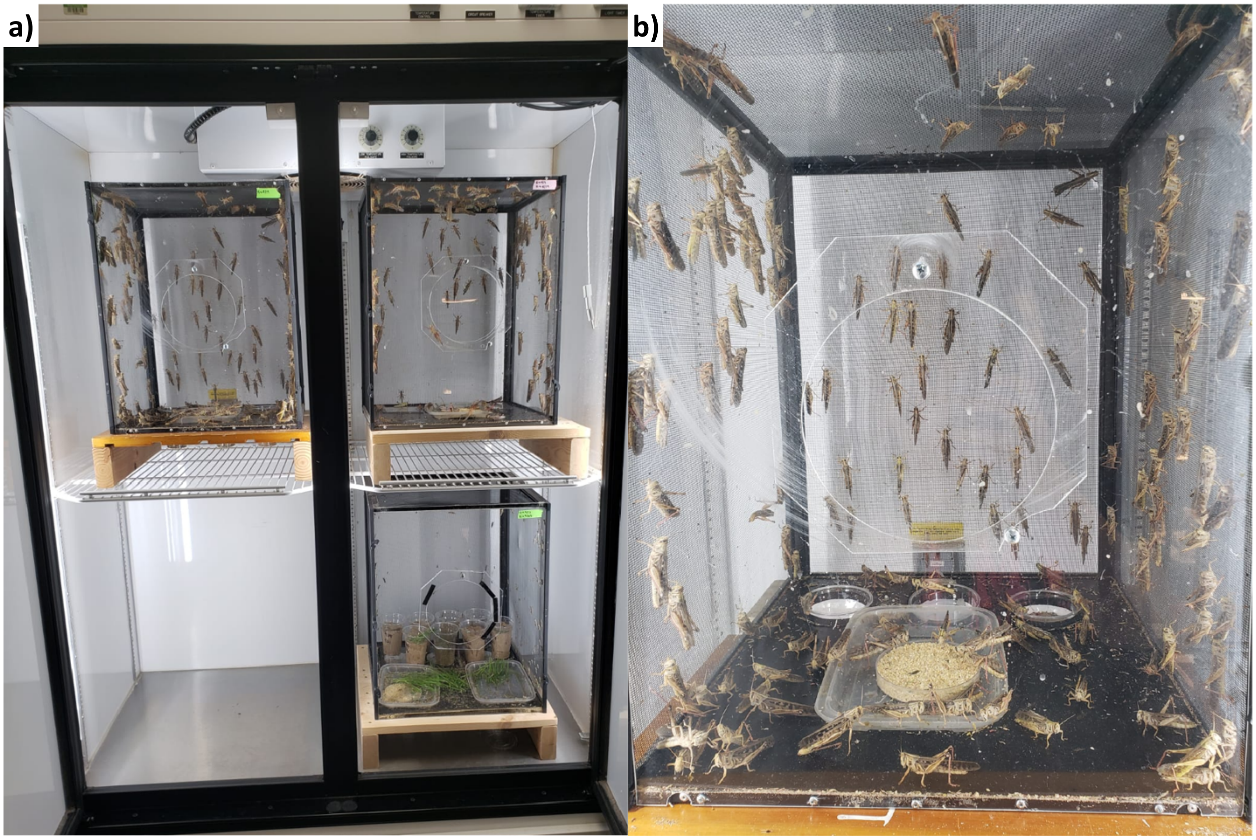

Figure 2.16 | Adult Locust Husbandry. Locust colony was maintained in a light and temperature-controlled incubator. Locusts of different life cycles were housed in separate cages. Cages were adapted to include a plexiglass front panel and locking door. Locusts were fed a diet of organic wheat grass and organic wheat germ.

as needed. Once reaching sexual maturity, cups were placed into each cage for oviposition. Two cups consisted of hydrated vermiculite and a third cup contained hydrated sand. Cups were left in the cages for 2-3 days, at which point, they were replaced with freshly made cups, lidded, and placed into a high-humidity incubator for hatching purposes (**Figure 2.17**). Each cup collecting cycle continued for 3-weeks. The incubation time for these egg-rich cups was approximately 17 days, at which time, cups that contained hatchlings were placed into nursery cages and de-lidded. Once locusts were large enough (3rd instar), cages were vacuumed every 2-3 days to remove any frass, deceased individuals, and/or other debris.

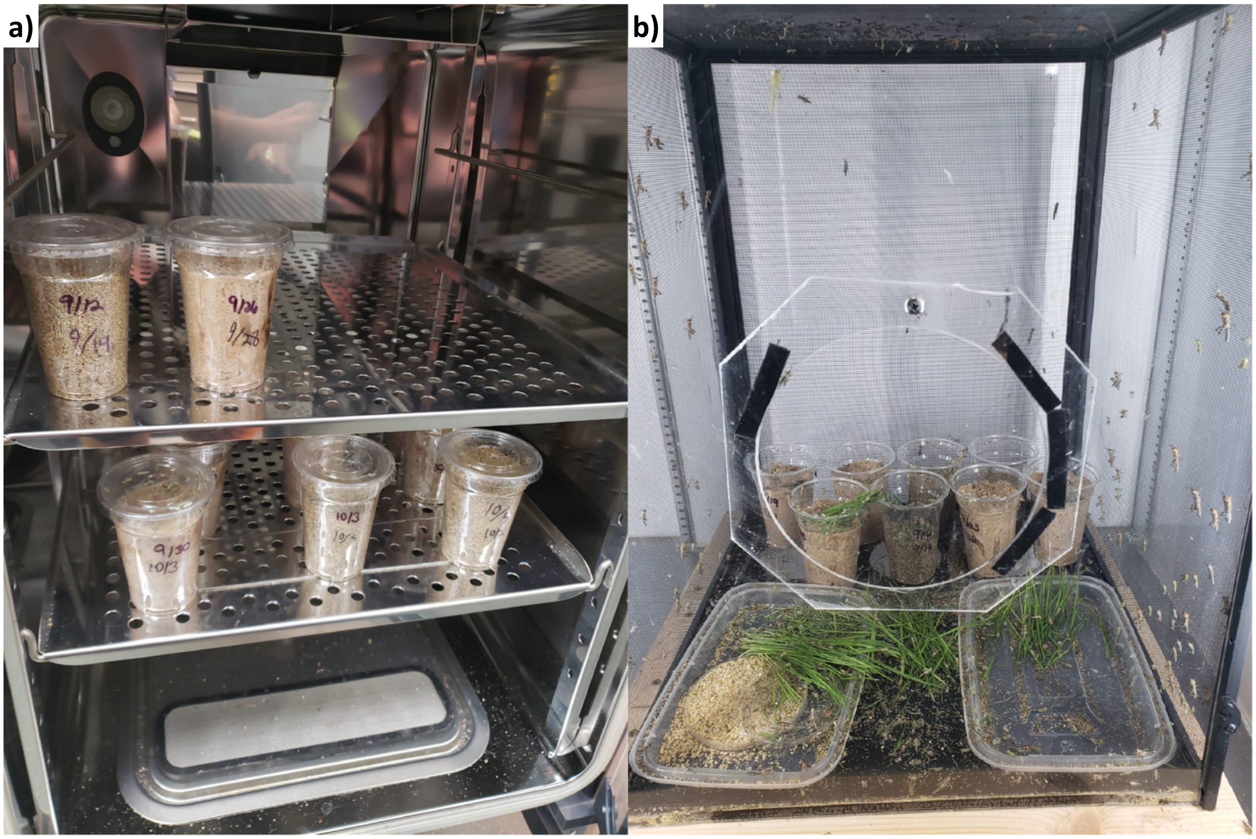

Figure 2.17 | Hatchling Locust Husbandry. Locust colony maintenance included ensuring reproductive success with future generations. **a)** Cups filled with sand or vermiculite contain egg sacs from which locust emerge. **b)** Hatchling cage one week after initial hatching depicts numerous first and second instar locusts.

Honeybees

Honeybee cages were custom fabricated. Wooden back, side and top panels framed the cage with #8 metallic screens covering the bottom. A pair of one-inch diameter holes were drilled into the wood panel atop the cage and metallic screening was secured underneath. A front plexiglass panel was installed to allow for adequate visibility (**Figure 2.18**). The honeybee incubator (Powers Scientific, Inc.) was set to a 24-hour dark cycle at a constant temperature of 34.2°C. Two vials of simple syrup (50% sucrose, 50% DI H2O) with small holes drilled in the lids for accessibility were placed in the holes atop the wire mesh affixed to the top wood panel to allow bees constant

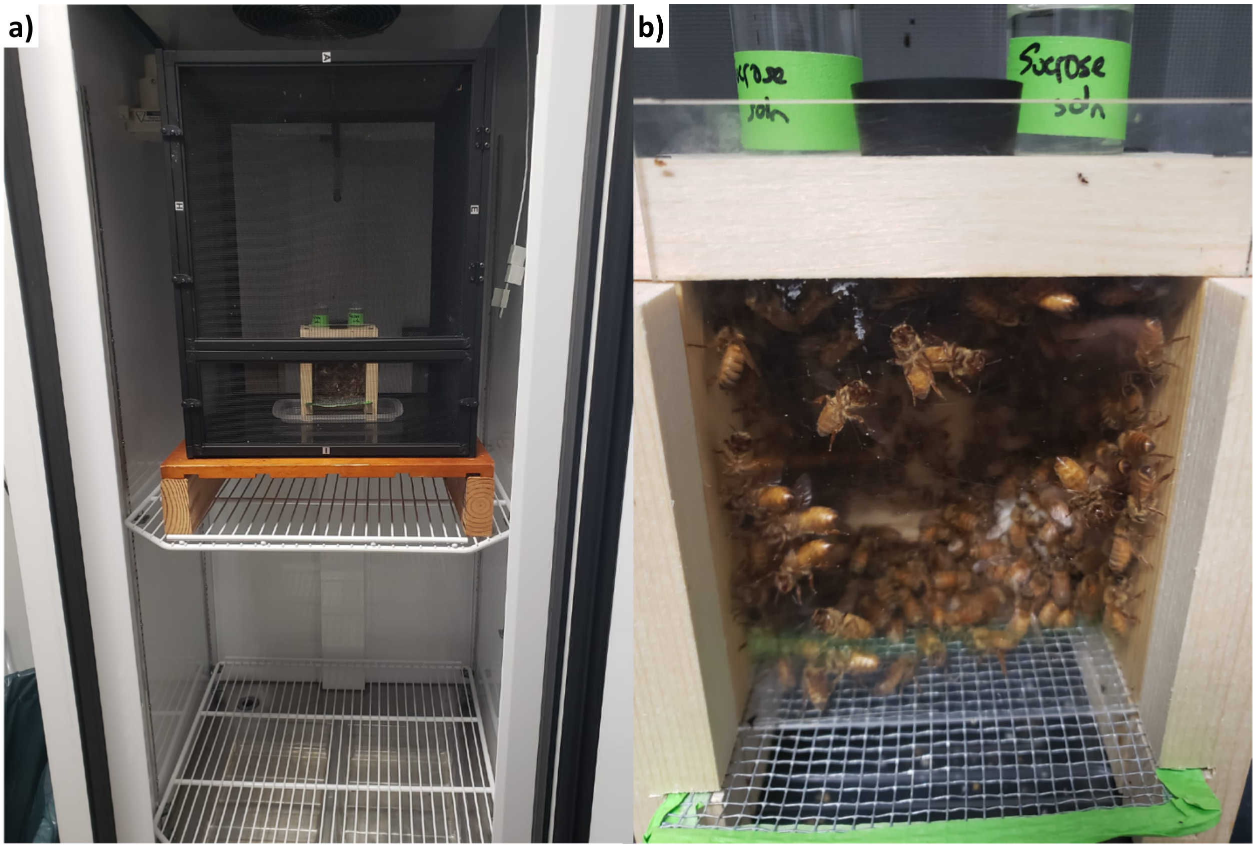

Figure 2.18 | Honeybee Husbandry. Worker honeybees are housed in a dark, temperature- and humidity-controlled incubator. Custom bee boxes were fabricated featuring a plexiglass front panel for visualization. Bees were allotted a 50% sucrose solution and a pollen substitute as needed.

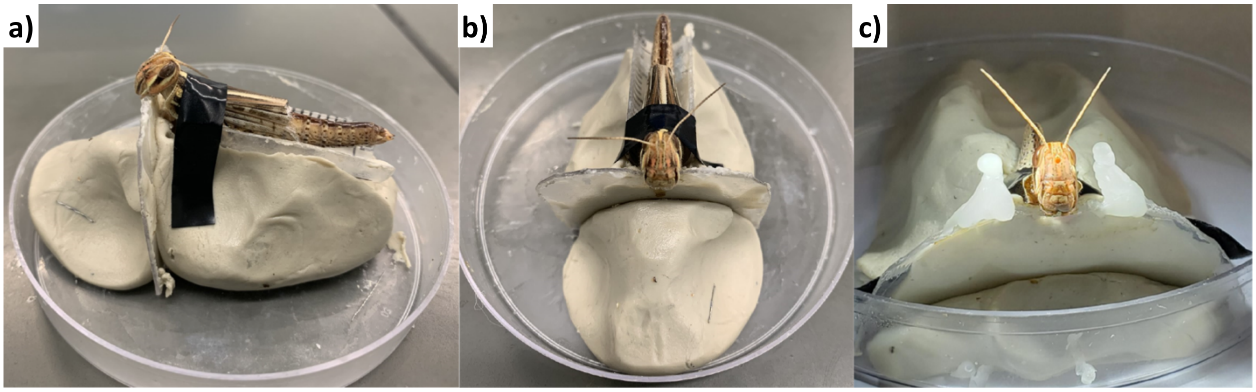

Figure 2.19 | Locust Exoskeleton Stabilization. a, b) Young adult locust stabilized on a clay platform with plastic body and head supports. **c)** triangular pillars were constructed from batik wax.

access to adequate nutrients. A vat of DI H2O was kept in the bottom of the incubator to maintain a ~50% humidity level.

Surgery & Electrophysiology

Locusts

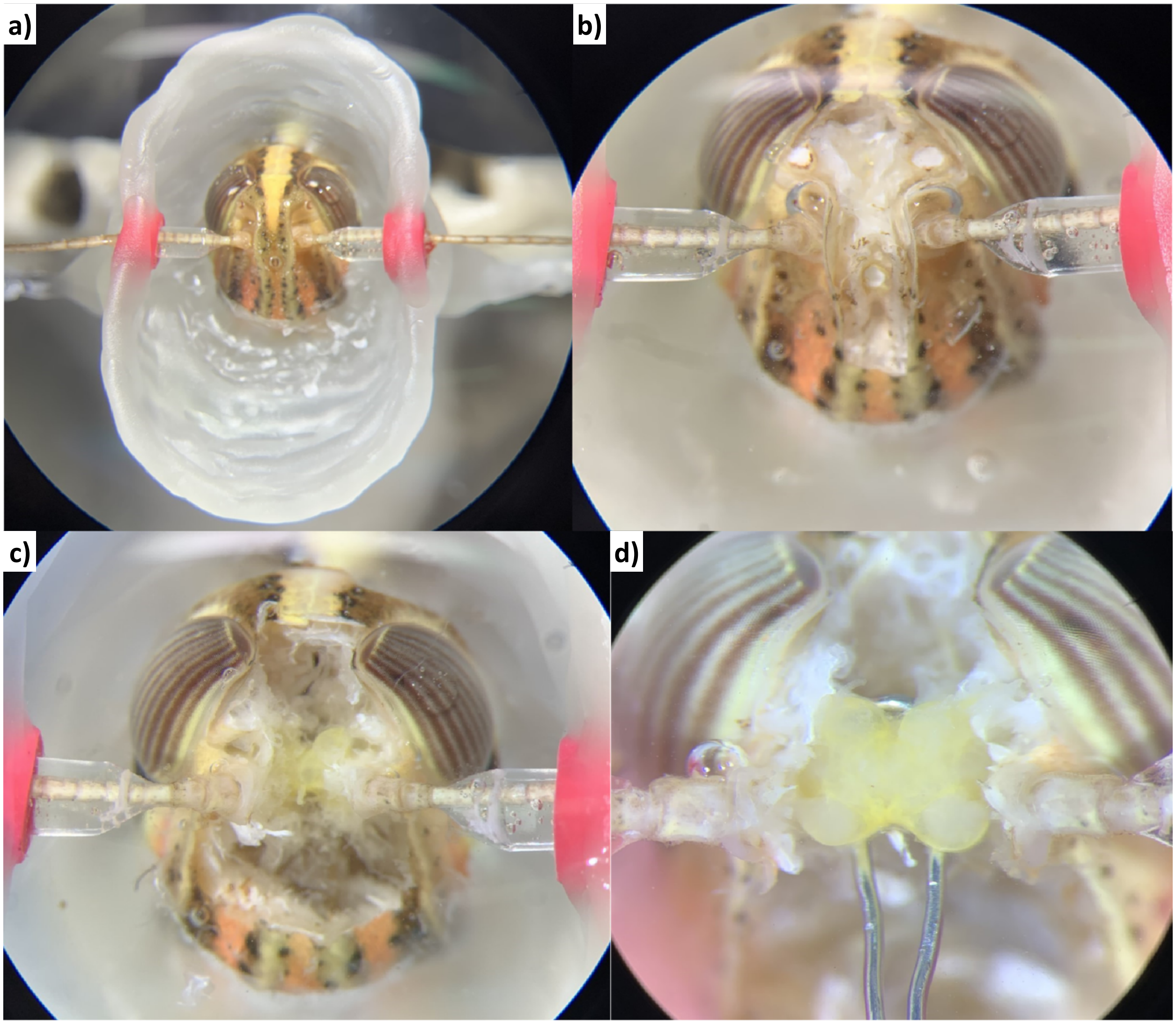

Figure 2.20 | Locust Exoskeleton Excision and Neural Surgery. A batik wax bowl was constructed to stabilize and isolate the locust head. Prior to initial incision, the bowl was filled with a room temperature locust saline to prevent tissue desiccation. The exoskeleton was excised using microscissors and glandular tissue was removed with microtweezers. The brain was stabilized on a wire platform and desheathed.

All neural recordings were conducted on post-fifth instar locusts (*Schistocerca americana*) of either sex raised in a crowded colony. Locusts were initially immobilized on a surgical platform (**Figure 2.19a, b**). Batik wax towers were constructed on either side of the head (**Figure 2.19c**). Antennae were fed through 1/32" inner diameter polyethylene tubes and stabilized to the towers using additional batik wax. A quick-acting, two-part epoxy was used to secure the antennae to the inner walls of the polyethylene tubing. While the epoxy cured, a bowl of batik wax was built to isolate the head region. The bowl was then filled with a room temperature, physiologically balanced locust saline solution before removing exoskeleton and glandular tissue until the brain was fully apparent (**Figure 2.20**). A drip tube supplying fresh saline was installed through the wax bowl. Using super fine tip tweezers, the antennal lobes were desheathed following treatment with protease.

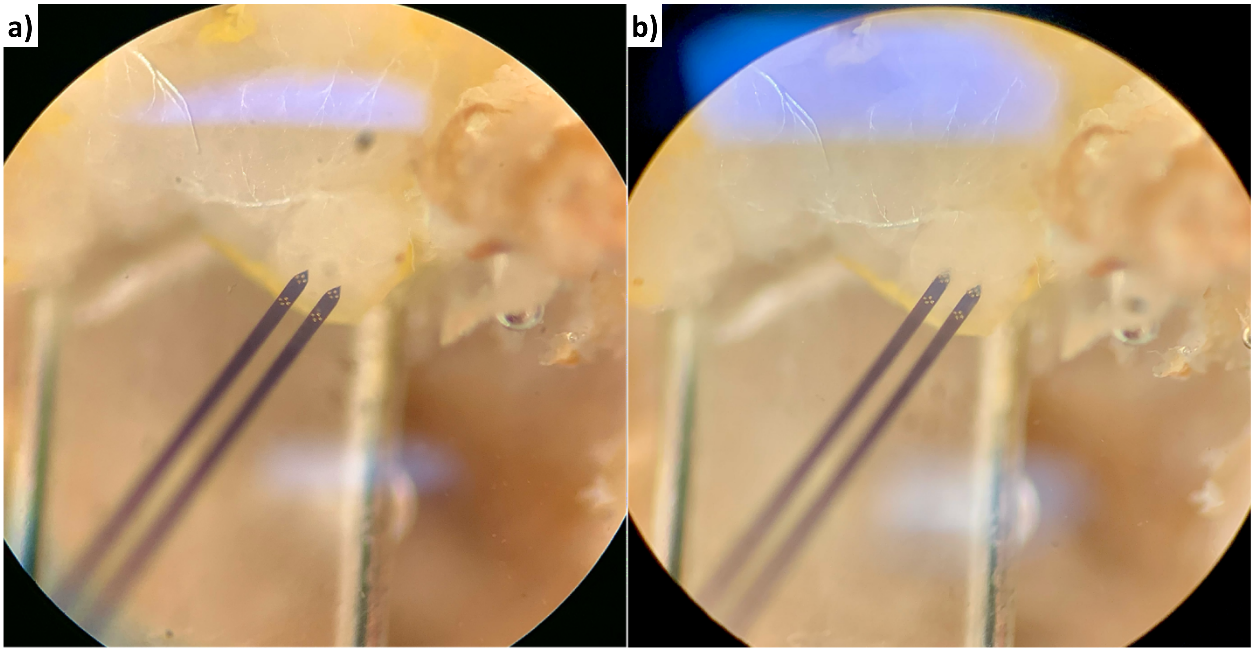

Figure 2.21 | Locust Electrode Insertion. Dual shank Neuronexus probe before and after insertion. Required penetration depth is only 50-100 μm as the antennal lobe glomeruli are positioned around the cortex of the lobe. Shanks were advanced slowly while watching for high signal-to-noise ratios and action potentials on the Intan GUI.

Surgically prepared locusts were set inside a faraday cage to mitigate environmental electrical noise. A 30-AWG silver reference wire coated with chloride ions was submerged into the saline within the wax bowl. A 16-channel Neuronexus multi-electrode array was connected to a 16-channel DIP socket and adjusted by a micromanipulator (WPI) for appropriate targeting. The tips of the probes were placed directly atop the antennal lobe and slowly lowered (**Figure 2.21**) until neural spikes were clearly visible (~50-100 μm) on the Intan USB board interface GUI. Odorants were then presented in a pseudorandomized order and neuronal responses were recorded.

Honeybees

All honeybees were of foraging age and sourced from Arizona State University (Social Insect Research Group, Smith Lab). The day prior to experiments, honeybees were collected from cages within the incubator and placed into 50 mL conical vials. Six individuals were cryoanesthetized by

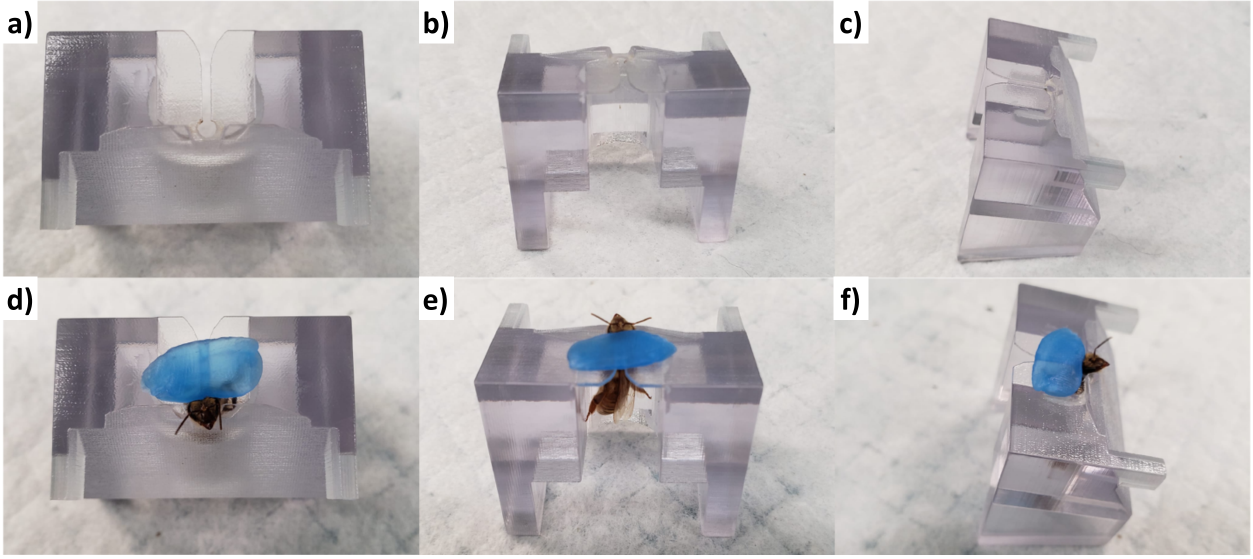

Figure 2.22 | Honeybee Harness and Surgical Preparation. Honeybees were placed inside a custom-designed, 3D-printed harness and secured with dental wax.

inserting the conical vials into an ice bucket for ~1 minute until motion cessation. Using entomological forceps, honeybees were removed from the vials and secured into a custom-designed, 3-D printed harness by placing a piece of dental wax directly behind the head (**Figure 2.22**). Honeybees were left undisturbed for 30-minutes and then fed with a 50% sucrose solution to satiation (**Figure 2.23**). All individuals were placed in a humidified cardboard box and left in the dark overnight. The following day, restrained honeybees were given a small amount of the

Figure 2.23 | Honeybee Proboscis Extension Response. Honeybees were allotted simple syrup the night before and morning of experiments. Here, a honeybee is engaging in a proboscis extension response after having her antennae stimulated with the sugar water mixture.

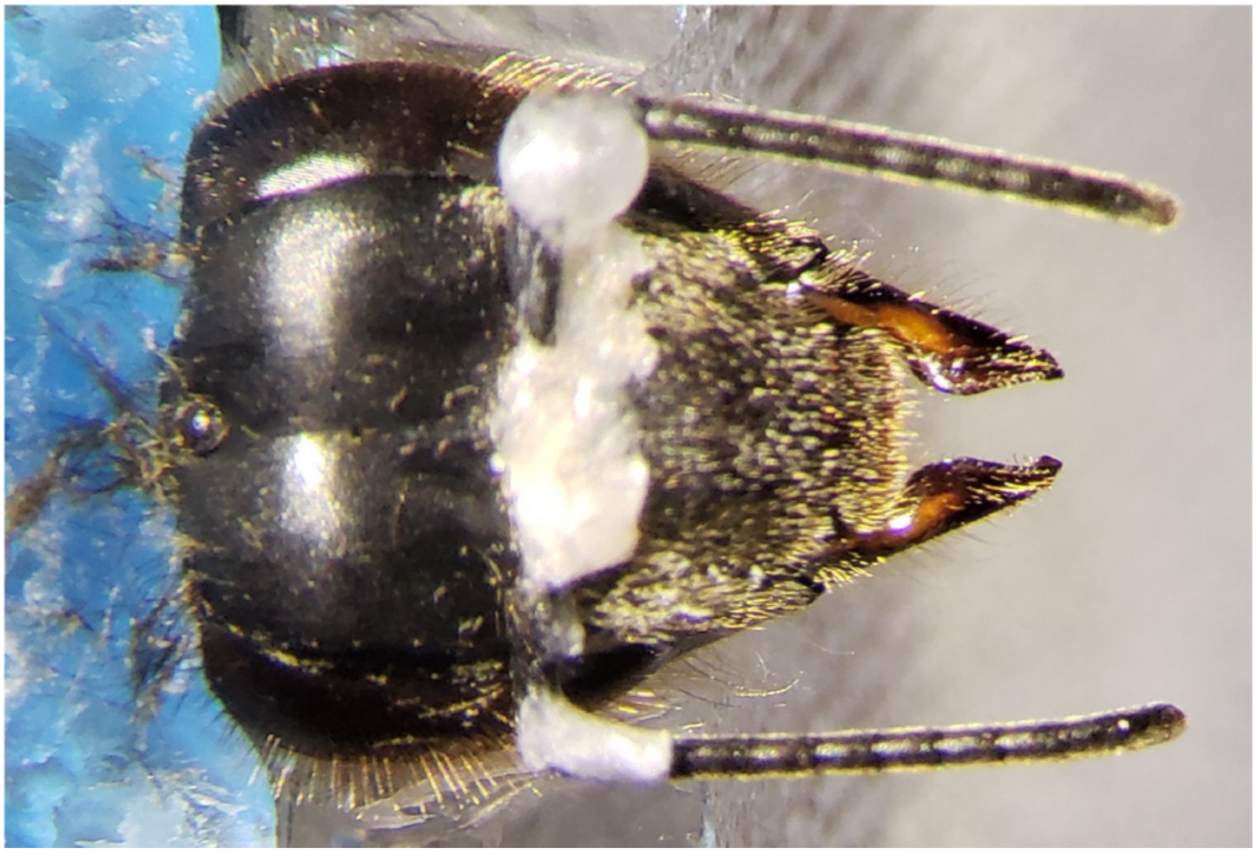

Figure 2.24 | Surgically Prepared Honeybee. Honeybee has been prepared for neurosurgery by affixing the antennae forward-facing with eicosane. The head capsule has also been shaved with a microscalpel.

1:1 water-sucrose solution to check for proboscis extension response. Individuals that did not present their proboscis were not used for electrophysiological experiments. Antennae were maneuvered into a forward-facing orientation using a custom-designed antennae tool and stabilized at the base of the scape and the pedicel with eicosane (**Figure 2.24**). The head was shaved using a microscalpel and a window of the head capsule exoskeleton was excised (**Figure 2.24**). Any glandular tissue atop the brain was removed to allow for direct electrode access.

Honeybees were placed inside a faraday cage and a small piece foam was placed behind the abdomen, to reduce body movement. A 30-AWG silver reference wire coated with chloride ions was hooked inside the head capsule window. A four-channel twisted wire tetrode was connected to the 16-channel DIP socket and adjusted by a micromanipulator for appropriate

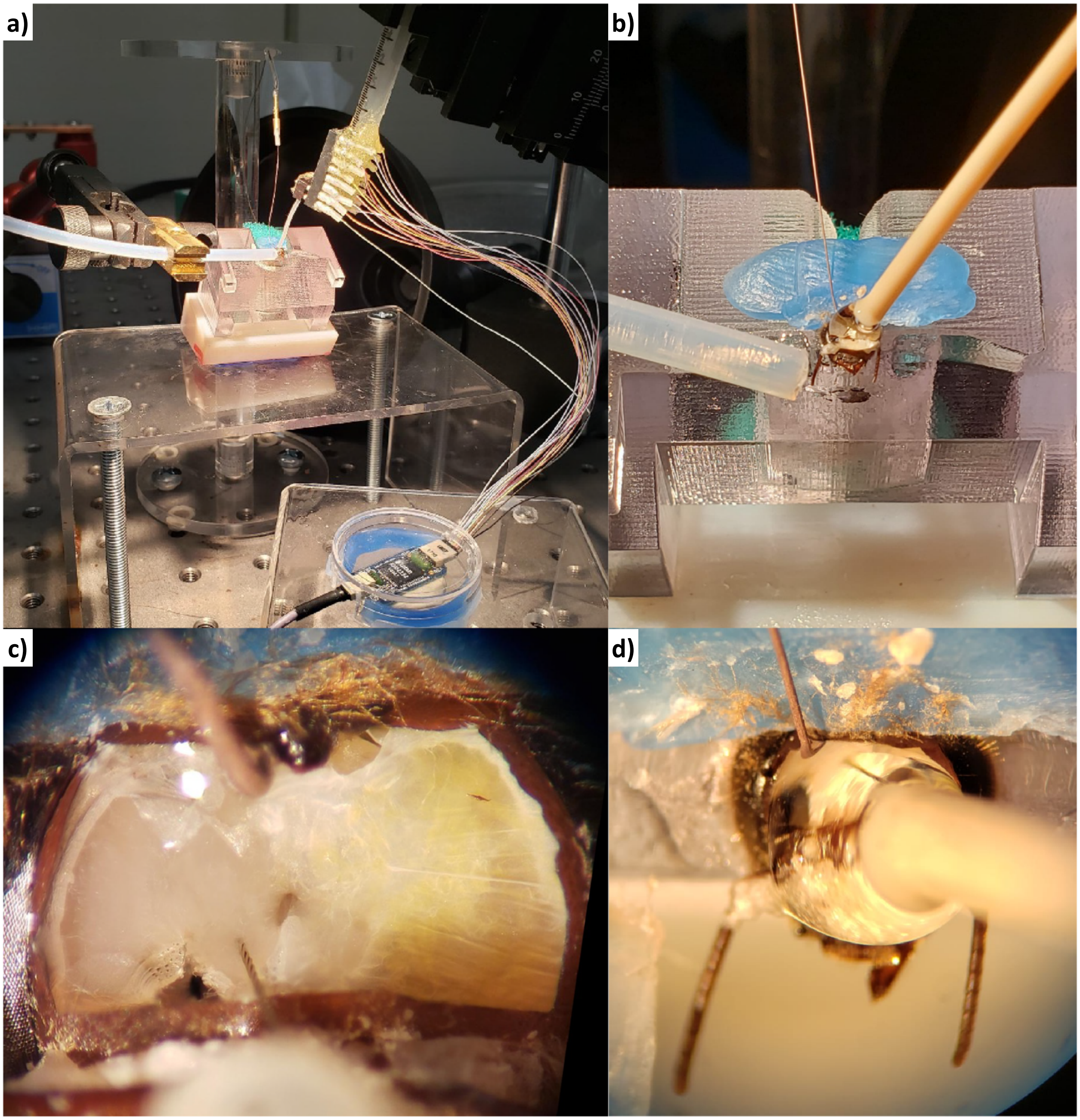

Figure 2.25 | Honeybee Electrode Insertion. Custom made tetrodes have been inserted into the antennal lobe to a depth of 100 μm. **c)** The twisted, 4-channel probe is clearly visible and the Ag-Cl reference wire has been hooked underneath the head capsule cavity. **d)** A single drop of honeybee saline solution is applied to prevent tissue desiccation during neural recordings.

targeting. The tetrode tip was brought to the antennal lobe surface. The tetrode was lowered into the antennal lobe (**Figure 2.25**) until clear neuronal spikes were observed (<100 μm) on the Intan USB board interface GUI. Adequate electrode targeting was confirmed by presenting a test odorant and checking odor-evoked responses. Once electrode positioning was finalized, 20 μLs of honeybee ringer solution was added to prevent tissue desiccation (**Figure 2.25**). Individuals were left undisturbed for 10 minutes to allow for the brain to settle around the electrode. Odorants were then presented in a pseudorandomized order and neuronal responses were recorded.

Signal Analysis

Data Preprocessing

All analysis of neuronal signals was performed using MATLAB, R2021b (MATHWORKS, Inc.) and IGOR-Pro 3.04. The MATLAB RHD file reader program, provided by Intan Technologies, was adapted to enable highly efficient file reading and data processing. All data was high pass filtered using a sixth order Butterworth filter with a cutoff frequency of 300 Hz. Stimulus presentation periods were identified using an external signal delivered to the Intan USB Interface Board. If necessary, data were aligned according to the stimulus presentation owing to the use of different software programs with independent clock cycles. Data were saved in experiment-specific folders, corresponding to individual electrode positions. At this point, all data underwent a spike sorting procedure as well as root mean square transformation.

Spike Sorting

Data were converted to big-endian format in order to enable file importation into IGOR-Pro 3.04. A supervised spike sorting program was used to identify spiking events based on experimentally derived parameters. Covariance matrices were generated for waveforms that exceeded a threshold between 2.5-3.5 times the standard deviation of the data. Sweep width and peak position of identified super-threshold waveforms were chosen to ensure the entirety of the waveform was captured. Common values for sweep width and peak position were 55 samples and 25 samples, respectively. A model was generated based on the identified spiking events and their time discrepancies that were seen in all four channels of the tetrodes. Sorted spike classes, corresponding to potential putative neurons, were required to pass a number of tests before further consideration. The distance (based on covariance) to a spike's nearest neighboring spike was considered. Additionally, the standard deviation within an individual spiking class and the percentage of interspike intervals that were less than 20 ms were also considered. For locust recordings, Neuronexus-based tetrodes, with an inter-electrode pitch of 25 μm, were sufficiently separated in space to consider all three tests. Here, the nearest projection was required to be greater than five standard deviations away and the percentage of inter-spike intervals less than 20 ms as well the intra-spike standard deviation could not be over 10%. For honeybee recordings, custom-made twisted wire tetrodes did not provide enough spatial separation to apply the same demands. In this case, the nearest projection was also set to a minimum of 5 standard deviations away, but the intra-spike standard deviation was not considered Additionally, due to the spiking nature of local neurons in the honeybee antennal lobe, the minimal percentage of inter-spike intervals less than 20 ms was increased to 20%. Any spikes that did not meet these criteria for locusts or honeybees did not undergo further consideration and were discarded. Raster plots from the remaining spike classes of putative neurons were visually inspected to ensure adequate inter-trial reliability and inter-stimulus reliability for pre-stimulation baseline periods. Those spikes that passed this subsequent inspection were included in a model applied to all stimuli of an individual experiment. The model identified similar spikes in other neural traces from the same recording location across all stimuli. This process was repeated for all experiments, adjusting IGOR parameters as necessary to ensure spike consistency and reliability. The spike times of putative neurons were saved, converted to MAT files, and concatenated into master tensors corresponding to each stimulus.

Root Mean Square (RMS) Transformation

Data that were not subjected to spike sorting were processed according to an unsupervised root mean square transformation. Baseline values, considered to be voltage samples within 2 seconds prior to the stimulus onset, was averaged and subtracted from the entire neural trace in order to remove any bias due to electrode drift or signal-to-noise ratio variability. These baseline-subtracted voltages were trimmed to the time window of interest and subjected to a 500-point RMS transformation. Values that were less than 500 samples from either the beginning or end of the trace were gradually tapered off according to the mean of the remaining samples. A 500-point smoothing window was then applied to reduce any potential jitter due to natural biological variability or thermal noise. Signals from all four tetrode channels were averaged together to get an overall channel non-specific response. These RMS processed neural signals were concatenated into master tensors corresponding to the appropriate stimuli.

Data Processing & Neural Population Analysis

Experiment-specific analyses were performed to visualize the response characteristics of an individual electrode position or putative neuron. For raw signals, per-stimulus voltage traces depicted signal-to-noise ratio and variability of responses based on the presented stimulus. For

RMS-processed data, per-stimulus voltage traces could also be visualized. For spike sorted data, raster plots and peri-stimulus time histograms depicted possible stimulus-specific neuron response patterns as well as inter-trial reliability of spiking events. More often, population-wide responses were analyzed using the master tensors constructed from RMS-processed and spike sorted data. For spike sorted data, the average of the 2 seconds prior to the stimulus were subtracted from all experiments. For RMS-processed data, this was already performed during the pre-processing regimen. Data were then binned according to the user-defined bin size. Master tensors corresponding to individual stimuli were concatenated into one overall master tensor with the following dimensions: number of neurons (for spike sorted data) or electrode positions (for RMS-processed data) × number of binned samples × number of trials × number of stimuli.

Population peri-stimulus voltage traces or peri-stimulus time histograms with standard error of the mean indicators were created to visualize population-averaged responses to each stimulus. To further visualize population-wide response dynamics, principal component analysis (PCA) was used as a dimensionality reduction technique. Here, data were projected to new coordinates defined by the three largest eigenvectors of the dataset. This linear transformation maps data to a new coordinate system defined by the directions of maximal variance within a particular dataset and is routinely implemented to determine any potential underlying structure within high-dimensional data. Owing to the temporal evolution of neural responses, data were projected to this new PCA subspace and connected in a temporal fashion, forming neural trajectories. These neural trajectories were smoothed slightly for visualization with a low-grade cubic spline interpolation technique. Previous research has determined that these neural trajectories correspond to stimulus-specific features, such as chemical identity and concentration[516]. Additionally, linear discriminant analysis (LDA), was routinely used to visualize datasets in an alternate dimensionally reduced subspace more suited to classification-based problems. LDA differs from PCA in that it uses a priori class information to determine the optimal transformative subspace. The algorithm does this by finding a linear transformation that maximizes the between-class scatter while minimizing the within-class scatter of the projected classes. Here, the data was initially normalized according to the mean of the entire dataset. Means of all normalized data and of all stimulus-specific data were then calculated. The eigenvectors of these resultant scatter matrices were computed, and all data was projected onto the first three of these new component dimensions to form a new LDA subspace. An optional L2 regularization parameter was added to mitigate any potential overfitting of the algorithm when considering overdetermined systems.

For quantitative analysis, data was handled solely in the original high-dimensional space. Here, by using a leave-one-trial-out approach, training templates corresponding to each stimulus were constructed. Test trials were held out and thus, not used for template construction. Progressing through the temporal evolution of the neural signal, each sample was compared to each training template using an L^1 (Manhattan distance) or L^2 (Euclidean distance) norm metric. The training template that minimized this norm value, dictated classification of the test sample bin. Cycling through all combinations of trials for template construction, enabled each trial to be the held-out test trial exactly once. The classifier performance was then visualized by plotting the presented odor versus the odor predicted by the model in a confusion matrix. Here, correct classifications are indicated by entries along the main diagonal. Since insects rely heavily on both spatial and temporal response characteristics for stimulus identification, we performed a winner-take-all approach for a particular trial. This required taking the mode of all the bin predictions of an individual trial as the appropriate predicted class. We constructed trial prediction-specific confusion matrices for this subsequent approach. While the training templates and test trials are independent in the leave-one-trial-out approach, we also formulated completely non-overlapping train and test trial sets and performed similar norm calculations and confusion matrix visualizations.

CHAPTER 3 | DISCRIMINATING CANCER BIOMARKERS USING A NOVEL INSECT BIOSENSOR

Chemical Sensors

A key factor in the development of chemical sensing systems is the selection and integration of optimal sensing materials. For each stimulus, sensors must undergo rigorous testing regimens to determine whether they are effective for the application at hand. For example, a sensor designed to aid in the diagnosis of bronchial asthma, in which elevated levels of exhaled nitric oxide are present, must first and foremost be capable of detecting nitric oxide[1, 20-23]. Thus, the most critical quality of an effective breath-based diagnostic is responsiveness to the chemical(s) associated with the disease of interest. However, sensor response characteristics can be affected by a host of different factors that may be inherent to the sample itself or the sampling environment, complicating device reliability. One of the most prominent challenges for manmade sensors, such as GC-MS and enoses, is the processing of stimuli characterized by high levels of humidity. The presence of water vapor is well known to negatively affect sensor detection limits. In contrast, biological olfactory systems, having evolved in the natural world, may in fact benefit from the high water vapor concentration of breath samples[524, 525]. Another factor affecting chemical reaction kinetics is sensor operating temperature. Higher temperatures increase the rate of chemical reactions and can shorten processing time associated with manmade chemical sensors. Additionally, the shorter pre-sensing period mitigates the time allotted for the breakdown of highly sensitive volatiles. This enhanced sensing rapidity can help to maintain biomarker integrity and provide a more accurate profile of exhaled cellular metabolites. Yet the heating of volatile components can itself encourage molecular degradation.

Both vertebrates and invertebrates can rapidly process chemical signals and identify stimuli without the need for such highly controlled extrinsic thermal regulation[526, 527]. The fundamental goal of biological olfaction is to encode stimulus-specific information in such a way that reliably shapes perception and directs future behavior. As such, organisms must rapidly encode chemical stimuli in unique manners that allows for maximal perceptual discrimination. Canines, for example, have exquisite chemosensory abilities and are routinely employed as chemical biosensors. A number of experiments have demonstrated that canine olfaction can be used to diagnose pathological states using breath samples. To perform this feat, canines must be able to identify subtle alterations in metabolic byproducts contained in breath profiles indicative of the disease state.

Cellular Metabolism & Breath-Based Biomarkers

At any one time in the human body an assortment of up to 8700 possible biochemical processes are ongoing[528]. Intermediary metabolic reactions are responsible for synthesizing simple molecules or polymerizing them into complex macromolecules (anabolism), breaking down compounds to release energy (catabolism), and removing any chemical byproducts (waste removal). Chemically sensitive transporter proteins bind to and transport glucose molecules into cells where they are phosphorylated and most often undergo glycolysis[529]. In the presence of oxygen and two key substrate molecules, aerobic glycolysis converts glucose to the intermediate metabolite pyruvate. Pyruvate is then converted to acetyl coenzyme A before entering the TCA cycle to be converted into carbon dioxide, water, and adenosine triphosphate. In anaerobic conditions, glycolysis converts glucose into lactate, which does not undergo further oxidation[530]. Instead, the Cori cycle transports the lactate to the liver, which converts it back to glucose via gluconeogenesis. The overarching goal of this intricate interplay of cellular functions is to maintain homeostasis and the disruption of a single subprocess can lead to the development of a particular disease state[531].

Diabetes mellitus, for example, is a disorder that is characterized by elongated periods of hyperglycemia. Here, an enzymatic imbalance enhances gluconeogenesis while decreasing the rate of glycolysis. This in turn triggers excessive hepatic glucose production and high concentrations of glucose in the blood for extended periods of time[532]. The inability to effectively transport glucose into the cell alters feedforward and feedback regulatory pathways. Anabolic and catabolic dysregulation can exacerbate bouts of hyperglycemia inducing significant levels of oxidative stress[533-536]. Carbon dioxide, digested nutrients and metabolic waste are transported to the lungs via the pulmonary circulatory system. Here, carbon dioxide and other highly volatile chemicals can diffuse across the blood-air barrier into the alveoli of the lungs, and possibly airways, and be excreted in the breath[537]. The chemical profile of exhaled breath contains a substantial degree of information on underlying metabolic processes and the existence of particular pathologies can be inferred. For diabetics in particular, acetone production has long been known to increase during diabetic ketoacidosis[25, 538, 539] and breath-based concentrations correlate with glucose serum levels[540]. This allows for the development of effective breath tests to measure acetone concentrations, which are widespread in research and gaining traction for clinical implementation[26, 541-549].

Unlike acetone as a marker for diabetes, a single volatile biomarker indicative of cancer has not yet been discovered and is highly unlikely. Rather, complex patterns of specific VOC concentration increases and decreases have been observed in cancer-related breath testing research. The subtle changes in numerous breath constituents are suspected to reflect the underlying heterogeneity and multifarious nature of the disease. The molecular mechanisms of cancer have been studied ad nauseum for over two and a half centuries. Cancer cells deregulate natural metabolic signals for achieving homeostasis in favor of those promoting chronic proliferation. Warburg first demonstrated that even in oxygenated environments, most cancer cells preferentially engage in glycolysis but not subsequent oxidative phosphorylation, as often occurs in healthy cells[550]. The intermediary pyruvate molecule is converted to lactate and either secreted into the extracellular milieu or recycled for cell-specific nutrients[551, 552]. Inefficient energy production of aerobic glycolysis is compensated by upregulating glucose transporter proteins, enabling significantly more glucose to enter the cell[553]. The combination of the unfavorable energy output of glycolysis and the introduction of additional glucose transporter proteins into the cell membrane, causes the cell to deplete glucose from surrounding tissues[554]. Moreover, the elevated levels of lactate in the extracellular space promote immunosuppression, thereby preventing tumor cell recognition and enabling further proliferation[552, 555, 556]. A host of downstream effects are common including the synthesis of excessive fatty acids, tumor formation and acidification of the local cellular environment[557]. This leads to the aggregation of metabolic waste products at levels not seen in healthy conditions, which, if volatilized and excreted via the breath, can be indicative of underlying pathology. Numerous studies have investigated the efficacy of breath-based technologies for the diagnosis of lung, breast, and other types of cancers. Blood- and breath-based concentrations of certain aldehydes, alcohols, and ketones have been shown to differ based on the underlying disease as well as the affected organ[558].

Locust Olfaction

The desert locust (*Schistocerca gregaria*) is a widely used insect model for exploring biologically relevant olfactory processing schemes. Preliminary work by Laurent and others, elucidated several critical aspects locusts employ for odorant discrimination, including local signal processing networks and sparse signal transmission to higher neural regions[359, 360, 511, 516, 518, 559, 560]. The exact dynamics of these networks remain unknown but theoretical and computational models continue to elucidate key elements of functional schemes[514, 560-563]. Locust antennae display a variety of disparate chemosensory sensilla dedicated to olfaction. These sensilla house olfactory receptor neurons (ORNs), which are responsible for chemical recognition and signal transduction. For example, basiconic sensilla house anywhere from 30-50 ORNs, whereas trichoid sensilla house just three[480]. The majority of ORNs are broadly tuned, responding to a number of different volatile chemicals based on specific stereochemical properties. This enables a highly complex and competitive ligand binding environment within each sensillum, especially those with greater numbers of similarly tuned ORNs. Relative to other insects, locusts have been found to display unique anatomical features. Individual ORNs branch to and innervate several glomeruli within the antennal lobe, suggesting a highly adaptable network with extensive signal processing capabilities[564]. Interestingly, unlike the fewer (50-100), large glomeruli found in other insects, the antennal lobe of locusts contains 1000 microglomeruli[355, 564]. These highly interconnected glomeruli are positioned near the surface of the antennal lobe and arranged around a central fiber core **(Figure 3.1)** [515]. This dense fiber

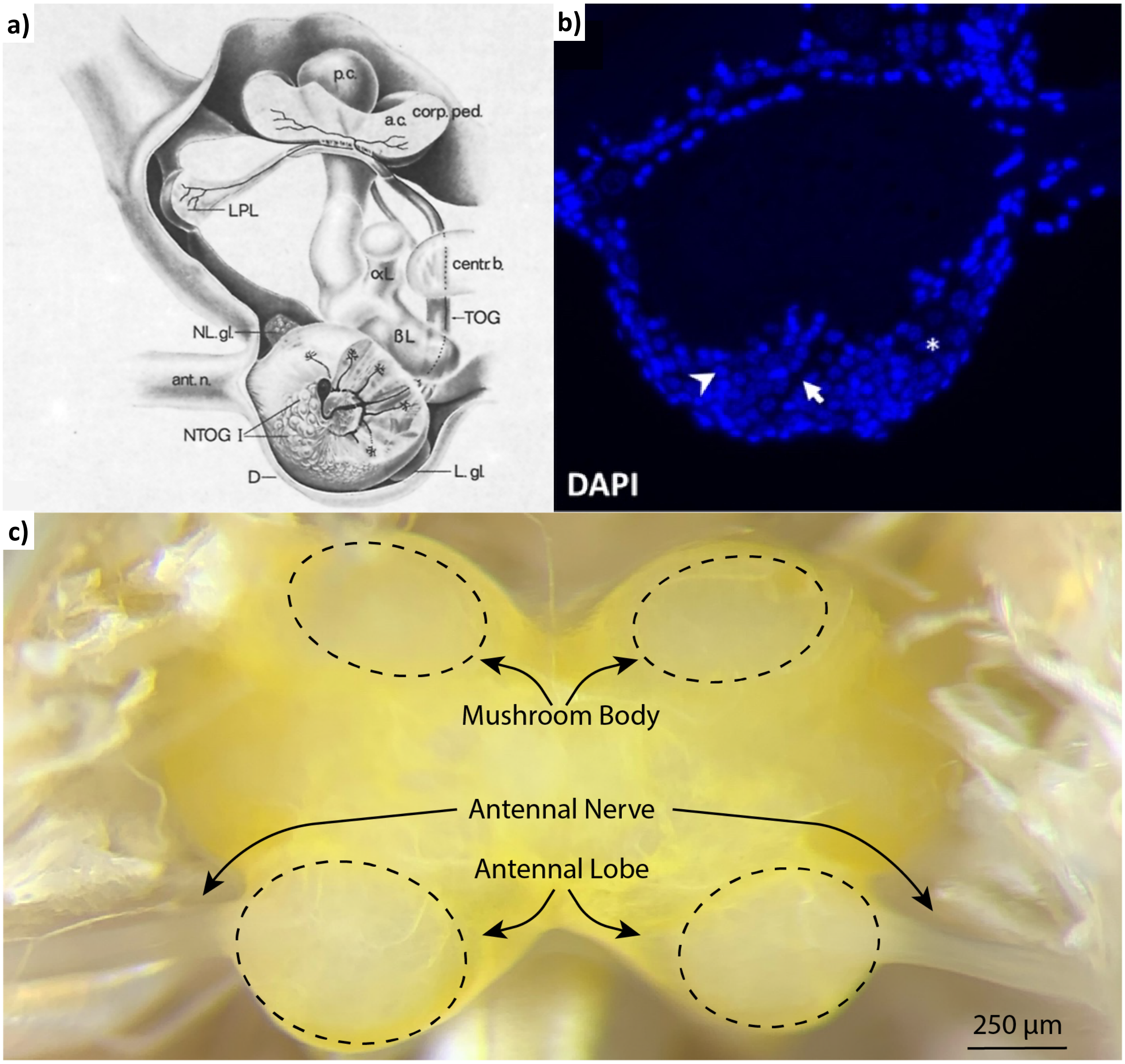

Figure 3.1 | Locust neuroanatomy. a) Schematic drawing of locust brain with emphasis on olfactory pathway. Olfactory receptor neurons project axons to the antennal lobe via the antennal nerve (ant n.). A projection neuron (labeled as NOTG I) is depicted. Locust projection neurons can receive signals from eight or more glomeruli, eliciting spikes with sufficient concurrent input activity. The axonal projections innervate Kenyon cells of the mushroom body (a.c.) in a sparse fashion. Reproduced from [564]. **b)** Microglomeruli can be visualized with a DAPI stain, confirming their presence around the cortical region of the antennal lobe. Reproduced from [565]. **c)** An exposed locust brain following surgery procedure. The antennal nerves, antennal lobes and mushroom bodies are clearly visible.

network efficiently converges input signals from a total of 50,000 ORNs onto a mere 300 inhibitory local neurons. Lacking axons, local neurons utilize dendrodendritic graded electrical potentials, instead of spike-based action potentials, to aid in local signal conditioning. The neural network within the antennal lobe is an immensely powerful signal processor, capable of improving signal-to-noise ratios and enabling background-invariant odor coding[311]. While some of these local neurons extend to only a few glomeruli, others arborize across the majority, if not all, of the antennal lobe neural circuitry. After signal conditioning, an assortment of 830 projection neurons, which receive input from multiple different glomeruli, transmits the signal

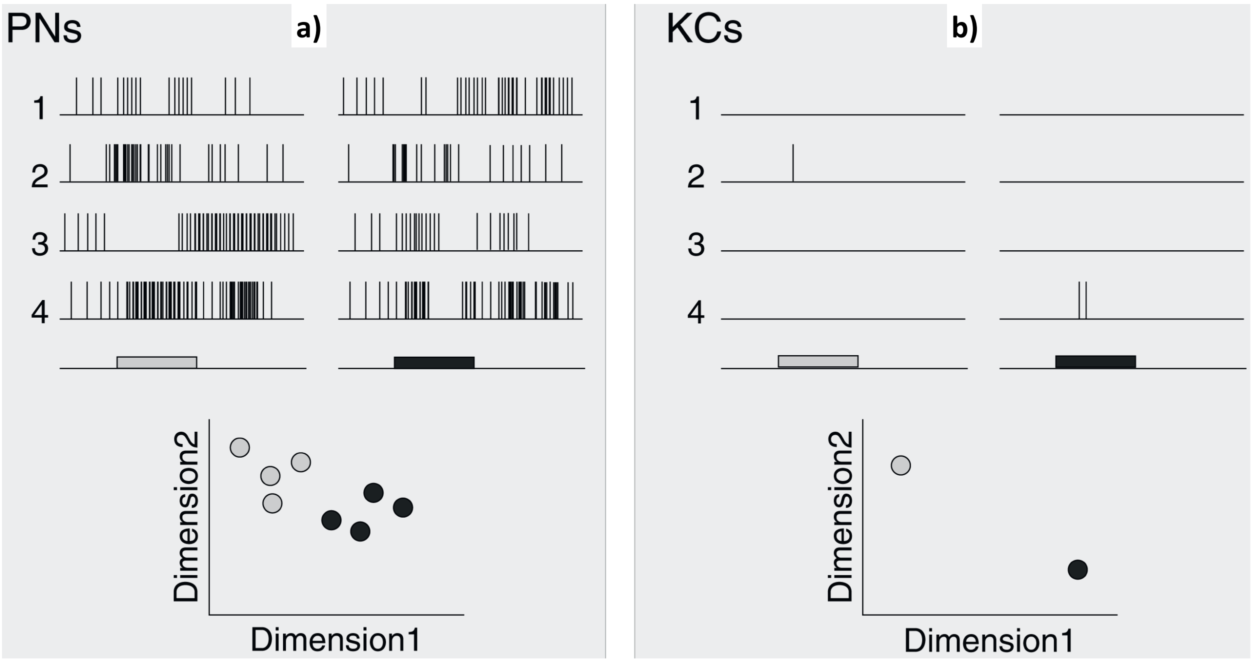

Figure 3.2 | Antennal lobe-mushroom body signal sparsening. a) Four projection neurons elicit unique bursting response properties to the same and different odorants. These neurons display a considerable amount of spontaneous baseline activity before the stimulus arrives (gray and black bars). The responses of these neurons are mapped to and visualized in a lower two-dimensional space as a cloud of points. **b)** Kenyon cells of the mushroom body exhibit extremely sparse firing activity and little to no background spiking. Note that there is a significant of divergence between the projection neurons (830) to Kenyon cells (50,000), suggesting considerable specificity. The signal transformation that occurs between projection neurons and Kenyon cells improves separability in this lower two-dimensional space. Reproduced from [566].

to higher order neural regions, such as the mushroom body. Here, 50,000 highly specific Kenyon cells exhibit little to no spontaneous activity and only fire one to two spikes when activated **(Figure 3.2)** [566]. Each of these Kenyon cells is contacted by approximately 50% of the PNs, providing a highly intricate, multidimensional input signal for each neuron[567]. Receiving a significant number of inputs, Kenyon cells function as coincidence detectors, only firing when a large portion of the afferent projection neurons all fire simultaneously. This decorrelating function of the mushroom body can reduce the complexity of the incoming signal, making it far more interpretable while maintaining a substantial encoding state space[560, 568]. The response dynamics of mushroom body neurons play a vital role in learning as well as memory formation, consolidation, and retrieval via feedback mechanisms.

Locust-Based Cancer Biomarker Differentiation

Previous work has demonstrated that locusts can detect and differentiate between various alcohols, aldehydes[516, 517, 519], and even explosive chemicals[523]. In order to determine the feasibility of using the locust olfactory system as a breath-based cancer diagnostic, we sought to test the responsiveness of projection neurons to a number of volatiles found to be significantly upregulated in lung and breast cancer[78, 132, 569]. Moreover, we intended to demonstrate that the chemicals could elicit unique and reliable responses capable of providing successful stimulus discrimination. For the lung cancer volatile chemical panel, we used decane, 2-methylheptane, 6-6-4-4 pentamethylheptane, propylbenzene and undecane. For the breast cancer volatile chemical panel, we used hexanal, nonanal, pentanal, trichlorotheylene and undecane. All odorants were diluted in paraffin oil (1% v/v) and stored in 20 mL glass vials with 1/32” diameter

Lung Cancer		Breast Cancer	
Decane	0.67 ppm	Hexanal	0.43 ppm
Methylheptane	3.14 ppm	Nonanal	0.2 ppm
Pentamethylheptane	0.83 ppm	Pentanal	10.8 ppm
Propylbenzene	1.61 ppm	Trichloroethylene	53.23 ppm
Undecane	0.22 ppm	Undecane	0.22 ppm

Table 3.1 | Biomarker stimulus panel. All odorants were chosen due to their identification as breath-based volatile biomarkers in lung and breast cancer. A large number of volatiles have been linked to cancer with significant variation between studies. Note that some chemicals may be implicated in more than one type of cancer, such as undecane seen here.

polytetrafluoroethylene (PTFE) tubing serving as inlet and outlet lines. For additional information on odorant preparation, see *Chapter 2: Methodology- Stimulus Creation*. Due to differences in volatilities, Raoult's law was used to approximate the gaseous concentrations (**Table 3.1**).

The brain of locusts was exposed and perfused with a custom-made locust saline throughout the duration of the experiment to prevent tissue desiccation. Microelectrode arrays

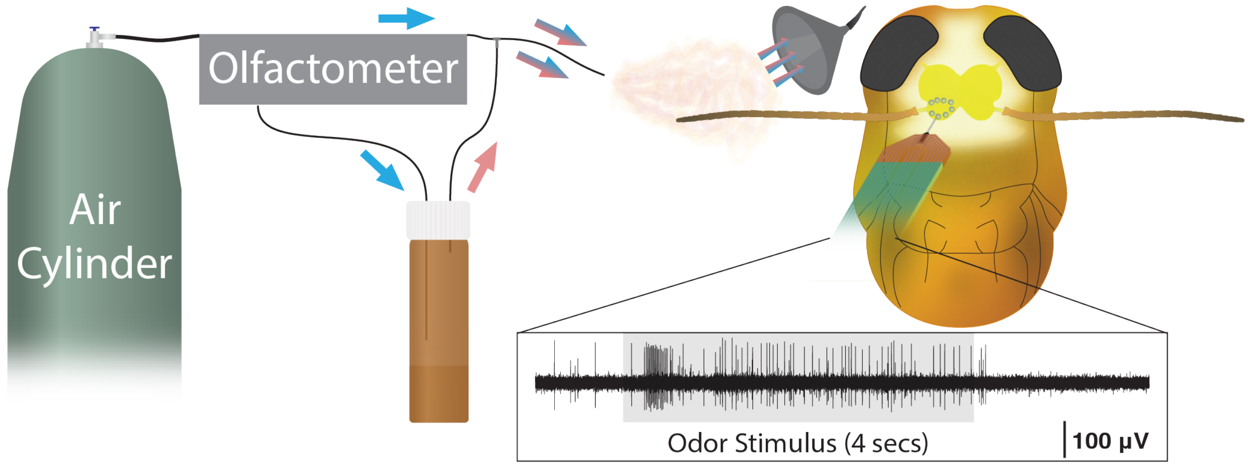

Figure 3.3 | Experimental design schematic. The air cylinder passes zero-contaminant air into the olfactometer, which controlled flow trajectories using a series of solenoid valves. Upon stimulus delivery a final valve (not shown) redirected the airstream in-line with the vial to the insect antenna. For more information see *Chapter 2: Methodology- Stimulus Delivery*. Here, odor delivery demarcated by the gray box elicits a sharp transient response from locust projection neurons. The neuron quickly moves into a steady state response before a return to baseline upon stimulus offset.

were inserted into the antennal lobe until spikes were visible and purified odorants were presented in a pseudorandomized fashion **(Figure 3.3)**. For more information, see *Chapter 2: Methodology- Stimulus* Presentation. The locust olfactory system appeared highly responsive to many of the presented odors. Though some stimuli, such as hexanal, seemed to generate distinctive responses in most neurons, others appeared to preferentially activate more select

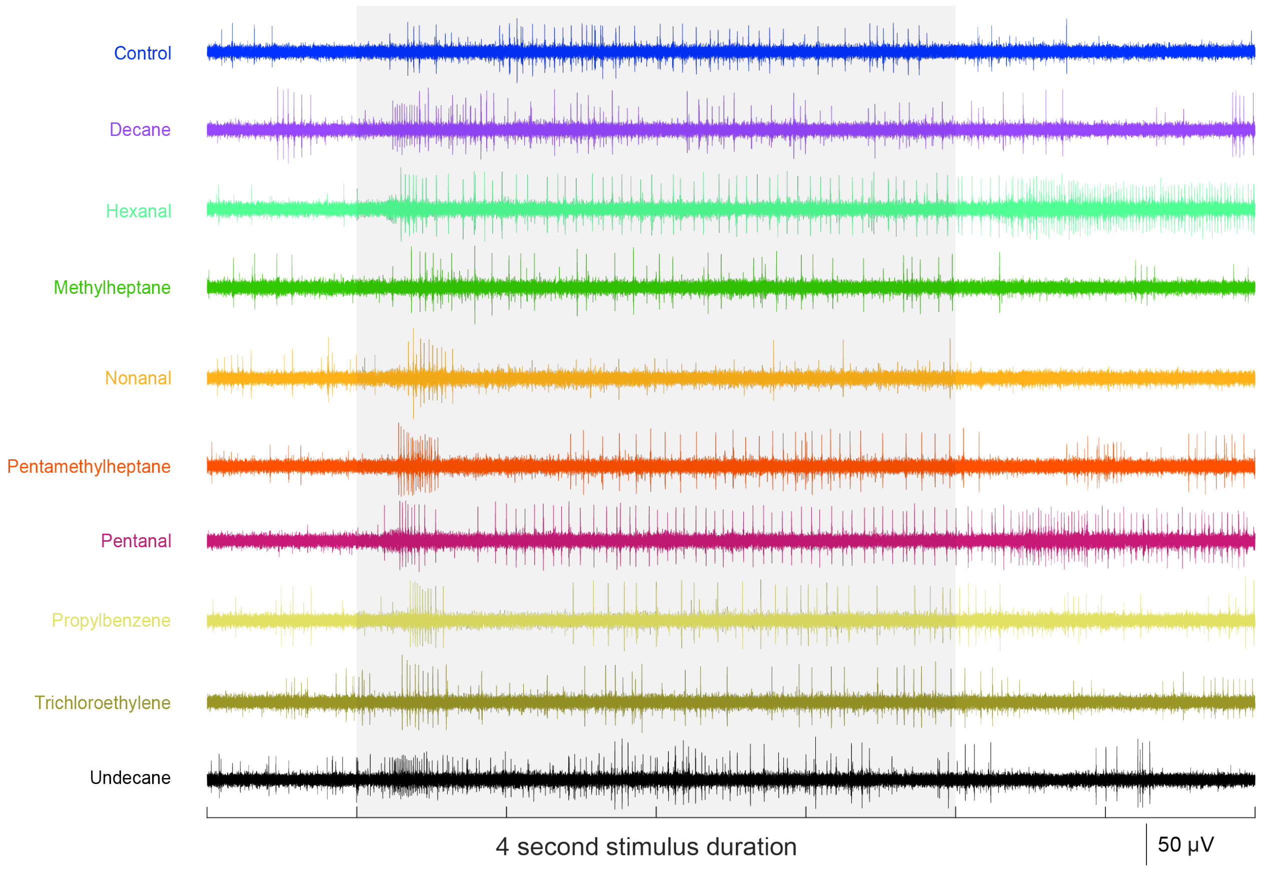

Figure 3.4 | Biomarker peristimulus voltage traces. Neural traces from a representative neural recording location demonstrate unique spatiotemporal responses to different odorants. Four second stimulus presentation indicated by gray box. Spontaneous spiking occurred prior to stimulus onset as is expected from projection neurons. Most odors caused a significant increase in spike rates, especially during the transient response period. Some odors, such as hexanal and pentanal, display a unique spiking response to the stimulus onset as well as a separate pattern to the stimulus offset. Note that in some of the traces, spikes of different amplitudes are discernible, suggesting the presence of multiple neurons from this recording location.

neuronal subsets. In order to investigate the quality of the data, we initially observed individual recordings and odor-evoked response dynamics. Neural signals recorded from an individual electrode elicited reliable temporal responses over all five trials. **Figure 3.4** depicts voltage traces after pre-processing with a 300-Hz high-pass filter to remove low frequency signals associated with local field potentials. Increased neural firing rates indicate that neuron(s) in this particular electrode recording vicinity were able to detect most of the volatile molecules included in our cancer odor panel. The broad tuning curves of many projection neurons in the locust antennal lobe suggests that each neuron may respond to a particular feature of the presented stimulus. On this basis, we recorded from 24 different electrode positions across nine individual locusts. Evidence suggests that the antennal lobe and associated neural circuitry is largely conserved within species. Thus, each recording was considered independent as different areas of the antennal lobe were targeted. To investigate the population-wide responses from all recordings, we first employed a spike sorting procedure (see *Chapter 2: Methodology- Signal Analysis*). Spike times corresponding to putative neurons were recorded. Owing to the 20-Hz oscillatory integration cycles observed in the antennal lobe and the corresponding spiking activity in Kenyon cells of the mushroom body, we considered the total number of spikes over a 50 msec window. A master tensor was created consisting of spikes per bin × trials × number of bins.

A population-wide peri-stimulus time histogram was constructed by plotting the average value across all binned neuron-specific responses for a given odor **(Figure 3.5)**. While these peri-stimulus time histograms demonstrated unique response properties of all neurons as an averaged group, more effective analyses were performed to further investigate the underlying structure of the data. Various time windows were considered to determine the response period

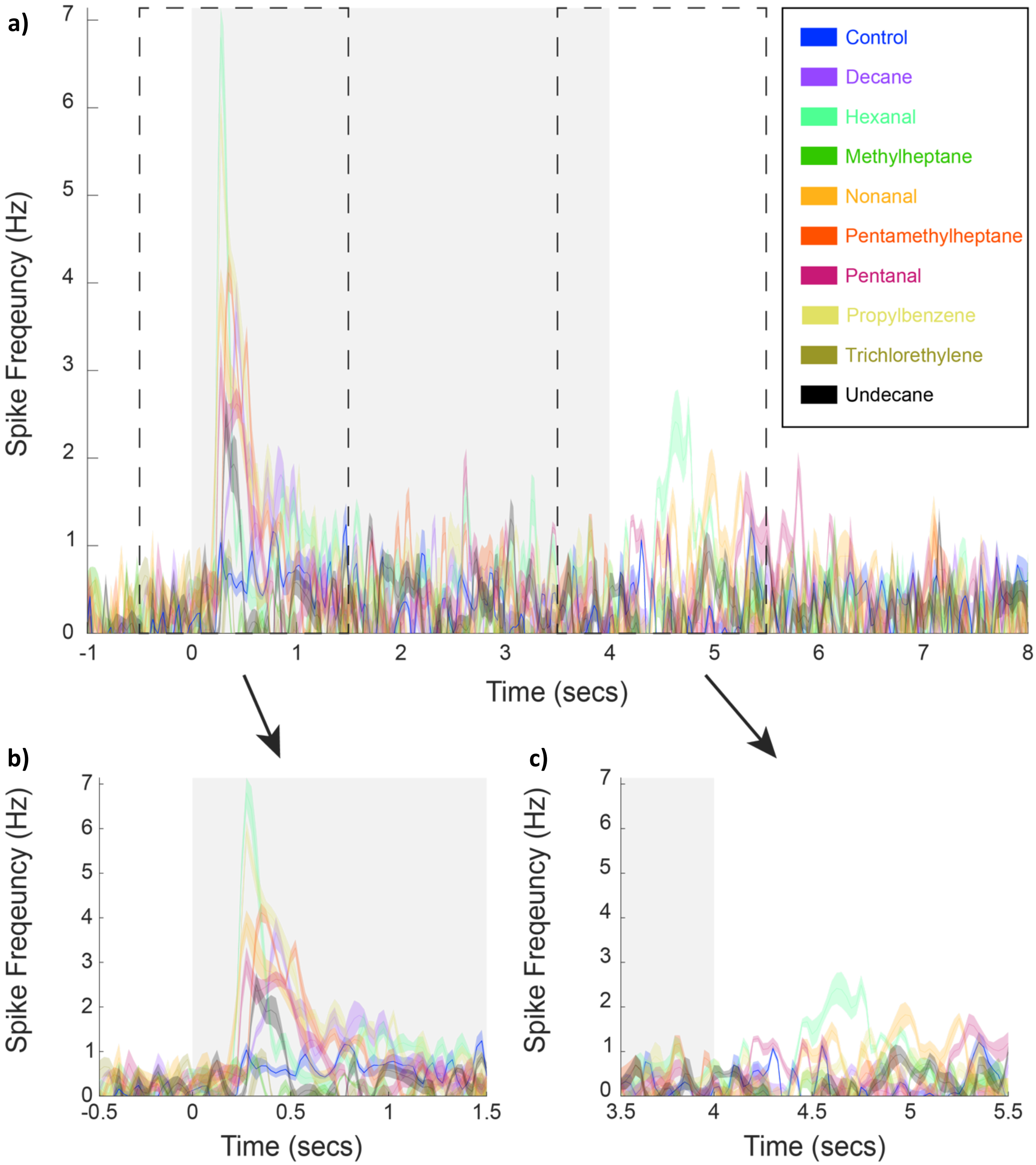

Figure 3.5 | Population-wide peri-stimulus time histogram demonstrates unique response trajectories. a) Neural traces are plotted from one second prior to stimulus onset to four seconds after stimulus offset, as response dynamics can continue well after stimulus cessation. Unique response patterns were observed with the transient period immediately after stimulus onset eliciting the most significant odor-evoked activity in response to all odors. **b)** On responses were seen approximately 300 msecs after stimulus delivery. This agrees with the latency for

Figure 3.5 (cont'd)
intracellular recordings and other insects. **c)** Some odors generated relatively informative off responses upon stimulus cessation, though, on average, they were less stark than the transient on responses. Note in all plots, mean averages are depicted with a dark colored line and the standard error of the mean over all trials is plotted as a semi-translucent colored patch surrounding the mean average.

capable of issuing optimal stimulus separability and classification. Linear dimensionality reduction techniques were utilized for data visualization purposes. Data was processed according to principal component analysis (PCA) and resultant neural trajectories were plotted as functions of time for the three dimensions explaining maximal variance across the dataset. For data processing specifications, see *Chapter 2: Methodology- Signal Analysis*. **Figure 3.6** depicts neural trajectories for the four seconds following stimulus onset **(Figure 3.6a)**, the two seconds following stimulus onset **(Figure 3.6b)**, and the one second following stimulus onset **(Figure 3.6c)**. For all analyzed time periods, trajectories are seen to move to different regions of the PCA subspace during the transient response period before returning to near baseline upon reaching a steady state. This suggests neurons exhibit unique, stimulus-specific response dynamics upon

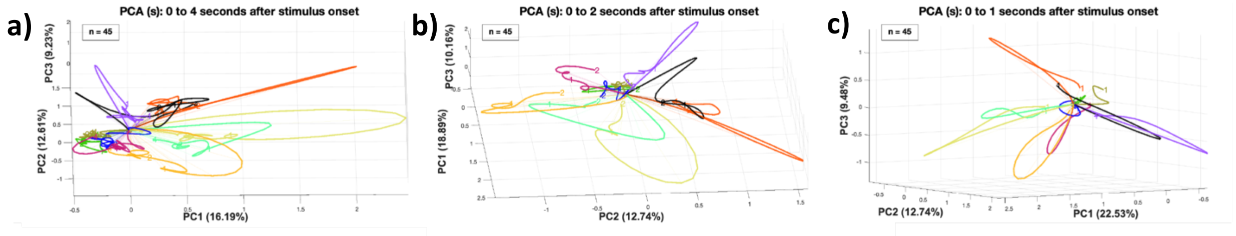

Figure 3.6 | Neural trajectories exhibit unique temporal dynamics after being projected into principal component space. The first bin of all trajectories are zeroed so that all traces begin at the same point in PCA space. Subsequent bins are subtracted by the initial value to maintain proper response dynamics. Neural trajectories evolve in specific manners for **a)** the four second period after stimulus onset, **b)** the two second period after stimulus onset, and **c)** the one second period after stimulus onset. Total number of neurons: n = 45.

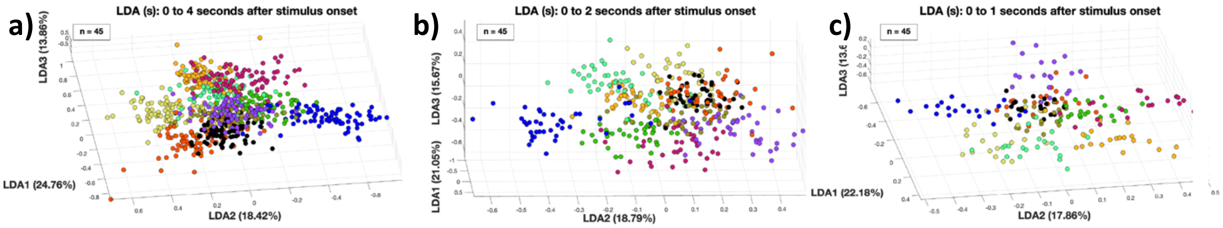

Figure 3.7 | Stimulus-specific clusters consisting of activity of individual time bins separate from one another in LDA space. Distinct groups begin to emerge by processing data according to a linear discriminant analysis transformation and projecting points corresponding to the activity of individual bins into this new subspace. This supervised dimensionality reduction technique was performed for a) the four seconds, b) two seconds, and c) one second after stimulus onset. Total number of neurons: n = 45.

stimulus presentation, especially during this initial transient period. To further investigate the underlying structure of the dataset, an alternative linear dimensionality reduction algorithm, linear discriminant analysis (LDA), was performed. This supervised technique serves to maximize the variance between different groups, while minimizing that within a particular group. Again, time periods of the four seconds **(Figure 3.7a)**, two seconds **(Figure 3.7b)**, and one second **(Figure 3.7c)** after stimulus onset were considered. Each dot corresponds to the activity of an individual time bin. As such, for longer time windows and smaller bin sizes, more dots were generated, and graphs became somewhat polluted. Nevertheless, the existence of stimulus-specific clusters began to emerge in this new LDA hyperspace. Dimensionality reduction techniques such as PCA and LDA are advantageous in their ability to present data in more interpretable manners. However, depending on the complexity of the dataset, a significant loss in overall information can occur.

For quantitative analysis, therefore, we generated stimulus-specific training templates using a leave-one-trial-out cross validation methodology in the original high dimensional encoding space. Training templates were formed from four out of the five trials, while holding the final trial out as a novel testing trial. Since our spike sorting algorithm was able to extract 45 putative neurons, each training template and testing trial consisted of a vector of 45 different values, each corresponding to an individual time bin over all suspected neurons. The stimulus-specific training templates were averaged over the time window of interest and a Euclidean norm metric was used to calculate the distance between each training template and individual bins for the testing trials. The training template that minimized the norm distance to the bin of the testing trial was considered to be the predicted class. For more details on our leave-one-trial-out classification approach, see *Chapter 2: Methodology- Signal Analysis*. Resultant predictions were plotted against the true values via a confusion matrix **(Figure 3.8a)**. This confusion matrix depicts the overall accuracy of classifying individual bins. While this allows for an expansive high dimensional encoding space, it treats each time bin as an independent unit. In contrast, biological systems can aggregate response information collected over a number of time bins until

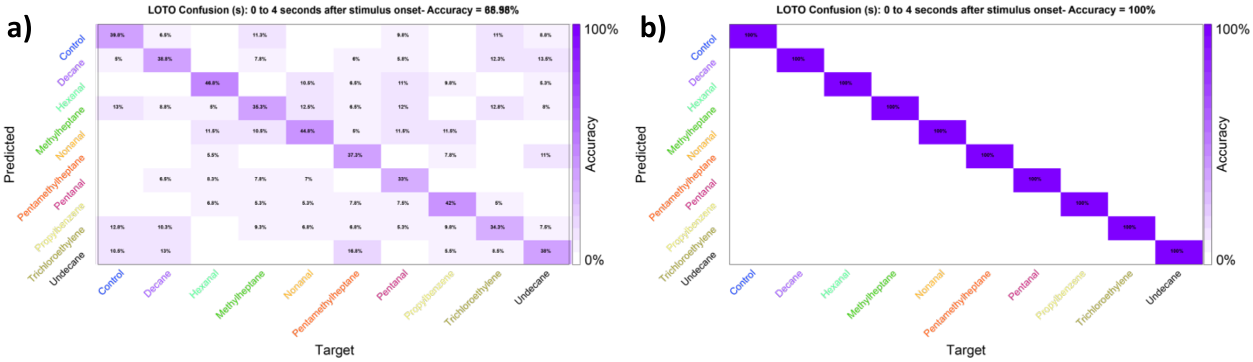

Figure 3.8 | Euclidian-norm based classifier performance. Here, classifier accuracies are displayed as confusion matrices. High classifier accuracy is indicated by dark colors along the main diagonal. The leave-on-trial-out train-test protocol was utilized in this scenario to train a linear classifier. To assign predicted classes for the test trial, we selected the training template that minimized the Euclidean distance (L_2). Results are shown for **a)** individual bins for each test trial and **b)** entire trials in a winner-take-all approach. Note in **a** the majority of test bins were classified correctly and in **b** the classifier achieved 100% accuracy.

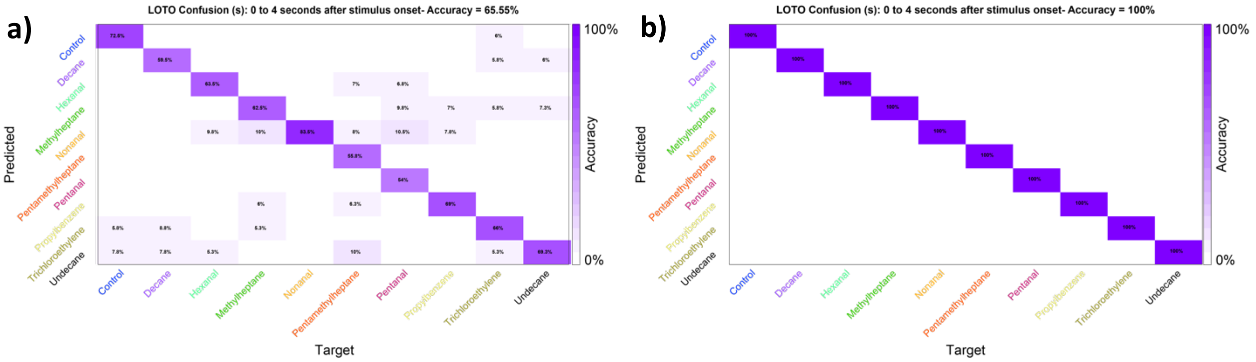

Figure 3.9 | Manhattan-norm based classifier performance. Similar to figure 3.8, classifier accuracies are displayed as confusion matrices. High classifier accuracy is indicated by dark colors along the main diagonal. The leave-on-trial-out train-test protocol was utilized in this scenario to train a linear classifier. To assign predicted classes for the test trial, we selected the training template that minimized the Manhattan distance (L_1). Results are shown for **a)** individual bins for each test trial and **b)** entire trials in a winner-take-all approach. A different norm metric applied here improved the bin-wise classification and did not affect the perfect performance seen previously in trial-wise classification.

sufficiently confident to predict stimulus identity. Therefore, we employed a winner-take-all approach where each trial in its entirety was classified, instead of individual time bins. This technique showed a marked increase in prediction accuracy evidenced by the associated confusion matrix **(Figure 3.8b)**. We also sought to determine classification effectiveness using the Manhattan norm distance **(Figure 3.9)** and maximum norm distance **(Figure 3.10)**.

Since locusts routinely integrate signals within a 20-Hz oscillatory cycle, our default bin size was 50 msecs. However, this time period may be an adaptation necessary for the rapid decision making within highly dynamic natural environments. The inclusion of more time windows, hence more oscillatory cycles, has been shown to be important for discriminating between stimuli with a higher degree of similarity[570]. While the inclusion of single odorants in our panel reduced the chemical complexity of the stimulus, these volatiles may not be ubiquitous in locusts' natural environment and classification accuracy may be highly dependent on allotted

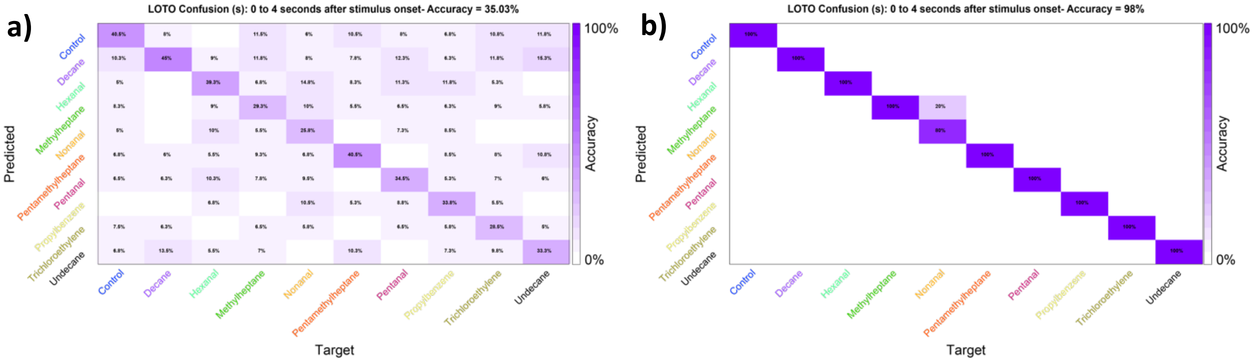

Figure 3.10 | Maximum-norm based classifier performance. Similar to figure 3.8, classifier accuracies are displayed as confusion matrices. High classifier accuracy is indicated by dark colors along the main diagonal. The leave-on-trial-out train-test protocol was utilized in this scenario to train a linear classifier. To assign predicted classes for the test trial, we selected the training template that minimized the infinity-norm (L_∞) distance. In this case, only the absolute value of the largest component of the vector is taken into account. Results are shown for **a)** individual bins for each test trial and **b)** entire trials in a winner-take-all approach. In this scenario, the classifier did not perform as well relative to using the Euclidean and Manhattan norms as distance metrics. Moreover, we see our first misclassification in the trial-wise confusion matrix.

processing time. Therefore, we tested alternate bin sizes of 100, 150, and 200 msecs. Peri-stimulus time histograms were characterized by smoother features with increasing bin sizes **(Figure 3.11)**. This is to be expected with a larger number of included data points, yet, critically,

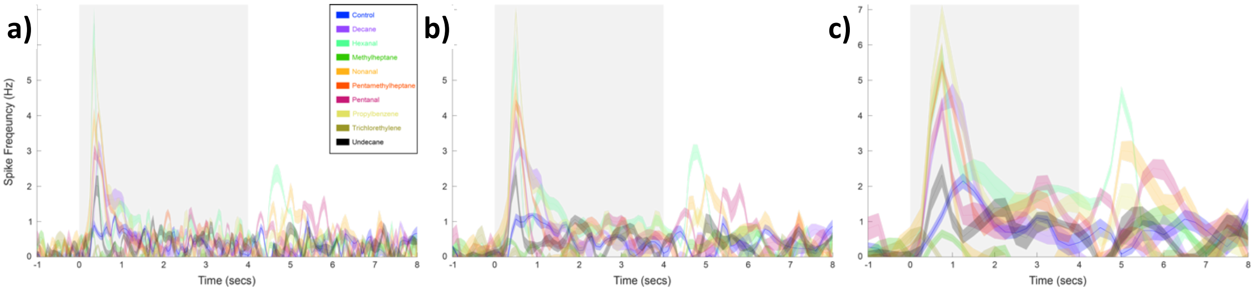

Figure 3.11 | Bin-size selection affects peri-stimulus time histogram dynamics. The graphs indicate the population average response for all neurons from one second prior to stimulus onset to four seconds after stimulus offset. The stimulus presentation period is demarcated by the light gray box. Different bin sizes were considered to examine their effect on response dynamics. **a)** 100-, **b)** 150-, and **c)** 200-msec bin sizes are shown. As the bin size increases, the data becomes smoother, reducing fine response dynamics that could be a result of noise or function as key information for stimulus classification.

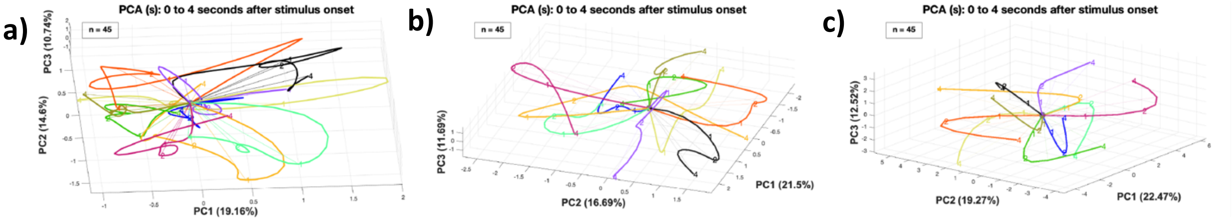

Figure 3.12 | Bin-size selection affects neural trajectories in PCA space. Data was plotted after processing via principal component analysis. As expected from the peri-stimulus time histograms, the minor voltage fluctuations evident in the **a)** 100-msec scenario were seen slightly with **b)** 150-msec and not at all with **c)** 200-msec bin sizes. In all three cases, unique neural trajectories are observed indicating that different odorants induce variations in temporal response patterns.

high consistency was observed in the overall response patterns regardless of bin size. All three bin sizes were processed via principal component analysis **(Figure 3.12)**, linear discriminant analysis **(Figure 3.13)**, and tested using the previously used leave-one-trial-out methodology **(Figure 3.14)**.

Spike sorting has the benefit of creating sparse matrices, significantly reducing computational complexity and overhead. Yet, the employed spike sorting algorithm used here was a supervised approach, requiring careful experimenter intervention and evaluation of each spike class as belonging to a viable putative neuron. Effective sensors, apart from permitting

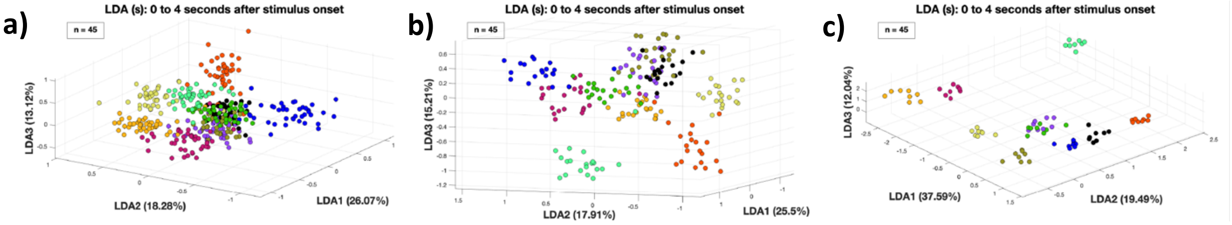

Figure 3.13 | Bin-size selection affects neural clusters in LDA space. Neural responses were processed using a linear discriminant analysis technique and the time bins were plotted in LDA space. Here we can clearly see fewer time bins with a larger bin size. **a)** With 100-msec bin sizes, stimulus-specific groups were beginning to emerge, but some still remained clustered together. **b)** 150-msec bins enabled well-separated clusters and **c)** 200-msec bins enabled clusters to occupy discrete points within the LDA subspace.

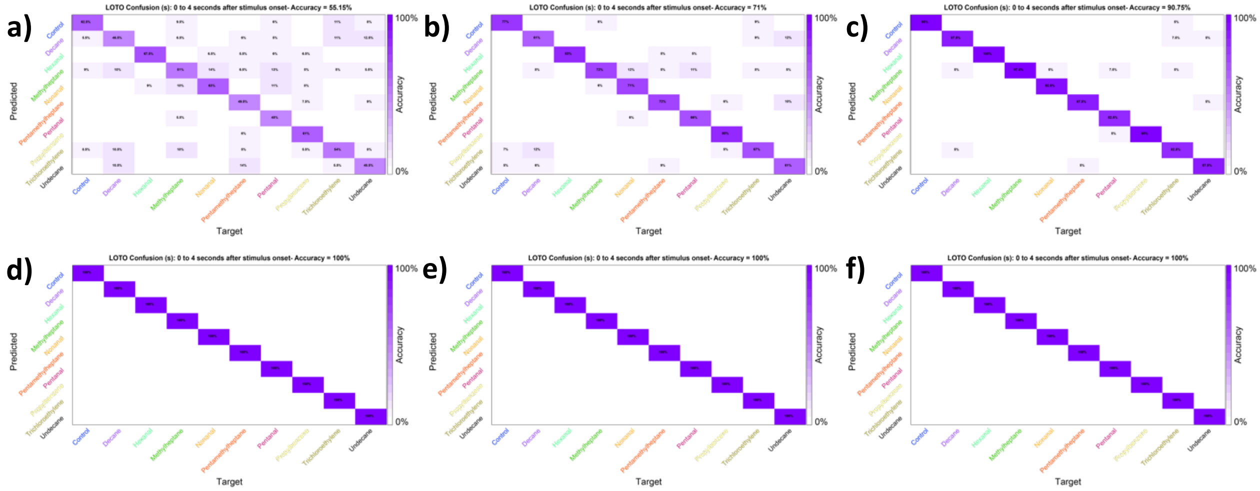

Figure 3.14 | Bin-size selection quantified via confusion matrices. We subjected data of different bin sizes to a leave-one-trial-out train-test procedure. We could visualize the accurate predictions and which odorants induced more similar neural responses via confusion matrices. Bin-wise classification results are shown for **a)** 100-, **b)** 150-, and **c)** 200-msec bin sizes. With increasing bin sizes the accuracy improves, though the classifier is also predicting fewer time bins. The trial-wise accuracies for **d)** 100-, **e)** 150-, and **f)** 200-msec bins all reached 100%. All classifier predictions were made using the Euclidean norm.

adequate classification performance, ought to enable rapid readout and minimal supervised intervention. Therefore, we performed a relatively simple, fully automated root-mean-square transformation capable of reducing the total number of data points while retaining the intricacies of spike response patterns **(Figure 3.15)**. A number of different point filters were tested to determine the minimal resolution necessary to retain unique stimulus-specific response patterns. Processing the data with a 500-point filter seemed to over-smooth the data, with the dissolution of potentially important signal elements. The 100-point filter retained a large number of these features, yet some of the minute voltage changes may reflect natural biological response variability and would not enhance future unknown stimulus classification. All RMS processing was conducted with a series of two 500-point filters, one for applying a smoothing algorithm and

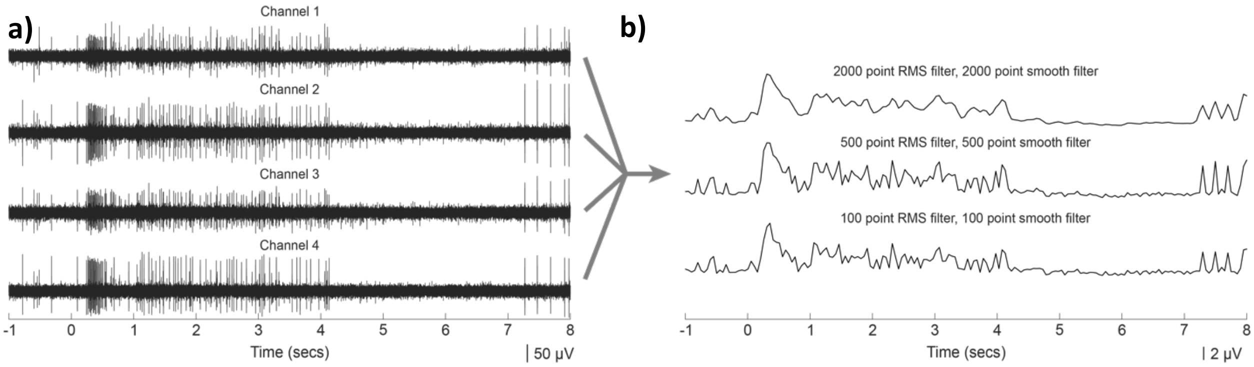

Figure 3.15 | Root-mean square transformation preserves signal integrity. In an effort to move towards real-time analysis and readout, data was initially smoothed and then subjected to a moving point RMS filter. For details on signal transformation, see *Chapter 2 Methodology- Signal Analysis*. **a)** Data from all four tetrode channels was efficiently combined and transformed from 20,000 samples per second to 20, while retaining signal integrity. **b)** A number of different point filter values were considered. For larger point filters (*top*), some fine neural response features were removed, while for smaller point filters (*bottom*), many of these were retained.

another for the root-mean-square transformation. For additional details, see *Chapter 2: Methodology- Signal Analysis*. We performed similar analytical techniques on the RMS-processed dataset, that we had utilized for the previous spike sorted data. Peri-stimulus voltage traces demonstrated clear population-wide neural responses unique to the presented odorant **(Figure 3.16)**. A more salient off response was observed for a number of the stimuli relative to the spike sorted data, suggesting that response dynamics of these neurons were not able to be captured by use of the spike sorting algorithm. Since the RMS analysis incorporates the total energy from the recording location, it may retain pertinent information that would otherwise be lost in spike sorting putative neurons. We then performed principal component analysis **(Figure 3.17a)** and linear discriminant analysis **(Figure 3.17b)** to aid in data visualization. Similar to spike sorted data visualization results, neural trajectories and stimulus-specific clusters began to emerge in the PCA and LDA subspaces, respectively. A total of 24 recording locations defined the

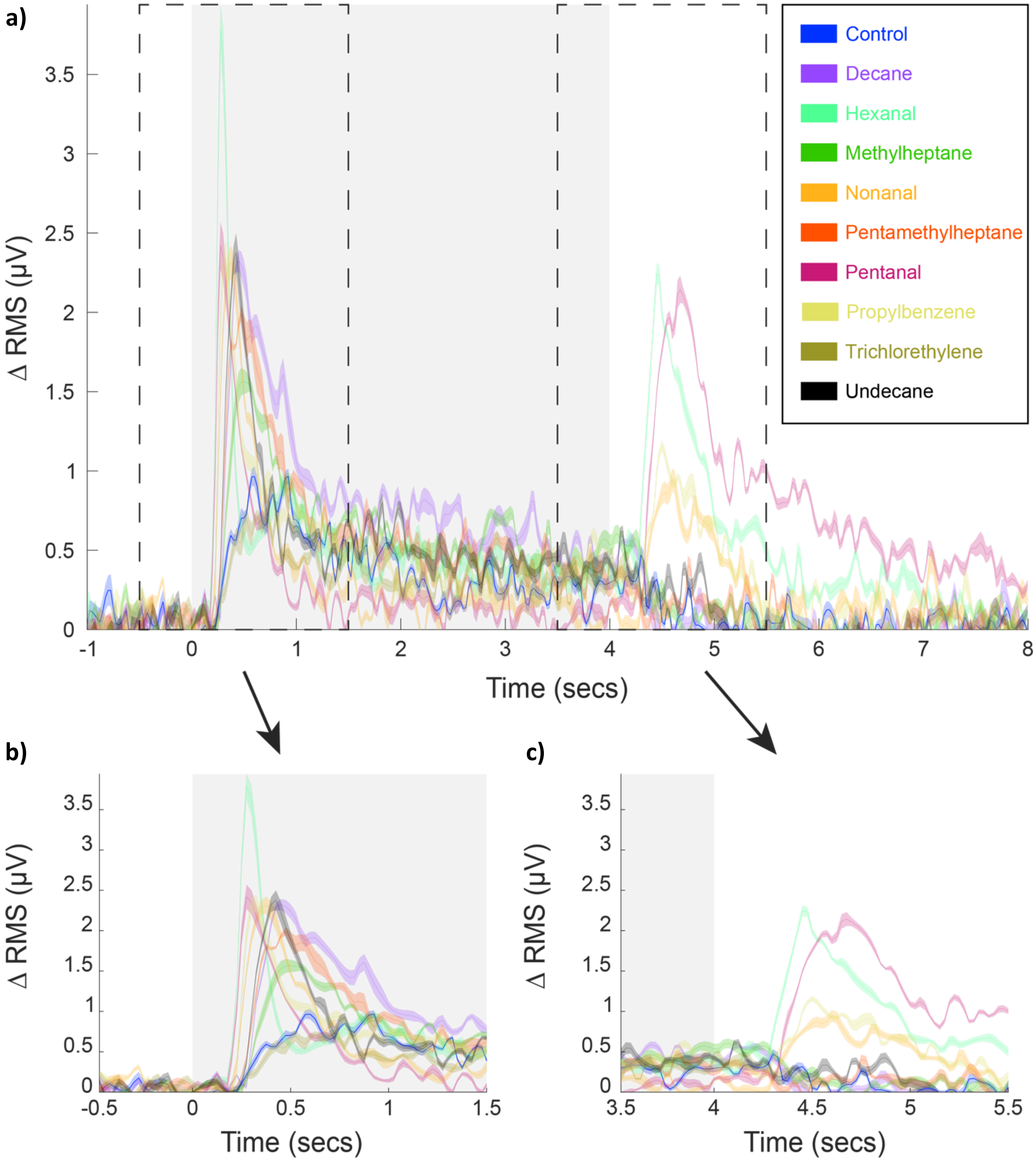

Figure 3.16 | Peri-stimulus voltage trace of RMS-processed data. Intricate neural response dynamics can be observed from population-wide averages of RMS-processed data. Here, clear **b)** ON and **c)** OFF responses are apparent. This may be a result of retaining more stimulus-specific information from the total energy signal of the recording location that was previously filtered out during spike sorting.

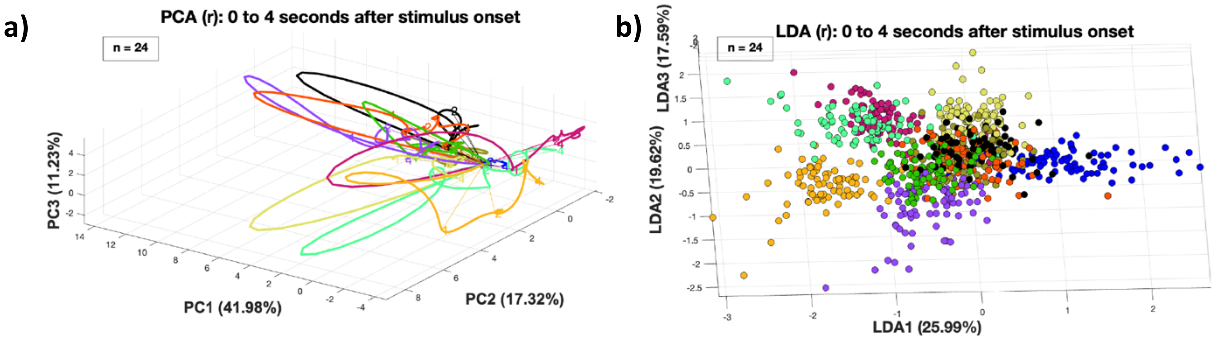

Figure 3.17 | Unique population dynamics observed in PCA and LDA subspaces. Here, we performed similar dimensionality reduction algorithms as before, namely principal component analysis and linear discriminant analysis. We kept only the three most prominent dimensions in order to effectively analyze the underlying structure. The RMS-processed data generated **a)** uniquely evolving neural trajectories in PCA space and **b)** stimulus specific clusters in LDA space.

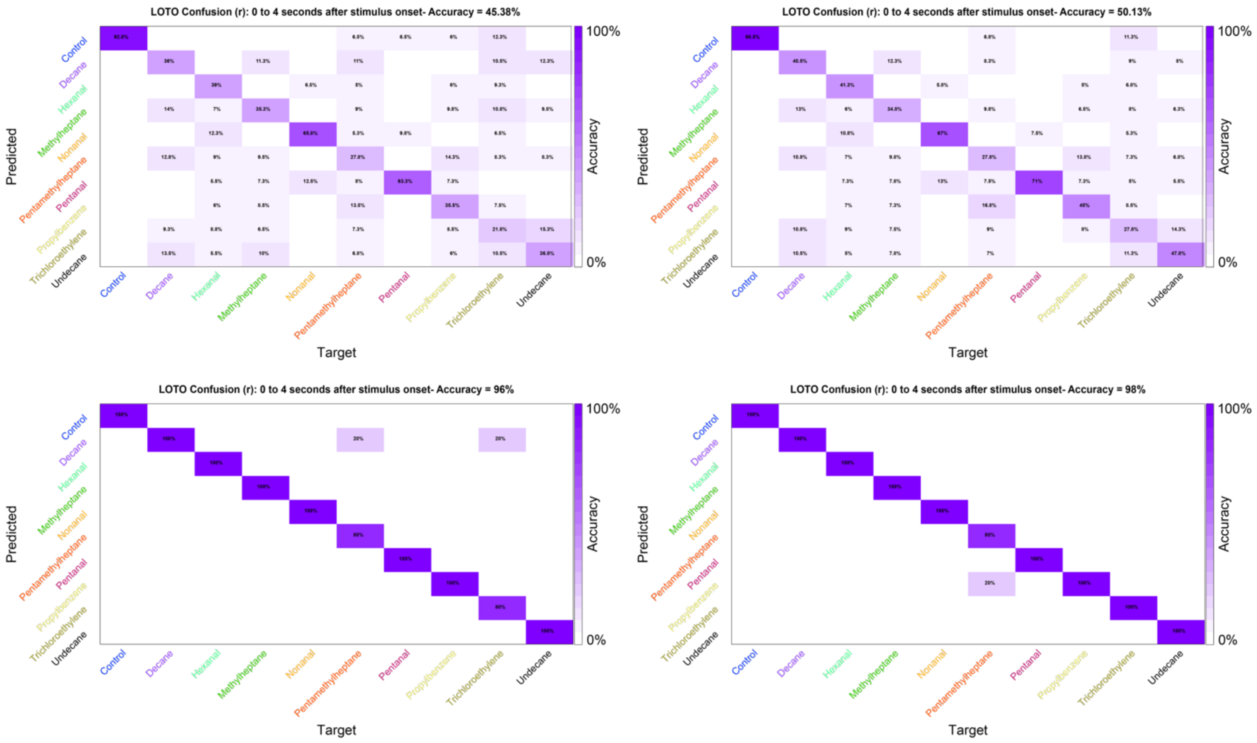

Figure 3.18 | Confusion matrices for RMS-processed data. To quantify the performance of a relatively simple linear classifier in 24-dimensional space, we used the leave-one-trial-out training-testing procedure. Results were comparable to those attained by spike sorting. **a, c)** Bin-wise and trial-wise based classification using the Euclidean norm as the distance metric. **b, d)** Bin-wise and trial-wise accuracy using the Manhattan norm as the distance metric. Similar to the spike sorting data, the Manhattan norm produced slightly better results that using the Euclidean norm metric. The rapid processing and readout is a step towards real-time and completely unsupervised analysis.

encoding state space, in which training templates were generated using the leave-one-trial-out cross validation technique. This high dimensional classification in a 24-dimensional RMS-based encoding space offered similar performance to the 45-dimensional space of spike sorted data **(Figure 3.18)**. Moreover, signal processing did not require experimenter supervision and total processing time was drastically reduced.

Outlook

Biological olfaction is an immensely powerful chemical processing system that has evolved over millions of years to sense a broad range of chemicals at minute concentrations. On the contrary, manmade gas sensing for diagnostic capabilities is a relatively new field. These sensors display extraordinary potential but, struggle to achieve the broad sensing capabilities and low parts-per-trillion to parts-per-quintillion detection limits seen in biological olfactory systems. Moreover, olfaction has evolved to perform background invariant stimulus identification, an extremely important quality for tasks in which natural variability is expected.

This study represents a crucial first step towards determining whether insect olfactory systems could be suitable as a medical diagnostic technology. Our work has demonstrated that the locust olfactory system can be readily utilized to detect a number of key volatiles present in the exhaled breath of cancer patients. It is important for a cross-reactive chemical sensing system to display unique encoding of various chemicals or molecular features. Recognition of individual features dramatically enhances the capacity of the system—an essential characteristic for any device designed to characterize highly heterogeneous stimulus mixtures adequately and reliably. We have also proven that stimuli containing unique chemical structures elicit stereotypical responses in projection neurons of the locust antennal lobe and these spatiotemporal readouts can be used to classify stimulus identity with an extremely high degree of accuracy. Even odorants with similar chemical structures, such as hexanal and pentanal, were distinguished from one another. These two volatiles have also been identified as chemical biomarkers of maladaptive metabolic states, such as oxidative stress and lipid peroxidation. While our goal is to test the efficacy of the locust olfactory system as a non-invasive cancer diagnostic specifically, it may also have use as a broad-spectrum screening tool. Processes such as oxidative stress occur in diseased populations as well as healthy individuals and is likely a natural phenomenon indicative of aging. Depending on detection limits and disease separability, the locust olfactory system could offer a modality by which to investigate underlying maladaptive metabolic processes that are not necessarily considered to be pathogenic.

CHAPTER 4 | CANCER CELL LINE DIFFERENTIATION BY AN INSECT CHEMICAL BIOSENSOR

Cancer Metabolism

Cancer is a highly complex and multifaceted disease consisting of hundreds or thousands of different genotypes[571]. While some key features can be identified, different types and sub-types of cancers can lead to significantly different biomolecular reactions. The Warburg effect of aerobic glycolysis is considered to be a metabolic hallmark of cancer. However, the ubiquity of this metabolic pathway has been questioned relentlessly since its original proposition. While some evidence suggests the existence of damaged mitochondria[572, 573], others point to decreased mitochondrial activity triggered by upregulations in specific transcription factors[574-576]. Ultimately, given the rapid speed of glycolysis relative to that of oxidative phosphorylation[577, 578], the mitochondria cannot process the plethora of resultant pyruvate molecules. While these two models seem contradictory, different cancers may, in fact, be characterized by these distinct features due to the impact of genetic variation or environmental influences. This could lead to alterations in subsequent downstream molecular processes and, in part, explain the subtle variations in biomarkers associated with different types of cancers. Disease variability also stems from the identity of the affected organ and even the region within said organ. Tumor formation is highly dependent on the local cellular environment, which is shaped in large part by the excessive release of lactate by cancerous cells into the extracellular milieu. Extracellular signals can be dictated by lactate-specific chemical reactions, which are differentially impacted by variables such as the efficacy of the nutrient delivery system and the distance to surrounding blood vessels[579-582]. The multifarious nature of cancer emphasizes the pressing need to consider type- and subtype-specificity for effective diagnosis, prognosis, and treatment.

Volatile-Based Cancer Detection

Breath-based chemical sensors have proved to be an enticing option for cancer detection. Groundbreaking experiments over the past three decades have shown that the excretion of trace-level volatiles differs between healthy and diseased individuals[583]. Generic volatile biomarkers representative of oxidative stress and lipid peroxidation, such as ethane and pentane, are often observed in higher quantities for those with underlying illnesses. However, the real power of breath-based gas sensing is due to the subtle changes in other volatile metabolites that are more indicative of certain types and subtypes of diseases[114, 140, 265, 584]. One study has demonstrated that breath concentrations of several compounds not only differ between breast cancer patients and healthy controls, but also among those with genetically determined breast-cancer subtypes[134]. Here, GC-MS and electronic nose-based analyses were fairly accurate in distinguishing group identity based on breath profiles alone. The ability to discriminate between different disease states necessitates that the underlying biochemical processes related to a specific disease state will elicit a unique assortment of volatiles, indicative of those processes. Furthermore, accurate diagnosis requires sufficiently sensitive gas sensing technology to detect at least some of these volatiles and discern an appropriate combination that allows for group separability based on underlying pathology.

In vitro cell culture models are commonly used to test the efficacy of gas-sensing technologies for volatolomics research[129-131, 137, 138, 266, 583, 585-587]. For volatile headspace sampling, either an adsorbent material can be placed in the sealed flask or direct headspace can be passed to the gas sensor. In the sorbent-based technique, metabolites volatilize out of the cell culture medium and are absorbed by the sorbent trap. Subsequent thermal desorption can be used to increase molecular energy and break chemical-sorbent bonds. A high concentration of chemicals with relatively similar volatilities will be released at any one time. In order to maximize the number of chemicals released from the trap, especially those with lower volatilities, the temperature is incrementally increased over time. For technologies, such as gas chromatography-mass spectrometry and ion mobility spectrometry, this is perfectly appropriate as each chemical is considered independently of others in the mixture. However, for electronic noses and biological olfaction, which create breathprint templates for entire samples, the temporal nature of odorant delivery is critical. Passing the volatile headspace directly, ensures a more homogeneous stimulus between individual presentations.

Having demonstrated biosensor responsiveness to and discriminability of various cancer VOC biomarkers, our next set of experiments were designed to determine the ability of the locust olfactory system to effectively differentiate between the volatile headspace profiles of cancerous and non-cancerous cell lines. Evidence suggests that there are more than 500 volatiles in a single breath sample, though the actual number is likely much higher as volatile identification is a function of technological sensitivity[134]. Of these identified volatiles, approximately 10% appear to be universal[36]. As such, an effective breath-based sensor must be able to process highly complex mixtures with overlapping constituent chemicals. Additionally, considering the subtle changes in breath biomarkers brought about by disease, detecting concentration differences requires exceptional chemical sensitivity and highly effective pattern recognition capabilities. In addition to differentiating between cancer and non-cancer samples, we sought to test whether our forward-engineering biological-based approach was powerful enough to distinguish between oral cancer subtypes. The cell lines chosen were based on preliminary data demonstrating that the cancer cell lines (Ca922, HSC-3, and SAS) exhibit functional increases in both glycolysis and oxidative phosphorylation relative to the non-cancer cell line (HaCaT). All cell lines were grown

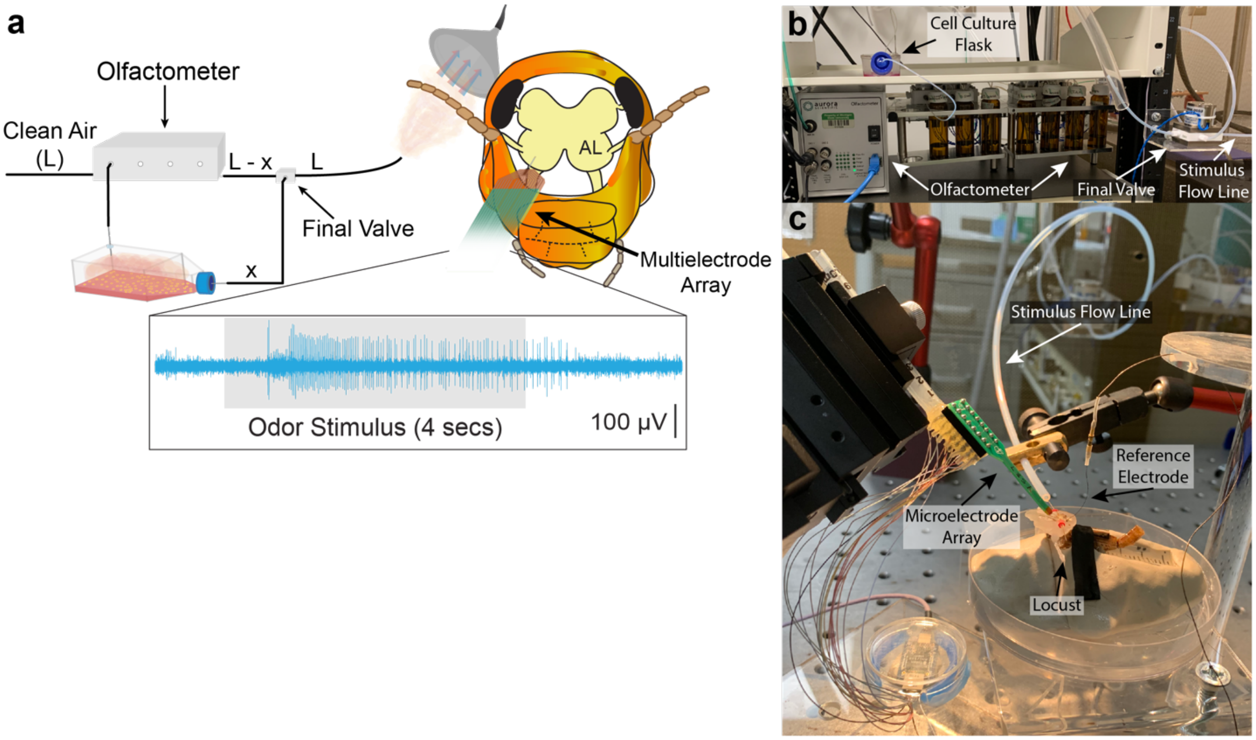

Figure 4.1: Electrophysiological recording setup. a) Schematic of the VOC delivery and in vivo neural recording setup. Cancer and non-cancer cell lines were cultured and placed inside airtight flasks. The culture medium was the same for all cell lines. Emitted VOCs from the cell cultures were sampled periodically by injecting a fixed amount of clean air into the closed flask using an olfactometer. The duration and volume of cell culture VOCs delivered to the locust antenna were controlled by the odor delivery setup. Extracellular neural recordings were obtained from the locust antennal lobe before, during, and after odor delivery. Total airflow to the antenna was kept constant throughout the experiment and delivered VOCs were removed quickly by an exhaust placed behind the locust antenna. A raw voltage response of a neural recording is shown for a 4 s long odor pulse. **b)** Image depicting the olfactometer unit connected to an in-line cell culture flask. The final valve, with exhaust and stimulus flow lines, is shown in the lower right portion of the image. **c)** Experimental setup depicting an in vivo locust preparation housed inside a faraday cage. The brain has been implanted with a microelectrode array and an Ag-Cl reference electrode completes the electrical circuit. The stimulus flow line passes either zero contaminant clean air or air containing volatiles from the cell culture headspace to the locust antenna, depending on stimulation parameters.

in identical conditions to ensure background VOC consistency, a critical component for any in vitro volatolomics study[588]. For precise culturing conditions see *Chapter 2: Methodology-Stimulus* Creation. Stimuli consisting of headspace volatiles were systematically passed to locust antennae over a period of four seconds. Stimulus presentation was repeated five times with an inter-stimulus interval of 60 seconds in order to ensure responses remained consistent over time and to enable accurate sensor calibration. Microelectrodes were used to record neuronal action potentials from projection neurons within the antennal lobe (**Figure 4.1**). Prior to each experiment, ten pictures were taken from each flask to investigate cell health and density (**Figure 4.2**). Cells in each of these pictures were manually counted using ImageJ and longitudinal growth curves were constructed (**Figure 4.3**).

Locust-Based Cancer Biosensor

We began by investigating odor-evoked individual projection neuron (PN) responses in the locust antennal lobe to the volatile headspace of cancer and non-cancer cells. Cell culture VOC samples were examined at 24 h intervals by *in vivo* PN recordings. Additionally, we used two control odorants, hexanal and undecane, which have been implicated in earlier studies as putative cancer biomarkers[589].

We observed VOC-evoked changes in neural spiking responses in most of the PNs recorded. Since PNs are broadly selective to several odor stimuli and respond to specific odorants or odor mixtures with distinctive temporal firing patterns [516, 518, 523, 590], we targeted this neuron population for oral cancer classification. At the individual neuron level, the three oral

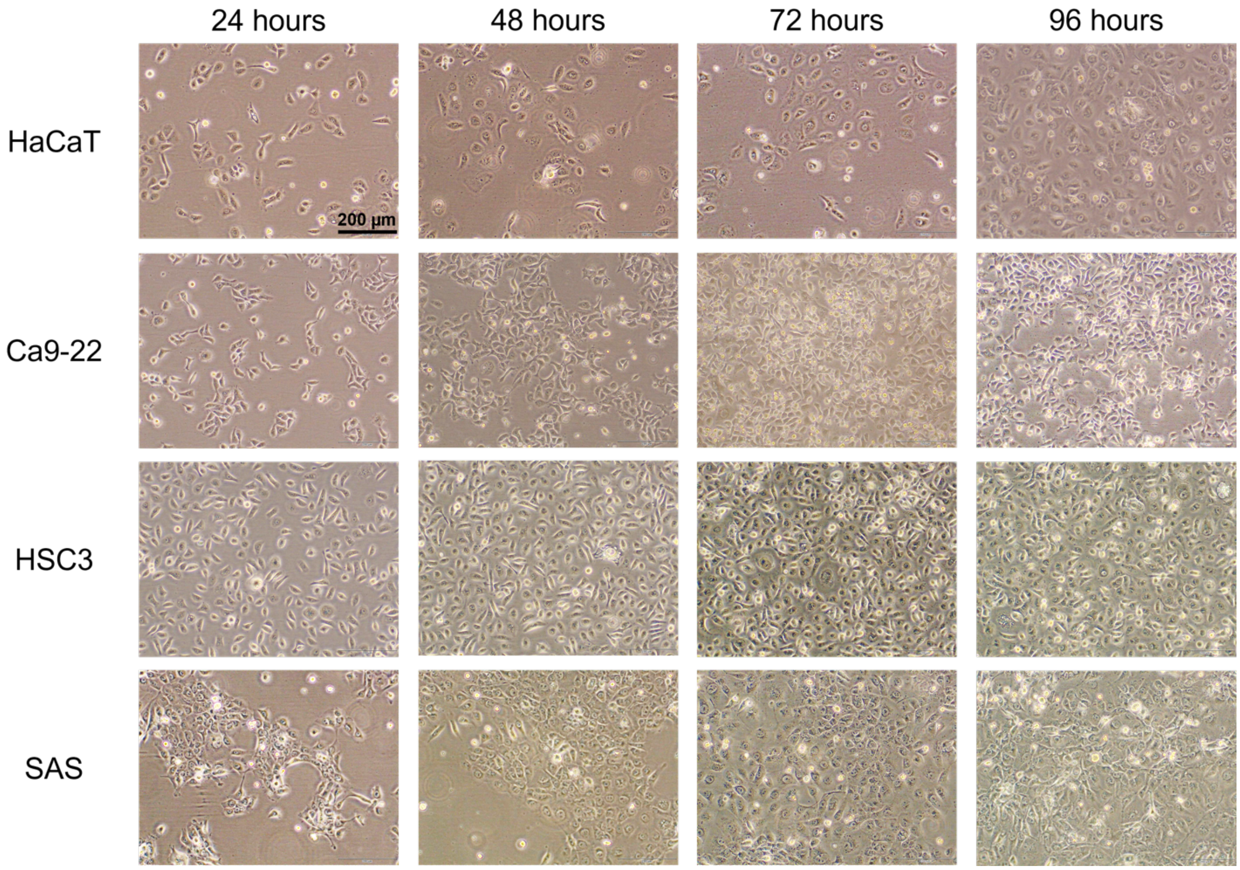

Figure 4.2: Representative images of cell cultures over days. Images are shown for a replicate of the cell culture used for electrophysiological recordings. All four cell lines are shown over four days. Healthy cells were observed at all four time points (24-, 48-, 72-, and 96-h).

cancer and the non-cancer VOC mixtures elicited distinct spiking responses over the odor presentation window. Raw voltage traces of representative extracellular neural recordings showed clear differentiation between the oral cancer cells, non-cancer cells, and cell culture medium. We noted differences in PN spiking responses between the three oral cancer cell lines (**Figure 4.4**).

Next, we investigated how total spike counts (over the entire 4 s stimulus window) varied for each recorded neuron corresponding to different VOC exposures (**Figure 4.5)**. To identify single neurons, spike-sorting of extracellular multi-channel recordings was performed following

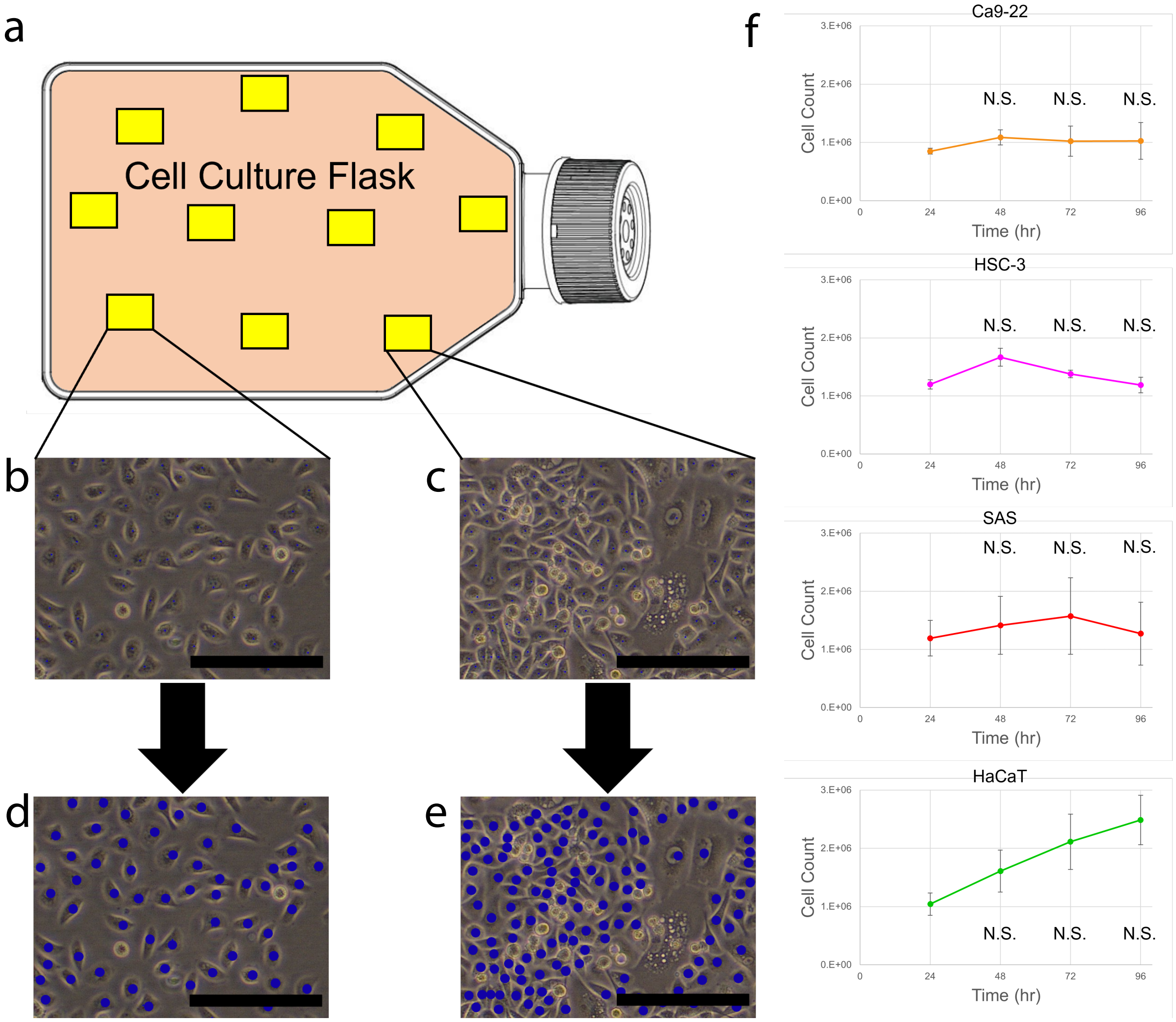

Figure 4.3: Cell counting procedure and growth curves. a) Schematic of a T25 cell culture flask. Prior to conducting electrophysiology experiments, the flask for each cell line was imaged 10 times pseudo-randomly. Example imaging locations shown by yellow rectangles. **b)** Image from the flask prior to counting is shown. Black scale bar indicates 200 µm. **c)** An image from a different location within the same flask is shown. **d, e)** The same images from **b**, **c** are shown post counting with all live cells marked by a blue dot using FIJI/ImageJ. The mean of the 10 images were taken to determine the total cell count of each flask. **f)** Initially, cells were seeded at 1 x 106 cells per flask at 0 h. Cells were counted from each flask at 24-hour intervals after seeding (24-, 48-, 72-, and 96-h). At each time point, the total cell count of each flask was averaged over 8seven replicates. Error bars are S.E.M from the seven replicates. No significant difference in cell counts were observed between 24-h and 48-, 72-, or 96-h ($P < 0.05$, d.f. = 6, 16, one-way ANOVA with Bonferroni correction).

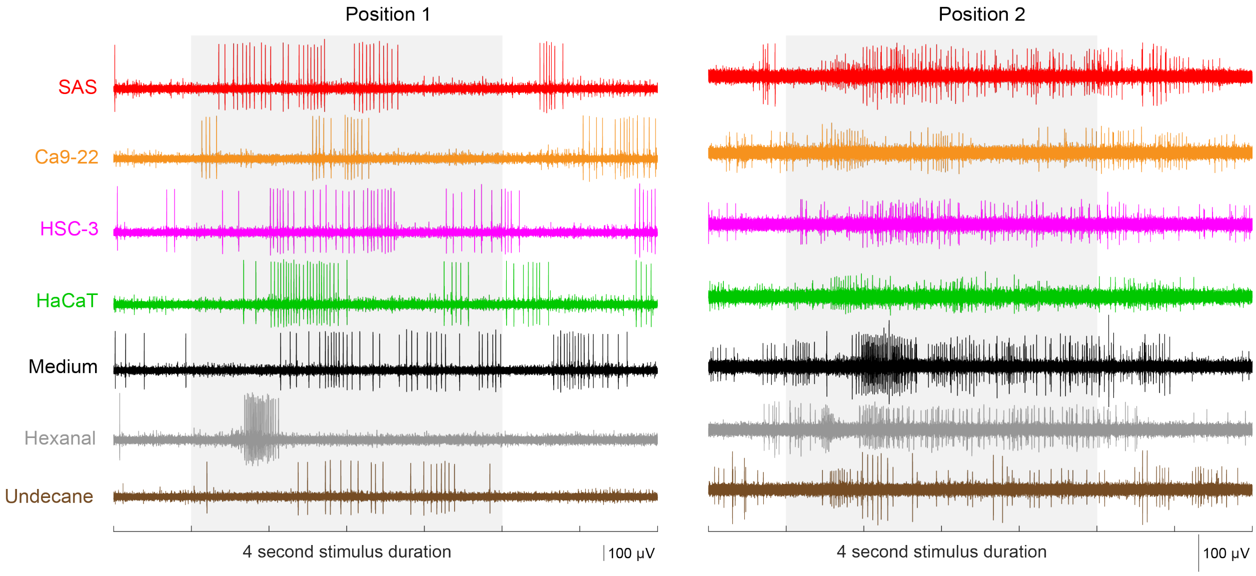

Figure 4.4: Headspace from cell lines and control odors evoke unique spatiotemporal patterns in multiple neurons. VOC-evoked raw neural voltage responses of a recording location are shown for the three oral cancer cell lines, the non-cancer cell line, the cell culture medium, and two control VOCs (Hexanal and Undecane). The light grey box indicates the 4 s stimulus presentation window. Two different recording locations are shown. Position 2 had multiple PNs, which resulted in different spike amplitudes in the multiunit voltage trace.

previously published methods [591]. Then, we used a simple metric of VOC-evoked time-averaged and trial-averaged spike counts of individual PNs for each stimulation condition. Individual PN spike counts were summed over the 4 s stimulus presentation window and averaged across trials (n = 5 trials) to quantify these changes. Next, we compared the average spike count of each PN across two stimulus conditions. For example, PN spike counts corresponding to each oral cancer cell line were compared to the spike counts of the same set of PNs elicited by the culture medium VOC composition. When all recorded PNs were analyzed, several PNs showed significant changes in spike counts across two stimulus conditions ($P < 0.05$, d.f. = 4, 28, one-way ANOVA with Bonferroni correction). These results demonstrated that there were differences in individual PN spike counts elicited by cancer vs. non-cancer vs. control VOCs. Notice that this analysis only compared total PN spike counts corresponding to different stimuli,

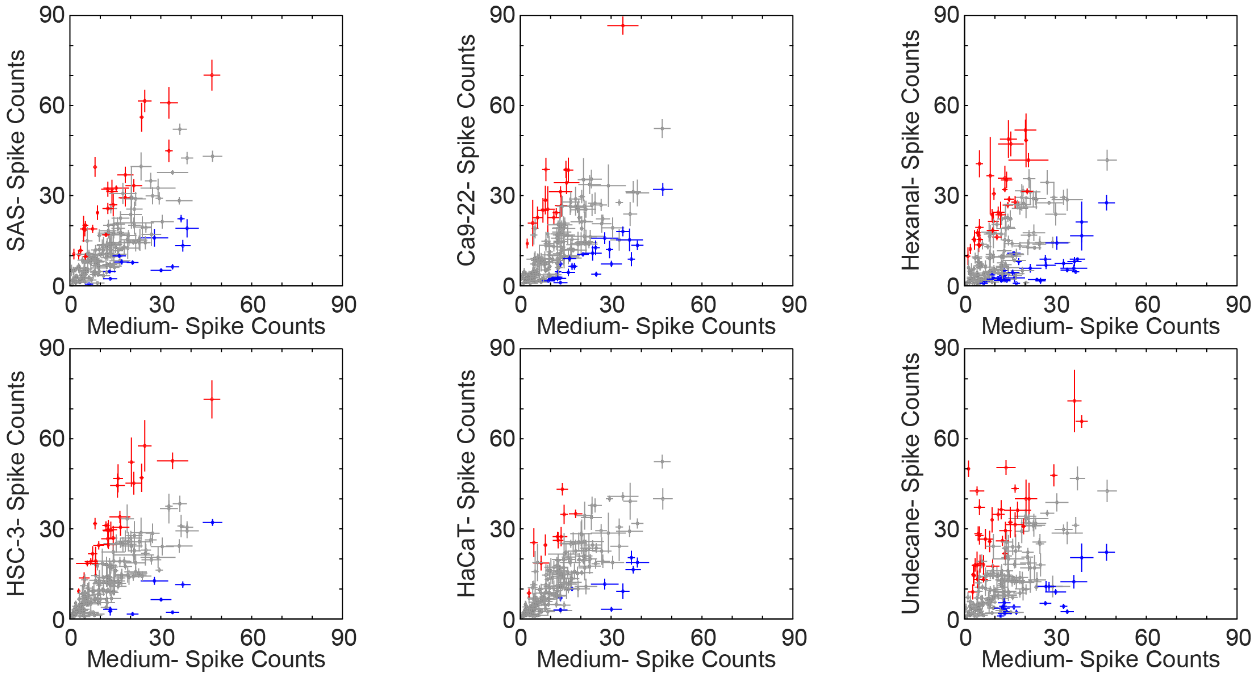

Figure 4.5: Neurons demonstrate stimulus-specific spiking rates. VOC-evoked total spike counts (over 4 s) of individual PNs are compared across two stimulus conditions. For each PN, the trial-averaged total spike count is plotted with the error bars representing S.E.M. of the trial-wise variations for two stimulus conditions. All comparisons were made with the cell culture medium evoked spike counts (plotted along the X-axis). All 194 recorded PNs are plotted in every scatter plot. Individual PNs were identified after spike-sorting of the extracellular recordings. PNs that responded significantly higher (or lower) to the stimulus VOCs compared to the cell culture medium VOCs were plotted in red (or blue), respectively ($P < 0.05$, d.f. = 4, 28, one-way ANOVA with Bonferroni correction). PNs that did not show significant differences in total spike counts across two conditions were plotted in grey.

but differences in temporal firing motifs of individual PNs as seen in **Figure 4.4** were not reflected in this analysis.

Oral Cancer Classification via Multi-Dimensional Neural Signal Analysis

To incorporate the temporal spiking characteristics, we analyzed the spatiotemporal PN responses elicited by the three oral cancer cell lines, the non-cancer cell line, and the cell culture medium. To generate ‘spatial’ (neuronal identity) – ‘temporal’ (spiking dynamics) response vectors of the entire PN population, trial-averaged firing rates of each neuron were binned into 50 ms non-overlapping time windows. Individual neuron responses were temporally aligned following stimulus onset. For this analysis, we combined spiking responses from all recorded PNs

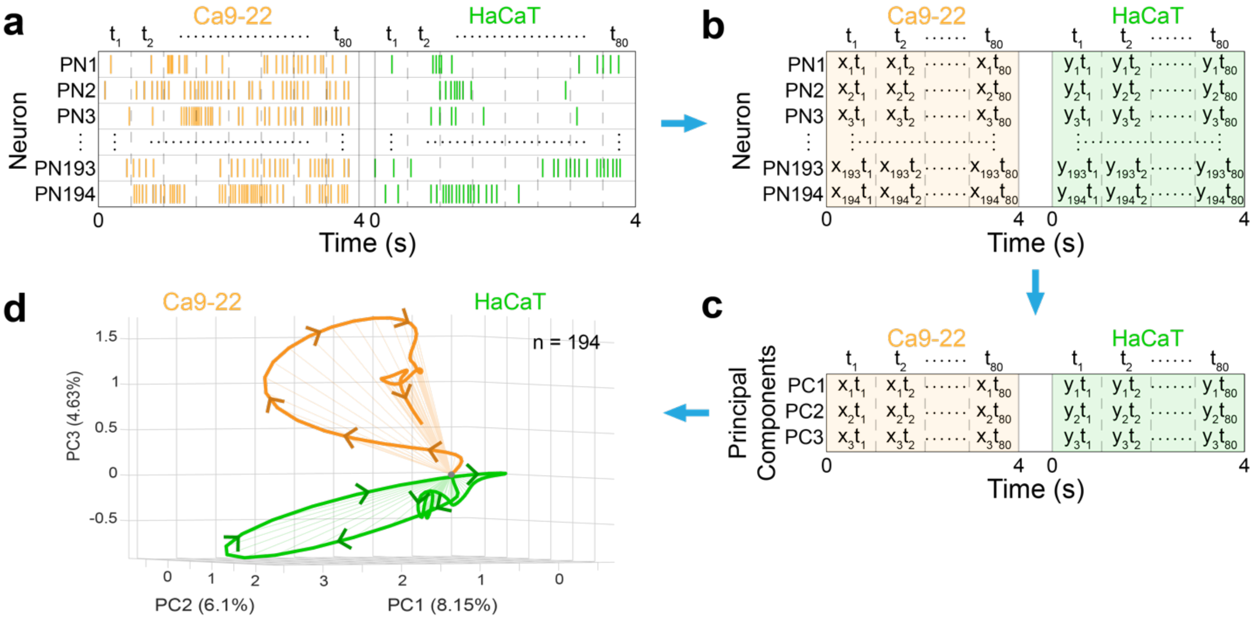

Figure 4.6: Cancer vs. non-cancer VOCs are distinguished by spatiotemporal PN responses. Schematic representation of the spatiotemporal PN response analysis. This analysis contains spiking responses from all recorded PNs (spatial) and their response dynamics (temporal) over the 4 s stimulus presentation window. **a)** Raster plots of all recorded PNs pooled across experiments are combined for each stimulus (represented by PN1 to PN194). Then the 4 s duration VOC-evoked spike counts are divided into 50 ms non-overlapping time bins (total 80 time bins for 4 s). Two different stimuli are used for illustration (Ca9-22 and HaCaT). Notice that the same PNs are recorded for all stimuli. **b)** A neuron number (n = 194) × time (t = 80) matrix is constructed, where each element in the matrix corresponds to the spike count of one neuron for a single time bin (denoted by xitj or yitj). **c)** The high dimensional population response time-series is dimensionally reduced using PCA and data corresponding to the first three principal components are kept. **d)** The 4 s time-series data is plotted along the three principal component axes. Each point is connected temporally with the next time point to generate individual VOC-evoked neural trajectories that take into account both temporal and spatial motifs of the recorded PN ensemble. Notice that the two PN trajectories corresponding to the Ca9-22 and HaCaT track along different manifolds in the principal component space. Angular separation between the two neural trajectories signifies the distinction between the two VOCs. The percentage of variance captured along the first three principal components is plotted along the axes. Because of the large number of recorded PNs and their complex response dynamics, the total variance captured along the first three principal components is low. Therefore, PCA-based neural trajectories are only used for qualitative comparisons.

over multiple days of cell culture. This resulted in a high dimensional population neuron response, which was represented by an *n x m* matrix (**Figure 4.6a**, *n* = 194 PNs; *m* = 80 time bins with 50 ms bin size over 4 s of odor presentation). Next, all recorded PN responses corresponding to each stimulus were concatenated to generate the population PN time-series data for the stimulus panel corresponding to Ca9-22, HSC-3, SAS, HaCaT, and the cell culture medium.

To visualize these cell culture VOC-evoked spatiotemporal neural responses, we projected the high dimensional data onto three dimensions using a linear principal component analysis (PCA, **Figure 4.6d**, see *Chapter 2: Methodology- Signal Analysis*). The points in the three-dimensional PCA subspace were connected in a temporal order to generate stimulus-specific neural response trajectories. We observed that each VOC profile generated a closed loop neural trajectory, which evolved in a unique direction. A long line of work in insect olfaction has established that the unique direction of the population PN trajectories are specific to odor identity and intensity [516, 590, 592]. Our previous work demonstrated that larger angular distances between PN trajectories signify better separability between two odorants [590, 592]. Therefore, unique neural trajectories corresponding to individual VOC mixtures indicate that oral cancer VOC profiles are distinct from the non-cancer cell line. Moreover, we observed distinctions among the neural trajectories evoked by the three oral cancer cell lines (**Figure 4.7**), which signify that differences between various oral cancers can be identified by this approach as well.

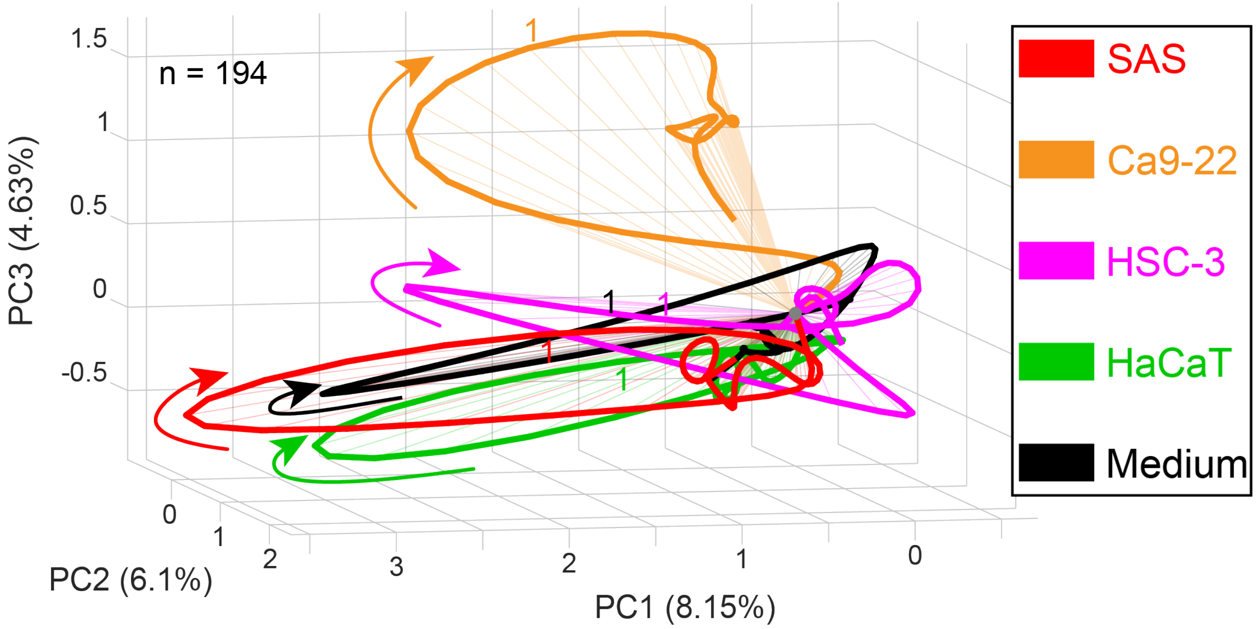

Figure 4.7: Neural responses follow unique temporal trajectories in PCA space. Population PN trajectory plots are shown after dimensionality reduction using PCA for the three cancer cell lines (SAS, Ca9-22, and HSC-3), the non-cancer cell line (HaCaT), and the control cell culture medium. For each stimulus, PN population trajectory is plotted for 0–4 s of VOC exposure. Numbers along the neural trajectories indicate time in seconds from the stimulus onset. Total number of PNs used in this analysis is n = 194, which was computed by pooling neurons across all timepoints and replicates of the cell cultures.

To determine the separation between the cell line specific neural response clusters, we performed linear discriminant analysis (LDA) on the population PN time-series data (**Figure 4.8**). Similar to the PCA analysis, we used the population PN time-series dataset and plotted the VOC-evoked PN responses in a three-dimensional LDA subspace. This linear dimensionality reduction technique maximized the neural response cluster separation between stimuli. We observed distinct clustering of PN responses corresponding to all five stimuli, indicating that a linear classifier in a three-dimensional LDA space is sufficient to classify cancer vs. non-cancer successfully based on their corresponding VOC profiles.

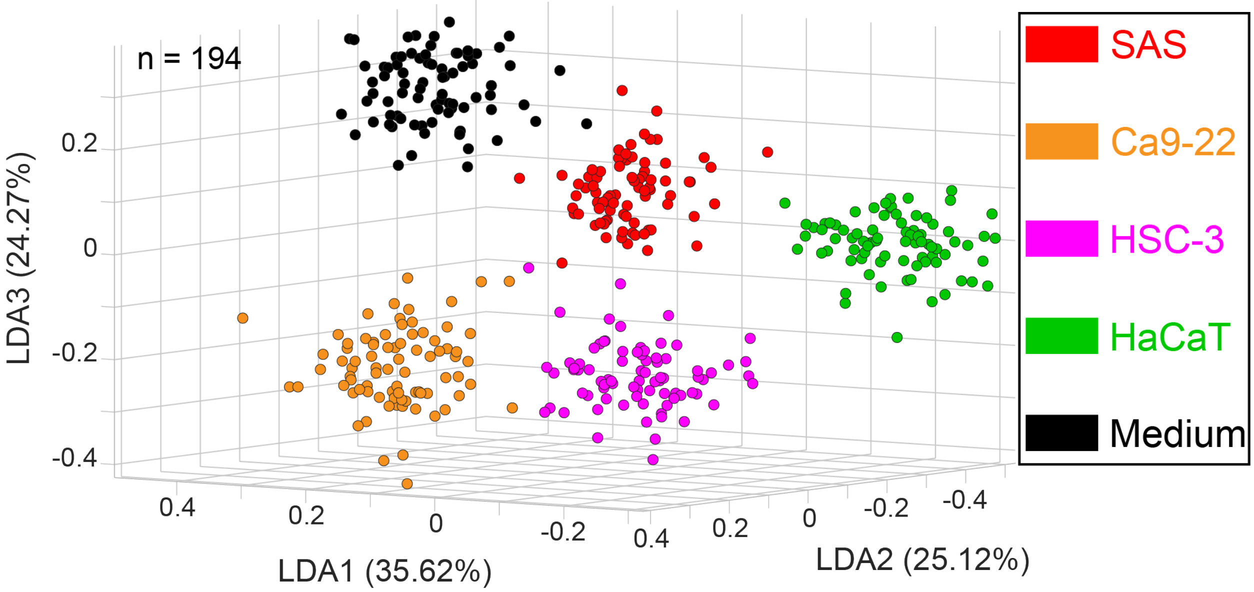

Figure 4.8: Linear discriminant analysis can elicit clear group distinctions across spatiotemporal neural responses. Spatiotemporal PN responses (n = 194) for the 4 s stimulus presentation window (50 ms bin size, total 80 points for each odor) are visualized after dimensionality reduction using LDA (see *Chapter 2: Methodology- Signal Analysis*). LDA minimizes within-class variance and maximizes the variance between classes. Numbers along the axes indicate the variance captured along that dimension. Distinct clustering of neural responses corresponding to different VOC profiles indicates that the cell culture VOCs (cancer vs. non-cancer) can be segregated based on the neural response they elicit.

To get a quantitative estimate of the classification performance, we performed a *leave-one-trial-out* cross validation analysis of the PN time-series data (see *Chapter 2: Methodology- Signal Analysis*, **Figure 4.9**). This analysis was performed on the high dimensional dataset (*n* = 194 PNs, *m* = 80 time bins) without any dimensionality reduction. During the odor presentation window, PN spikes are accompanied by a global 20 Hz local field oscillation generated by synchronized sub-threshold activities of inhibitory local neurons present in the locust antennal lobe [593-595]. It has been proposed that the Kenyon cell population, which receives direct inputs from PNs, integrate PN responses within each of these 50 ms time windows generated by the 20 Hz oscillation. It has been shown that PN responses are most discriminatory within this 50

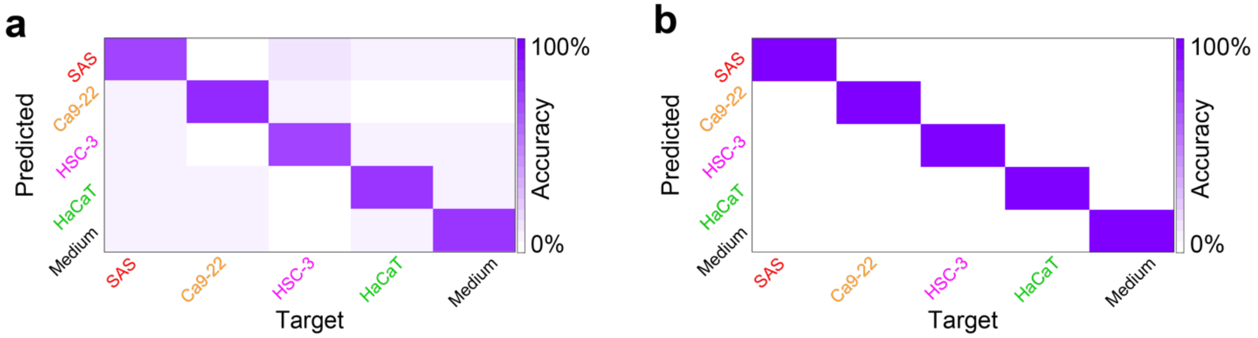

Figure 4.9: Neural responses are well separated in high-dimensional space. Classifications of VOC-evoked population PN responses without any dimensionality reduction are analyzed by leave-one-trial-out cross validation analysis (see *Chapter 2: Methodology- Signal Analysis*). These quantitative classification results are summarized by a confusion matrix. Each column and row correspond to the target stimulus and the predicted class, respectively. Here, each 50 ms time bin of the testing trial is classified as one of the 5 target VOCs based on the minimum Euclidian distance. The high values along the diagonal of the confusion matrix indicate that most of the predicted responses match the target labels. This result signifies that information contained within the 50 ms time bins of the VOC-evoked neural response is sufficient to classify oral cancer vs. non-cancer and to distinguish different oral cancers from each other. (e) Similar analysis as shown in panel d except we classified the test trial as a whole by taking the mode of the bin-wise classification for the 4 s long trial (mode of total 80 time bins for each test trial). This trial-wise classification of VOC profiles shows flawless distinction of all 5 stimuli tested and reveals the strength of this neural response-based cancer detection approach.

ms time window. Therefore, to take advantage of this biological neural computational scheme, we divided the stimulus VOC-evoked population PN responses into 50 ms time bins, starting from the stimulus onset. For this analysis, Euclidian distances of neural response vectors at each time bin (50 ms duration) were compared between the testing and the training data (total 80 comparisons over 4 s for each test trial), generating a bin-wise classification (**Figure 4.9a)**. This bin-wise confusion matrix had its highest values along the diagonal, which implied a high rate of successful detection of all five stimuli (76% average classification success). Next, we plotted a trial-wise confusion matrix by calculating the mode of the predicted responses for all 80 time bins (**Figure 4.9b**). The trial-wise analysis was implemented to assign one stimulus class value for each test trial of 4 sec duration. This analysis showed 100% classification for all three oral cancer VOC

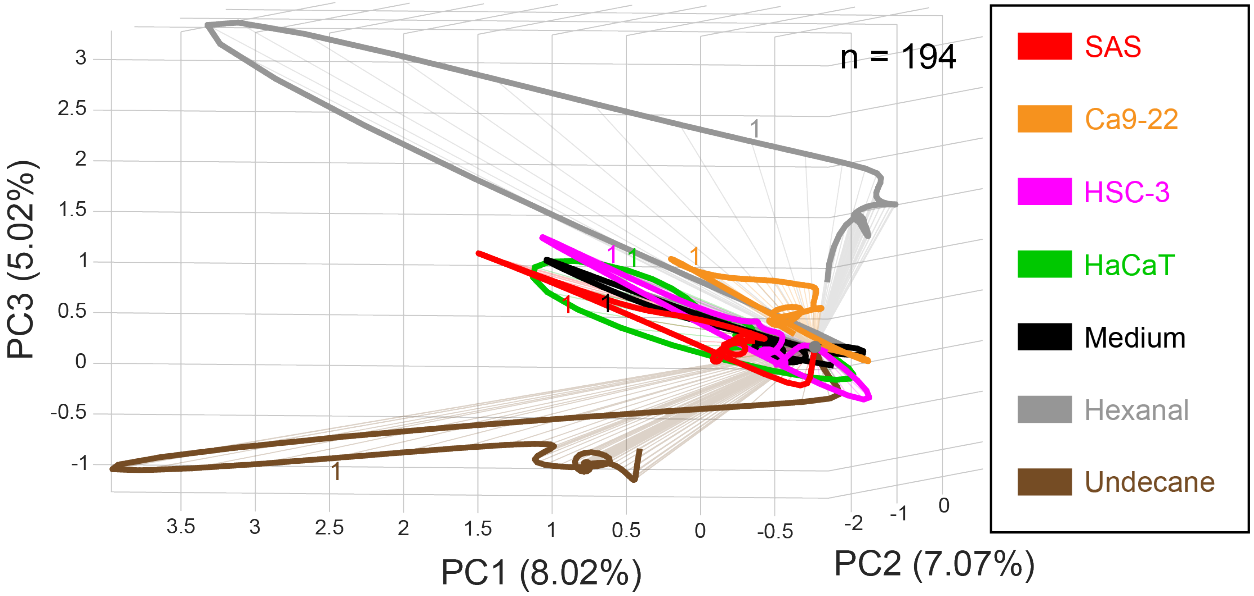

Figure 4.10: Neural responses follow unique trajectories when including entire odor panel in PCA space. Ensemble neural trajectories over the 4 s stimulus presentation window are shown for all 7 stimuli after PCA dimensionality reduction. Volatiles from putative cancer biomarkers (Hexanal and Undecane 1% v/v diluted in mineral oil) elicited PN responses that traced different manifolds than those from the cell lines and control media. Numbers along trajectories indicate time in seconds from the stimulus onset. Total number of PNs used in this analysis is n = 194.

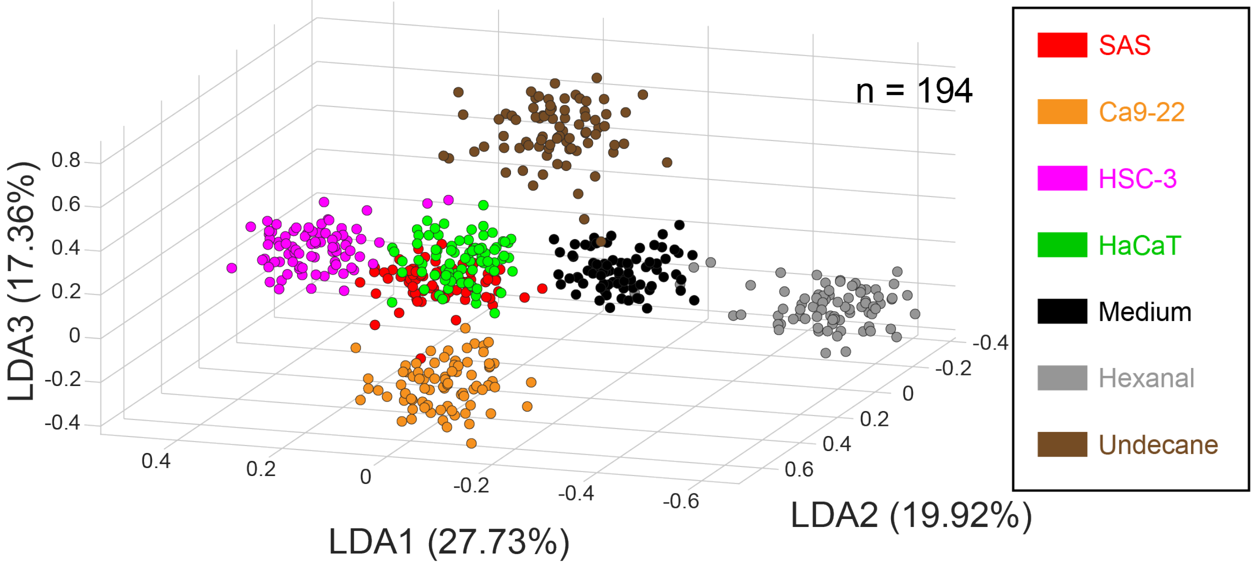

Figure 4.11: LDA dimensionality reduction shows clear distinction between entire odor panel. Population PN responses corresponding to each stimulus plotted in 3-dimensional LDA space showed separability between response clusters. Total number of PNs used in this analysis is n = 194.

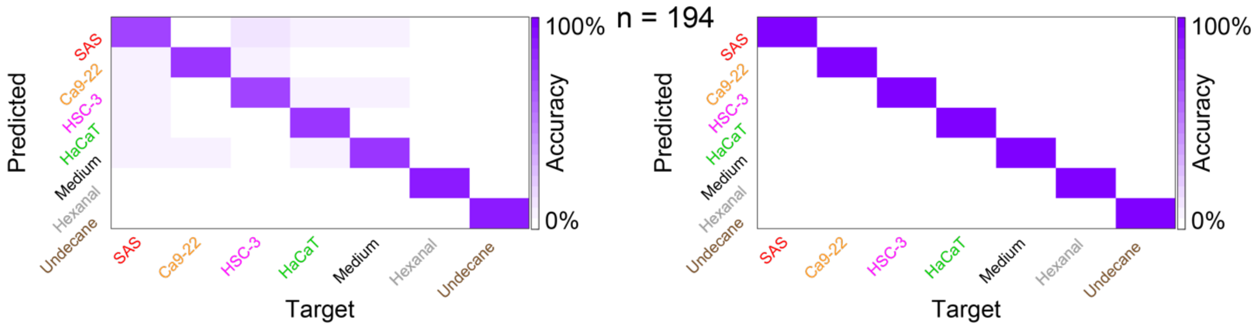

Figure 4.12: High dimensional quantitative analysis enables reliable distinction between entire odor panel. a) Quantitative classification was performed using a leave-one-trial-out cross-validation methodology to train and test a linear classifier in the high dimensional feature space. The time bin-wise confusion matrix shows highest values along diagonal for all cases which indicates successful classification of all 7 stimuli using PN time-series data. Note the high accuracy for hexanal and undecane, suggestive that they are mapped to different regions of the encoding state space **b)** Trial-wise confusion matrix is plotted for all stimuli. Total number of PNs used in this analysis is n = 194.

mixtures among themselves and in comparison with the non-cancer and control VOCs. Similar dimensionality reduction (**Figure 4.10 and 4.11**) and confusion matrix (**Figure 4.12**) analyses were performed on the dataset while including the two other control odorants. Neural trajectories corresponding to the two control odorants were significantly different from all cell culture VOCs

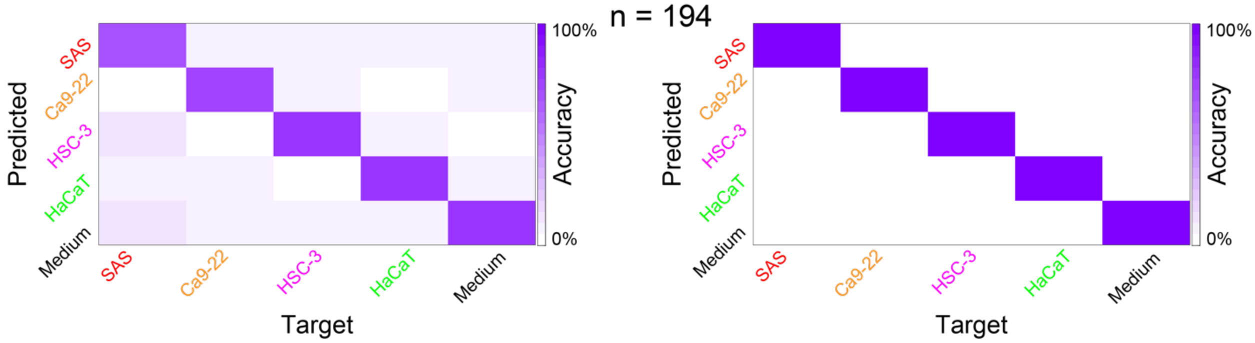

Figure 4.13: Non-overlapping train-test datasets produces similar results to leave-one-out based classification. Cancer vs. non-cancer classification using non-overlapping train-test PN response datasets. VOC exposure trials 1-2 were used for training template construction while trials 3-5 were used as the test set. This allowed for completely non-overlapping training and testing sets. Confusion matrices summarize classification results based on a linear classifier in high-dimensional feature space (see *Chapter 2: Methodology- Signal Analysis*). **a)** Bin-wise and **b)** trial-wise confusion matrices are plotted for all 5 VOC mixture classified.

and the confusion matrix analysis showed high classification success for all seven VOCs tested. We also performed confusion matrix analysis using completely non-overlapping training and testing dataset (**Figure 4.13**), which showed similar results as the *leave-one-trial-out* cross validation analysis. We tested bin-wise and trial-wise classification using multiples of 50 ms bin size (i.e., 100 ms and 200 ms time bins), which yielded comparable results as obtained using 50 ms duration time bin (**Figure 4.14**).

Time-Matched Cancer Volatile Detection

We anticipated that emitted VOC compositions corresponding to each cell line would vary over time due to cell growth and ongoing metabolic processes in a fixed cell culture medium. We also hypothesized that the neuronal template-based VOC classification approach would be able to compensate for these variations. To investigate this, the neural data that were previously combined were split and analyzed at four different time points: 24-, 48-, 72- and 96-h after seeding. All PNs recorded at a specific time point across multiple repetitions of the cell cultures were combined to generate the population PN response vector for that time point. For example, each cell culture was repeated 7 times, and the VOC analysis at the 24-h time point resulted in a total of 42 PNs. All the cell cultures remained viable over 96-h from initiation, which was verified by manually counting healthy cells at different time points of the cell cultures (**Figure 4.2**).

We began by examining VOC-evoked population PN time-series data at 24-h post seeding. We noticed that dimensionally reduced neural trajectories evolved in different directions for different VOC profiles in the PCA space (**Figure 4.15a**). When we performed the same analysis at

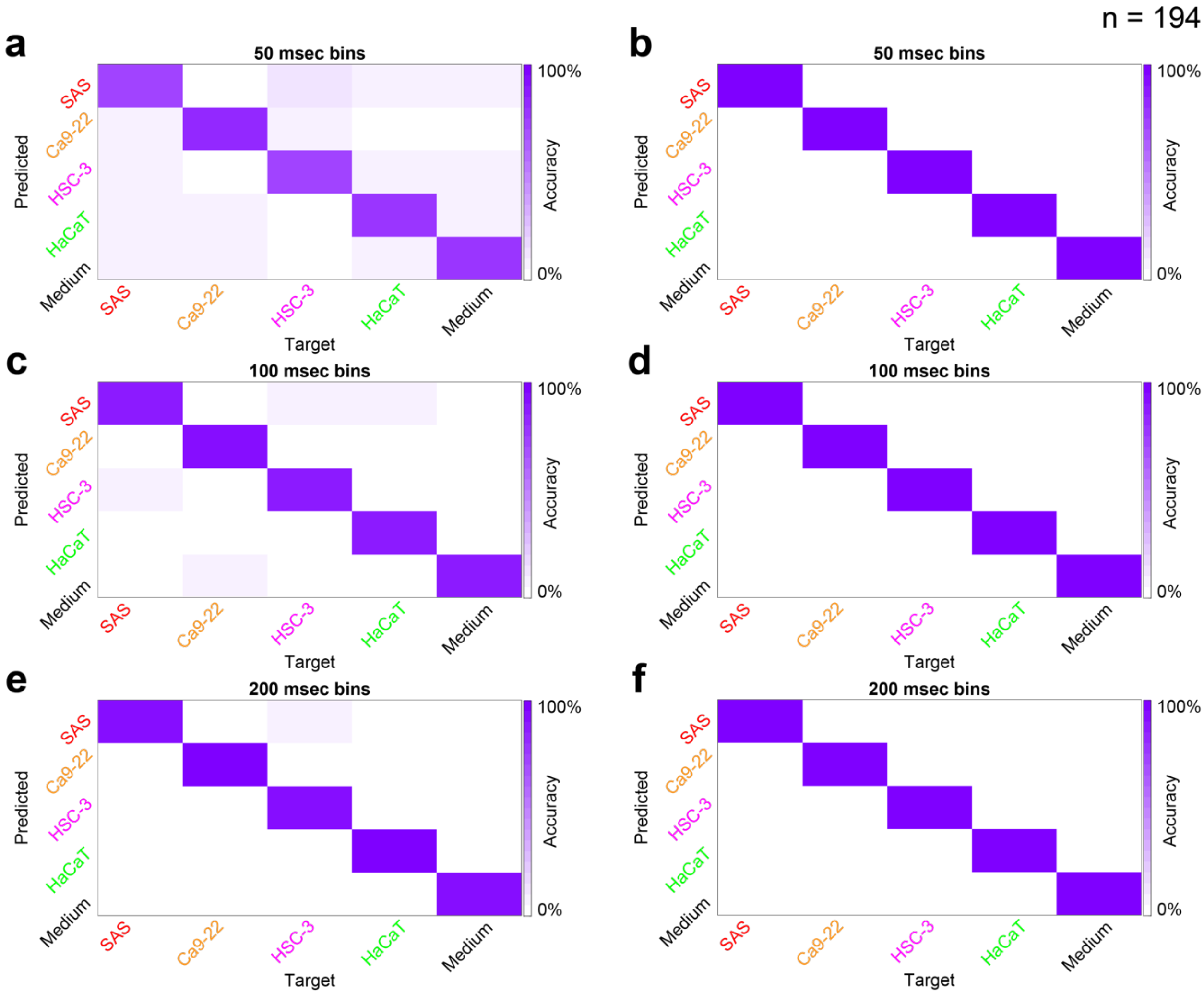

Figure 4.14: Spatiotemporal PN response-based VOC mixture classification is robust. Three different bin sizes (50 ms, 100 ms, and 200 ms) were tested for bin-wise and trialwise classification. Both **a, c, e)** bin-wise and **b, d, f)** trial-wise classification results remained largely similar across different bin sizes used for the high-dimensional VOC classification analysis.

48-h, 72-h and 96-h time points, we continued to observe distinct cell line specific neural trajectories, which indicated that all the tested stimuli were distinguishable from each other at different time points of cell growth (**Figure 4.15**). This observation demonstrated that cultured cells started emitting VOCs specific to their identity about 24 hours after seeding and remained separable over multiple days based on their emitted VOC profiles. Next, we analyzed the neural cluster separation between the three oral cancer cell lines, the non-cancer cell line, and the

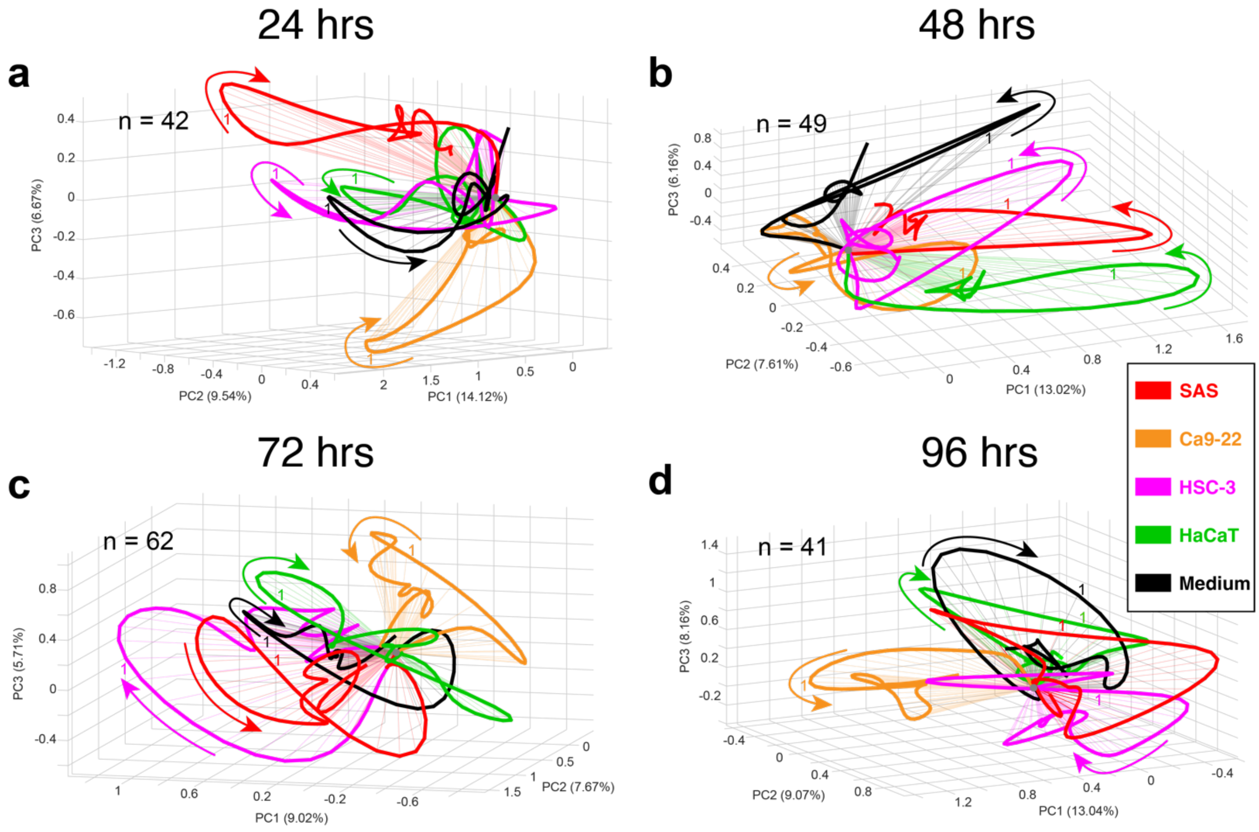

Figure 4.15: Unique neural trajectories observed at different time-matched points of growth. PN response trajectories corresponding to the cancer cell lines, the non-cancer cell line, and the cell culture medium VOC mixtures are plotted after dimensionality reduction by PCA. In this analysis, neurons were pooled only across experiments performed at predefined time post seeding. **a)** A total of 42 PNs were recorded for different cell cultures at this time point. Notice that neural trajectories are distinct from each other even when the recorded neuron numbers are lower and the cultured cells are grown for only 24-h. **b-d)** Cell culture VOC-evoked neural trajectory plots are shown for 48-, 72-, and 96-h time points of the cell cultures, respectively. At each time point, PN trajectories traversed distinct manifolds indicating the distinguishability between cell cultures over multiple days of growth. Note that different PNs (n) were recorded at different time points.

control medium at different time points of the cultures using LDA (**Figure 4.16**). Since the number of PNs recorded at each time point was low, PN response clusters showed some overlap in the LDA space. This was also reflected in the time bin-wise confusion matrix classification results performed in the high-dimensional space (**Figure 4.17a-d**). However, the trial-wise classification result yielded 100% classification success for each test trial for all the VOCs at all four time points

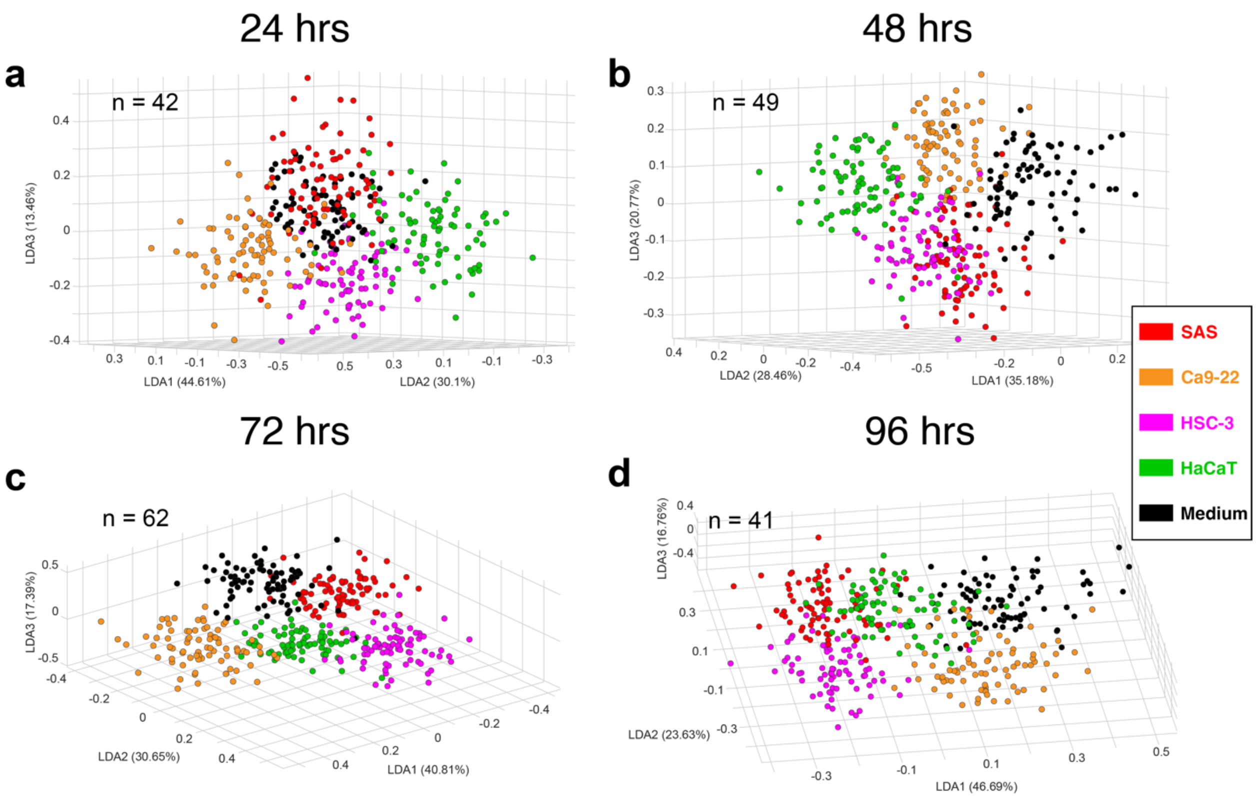

Figure 4.16: Neural response clusters demonstrate visible distinction between stimuli at time-matched points of growth. a–d) PN population responses cluster distinctly for different VOCs after dimensionality reduction by LDA at 24-, 48-, 72-, and 96-h of cell growth. In all cases, LDA shows separability between VOC-evoked neural response clusters.

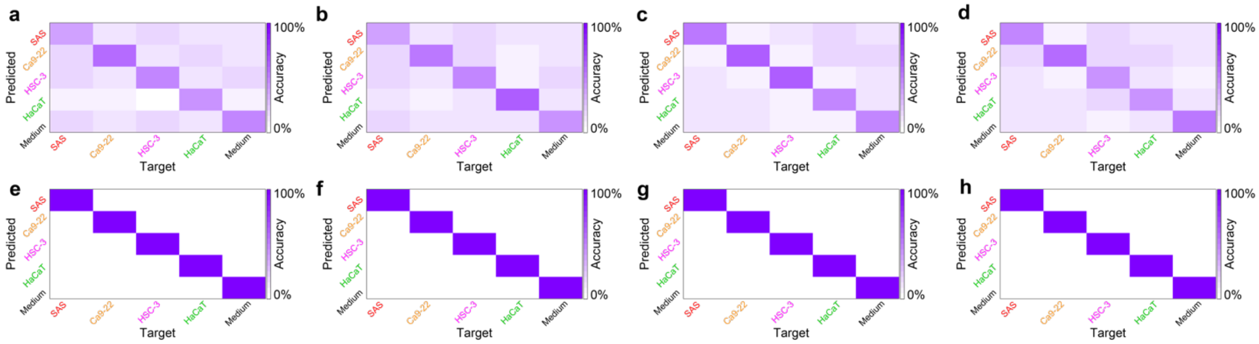

Figure 4.17: Stimulus-induced neural responses clearly distinguishable in high-dimensional space at time-matched points of growth. a-d) Time bin-wise high dimensional confusion matrix analysis of PN responses by leave-one-trial-out approach at 24-, 48-, 72-, and 96-h post seeding. The confusion matrices have higher values along the diagonal, which indicates that most of the test trials time bins are classified correctly. However, the confusion matrices also have non-zero off-diagonal elements, indicative of some misclassification. **e-h)** Trial-wise confusion matrices are shown at 24-, 48-, 72-, and 96-h of cell cultures. Here, each test trial was classified based on the mode of the bin-wise classification results. This analysis elicits diagonal confusion matrices for all cases, which indicates clear distinction of oral cancer vs. non-cancer VOC profiles based on population PN spiking responses.

(**Figure 4.17e-h**). Notice that we generated VOC-specific neural fingerprints at each time-matched points of growth of the cell cultures and performed *leave-one-trial-out* cross validation between the test and the training templates generated at that time point.

These results validated our hypothesis that neural response-based classification between multiple types of oral cancers cells and a non-cancer cell remained unaffected by the variations in VOCs caused by evolution of cancer and non-cancer cells in the culture medium.

Rapid Detection and Identification of Complex Cancer Volatile Headspace

We investigated how short of a VOC exposure will result in robust cancer classification. We hypothesized that a neuron response-based classification approach would be fast and able to classify different VOCs with a short inter-stimulus interval (~ 1 minute). Based on the fast PN response dynamics, we anticipated that distinction between cancer VOCs would be achieved

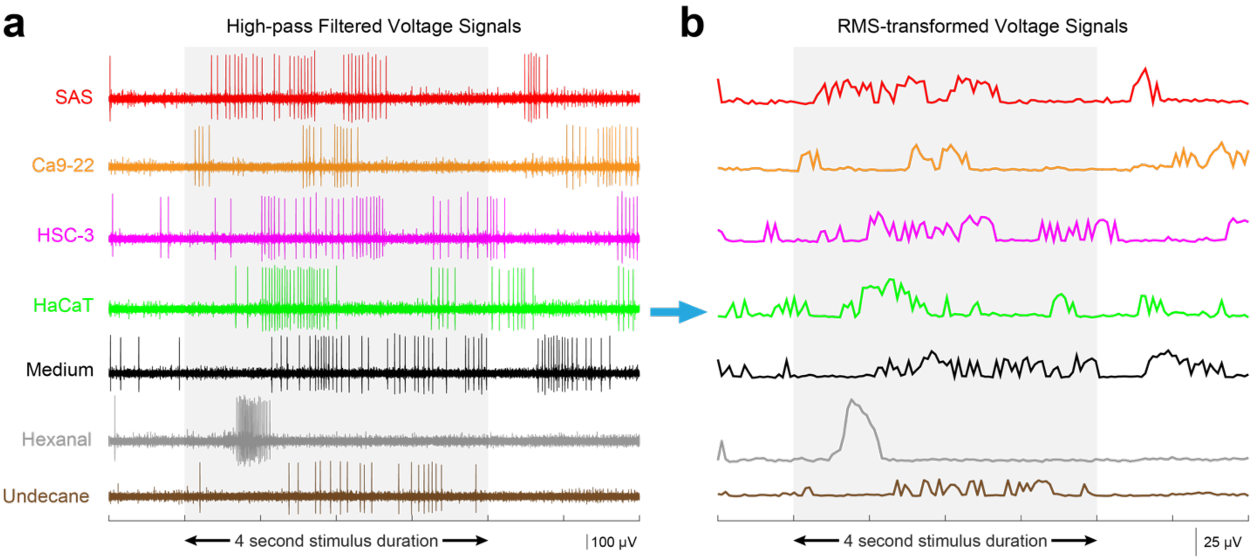

Figure 4.18: Root-mean squared (R.M.S) transformation largely preserved stimulus-specific spiking dynamics. a) Representative recordings from an individual electrode are shown for all stimuli after high-pass filtering. The gray box delineates the 4 s stimulus presentation period. **b)** R.M.S. transformed data traces of panel **a** recordings reflect the spiking rate-based response dynamics, while reducing computational overhead. The gray box delineates the same 4 s stimulus presentation period as in **a.**

within a few hundred milliseconds of stimulus exposure. To achieve fast analyses of neural signals, we employed a different metric of neural response, which was obtained by root mean squared (R.M.S.) filtering of raw neuron voltage responses (**Figure 4.18**, see *Chapter 2: Methodology- Signal Analysis*). Until now, all classification analyses were performed after spike-sorting of multi-unit extracellular voltage responses obtained from each recording location. However, this approach eliminated neurons that did not pass the statistical test necessary to be counted as single units. These lost signals from unresolved neurons could potentially be important for odor discrimination, therefore, we decided to employ the R.M.S.-based approach which takes into account the total energy of the signal acquired from each location. This approach was computationally less expensive, unsupervised and shown to be odor specific in our previous

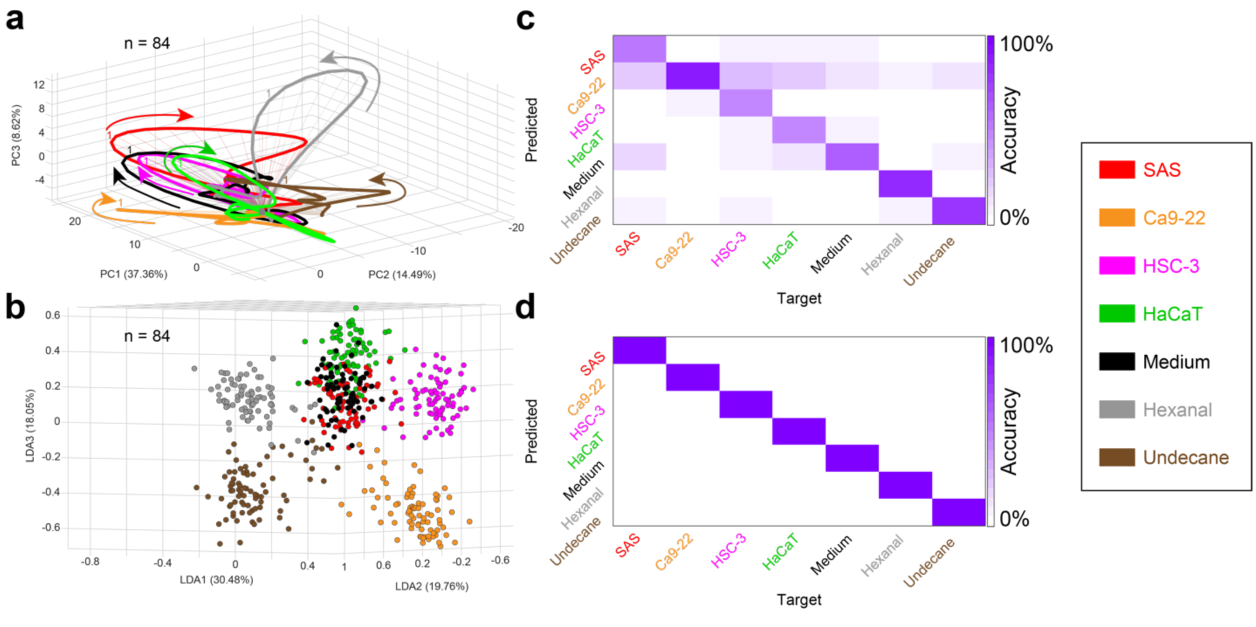

Figure 4.19: Using R.M.S transformed population PN voltage responses to classify the stimulus panel. Similar plots as shown in Figure S1, but here, we have used R.M.S transformed PN voltages to generate, **a)** VOC evoked ensemble neural trajectories after PCA; **b)** PN response clusters after LDA; **c)** Bin-wise confusion matrix in high dimensional space; and **d)** Trial-wise confusion matrix corresponding to all 7 stimuli. Spike-based and R.M.S-filtered PN time-series data both yielded excellent classification for all VOCs tested.

work [523]. Using the R.M.S. filtered population PN voltages, we observed distinct classification of all 7 VOCs tested (**Figure 4.19**). These classification results were qualitatively similar to the results obtained from spike sorted single unit data.

To determine the speed and efficacy of this method, we performed VOC classification during four different 250 ms time segments of the 4 s stimulus presentation window (**Figure 4.20**). The rationale behind choosing different time windows follows from the unique odor-evoked response dynamics of the projection neurons. PNs generally fire strongly with high spiking rates within the first ~1.5 s of stimulus onset, which is known as the 'transient state'[516-518, 596]. After about 2 s of stimulus exposure, the population PN firing rate converges to a stable firing rate, which stays above baseline firing but does not change significantly over the rest of the odor presentation duration. This is known as the 'steady state' response period. It is shown in our and others' work that odor-evoked transient PN responses are more discriminatory[516, 523, 590]. Therefore, we expected the cell culture VOCs to display the best separation when the population PN responses are within the transient state. We observed that odor plumes took about 0.5 s to elicit spiking responses in PNs. This time corresponded to the delay between the final olfactometer valve opening and the odor plume hitting the antenna. Therefore, we chose the analysis time windows for transient PN response period as 0.5 – 0.75 s and 0.75 – 1 s and the steady state time windows as 2 – 2.25 s and 2.25 – 2.5 s (**Figure 4.20**).

We performed PCA dimensionality reduction analysis to visualize population neural trajectories, which showed distinct trajectories at the earliest of the time windows (0.5 to 0.75

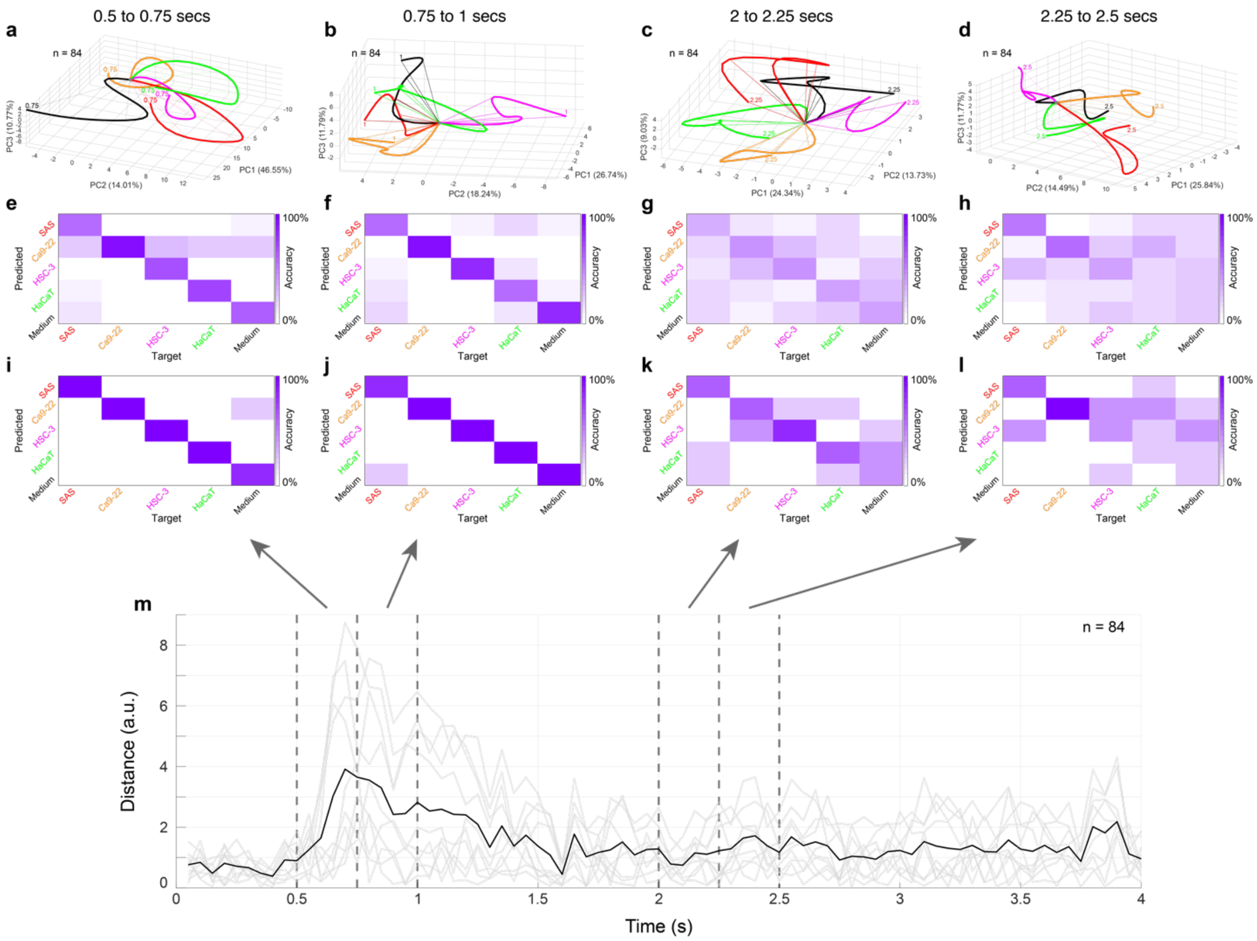

Figure 4.20: Rapid classification of oral cancer VOC profiles using neural voltage responses. a–d) High dimensional neuron response vector, where each row represents R.M.S. filtered PN signals of a recording position (n = 84) and each column represents a 50 ms time bin (total 5 time bins over 250 ms), was dimensionally reduced using PCA and ensemble neural response trajectories are plotted (see *Chapter 2: Methodology- Signal Analysis*). Cancer vs. non-cancer VOC-evoked neural response trajectories are shown for the stimulus presentation windows of 0.5–0.7 5 s, 0.75–1.0 s, 2.0–2.25 s, and 2.25–2.5 s, respectively. Notice that population trajectories generated from R.M.S. filtered neural voltages are distinct within just 250 ms of odor exposures. Two 250 ms time windows are shown during the transient state of the PN response (0–1.5 s), while two other time windows are chosen during the steady state neural response period (2 s to the termination of the stimulus). **e–h)** Confusion matrix analysis of the predicted vs. target responses are shown for the ensemble neural voltage time-series data for the same time windows as shown in panel a-d. Note that the confusion matrix analysis is done without any dimensionality reduction. Transient state time windows of 0.5–0.75 s and 0.75–1.0 s show better VOC classification compared to the steady state time windows. **i–l)** The same confusion matrices are plotted for the trial-wise classification, which results into near perfect classification of VOCs in 250 ms time windows during transient state. Steady state windows show relatively low trial-wise classification. **m)** Pairwise distances between ensemble R.M.S. voltages (from n = 84 PN recordings) corresponding to five different VOCs are plotted in light grey (total 10 pairwise

Figure 4.20 (cont'd)
distances) during the stimulus exposure (4 s). The mean of pairwise distances is plotted in black, which indicates that there are differences in ensemble PN voltage responses corresponding to different VOCs and these differences are highest during 0.5–1 s of the transient response period. Note that in our setup, odorants took about 500 ms to reach the antenna from the opening of the final olfactometer valve (t = 0) and therefore, the earliest transient state time window that could be chosen was 0.5–0.75 s.

s). The VOC-evoked neural trajectories remained distinct during both transient and steady state time epochs (**Figure 4.20a-d**). Next, we performed the quantitative high dimensional confusion matrix analysis using *leave-one-trial-out* methodology. We observed better classification during transient state time windows compared to the steady state time windows, evident from the higher value of diagonal elements in the confusion matrix shown in **Figure 4.20e, f** in comparison to **Figure 4.20g, h**. Trial-wise classification also showed better predictability during transient state response periods (0.5 – 0.75 s and 0.75 – 1 s) compared to the steady state segments (2 – 2.25 s and 2.25 – 2.5 s, **Figure 4.20i-l**). Finally, when we compared the pairwise R.M.S. response distances of the PN population elicited by all 5 VOCs, we observed the largest separation was also during the transient periods. These results demonstrated that once the brain-based recording and VOC delivery is set up, neuronal population responses can classify VOCs within 250 ms of stimulus onset.

To verify that a one-minute inter-stimulus interval is sufficient for the VOC classification and our results are consistent with the PN response dynamics, we employed the R.M.S.-based classification analysis on the baseline, transient, and steady state epochs of the population PN response (**Figure 4.21**). Each analysis epoch was 1.5 s in duration and the 0.5 s delay for the odor stimulus to reach the antenna was included in the pre-stimulus period. We observed no

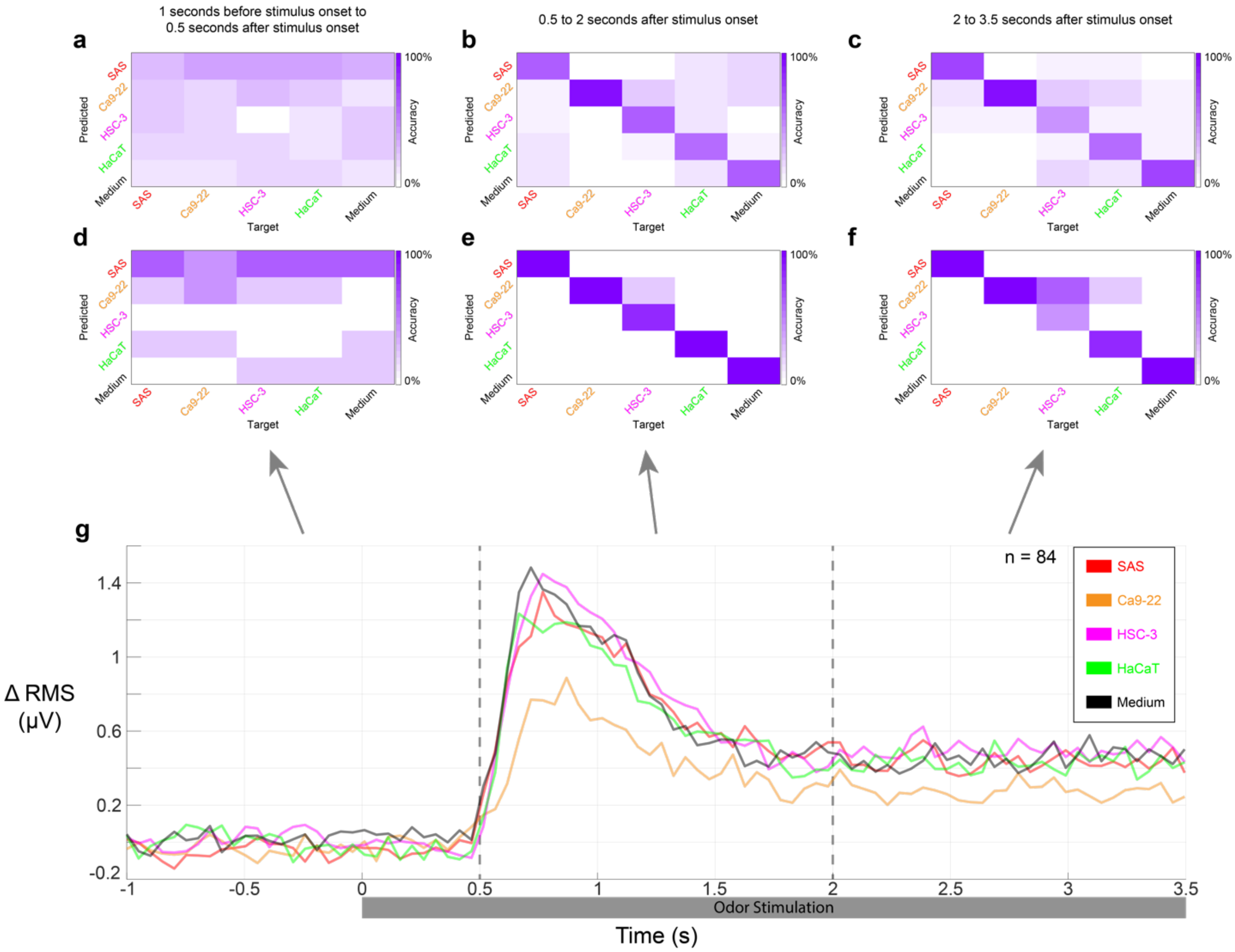

Figure 4.21: Cancer VOC classification during transient vs. steady state response periods of PN response. Time bin-wise confusion matrix analysis results shown for three 1.5 s duration time periods- **a)** 1 s prior to 0.5 s after final olfactometer valve opening (pre-stimulus period). **b)** 0.5 to 2 s after final olfactometer valve opening (transient state), and **c)** 2 to 3.5 s after final olfactometer valve opening (steady state). The pre-stimulus time period shows no stimulus specific classification as expected because VOCs had not yet reached the antenna at this time. The transient state period (0.5 to 2 s) shows the best bin-wise classification of all 5 VOCs. The steady state period (2 to 3.5 s) also shows high classification success, but the diagonal values are relatively lower compared to the transient state period. **d-f)** Trial-wise confusion matrices are shown for the same time windows as in panel **a**. **g)** A population-based peri-stimulus time histogram (PSTH) plots the change in R.M.S. transformed values of all recording positions (n = 84) as a function of time. Time labels along the X-axis are relative to the stimulus onset time. A significant change in R.M.S. values is seen approximately 500 ms after the final valve was opened (i.e., stimulus onset).

classification in the baseline period (-1 to 0.5 s), but VOC classification was distinct during the transient (0.5 to 2 s), and steady state (2 to 3.5 s) periods. Overall, VOC-evoked neural responses during the transient period yielded best classification results as expected from the PN response dynamics [590].

Outlook

While mass spectrometry based techniques have proven essential for volatile chemical identification for cancer detection [99, 108, 122, 190, 589, 597-616], the desire for portable and real-time gas sensor has fueled interest in developing electronic nose devices, which mimics biological principles for odor detection[617, 618]. Electronic noses have increased in popularity owing to advancements in materials science, nanotechnology, and pattern recognition algorithms. These devices have demonstrated the ability to distinguish between breathprints of healthy controls and those afflicted with different types of cancer [216, 263, 269, 602, 619-631]. Although, many of these portable chemical sensors are able to process breath samples in real time and potentially can be used as point-of-care devices, performance deficiencies due to sensor drift, humidity and temperature-induced changes significantly complicate implementation as a breath-based diagnostic. Moreover, electronic noses struggle to attain the high sensitivity necessary for detecting and differentiating between disease-specific volatiles at the trace-levels found in breath[617, 618, 632-635]. Despite drawing inspiration from biological olfaction, the prowess of electronic noses as chemical sensors is minimal relative to their biological counterpart.

In biological olfaction, natural selection has forced animals to develop highly sensitive olfactory capabilities while preserving chemical specificity. In the olfactory sensory system, a target VOC mixture as a whole is encoded by a distinct neuronal response template (or a neuronal 'fingerprint' of a VOC), while a different gas mixture is uniquely encoded by a different neuronal fingerprint. It is important to note that biology does not perform component-wise classification of gas mixtures, but instead achieves optimal separation between the VOC-evoked neural fingerprints. Many implementations of biological olfaction for disease detection has relied on behavioral readouts, which require extensive training and significantly limit the response resolution. Other attempts at creating medical bio-diagnostics have focused solely on the first order sensors used in animals for chemical recognition and signal transduction[636-646]. This biohybrid approach of integrating sensory neurons into signal processing platforms has proven challenging and devices often lack chemical discriminability and long-term performance[618].

Here, we took a forward engineering approach by ‘hijacking’ an insect brain to detect oral cancers from their VOC signatures. We combined *in vivo*, multi-electrode, population neuronal recordings with a multi-channel micro-amplifier, high speed data acquisition, and biological neural computations to achieve cancer detection. This approach is fundamentally different from current gas sensing devices and animal behavior-based disease detection as it uses a fully functional biological chemosensory array (antennae) and olfactory neural circuits as a gas sensor, and neuronal ‘fingerprints’ of cancer VOC profiles as decoding schemes. This *in vivo* neural recording technique can be portable as shown in previous work [523]. We envision this study as the first step in ‘sniffing out cancer by neurons’ research.

Our brain-based cancer detection method is an untargeted sensing approach for which we do not need to know the exact chemical composition of the cancer VOC mixture, which is essential for component-wise classification. Therefore, our method does not identify specific VOC biomarkers. However, this is also a key strength of biology-based VOC sensing. Biological olfactory systems detect the entire gas mixture as a single entity (e.g., coffee, banana, specific cancer cell VOC mixture) and encode this information in the brain as a spatiotemporal neural pattern. By identifying these neural patterns, we can create a template associated with each VOC

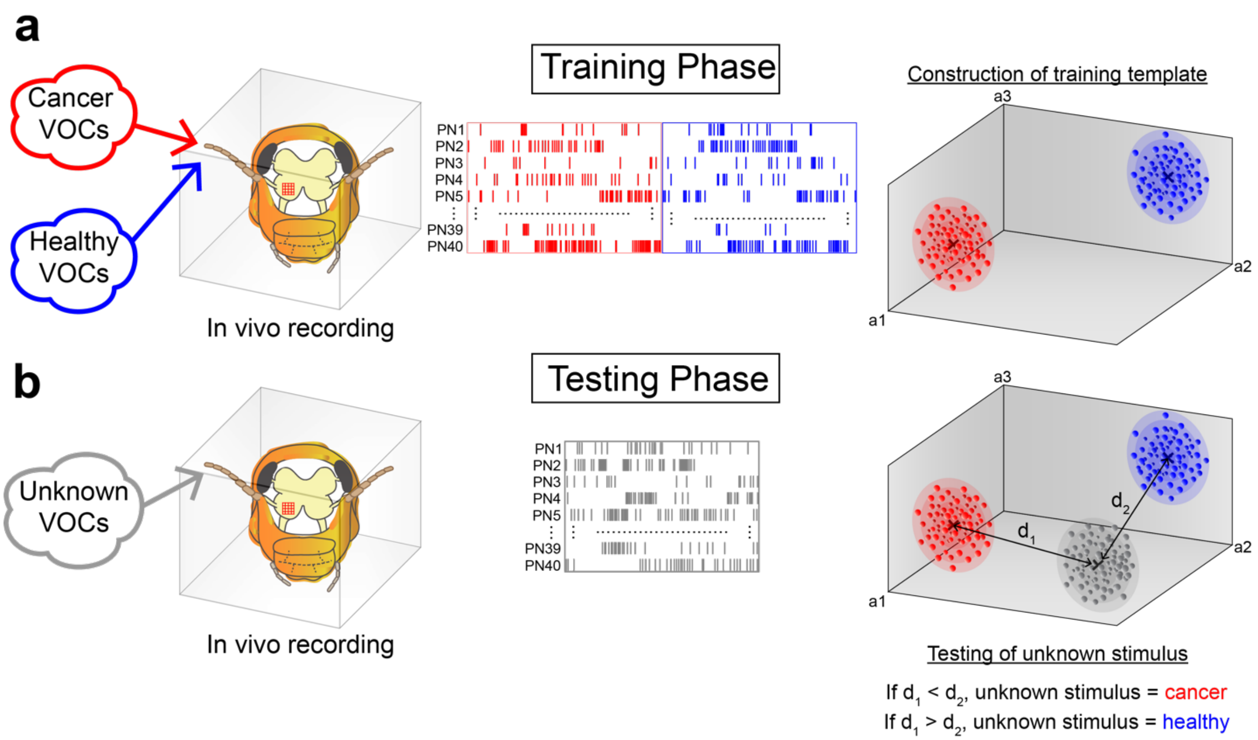

Figure 4.22: Principles of neuronal response-based noninvasive cancer detection. a) This approach employs VOC mixture-evoked neural response templates for distinction between cancer and healthy samples. During the training phase, target (e.g., breath samples of oral cancer patients) and control (e.g., healthy human breath samples) VOC mixtures will be exposed to the locust antenna and in vivo neural recordings will be obtained from multiple projection neurons in the antennal lobe, simultaneously. The entire in vivo electrophysiological setup will be placed inside a closed Faraday chamber with inlet and outlet port for VOC delivery and removal. Trained VOC-evoked population neural responses will be used to construct optimally separated heathy vs. cancer clusters in the neural space as illustrated in our analysis. Our results indicate that ~40 recorded PNs is sufficient for classification of multiple oral cancer cell lines from healthy controls. Notice that the training/calibration will be performed for each brain-based sensor, where the separation between target VOCs will be maximized by optimal placement of the microelectrode array in the antennal lobe. **b)** During testing phase, unknown VOC samples (e.g., breath sample of an early-stage oral cancer patient) will be presented to the antennae and neural responses will be obtained from the same set of neurons. In our study, we have used the minimum Euclidian distance between the unknown sample and the healthy vs. oral cancer neural clusters as the classification metric. However, other distance metrics can be used to classify unknown VOCs. Since the PN responses reach near baseline within 2 s of odor onset and we have demonstrated that reliable classification can be performed for 1 min inter stimulus interval, this technique can work as a high throughput cancer screening device.

mixture. Then, an unknown VOC mixture can be tested by comparing it to the known templates **Figure 4.22)**. In this study, training neuronal templates are generated for the VOC profile of each cell line and template-matching analyses are done between the training and testing templates to determine the test cell line identities. By harnessing the gas sensing power of the entire repertoire of the locust olfactory sensors, which are cross-selective and extremely sensitive, we can generate distinct neural response templates for different oral cancer cells. Moreover, this biology-based non-specific detection technology can be generalized to detect other cancers in the future.

Acknowledgments

A.F. was supported by D.S. The author thanks M. Parnas for assisting in cell culture flask modification, electrophysiological data collection, spike sorting analysis, and cell counting. E. Hoque Apu provided support in cell culture seeding and maintenance. E. Cox assisted in locust colony husbandry and cell counting. N Lefevre and S. Miller assisted in cell counting.

CHAPTER 5 | DISCRIMINATING CANCER BIOMARKERS USING HONEYBEE NEURAL RESPONSES

Application-Specific Chemical Sensors

Chemical gas sensing is a highly interdisciplinary scientific field, drawing upon principles from molecular chemistry, nanomaterial fabrication, and signal analysis to name but a few. One reason why it is such an intricate process is due to the millions of chemical combinations in existence. These molecules can be combined in highly heterogeneous matrices, forming exceptionally complex stimuli. The resultant stimulus state space would simply be infeasible to cover with a labeled line approach, in which individual sensors were responsible for encoding specific stimuli. Fortunately, stimuli are often constructed in stereotypical manners, relying heavily on relatively basic yet highly efficient chemical configurations. This chemical redundancy has prompted sensors, such as electronic noses and biological olfactory neurons (ORNs), to implement a combinatorial pattern recognition scheme. In this case, sensors can be tuned to highly conserved features, which can then be combined into ensembles to efficiently encode a large number of stimuli[647]. By incorporating an assortment of highly selective as well as broad range sensors, this approach can optimize chemical sensitivity, selectivity, and generalizability based on a finite stimulus space[371, 648]. This can be thought of in comparison to our sense of hearing. Within the ear, inner hair cells are arranged in a tonotopic pattern with adjacent cells being maximally responsive to sounds of near similar frequencies. Importantly, the response curves for a number of successive hair cells overlap, enabling a much finer resolution of tone discrimination[649]. The overlapping sensitivity between different sensors is a critical component for systems incorporating combinatorial coding information processing schemes.

Olfactory receptor neurons (ORNs) and electronic nose sensors display variability in their tuning curves. That is while one sensor may be highly selective and display high affinity for a particular chemical, others are responsive to a broad range. In electronic nose sensor development, the guiding force is based on an iterative process of fabricating or combining new materials and testing their response characteristics to a particular stimulus. While great strides in electronic nose technology have been made since its inception 40 years ago, state-of-the-art devices struggle to achieve sufficient detection limits for the wide range of disease-specific volatiles found in exhaled breath. While improvements in sensor material technology and signal processing algorithms will improve the gas sensing abilities of electronic noses, the performance of current systems lags behind that of biological olfaction. In biology, the force dictating the response characteristics of ORNs is evolution via natural selection. It reasons that ORNs providing a selective advantage for an organism within its immediate environment, are much more likely to be maintained through successive generations. For example, humans are highly responsive to odors in blood, information critical for assessing injury or danger, while unresponsive to carbon monoxide, as prior to the advent of fire, it provided no selective advantage[650, 651]. As such, organisms display species-specific olfactory receptor genes and differentially tuned ORNs based on unique environmental pressures.

Previous research on insect olfaction has demonstrated that locusts respond to a broad range of odors, from those that hold biological significance to those that have had no influence in their evolution. Moreover, even these novel, non-biologically relevant stimuli were mapped to different regions of their chemical encoding state space, allowing for efficient signal discriminability. Our previous work has demonstrated that locusts can not only identify unique cancer biomarkers, but their olfactory system is powerful enough to differentiate between the complex volatile headspaces of cancer and non-cancer cells. Like all sensors, however, locust olfaction has a limited scope across a subset of possible odor space. It is improbable that the locust olfactory system, which has developed to function optimally in a particular ecological niche, is the best sensor for classifying disease from breath samples.

Honeybee Olfaction

A significant amount of research has been conducted using honeybees, due to their impressive learning abilities, gregarious nature, and critical role in the environment[652]. Like other insects, honeybees rely strongly on their olfactory abilities, rapidly identifying pertinent volatiles, localizing plumes and occasionally using them for long-distance flights[653]. As a result of wide interest in honeybee neurobiology and behavior, multiple standard brain atlases have been constructed, aiding in understanding network topologies and functional processing schemes **(Figure 5.1)** [654-657]. A variety of studies incorporating genomic, behavioral, electrophysiological, and calcium-based imaging data, have elucidated key anatomical and functional features specific to honeybees that are integral for their highly acute chemical sensing abilities[498, 658, 659]. Preliminary research has indicated that honeybees can be conditioned to engage in stereotypical behavioral responses to highly specific stimuli. Importantly, like other biological olfactory systems, they analyze complex patterns of chemoreceptor activations to recognize relative concentrations of chemical constituents and identify unique odorants[499]. A deeper look into their anatomical and functional neurobiology can help to unveil some of the mechanisms used to perform this impressive feat.

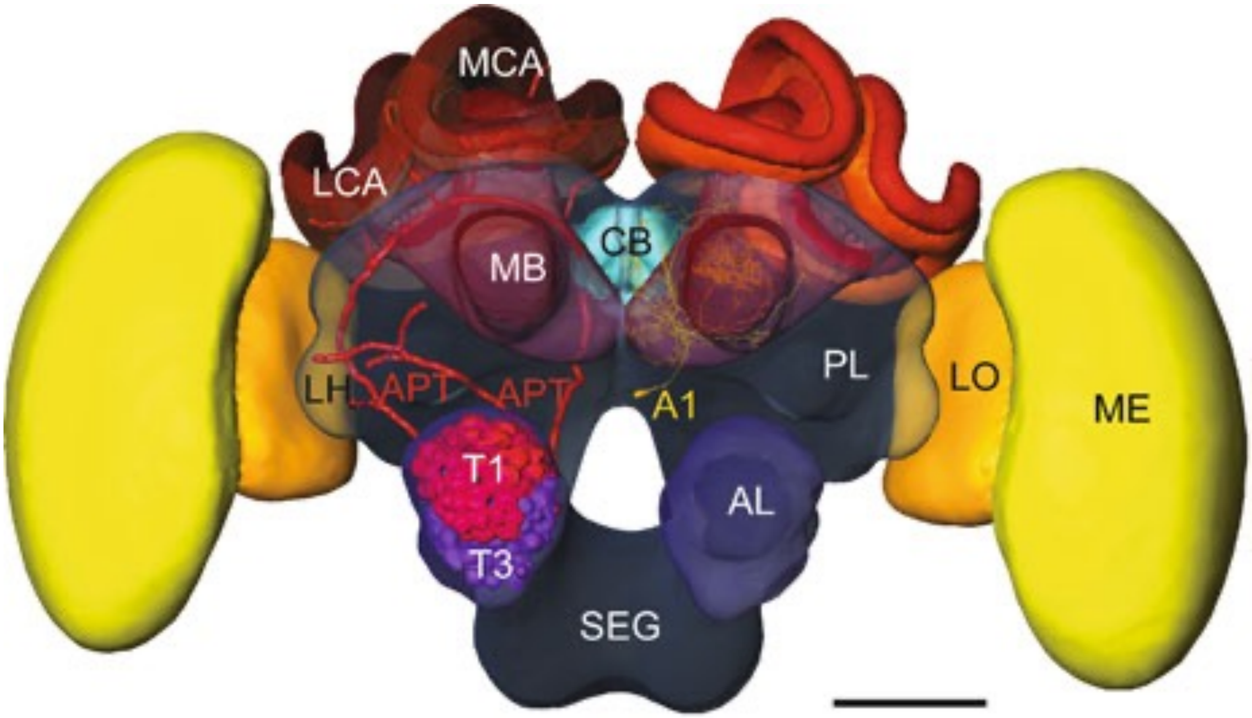

Figure 5.1 | Surface model of the honeybee standard brain. Olfactory receptor neurons converge onto glomeruli in the antennal lobe. Here, two distinct populations of glomeruli are shown, T1 and T3. These neuronal populations project axons along particular paths to higher-level processing areas such as the median calyx (MCA) and lateral calyx (LCA) of the mushroom body (MB). Scale: 250 mm. Reproduced from [657].

Honeybees contain three types of olfactory-specific sensilla: placoid (poreplate), trichoid (hair-like), and basiconic (peg-shaped)[660]. The placoid sensilla contain between five and 35 ORN dendrites[323, 661]. Hydrophobic volatiles are bound by odorant binding proteins and transported to the appropriate ORN. Interestingly, honeybees have the smallest set of odorant binding proteins (21) of all studied insects[662] but a rather expansive set of ORNs (163)[663]. While the activity of one ORN can alter that of its neighbors due to the shared lymphatic ionic environment, direct ligand binding competition is rare as neurons with similar tuning curves are likely to be found in different sensilla[664]. A total of 60,000 ORNs extend axonal processes into the antennal lobe, where a portion splits into four different tracts and innervates the 165 glomeruli[665]. Like most other insects, ORN axons of a particular type innervate a single glomerulus[666]. Within each glomerulus, a stereotypical topography is observed: ORN axons innervate the cortex and PNs innervate the core[654, 666]. The honeybee antennal lobe consists of 800 projection neurons and 4000 local neurons. This is in striking contrast to the locust antennal lobe, which displays 830 projection neurons and 300 local neurons. Differences in total neuronal populations suggest that these insects use highly disparate processing schemes in order to effectively encode olfactory stimuli. Moreover, the local neurons in locusts issue graded dendrodendritic potentials, whereas those in honeybees fire sparse action potentials. The inhibitory local networks in both species play a vital role in effectively encoding different odorants[364]. Projection neurons transmit conditioned signals to higher-level brain regions, such as the mushroom body characteristic of signals divergence and sparse neuronal activity[365]. Each glomerulus can be thought of as encoding for a particular stimulus related feature. On average, a single glomerulus contains axons from 400 ORNs, 1000 local neurons and a mere five projection neurons[323, 667]. This crude breakdown indicates massive convergence of chemical signals onto a small number of extrinsic neurons, emphasizing the critical nature of temporal dynamics for maximizing discriminability.

Honeybee-Based Cancer Biomarker Differentiation

In our current study, we sought to determine the efficacy of the honeybee olfactory system in detecting and discriminating between key cancer biomarkers found in exhaled breath. Microelectrodes were used to record neuronal action potentials from the antennal lobe. We included a panel of 10 odorants, identical to those used in our previous research intended to use the locust olfactory system to identify individual cancer biomarkers. Our stimulus panel consisted of five odors affiliated with breast cancer (hexanal, nonanal, pentanal, trichloroethylene, and undecane), five odors affiliated with lung cancer (decane, methylheptane, pentamethylheptane, propylbenzene, and undecane) and one stimulus (paraffin oil) as a negative control. Note that some biomarkers, such as undecane, are observed to be elevated in a number of different cancers owing to common underlying pathophysiological adaptations. All odorants were diluted in paraffin oil (1% v/v) and stored in 20 mL glass vials with 1/32” diameter

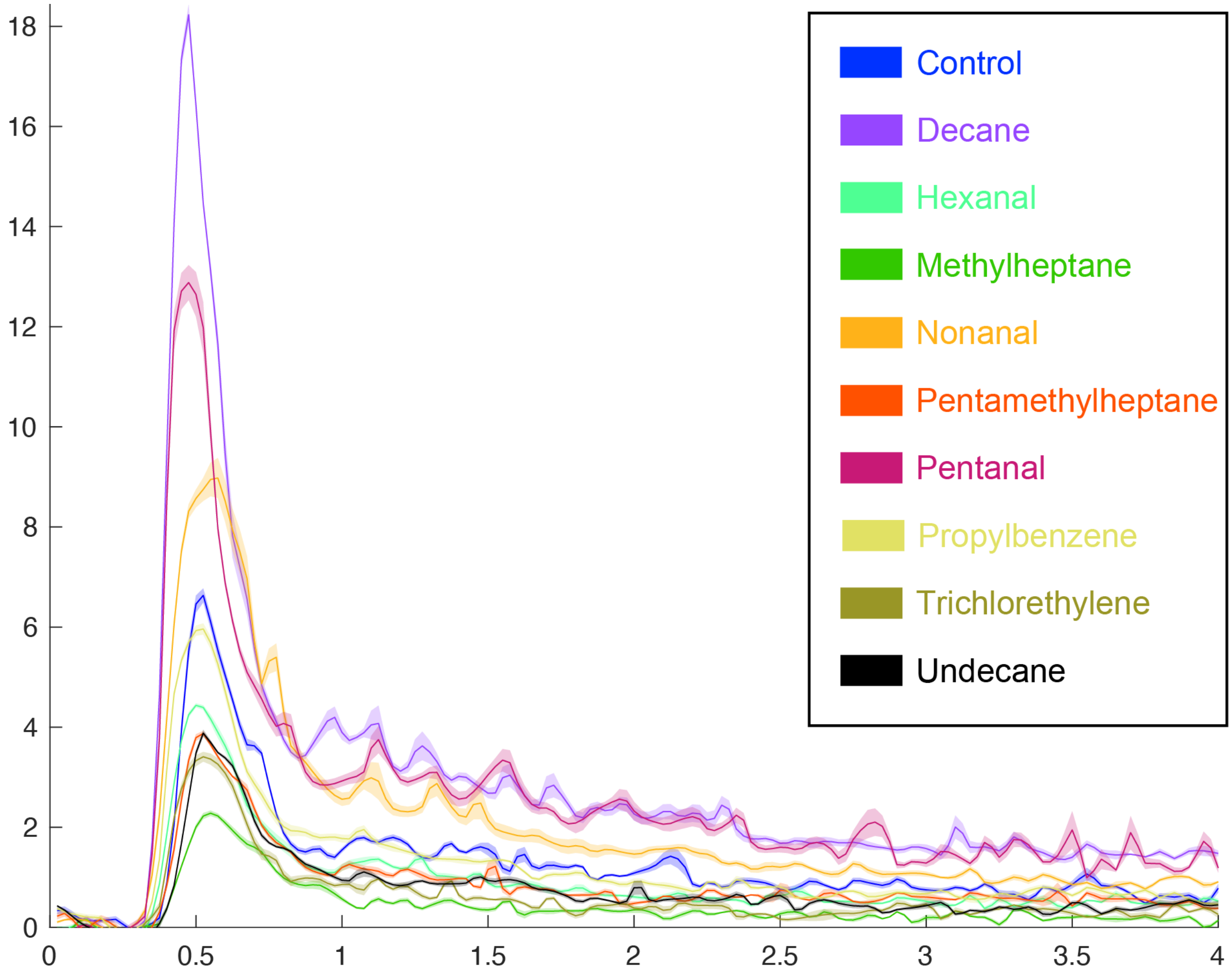

Figure 5.2 | Peri-stimulus voltage trace. Honeybee antennal lobe neurons were initially processed using an RMS transform and population average voltages were plotted as a function of time. Here, different stimuli seem to elicit unique response patterns corresponding to stimulus-specific spatiotemporal encoding of stimuli.

polytetrafluoroethylene (PTFE) tubing serving as inlet and outlet lines. For additional information on odorant preparation, see section *Chapter 2: Methodology- Odor Vials*. All stimulus presentation periods lasted for four seconds. For additional information on odorant preparation, see section *Chapter 2: Methodology- Odor Presentation*.

Similar to the encoding state space of enoses, the responses of individual electrodes or neurons can be conceptualized as unique orthogonally oriented dimensions in an encoding hyperspace[203]. Given current limitations in microelectrode design and fabrication, we pooled the total number of electrode positions across 39 different individuals. This technique, well-established for other insect models, is based on a breadth of data demonstrating that response patterns remain consistent between species-specific individuals[498-500].

Owing to the positive results gained from locust research, we processed data with our RMS technique. Population-wide neural responses demonstrated honeybees successfully detected the presented odorants (**Figure 5.2)**. We observed unique response dynamics with a large transient response for the majority of the presented stimuli. This could potentially allow for stimulus discrimination based on neural responses alone. We performed similar dimensionality reduction techniques as we had done with our locust dataset. Initially, we plotted neural trajectories after processing the data according to principal component analysis **(Figure 5.3a)**. This again showed unique neural trajectories for each individual odorant. Data mapped to and plotted in linear discriminant analysis subspace demonstrated disparate stimulus-specific neural cluster formation **(Figure 5.3b)**. We performed quantitative analysis using our leave-one-trial-out technique. Bin-wise predictions and trial-wise predictions were plotted in a confusion matrix for the four second period following stimulus onset. This constituted the entirety of the odor

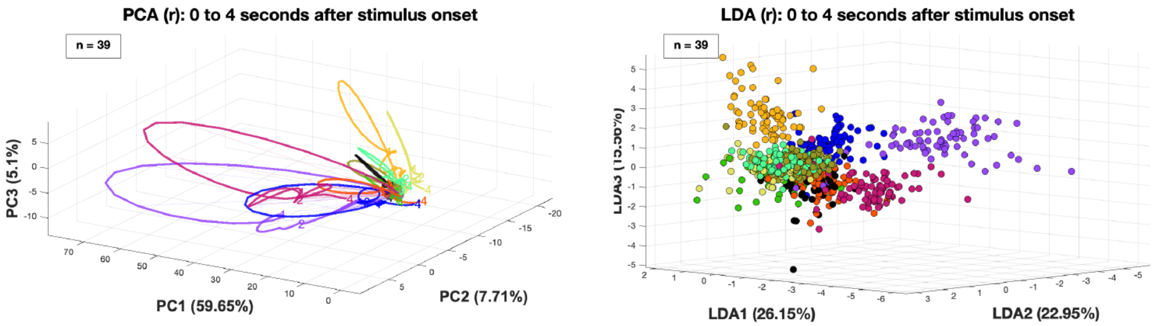

Figure 5.3 | Dimensionally reduced population-wide response dynamics. a) Principal component analysis allows for visualization of neural response trajectories according to the degree of variance they express. Highly unique trajectories indicate that the response state corresponding to each stimulus at each point in time differ dramatically from one another. **b)** Stimulus-specific clusters begin to emerge from linear discriminant analysis processing. This suggests that an underlying structure exists for encoding and processing this data in the honeybee brain and these responses may be linearly separable with enough recording locations.

presentation period, including the initial transient response and subsequent steady state. Bin-wise predictions showed adequate classifier performance **(Figure 5.4a)**. Trial-wise performance was near perfect, with only two out of 50 trials predicted incorrectly **(Figure 5.4b)**.

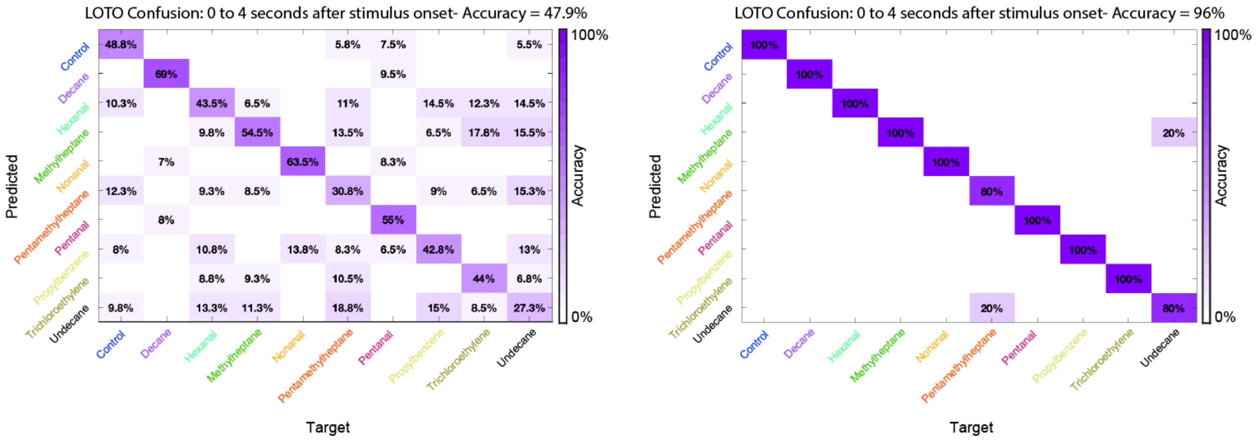

Figure 5.4 | Classification of cancer biomarkers. We used a leave-one-trial-out method for training and testing a linear classifier in the original 39-dimensional neural encoding state space. **a)** Results from bin-wise classification show moderate levels of classification accuracy using the Manhattan norm. **b)** Trial-wise based classification generates near perfect results. A total accuracy of 96% was attained using the Manhattan norm as a distance metric.

Outlook

It is important in gas sensing applications to consider the particular application as well as the strengths and weakness of different sensor technologies. This iterative process is relatively straightforward for manmade sensors, but a nearly limitless number of confounding factors can threaten readout integrity. It is also immensely time-consuming as application-specific devices must be fabricated, each tested within an assortment of different environmental conditions . Biological olfaction has evolved to function over a wide range of environments. It is likely less affected by the high humidity levels found in exhaled breath and is robust to minor alterations in background noise or interferants. This ability stems from the highly intricate processing schemes that incorporate spatial and temporal aspects for enhanced encoding capabilities. This imbues biosensors as highly attractive models for processing complex gas mixtures. In this case, biosensor tuning is likely based on evolutionary pressures forcing organisms into particular ecological niches. Having demonstrated that the locust can effectively detect cancer biomarkers, we sought to test the same capabilities in the honeybee, which exhibit disparate sensory processing capabilities. We found that honeybees can, in fact, differentiate between stimuli with a high degree of accuracy. While tempting to compare the classification accuracies between locusts and honeybees as an indicator for olfactory performance, it should be noted that different technologies for interfacing with the neural system were utilized owing to alternate morphological features of the two species. To our knowledge, this study represents the first extracellular recordings from the honeybee antennal lobe and, hopefully, paves the way for future experiments using honeybees as a non-invasive cancer diagnostic.

Acknowledgments

A.F. was supported by D.S. The author thanks E. Cox and S. Sanchez for performing odor vial construction and electectrophysiological recordings. E. Cox, S. Sanchez, and M. Parnas also provided support in honeybee colony maintenance and husbandry.

CHAPTER 6 | ONGOING WORK AND FUTURE DIRECTIONS

Introduction

Bio-hybrid sensors offer fundamental advantages over current state-of-the-art manmade sensors for the purpose of disease detection. Gas chromatography-mass spectrometry and ion mobility spectrometry offer excellent component wise separation abilities. These analytical approaches have provided insight into underlying metabolic processes by identifying analytes tied to specific biological pathways. However, the goal of a medical diagnostic is to identify the presence (or absence) of an underlying disease. While individual volatiles can be indicative of a few different pathological conditions, breath profiles are combinations of hundreds to potentially thousands of trace-level compounds. Subtle variations in a broad range of these chemicals are often much more informative for disease diagnoses, especially when considering complex pathologies. Importantly, the production of intermediary metabolites can alter subsequent biochemical reactions, eliciting further changes in metabolites. As such, diseases often have broad scale effects dependent on numerous genetic as well as environmental variables. These component-wise breath analysis methods as medical diagnostics require extensive signal processing to identify patterns particular to a disease state. In order to bypass the limitations of such systems, electronic noses are based on a functional combinatorial coding scheme. The incorporation of broadly selective, cross-reactive sensors prevents the identification and quantification of individual analytes. Instead, these devices aim to classify entire gaseous mixtures as points in a high-dimensional space. Although inspired by biological olfaction, the performance of electronic noses pale in comparison. They lack the broad response characteristics seen in biological olfactory systems and fail to achieve sensitivity levels for the detection of many trace-level volatiles present in exhaled breath. Instead of attempting to reverse-engineer gas-based sensors, our approach harnesses the power of biological olfaction directly by incorporating complete biological chemosensory arrays involving diverse olfactory receptors (antennae), biological signal transduction, and neural computations all in one device. We have demonstrated that multiple different insect biosensors are able to reliably detect and differentiate between cancer biomarkers. Moreover, the locust olfactory system is capable of differentially encoding heterogeneous mixtures such as the volatile headspace of cancer cells. Our proof-of-concept testing indicates that insect biosensors have tremendous potential as medical diagnostics.

Current Limitations

All insect brain surgeries were performed manually. For locusts, each surgery took one to one and a half hours depending on the experimenter's surgical experience and expertise. Success rate of electrode insertion was moderate (~80% per surgery). In future iterations, these limitations can be mitigated by incorporating robotic surgeons to automate the surgery and electrode insertion processes[668-670]. In our lab, the supply of insects was relatively abundant and inexpensive. For large scale operations, significant increases in colony sizes would be necessary, requiring some trained operative personnel.

One significant concern regarding brain-machine interface technologies is the potential damage to neurons and glial cells. While for acute experiments this has limited impact, the induced damage can initiate an inflammatory response and significantly affect signal-to-noise ratios in chronic models[671]. Based on our current neural recording setup, the number of PNs recorded per experiment was low (on average ~3 PNs/recordings). Therefore, PN responses were pooled across multiple recordings which is standard in neuroscience studies[523, 590, 596] but not optimal for one-shot cancer VOC analysis. In the future, high density multi-electrode arrays and signal processing circuitry can be employed to record large amount of PNs simultaneously, thereby eliminating the need for multiple experiments and achieving one-shot classification [670, 672-674].

In the locust antennal lobe, projection neurons are the only neurons to exhibit a spiking response. Thus, we each class of spike sorted data belonged to a putative projection neuron. In honeybees, however, both local neurons and projection neurons exhibit spike-based signaling. We could not positively determine whether our spike sorting algorithm was identifying a local or projection neuron, though the activity of both might be beneficial for stimulus classification. Waveform analysis algorithms may be effective in discriminating between the functional characteristics and separating out activity from these distinct populations.

One significant concern of manmade sensors as medical diagnostics is their limited sensitivity. While biological olfactory systems, such as canines, have shown to exhibit very low detection thresholds, our current study did not investigate whether these insect biosensors could detect and differentiate between volatiles or volatile mixtures at the concentrations typically found in exhaled breath. The selection of cell culture stimuli in our locust study enabled a highly controlled environment limiting the presence of confounding variables. However, *in vitro* cell cultures do not fully reflect the *in vivo* tumor microenvironment and cellular matrix, and *in vivo* VOC profiles may differ from the VOC profiles observed in *in vitro* cultures for different cancer types [146, 147, 675, 676]. Therefore, further studies involving *in vivo* cancer VOC analysis will be necessary to validate this brain-based sensing technology for cancer detection.

Multi-Electrode Array Modifications

Sensor response characteristics are vital for determining a system's performance in a given task. By tapping into the neural signals from insects, we eliminate the difficulty in designing and testing effective sensors for a broad range of chemicals. Yet, we still need optimal technologies to read the electrical signals that have been transduced by olfactory receptor neurons and processed by the dense neural network of the antennal lobe. State-of-the-art multi-electrode array fabrication technologies are generally geared towards device implantation in humans to restore normative sensory functioning. As such, the dimensions of these arrays are not suitable for insect-based neural recordings. We explored different avenues for the creation of novel high-density electrode arrays that eliminate the need to pool data across multiple insects. The antennal lobes of locusts and honeybees are ~500μm and ~300μm in diameter, respectively. For our locust recordings, we used micromachined probes, however, microwire arrays minimize the amount of displaced tissue

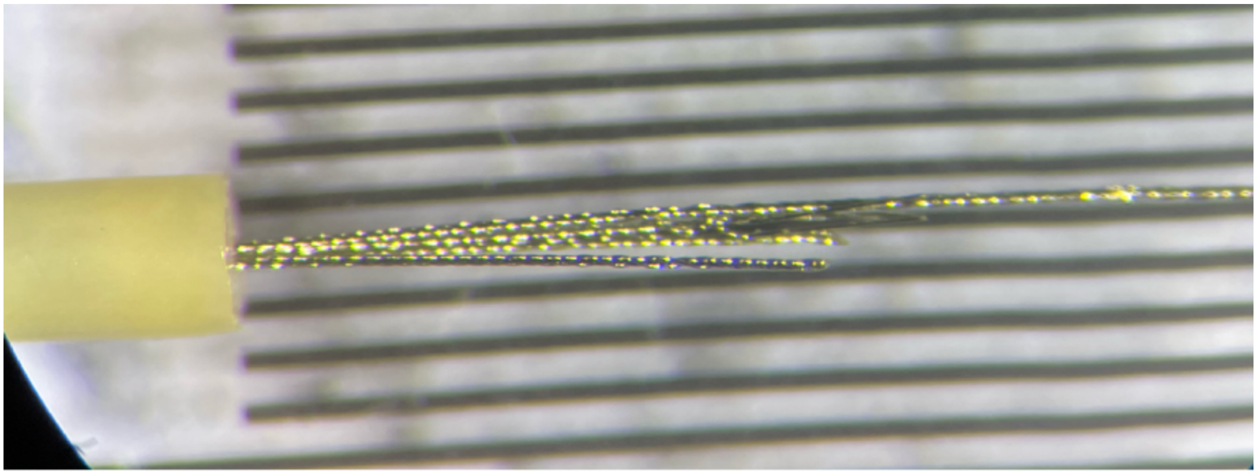

Figure 6.1 | Multi-tetrode device. A single guide tube contains five different tetrodes, consisting of four channels each. While this technique could be beneficial for recording from a large number of neurons, it lacks reproducibility as tetrode bundles are not stabilized within the guide tube.

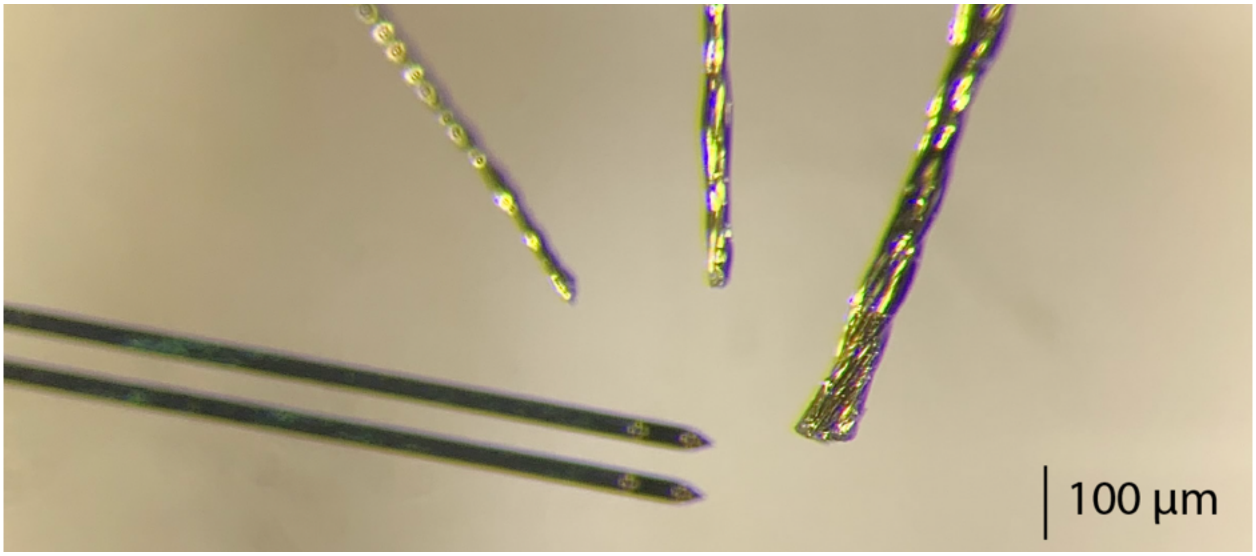

Figure 6.2 | Multi-electrode array size comparisons. *Left to right:* Dual shank Neuronexus probe with two tetrodes per shank, 4-, 8- and 16-channel twisted wire tetrodes. As the number of channels increases for the twisted wire tetrodes so too does the device footprint. For insertion points with no space between individual wires, device implantation was not viable and a significant amount of neural damage occurred.

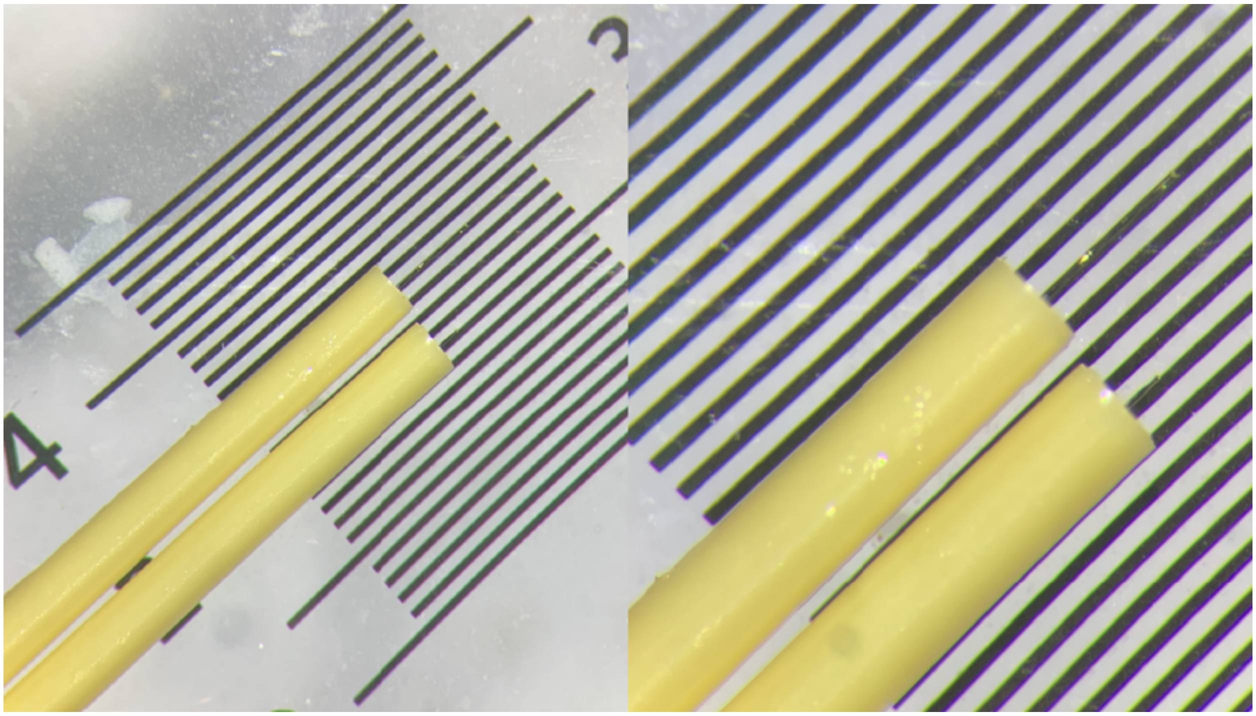

Figure 6.3 | Dual guide tube single wire electrodes. Individual 12.7 μm diameter wires were fed through micro-capillary columns with an inner diameter of 50 μm. The hole—wire size mismatch permitting significant maneuverability within the tubes and the relatively large tube thickness limited using a large number of tubes for a highly dense array. Line-to-line width in the above images is 200 μm.

and are often characterized by much smaller device profiles. As such, twisted wire tetrodes were used for honeybee recordings to minimize the extent of insertion damage. For locusts, the larger working area permitted multiple tetrodes to be paired within the same device **(Figure 6.1)**. However, inter-tetrode pitch was highly variable and twisting of the wires created a solid mass at the insertion point **(Figure 6.2)**, issuing substantial redundancy among a tetrode's channels. Initial attempts to reduce the electrode footprint and maximize information content were attempted by inserting individual electrode wires into adjacent tubes to enable sufficient inter-electrode separation **(Figure 6.3)**. Yet, the resulting gap between electrodes was too large to enable the construction of high-density arrays. Next, we attempted to splay electrode wires at the ends of a spun tetrode **(Figure 6.4)**. The splayed channels achieved appropriate inter-electrode distances but, similar to the variable pitch between tetrodes observed in our multi-tetrode devices, the pitch between individual wires varied significantly. This technique not only produced inconsistent channel spacing but was difficult to scale up to polytrodes containing the high number of channel counts intended. Instead a jig template was designed and printed using a Stratasys J750 3D printer **(Figure 6.5)**. Test pieces containing 400 μm, 300 μm, 200 μm, and 100

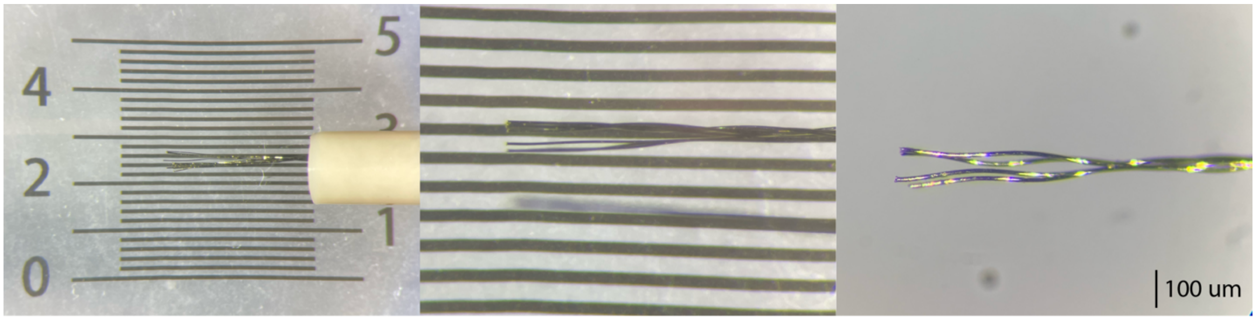

Figure 6.4 | Flared multi-electrode array. Tetrodes were fabricated as seen in *Chapter 2: Methodology- Tetrode fabrication*. Once finished construction, tetrode tips were splayed to form close, yet identifiably separate channels. These devices proved viable but lacked inter-device reliability and proved difficult to scale up to higher channel counts. Line-to-line distance is 200 μm.

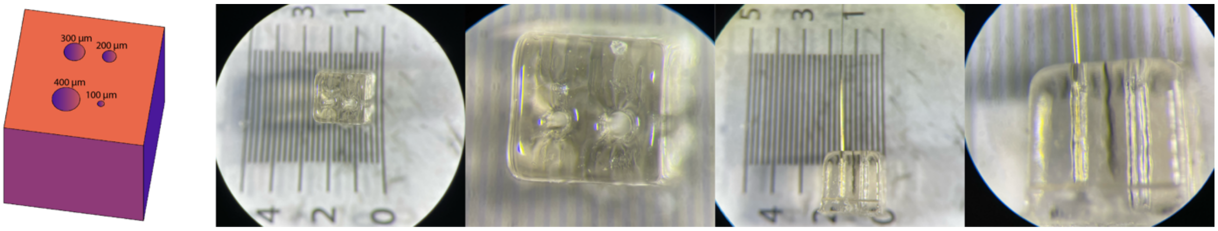

Figure 6.5 | 3D-printed multi-electrode template. Template piece for testing Stratasys J750 resolution and minimal feature size capabilities. Printer successfully printed 400 µm and 300 µm holes but failed to print 200 µm and 100 µm holes. While the larger holes were visible, the channel did not extend the entire way through the piece.

µm diameter holes were initially printed to determine the maximal feature resolution of the printer **(Figure 6.5a)**. Holes exceeding 150 µm failed to be printed **(Figure 6.5b)**. This test showed that the resolution of the printer was inadequate for generating jigs with necessary inter-

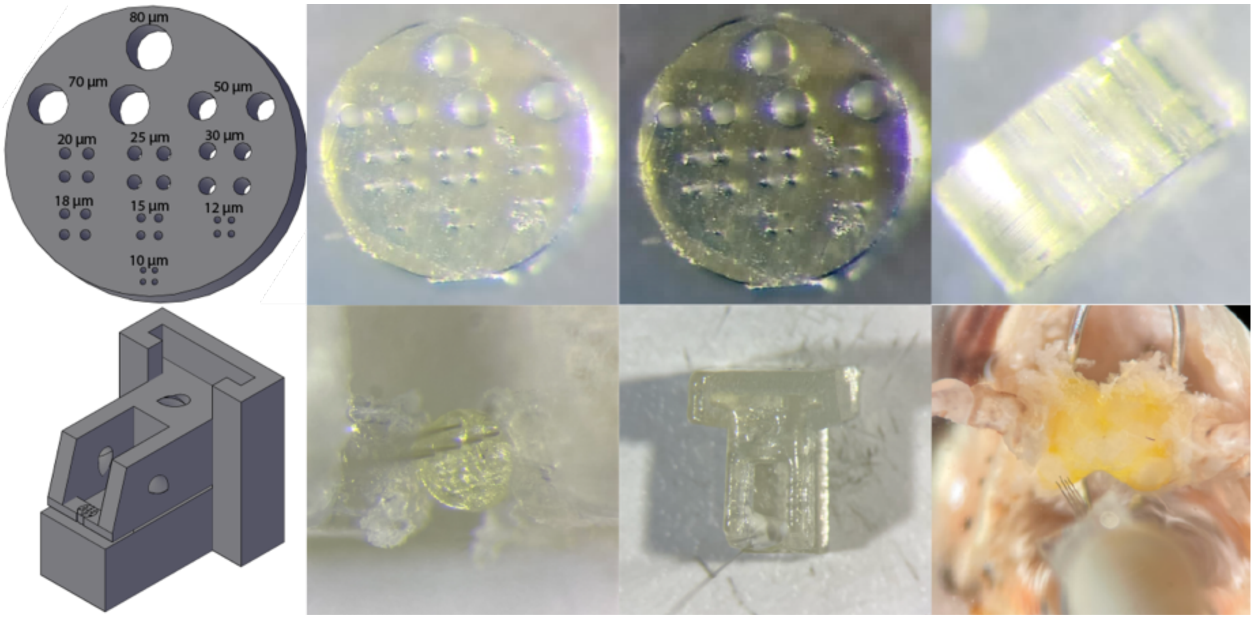

Figure 6.6 | Boston Micro Fabrication 3D-printed multi-electrode template. A template piece for testing the resolution and minimal size feature capabilities of a 3D printer specializing in micro-scale technology was printed. Hole diameters included 80 µm, 70 µm, 50 µm, 30 µm, 25 µm, 20 µm, 18 µm, 15 µm, 12 µm, and 10 µm. The printer successfully printed most, if not all, of the holes, though this was difficult to assess for the smaller ones even with the use of a stereomicroscope. **a-d)** Template test piece. **e)** Supplementary 3D printed holding device to stabilize piece during wire feed through. **f, g)** Wires successfully fed through the larger holes of the device, demonstrating excellent printer resolution. **h)** Custom-made 3D multi-electrode array just prior to device insertion.

electrode pitch distances and the large hole size would induce variability in pitch distance. A new test piece printed by a company specializing in micro-scale 3D printing applications (Boston Micro Fabrication). Holes of various diameters were tested, and the printer achieved resolution adequate for our intended application **(Figure 6.6)**. Handling of the 3D printed jig template was exceptionally difficult owing to its small profile and extremely light weight. However, some

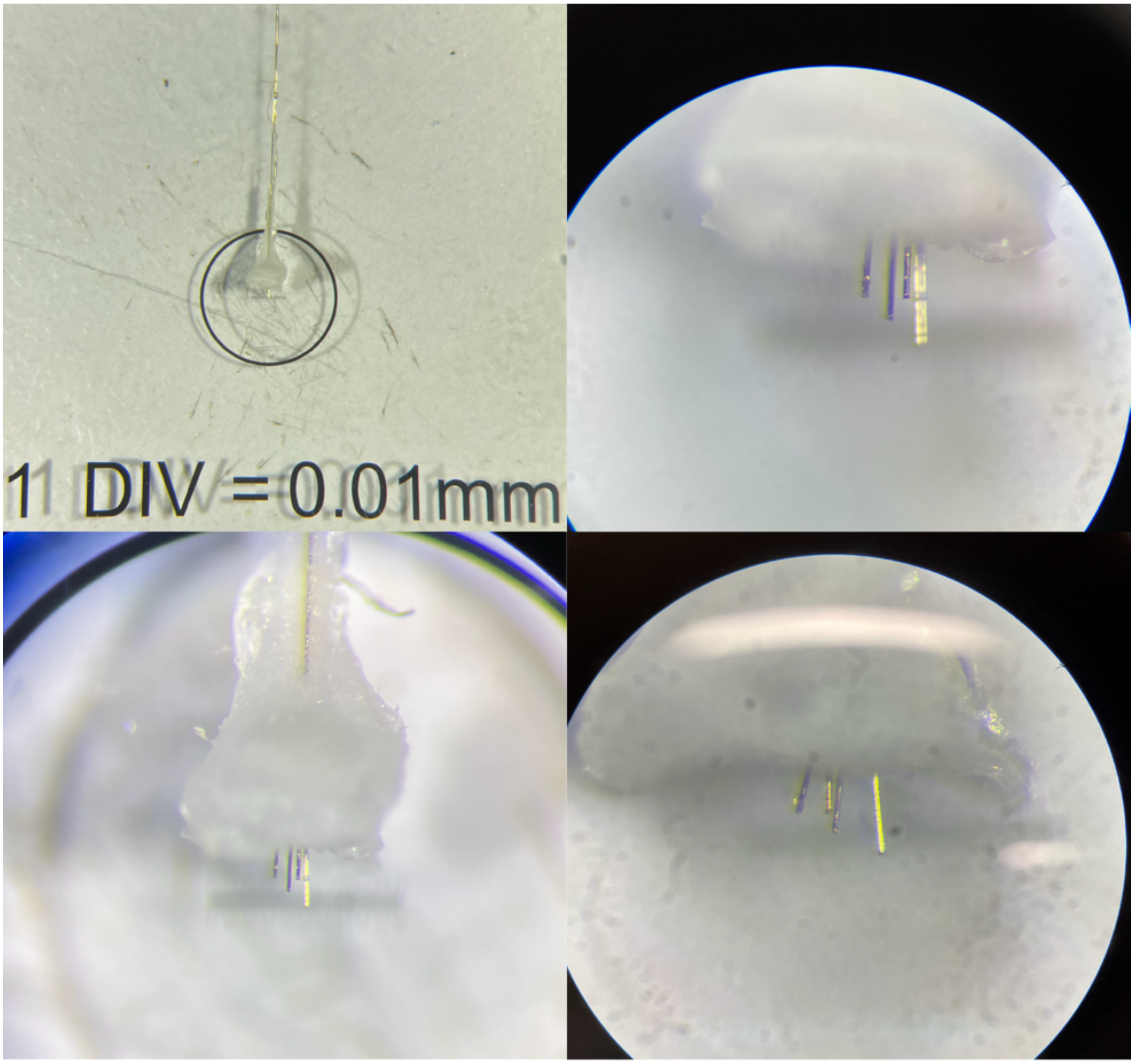

Figure 6.7 | 3D multi-electrode array. Close up images of an additional 3D multi-electrode array as seen through a stereomicroscope.

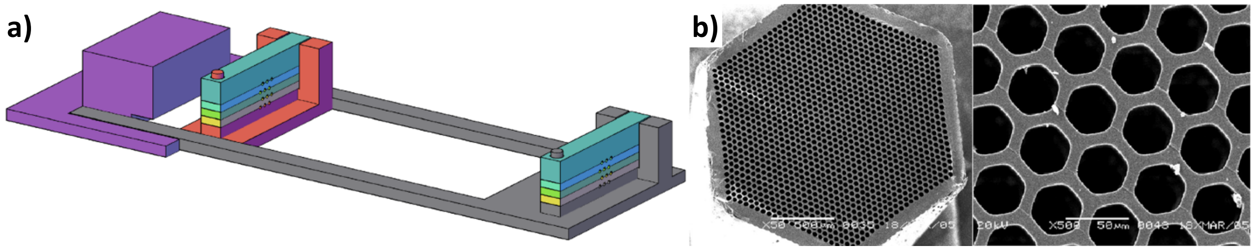

Figure 6.8 | Alternative multi-electrode array designs. **a)** Custom-design 3D printable horizontal jig. **b)** Micro-capillary column with numerous microscopic hole channels.

electrode wires were able to be fed through individual holes and a layer of two-part epoxy was placed atop the template, thereby stabilizing electrode positioning. Once cured, the epoxied wire was removed from the jig template to expose tips of the 3D high-density probe **(Figure 6.7)**. Alternative design schematics were considered but not pursued **(Figure 6.8a)**. Moreover, microcapillary columns, occasionally used in gas chromatography-mass spectrometry and ion mobility spectrometry, could be used to serve as a template substrate **(Figure 6.8b)**.

In addition to 3D geometries, 2D configurations were also explored. One design used wires aligned in parallel, which resulted in excellent configurations, but the fabrication of such probes was painstaking and difficult to reproduce **(Figure 6.9)**. Alternatively, wires were drawn

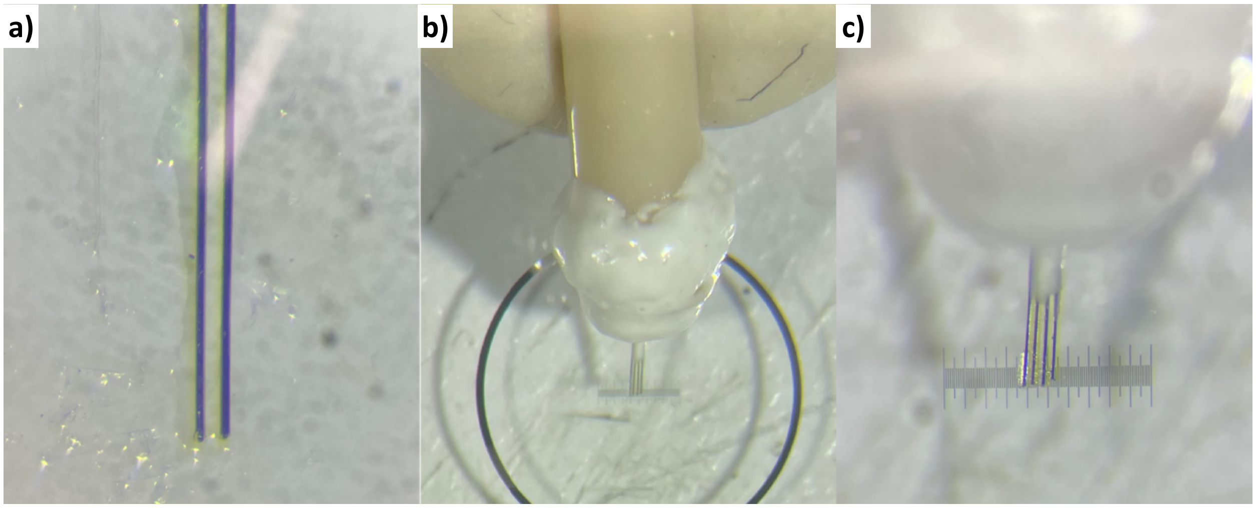

Figure 6.9 | 2D straight-wire multi-electrode array. a) Test array of two individual wires. **b, c)** Test array demonstrating multi-channel capabilities at micron level resolution.

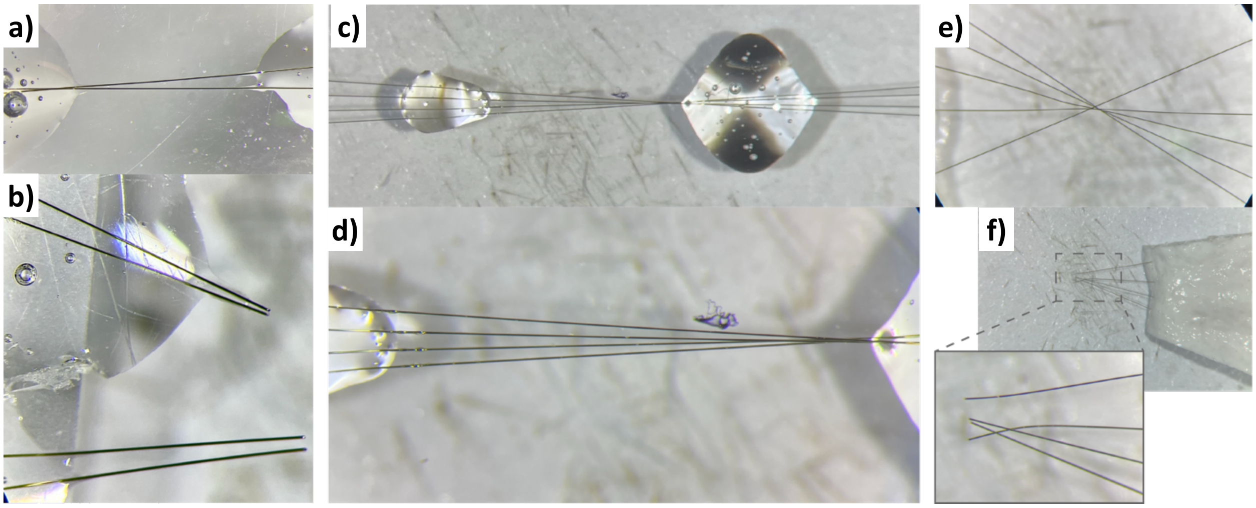

Figure 6.10 | 2D angled-wire multi-electrode array. a, b) Test array of two individual wires. **c-f)** Array testing multi-channel capabilities at micron level resolution.

at angled geometries crossing over a central point. Cyanoacrylate adhesive was applied to stabilize the wires adjacent to the point of cutting. However, even with sharp microscissors, minor hand movements put undue tension on the wires and unintentionally altered relative tip positions **(Figure 6.10)**. Laser cutting could be applied to mitigate tip position alterations, but this avenue was not explored.

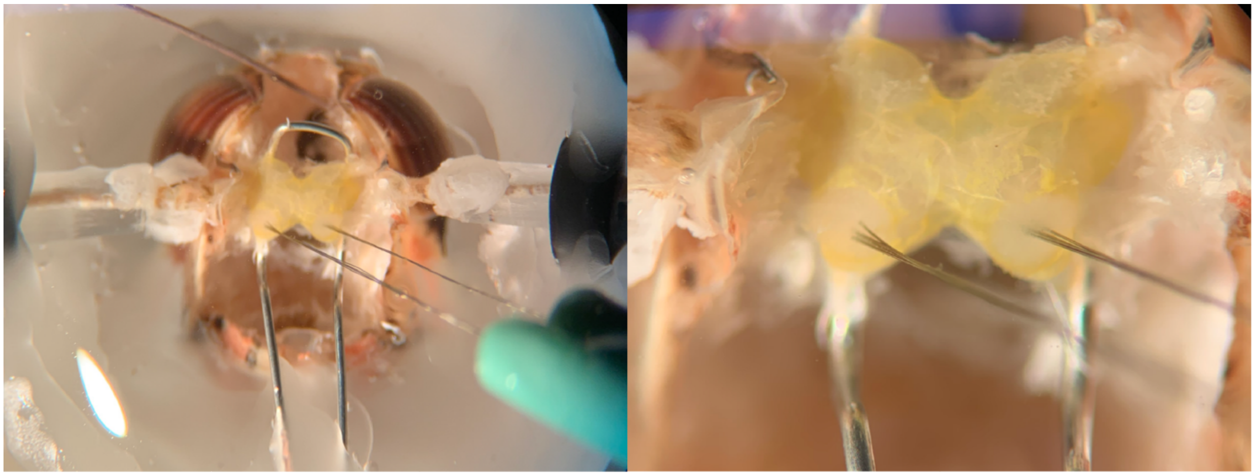

Figure 6.11 | Dual-lobe multi-tetrode device. Both antennal lobes could be targeted at the same time, doubling the number of recording locations and potentially putative spike sorted neurons.

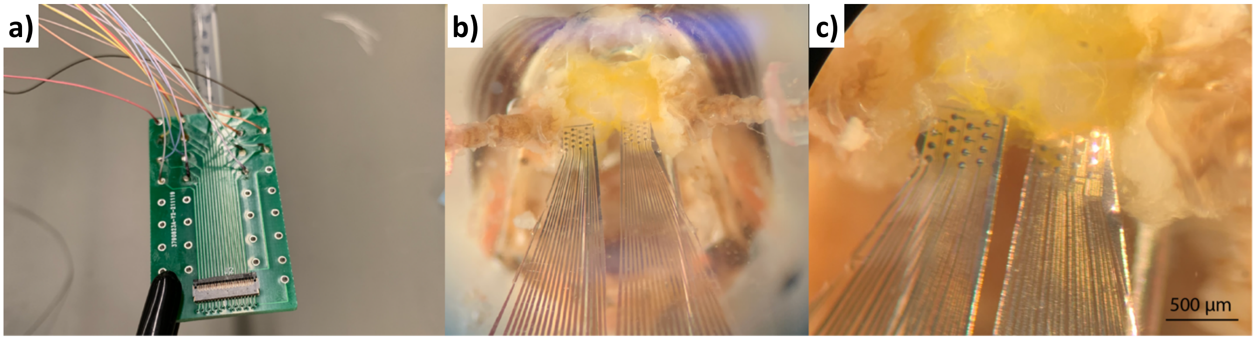

Figure 6.12 | Planar multi-electrode array. Microfabricated flexible surface-level electrode arrays targeting both antennal lobes. **a)** PCB board facilitating electrode connections. **b, c)** Planar array implanted on top of the locust antennal lobe.

In addition to microwire arrays, a planar array device was custom fabricated and tested for in vivo recordings **(Figure 6.12)**. This flexible device was fitted with multiple surface electrodes intended to record from the projection neurons residing in the cortex of the locust antennal lobe. Unfortunately, even with hydrophilic and hydrophobic film applications, the planar array did not adhere to the antennal lobe surface sufficiently. A future microfabricated iteration consists of a foldable device with penetrating electrode shanks **(Figure 6.13)**. Probes can contain a variety of individual electrode channels, however, these have yet to be tested in vivo.

Other electrode modifications could be made to enhance recording capabilities that do not necessitate increasing channel density. Electrochemical etching of the wire tips could reduce the electrode tip footprint, thereby minimizing probe insertion damage. This could potentially increase device longevity and improve signal-to-noise ratios. Alternative electrode wire materials that have enhanced conductivity could be explored. While for the majority of brain implants, the stiffness or young's modulus of a metal ought to be considered, removal of the neural sheath covering the antennal lobe exposes an extremely soft surface. This requires minimal material rigidity for penetration, allowing electrode material selection to optimize electrical properties with little mechanical constraints. We electroplated the wire tips with pure gold for all experiments, but other plating materials, such as carbon nanotubes, that may enhance signal-to-noise ratios may be considered.

Sensor Calibration

Device longevity and sensor calibration are significant concerns for any chemical sensor, especially those incorporating biological componentry. Optical imaging techniques benefit from the topological and functional glomerular conservation observed between individuals within the same species. This allows for the generalization of odor-specific glomerular response profiles across different individuals. For biosensors incorporating electrode-based neuronal signals, it is highly unlikely that electrodes will be positioned at the exact same location in different individuals. Therefore, sensor calibration procedures ought to be performed for each individual based on the encoding state space generated by the electrode array's positioning within the antennal lobe. This sensor initialization process is effective due to the spatiotemporal combinatorial coding scheme implemented by the insect olfactory system. Instead of relying on the identity of individual neurons, distinct neuronal response training templates can be formed from the entire signal population of putative neurons or recorded electrodes. While some variation will be observed between the effectiveness of each individual sensor, ensembles of broadly tuned projection neurons will recognize stimulus-specific features and encode disparate stimuli in unique manners.

Various experimentally derived parameters can be selected for the application at hand. For example, during training template formation, a maximum of 10% overlap could be allowed between population PN responses. Additionally, during the testing phase, a minimum of 80%

classification success rate may be chosen. The tuning of these parameters enables altering the balance between accuracy, precision, and recall, a highly useful ability when implementing the chemical sensor as a screening tool versus a later stage diagnostic to determine disease progression.

The limited system lifetime is offset by significant sensor reversibility, which promotes high sample throughput capabilities. Unlike the substantial processing and recovery times associated with artificial sensors, the insect olfactory system is capable of rapidly binding,

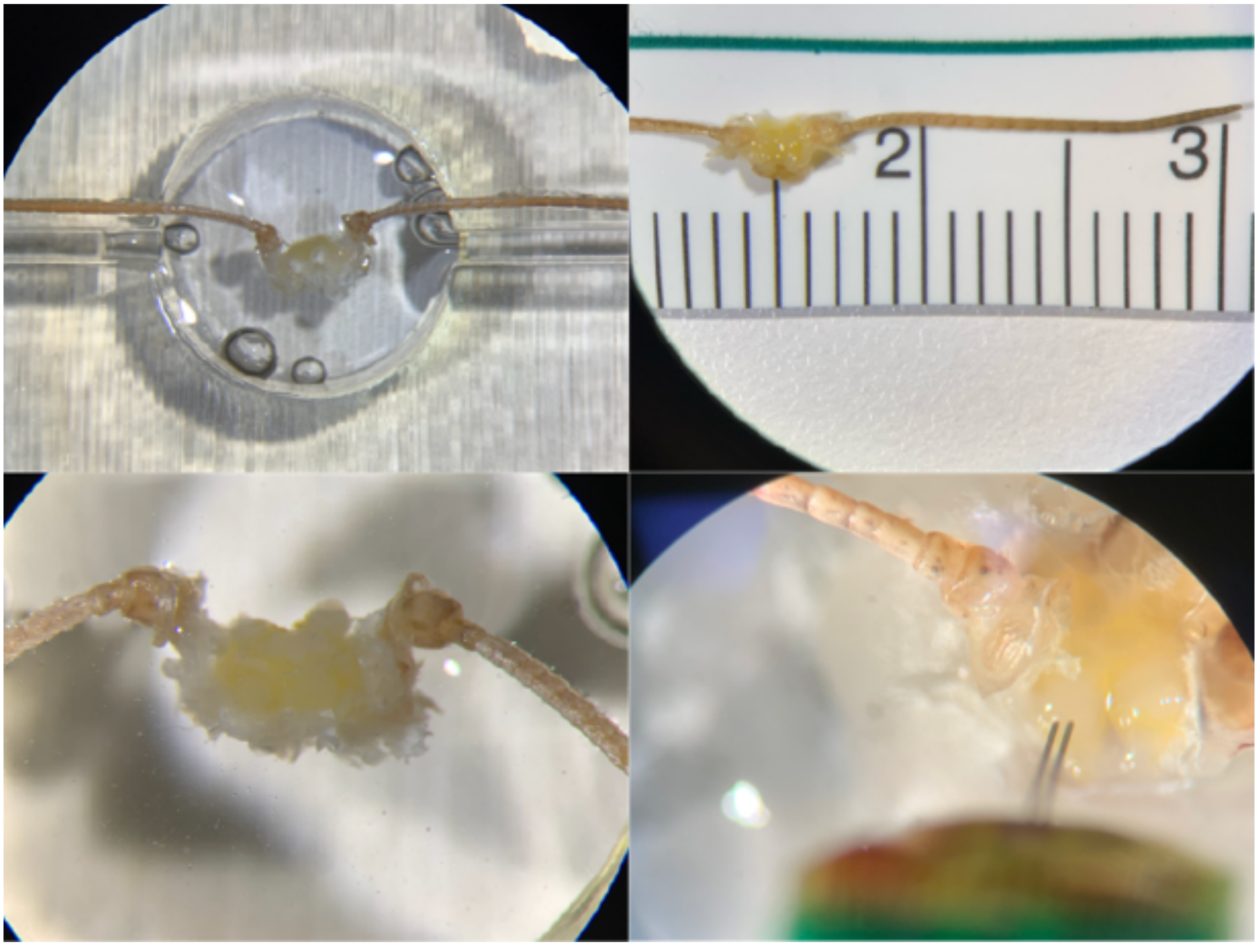

Figure 6.13 | Excised locust antennae and brain. The brain was able to be extracted but significant strain was enforced upon the antennal lobe, corrupting incoming electrical signals.

sensing, and removing odorant molecules. The real-time processing capabilities of this biologically based chemical sensor allows for odorants to be delivered on the second- and minute-timescale. Repeated presentations with such low intervals could serve to substantially increase stimulus encoding and effective discrimination.

Brain-on-a-Chip

In an effort to move towards highly portable devices, we are actively exploring brain-on-a-chip technologies. Essentially, the insect body is unnecessary as long as the antennae neural circuitry remains intact. Efforts to remove the locust antennae and brain as chemical sensors and an

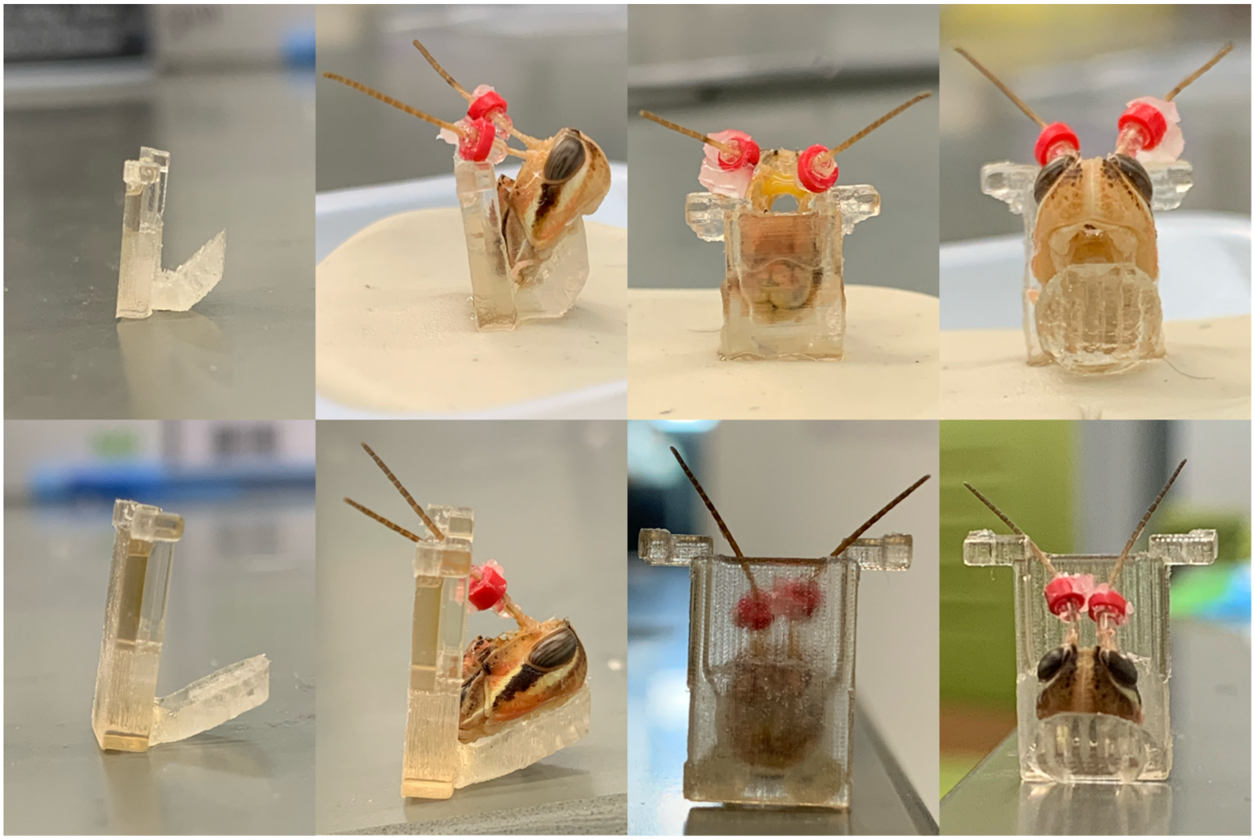

Figure 6.14 | Ex vivo v2. Attempts were made to decapitate the locust and subsequently perform a brain extraction method. The inserts seen above slid into a secondary surgical reservoir filled with locust saline to mitigate tissue desiccation. However, a lack of head stability prevented this technique from being effective.

associated processing unit have been undertaken. Preliminary extraction methods were attempted by performing usual in vivo brain surgery followed by excising the exoskeleton surrounding the antennae and brain. We were able to keep structures intact, but these methods induced considerable damage to the antennal lobe and nerve, thus corrupting signal transmission **(Figure 6.13)**. Other efforts included a decapitation method and subsequent antennae and brain excision in a secondary 3D printed surgical basin **(Figure 6.14)**. Here, however, the structure of the basin complicated surgical accessibility and the locust head did not remain stable during surgery. A third strategy involved designing an entire in vivo surgical platform followed by antennae—brain extraction with particular focus on preserving the integrity of the antennal nerve **(Figure 6.15)**. The device proved to be effective during surgical procedures but attempts to determine whether stable electrophysiological-based recordings can be attained have not yet been conducted.

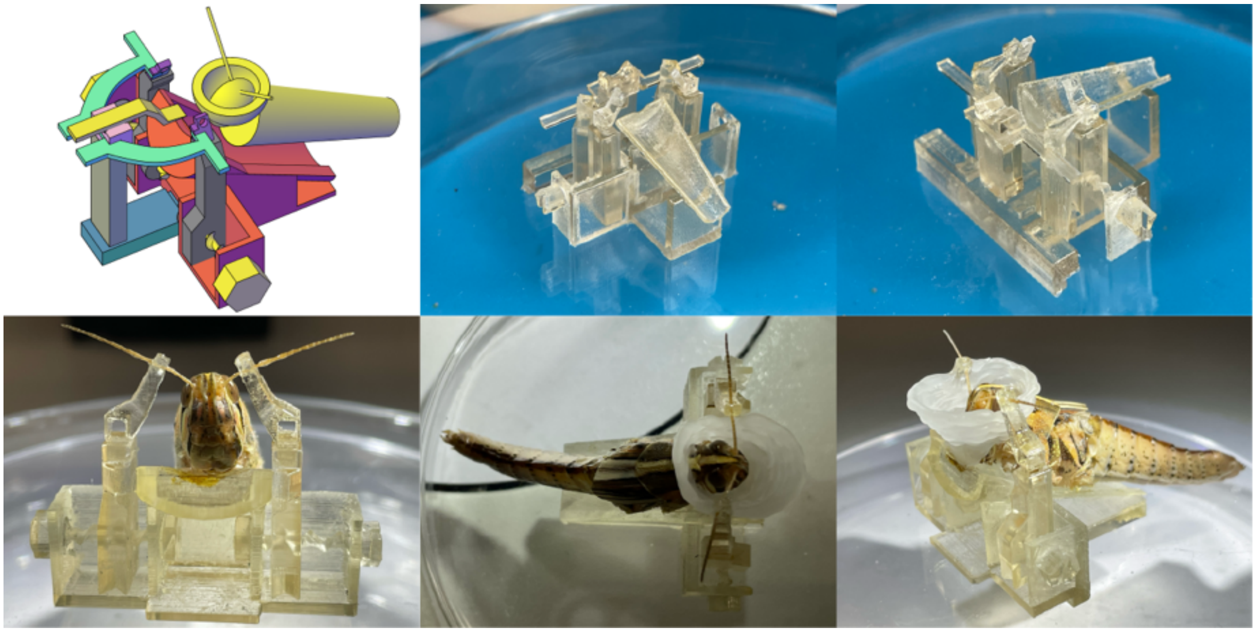

Figure 6.15 | Ex vivo v3. A novel design was cadded and 3D printed. The device performed as expected during the surgical procedure, however brain extraction techniques have not yet been attempted.

In Vivo Diagnostic Validation

Apart from the aforementioned innovations, further research should be conducted incorporating more realistic models to determine the diagnostic feasibility of our insect-based biosensor. Such testing can include 3D cell culture models, volatiles from diseased animal models or preclinical experiments processing breath samples from human patients.

Outlook

Manmade gas sensing technologies are powerful and exhibit a number of positive features. Component-wise methods are integral technologies for exploring the individual analytes of a mixture and for identifying chemical concentrations. In particular, gas chromatography-mass spectrometry is an essential method for laboratory research in a variety of scientific domains. Electronic noses offer rapid sample processing times and high potential for device miniaturization and portability. However, no manmade sensor has demonstrated the impressive chemical sensing capabilities characteristic of biological olfactory systems. We have successfully demonstrated that both locusts and honeybees can be used to detect and differentiate between cancer biomarkers. We believe that using biosensors as chemical sensing devices provides a number of advantages over conventional sensors. While biological olfaction has been lauded for its impressive sensitivity and broad ranging specificity, the development of biosensors as medical diagnostics is an interdisciplinary approach that requires expertise in a number of areas. As related technologies and signal processing algorithms continue to improve, the potential of the field will follow suit. We hope that this research paves the way for future investigations of novel biosensors for disease detection and other practical, real-life applications.

REFERENCES

1. Davis, C., J. Pleil, and J. Beauchamp, *Breathborne biomarkers and the human volatilome.* 2020.

2. Domínguez, R., et al., *A comprehensive review on lipid oxidation in meat and meat products.* Antioxidants, 2019. **8**(10): p. 429.

3. Wilson, A.D. and M. Baietto, *Advances in electronic-nose technologies developed for biomedical applications.* Sensors, 2011. **11**(1): p. 1105-1176.

4. Pavlou, A. and A. Turner, *Sniffing out the truth: clinical diagnosis using the electronic nose.* 2000.

5. Asha, P., et al., *IoT enabled environmental toxicology for air pollution monitoring using AI techniques.* Environmental Research, 2022. **205**: p. 112574.

6. Fan, W. and J. Almirall, *High-efficiency headspace sampling of volatile organic compounds in explosives using capillary microextraction of volatiles (CMV) coupled to gas chromatography–mass spectrometry (GC-MS).* Analytical and bioanalytical chemistry, 2014. **406**(8): p. 2189-2195.

7. Miekisch, W., J.K. Schubert, and G.F. Noeldge-Schomburg, *Diagnostic potential of breath analysis—focus on volatile organic compounds.* Clinica chimica acta, 2004. **347**(1-2): p. 25-39.

8. Dent, A.G., T.G. Sutedja, and P.V. Zimmerman, *Exhaled breath analysis for lung cancer.* Journal of thoracic disease, 2013. **5**(Suppl 5): p. S540.

9. Das, S., S. Pal, and M. Mitra, *Significance of exhaled breath test in clinical diagnosis: a special focus on the detection of diabetes mellitus.* Journal of medical and biological engineering, 2016. **36**(5): p. 605-624.

10. Kim, K.-H., S.A. Jahan, and E. Kabir, *A review of breath analysis for diagnosis of human health.* TrAC Trends in Analytical Chemistry, 2012. **33**: p. 1-8.

11. Porter, R., *The greatest benefit to mankind: a medical history of humanity (the Norton history of science)*. 1999: WW Norton & Company.

12. Hayden, G.F., *Olfactory diagnosis in medicine.* Postgraduate medicine, 1980. **67**(4): p. 110-116.

13. Fitzgerald, F.T. and L.M. Tierney Jr, *The bedside Sherlock Holmes.* Western Journal of Medicine, 1982. **137**(2): p. 169.

14. Kelly, M., *Scent of a patient: an underestimated role in clinical practice?* British Journal of General Practice, 2012. **62**(600): p. 378-378.

15. Buszewski, B., et al., *Human exhaled air analytics: biomarkers of diseases.* Biomedical chromatography, 2007. **21**(6): p. 553-566.

16. Ortega, R., et al., *Monitoring ventilation with capnography.* The New England journal of medicine, 2012. **367**(19): p. e27-e27.

17. Kodali, B.S., *Capnography outside the operating rooms.* The Journal of the American Society of Anesthesiologists, 2013. **118**(1): p. 192-201.

18. Haick, H., et al., *Assessment, origin, and implementation of breath volatile cancer markers.* Chemical Society Reviews, 2014. **43**(5): p. 1423-1449.

19. Nardi-Agmon, I., et al., *Exhaled breath analysis for monitoring response to treatment in advanced lung cancer.* Journal of Thoracic Oncology, 2016. **11**(6): p. 827-837.

20. Taylor, D., et al., *Exhaled nitric oxide measurements: clinical application and interpretation.* Thorax, 2006. **61**(9): p. 817-827.

21. Barnes, P.J., et al., *Exhaled nitric oxide in pulmonary diseases: a comprehensive review.* Chest, 2010. **138**(3): p. 682-692.

22. Dweik, R.A., et al., *An official ATS clinical practice guideline: interpretation of exhaled nitric oxide levels (FENO) for clinical applications.* American journal of respiratory and critical care medicine, 2011. **184**(5): p. 602-615.

23. Smith, A.D., et al., *Diagnosing asthma: comparisons between exhaled nitric oxide measurements and conventional tests.* American journal of respiratory and critical care medicine, 2004. **169**(4): p. 473-478.

24. Owen, O., et al., *Acetone metabolism during diabetic ketoacidosis.* Diabetes, 1982. **31**(3): p. 242-248.

25. Tassopoulos, C., D. Barnett, and T.R. Fraser, *Breath-acetone and blood-sugar measurements in diabetes.* The Lancet, 1969. **293**(7609): p. 1282-1286.

26. Wang, Z. and C. Wang, *Is breath acetone a biomarker of diabetes? A historical review on breath acetone measurements.* Journal of breath research, 2013. **7**(3): p. 037109.

27. Broza, Y.Y. and H. Haick, *Nanomaterial-based sensors for detection of disease by volatile organic compounds.* Nanomedicine, 2013. **8**(5): p. 785-806.

28. Wang, C., A. Mbi, and M. Shepherd, *A study on breath acetone in diabetic patients using a cavity ringdown breath analyzer: exploring correlations of breath acetone with blood glucose and glycohemoglobin A1C.* IEEE Sensors Journal, 2009. **10**(1): p. 54-63.

29. Ruzsányi, V. and M.P. Kalapos, *Breath acetone as a potential marker in clinical practice.* Journal of breath research, 2017. **11**(2): p. 024002.

30. Kneepkens, C.F., G. Lepage, and C.C. Roy, *The potential of the hydrocarbon breath test as a measure of lipid peroxidation.* Free Radical Biology and Medicine, 1994. **17**(2): p. 127-160.

31. Phillips, M., J. Greenberg, and R.N. Cataneo, *Effect of age on the profile of alkanes in normal human breath.* Free radical research, 2000. **33**(1): p. 57-63.

32. Phillips, M., et al., *Effect of age on the breath methylated alkane contour, a display of apparent new markers of oxidative stress.* Journal of Laboratory and Clinical Medicine, 2000. **136**(3): p. 243-249.

33. Risby, T.H. and S.S. Sehnert, *Clinical application of breath biomarkers of oxidative stress status.* Free Radical Biology and Medicine, 1999. **27**(11-12): p. 1182-1192.

34. de Lacy Costello, B., et al., *A review of the volatiles from the healthy human body.* Journal of breath research, 2014. **8**(1): p. 014001.

35. Drabińska, N., et al., *A literature survey of all volatiles from healthy human breath and bodily fluids: the human volatilome.* Journal of breath research, 2021. **15**(3): p. 034001.

36. Phillips, M., et al., *Variation in volatile organic compounds in the breath of normal humans.* Journal of Chromatography B: Biomedical Sciences and Applications, 1999. **729**(1-2): p. 75-88.

37. Alving, K., E. Weitzberg, and J. Lundberg, *Increased amount of nitric oxide in exhaled air of asthmatics.* European Respiratory Journal, 1993. **6**(9): p. 1368-1370.

38. Kharitonov, S., et al., *Increased nitric oxide in exhaled air of asthmatic patients.* The Lancet, 1994. **343**(8890): p. 133-135.

39. Persson, M.G., et al., *Single-breath nitric oxide measurements in asthmatic patients and smokers.* The Lancet, 1994. **343**(8890): p. 146-147.

40. Massaro, A.F., et al., *Expired nitric oxide levels during treatment of acute asthma.* American journal of respiratory and critical care medicine, 1995. **152**(2): p. 800-803.

41. Robbins, R.A., et al., *Measurement of exhaled nitric oxide by three different techniques.* American journal of respiratory and critical care medicine, 1996. **153**(5): p. 1631-1635.

42. Lee, Y., B.K. Oh, and M.E. Meyerhoff, *Improved planar amperometric nitric oxide sensor based on platinized platinum anode. 1. Experimental results and theory when applied for monitoring NO release from diazeniumdiolate-doped polymeric films.* Analytical chemistry, 2004. **76**(3): p. 536-544.

43. Privett, B.J., J.H. Shin, and M.H. Schoenfisch, *Electrochemical nitric oxide sensors for physiological measurements.* Chemical Society Reviews, 2010. **39**(6): p. 1925-1935.

44. Brown, M.D. and M.H. Schoenfisch, *Electrochemical nitric oxide sensors: principles of design and characterization.* Chemical reviews, 2019. **119**(22): p. 11551-11575.

45. Baharuddin, A.A., et al., *Advances in chemiresistive sensors for acetone gas detection.* Materials science in semiconductor processing, 2019. **103**: p. 104616.

46. Diskin, A.M., P. Španěl, and D. Smith, *Time variation of ammonia, acetone, isoprene and ethanol in breath: a quantitative SIFT-MS study over 30 days.* Physiological measurement, 2003. **24**(1): p. 107.

47. Deng, C., et al., *Determination of acetone in human breath by gas chromatography–mass spectrometry and solid-phase microextraction with on-fiber derivatization.* Journal of Chromatography B, 2004. **810**(2): p. 269-275.

48. Hu, J., et al., *Synthesis and gas sensing properties of NiO/SnO2 hierarchical structures toward ppb-level acetone detection.* Materials Research Bulletin, 2018. **102**: p. 294-303.

49. Righettoni, M., A. Tricoli, and S.E. Pratsinis, *Si: WO3 sensors for highly selective detection of acetone for easy diagnosis of diabetes by breath analysis.* Analytical chemistry, 2010. **82**(9): p. 3581-3587.

50. Righettoni, M., et al., *Breath acetone monitoring by portable Si: WO3 gas sensors.* Analytica chimica acta, 2012. **738**: p. 69-75.

51. Li, G., et al., *Bimetal PdAu decorated SnO2 nanosheets based gas sensor with temperature-dependent dual selectivity for detecting formaldehyde and acetone.* Sensors and Actuators B: Chemical, 2019. **283**: p. 590-601.

52. Choi, S.-J., et al., *Selective detection of acetone and hydrogen sulfide for the diagnosis of diabetes and halitosis using SnO2 nanofibers functionalized with reduced graphene oxide nanosheets.* ACS applied materials & interfaces, 2014. **6**(4): p. 2588-2597.

53. Choi, S.-J., et al., *Selective diagnosis of diabetes using Pt-functionalized WO3 hemitube networks as a sensing layer of acetone in exhaled breath.* Analytical chemistry, 2013. **85**(3): p. 1792-1796.

54. Amiri, V., et al., *Nanostructured metal oxide-based acetone gas sensors: A review.* Sensors, 2020. **20**(11): p. 3096.

55. Spichiger-Keller, U.E., *Chemical sensors and biosensors for medical and biological applications*. 2008: John Wiley & Sons.

56. Kharitonov, S., K. Alving, and P. Barnes, *Exhaled and nasal nitric oxide measurements: recommendations. The European Respiratory Society task force.* European Respiratory Journal, 1997. **10**(7): p. 1683-1693.

57. Maziak, W., et al., *Exhaled nitric oxide in chronic obstructive pulmonary disease.* American journal of respiratory and critical care medicine, 1998. **157**(3): p. 998-1002.

58. Pavord, I.D., et al., *Inflammometry to assess airway diseases.* The Lancet, 2008. **372**(9643): p. 1017-1019.

59. Dotsch, J., et al., *Airway nitric oxide in asthmatic children and patients with cystic fibrosis.* European Respiratory Journal, 1996. **9**(12): p. 2537-2540.

60. Das, S. and M. Pal, *Non-invasive monitoring of human health by exhaled breath analysis: A comprehensive review.* Journal of The Electrochemical Society, 2020. **167**(3): p. 037562.

61. Issitt, T., et al., *Volatile compounds in human breath: critical review and meta-analysis.* Journal of Breath Research, 2022.

62. Montuschi, P., et al., *Diagnostic performance of an electronic nose, fractional exhaled nitric oxide, and lung function testing in asthma.* Chest, 2010. **137**(4): p. 790-796.

63. Nelson, N., et al., *Exhaled isoprene and acetone in newborn infants and in children with diabetes mellitus.* Pediatric research, 1998. **44**(3): p. 363-367.

64. Mendis, S., P.A. Sobotka, and D.E. Euler, *Pentane and isoprene in expired air from humans: gas-chromatographic analysis of single breath.* Clinical Chemistry, 1994. **40**(8): p. 1485-1488.

65. Sparkman, O.D., Z. Penton, and F.G. Kitson, *Gas chromatography and mass spectrometry: a practical guide*. 2011: Academic press.

66. Lisec, J., et al., *Gas chromatography mass spectrometry–based metabolite profiling in plants.* Nature protocols, 2006. **1**(1): p. 387-396.

67. Pasikanti, K.K., P. Ho, and E. Chan, *Gas chromatography/mass spectrometry in metabolic profiling of biological fluids.* Journal of Chromatography B, 2008. **871**(2): p. 202-211.

68. Jansson, B. and B. Larsson, *Analysis of organic compounds in human breath by gas chromatography-mass spectrometry.* The Journal of laboratory and clinical medicine, 1969. **74**(6): p. 961-966.

69. Gohlke, R.S., *Time-of-flight mass spectrometry and gas-liquid partition chromatography.* Analytical Chemistry, 1959. **31**(4): p. 535-541.

70. Horning, E. and M. Horning, *Human metabolic profiles obtained by GC and GC/MS.* Journal of Chromatographic Science, 1971. **9**(3): p. 129-140.

71. Horning, E.C. and M.-G. Horning, *Metabolic profiles: gas-phase methods for analysis of metabolites.* Clinical chemistry, 1971. **17**(8): p. 802-809.

72. Zlatkis, A., et al., *Profile of volatile metabolites in urine by gas chromatography-mass spectrometry.* Analytical chemistry, 1973. **45**(4): p. 763-767.

73. Zlatkis, A. and H.M. Liebich, *Profile of volatile metabolites in human urine.* Clinical Chemistry, 1971. **17**(7): p. 592-594.

74. Pauling, L., et al., *Quantitative analysis of urine vapor and breath by gas-liquid partition chromatography.* Proceedings of the National Academy of Sciences, 1971. **68**(10): p. 2374-2376.

75. Hiroshi, K., et al., *Evaluation of volatile sulfur compounds in the expired alveolar gas in patients with liver cirrhosis.* Clinica Chimica Acta, 1978. **85**(3): p. 279-284.

76. Gordon, S., et al., *Volatile organic compounds in exhaled air from patients with lung cancer.* Clinical chemistry, 1985. **31**(8): p. 1278-1282.

77. O'neill, H., et al., *A computerized classification technique for screening for the presence of breath biomarkers in lung cancer.* Clinical chemistry, 1988. **34**(8): p. 1613-1618.

78. Phillips, M., et al., *Volatile organic compounds in breath as markers of lung cancer: a cross-sectional study.* The Lancet, 1999. **353**(9168): p. 1930-1933.

79. Phillips, M., M. Sabas, and J. Greenberg, *Increased pentane and carbon disulfide in the breath of patients with schizophrenia.* Journal of clinical pathology, 1993. **46**(9): p. 861-864.

80. Phillips, M., et al., *Volatile organic compounds in the breath of patients with schizophrenia.* Journal of clinical pathology, 1995. **48**(5): p. 466-469.

81. Pleil, J.D. and A.B. Lindstrom, *Measurement of volatile organic compounds in exhaled breath as collected in evacuated electropolished canisters.* Journal of Chromatography B: Biomedical Sciences and Applications, 1995. **665**(2): p. 271-279.

82. Phillips, M., *Method for the collection and assay of volatile organic compounds in breath.* Analytical biochemistry, 1997. **247**(2): p. 272-278.

83. Grote, C. and J. Pawliszyn, *Solid-phase microextraction for the analysis of human breath.* Analytical chemistry, 1997. **69**(4): p. 587-596.

84. Baltussen, E., C. Cramers, and P. Sandra, *Sorptive sample preparation–a review.* Analytical and bioanalytical chemistry, 2002. **373**(1): p. 3-22.

85. Woolfenden, E., *Optimising analytical performance and extending the application range of thermal desorption for indoor air monitoring.* Indoor and Built Environment, 2001. **10**(3-4): p. 222-231.

86. Henderson, K. and I. Matthews, *Biological monitoring of midwives' exposure to N2O using the Bio-VOC breath sampler.* Journal of Exposure Science & Environmental Epidemiology, 2002. **12**(5): p. 309-312.

87. Poli, D., et al., *Determination of aldehydes in exhaled breath of patients with lung cancer by means of on-fiber-derivatisation SPME–GC/MS.* Journal of Chromatography B, 2010. **878**(27): p. 2643-2651.

88. Gashimova, E., et al., *Investigation of different approaches for exhaled breath and tumor tissue analyses to identify lung cancer biomarkers.* Heliyon, 2020. **6**(6): p. e04224.

89. Schubert, J.K., et al., *CO2-controlled sampling of alveolar gas in mechanically ventilated patients.* Journal of Applied Physiology, 2001. **90**(2): p. 486-492.

90. Miekisch, W., et al., *Impact of sampling procedures on the results of breath analysis.* Journal of breath research, 2008. **2**(2): p. 026007.

91. Horváth, I., et al., *A European Respiratory Society technical standard: exhaled biomarkers in lung disease.* European Respiratory Journal, 2017. **49**(4).

92. Aghdassi, E., et al., *Antioxidant vitamin supplementation in Crohn’s disease decreases oxidative stress: a randomized controlled trial.* The American journal of gastroenterology, 2003. **98**(2): p. 348-353.

93. Van den Velde, S., et al., *GC–MS analysis of breath odor compounds in liver patients.* Journal of Chromatography B, 2008. **875**(2): p. 344-348.

94. Xue, R., et al., *Investigation of volatile biomarkers in liver cancer blood using solid-phase microextraction and gas chromatography/mass spectrometry.* Rapid Communications in Mass Spectrometry: An International Journal Devoted to the Rapid Dissemination of Up-to-the-Minute Research in Mass Spectrometry, 2008. **22**(8): p. 1181-1186.

95. Altomare, D., et al., *Exhaled volatile organic compounds identify patients with colorectal cancer.* Journal of British Surgery, 2013. **100**(1): p. 144-150.

96. Altomare, D.F., et al., *Effects of curative colorectal cancer surgery on exhaled volatile organic compounds and potential implications in clinical follow-up.* Annals of Surgery, 2015. **262**(5): p. 862-867.

97. Altomare, D., et al., *Chemical signature of colorectal cancer: Case–control study for profiling the breath print.* BJS open, 2020. **4**(6): p. 1189-1199.

98. Wang, C., et al., *Volatile organic metabolites identify patients with breast cancer, cyclomastopathy and mammary gland fibroma.* Scientific reports, 2014. **4**(1): p. 1-6.

99. Li, J., et al., *Investigation of potential breath biomarkers for the early diagnosis of breast cancer using gas chromatography–mass spectrometry.* Clinica chimica acta, 2014. **436**: p. 59-67.

100. Phillips, M., et al., *Rapid point-of-care breath test predicts breast cancer and abnormal mammograms in symptomatic women.* MedRxiv, 2020.

101. Xu, Z., et al., *A nanomaterial-based breath test for distinguishing gastric cancer from benign gastric conditions.* British journal of cancer, 2013. **108**(4): p. 941-950.

102. Amal, H., et al., *Detection of precancerous gastric lesions and gastric cancer through exhaled breath.* Gut, 2016. **65**(3): p. 400-407.

103. Chen, Y., et al., *Breath analysis based on surface-enhanced Raman scattering sensors distinguishes early and advanced gastric cancer patients from healthy persons.* ACS nano, 2016. **10**(9): p. 8169-8179.

104. Tong, H., et al., *Volatile organic metabolites identify patients with gastric carcinoma, gastric ulcer, or gastritis and control patients.* Cancer Cell International, 2017. **17**(1): p. 1-9.

105. Mochalski, P., et al., *Ex vivo emission of volatile organic compounds from gastric cancer and non-cancerous tissue.* Journal of breath research, 2018. **12**(4): p. 046005.

106. Gruber, M., et al., *Analysis of exhaled breath for diagnosing head and neck squamous cell carcinoma: a feasibility study.* British journal of cancer, 2014. **111**(4): p. 790-798.

107. García, R.A., et al., *Volatile organic compounds analysis in breath air in healthy volunteers and patients suffering epidermoid laryngeal carcinomas.* Chromatographia, 2014. **77**(5): p. 501-509.

108. Guo, L., et al., *Exhaled breath volatile biomarker analysis for thyroid cancer.* Translational Research, 2015. **166**(2): p. 188-195.

109. Amal, H., et al., *Assessment of ovarian cancer conditions from exhaled breath.* International journal of cancer, 2015. **136**(6): p. E614-E622.

110. Kolk, A., et al., *Breath analysis as a potential diagnostic tool for tuberculosis.* The International Journal of Tuberculosis and Lung Disease, 2012. **16**(6): p. 777-782.

111. Amann, A., et al., *Applications of breath gas analysis in medicine.* International Journal of Mass Spectrometry, 2004. **239**(2-3): p. 227-233.

112. Manolis, A., *The diagnostic potential of breath analysis.* Clinical chemistry, 1983. **29**(1): p. 5-15.

113. Nardi-Agmon, I. and N. Peled, *Exhaled breath analysis for the early detection of lung cancer: recent developments and future prospects.* Lung Cancer: Targets and Therapy, 2017. **8**: p. 31.

114. Nakhleh, M.K., et al., *Diagnosis and classification of 17 diseases from 1404 subjects via pattern analysis of exhaled molecules.* ACS nano, 2017. **11**(1): p. 112-125.

115. Paredi, P., et al., *Exhaled ethane is elevated in cystic fibrosis and correlates with carbon monoxide levels and airway obstruction.* American journal of respiratory and critical care medicine, 2000. **161**(4): p. 1247-1251.

116. Peled, N., et al., *Non-invasive breath analysis of pulmonary nodules.* Journal of Thoracic Oncology, 2012. **7**(10): p. 1528-1533.

117. Capuano, R., et al., *The lung cancer breath signature: a comparative analysis of exhaled breath and air sampled from inside the lungs.* Scientific Reports, 2015. **5**(1): p. 1-10.

118. Lamote, K., et al., *Breath analysis by gas chromatography-mass spectrometry and electronic nose to screen for pleural mesothelioma: a cross-sectional case-control study.* Oncotarget, 2017. **8**(53): p. 91593.

119. Wang, C., et al., *Exhaled volatile organic compounds as lung cancer biomarkers during one-lung ventilation.* Scientific reports, 2014. **4**(1): p. 1-8.

120. Filipiak, W., et al., *Comparative analyses of volatile organic compounds (VOCs) from patients, tumors and transformed cell lines for the validation of lung cancer-derived breath markers.* Journal of breath research, 2014. **8**(2): p. 027111.

121. Corradi, M., et al., *Exhaled breath analysis in suspected cases of non-small-cell lung cancer: a cross-sectional study.* Journal of breath research, 2015. **9**(2): p. 027101.

122. Schallschmidt, K., et al., *Comparison of volatile organic compounds from lung cancer patients and healthy controls—Challenges and limitations of an observational study.* Journal of breath research, 2016. **10**(4): p. 046007.

123. Oguma, T., et al., *Clinical contributions of exhaled volatile organic compounds in the diagnosis of lung cancer.* PloS one, 2017. **12**(4): p. e0174802.

124. Callol-Sanchez, L., et al., *Observation of nonanoic acid and aldehydes in exhaled breath of patients with lung cancer.* Journal of breath research, 2017. **11**(2): p. 026004.

125. Sakumura, Y., et al., *Diagnosis by volatile organic compounds in exhaled breath from lung cancer patients using support vector machine algorithm.* Sensors, 2017. **17**(2): p. 287.

126. Saidi, T., et al., *Non-invasive prediction of lung cancer histological types through exhaled breath analysis by UV-irradiated electronic nose and GC/QTOF/MS.* Sensors and Actuators B: Chemical, 2020. **311**: p. 127932.

127. Koureas, M., et al., *Target analysis of volatile organic compounds in exhaled breath for lung cancer discrimination from other pulmonary diseases and healthy persons.* Metabolites, 2020. **10**(8): p. 317.

128. Di Gilio, A., et al., *Breath analysis for early detection of malignant pleural mesothelioma: volatile organic compounds (VOCs) determination and possible biochemical pathways.* Cancers, 2020. **12**(5): p. 1262.

129. Sponring, A., et al., *Release of volatile organic compounds from the lung cancer cell line NCI-H2087 in vitro.* Anticancer research, 2009. **29**(1): p. 419-426.

130. Filipiak, W., et al., *Release of volatile organic compounds (VOCs) from the lung cancer cell line CALU-1 in vitro.* Cancer cell international, 2008. **8**(1): p. 1-11.

131. Filipiak, W., et al., *TD-GC-MS analysis of volatile metabolites of human lung cancer and normal cells in vitro.* Cancer epidemiology, biomarkers & prevention, 2010. **19**(1): p. 182-195.

132. Deng, C., X. Zhang, and N. Li, *Investigation of volatile biomarkers in lung cancer blood using solid-phase microextraction and capillary gas chromatography–mass spectrometry.* Journal of Chromatography B, 2004. **808**(2): p. 269-277.

133. Ma, H., et al., *Analysis of human breath samples of lung cancer patients and healthy controls with solid-phase microextraction (SPME) and flow-modulated comprehensive two-dimensional gas chromatography (GC× GC).* Analytical Methods, 2014. **6**(17): p. 6841-6849.

134. Barash, O., et al., *Differentiation between genetic mutations of breast cancer by breath volatolomics.* Oncotarget, 2015. **6**(42): p. 44864.

135. Kalluri, U., M. Naiker, and M. Myers, *Cell culture metabolomics in the diagnosis of lung cancer—the influence of cell culture conditions.* Journal of breath research, 2014. **8**(2): p. 027109.

136. Filipiak, W., et al., *A compendium of volatile organic compounds (VOCs) released by human cell lines.* Current medicinal chemistry, 2016. **23**(20): p. 2112-2131.

137. Sponring, A., et al., *Analysis of volatile organic compounds (VOCs) in the headspace of NCI-H1666 lung cancer cells.* Cancer Biomarkers, 2010. **7**(3): p. 153-161.

138. Barash, O., et al., *Classification of lung cancer histology by gold nanoparticle sensors.* Nanomedicine: Nanotechnology, Biology and Medicine, 2012. **8**(5): p. 580-589.

139. Rutter, A.V., et al., *Quantification by SIFT-MS of acetaldehyde released by lung cells in a 3D model.* Analyst, 2013. **138**(1): p. 91-95.

140. Peled, N., et al., *Volatile fingerprints of cancer specific genetic mutations.* Nanomedicine: Nanotechnology, Biology and Medicine, 2013. **9**(6): p. 758-766.

141. Davies, M., et al., *Unique volatolomic signatures of TP53 and KRAS in lung cells.* British journal of cancer, 2014. **111**(6): p. 1213-1221.

142. Schallschmidt, K., et al., *Investigation of cell culture volatilomes using solid phase micro extraction: Options and pitfalls exemplified with adenocarcinoma cell lines.* Journal of chromatography B, 2015. **1006**: p. 158-166.

143. Thriumani, R., et al., *A Study on VOCs Released by Lung Cancer Cell Line Using GCMS-SPME.* Procedia Chemistry, 2016. **20**: p. 1-7.

144. Jia, Z., et al., *Detection of lung cancer: concomitant volatile organic compounds and metabolomic profiling of six cancer cell lines of different histological origins.* ACS omega, 2018. **3**(5): p. 5131-5140.

145. Thriumani, R., et al., *A study on volatile organic compounds emitted by in-vitro lung cancer cultured cells using gas sensor array and SPME-GCMS.* BMC cancer, 2018. **18**(1): p. 1-17.

146. Janssens, E., J.P. van Meerbeeck, and K. Lamote, *Volatile organic compounds in human matrices as lung cancer biomarkers: a systematic review.* Critical Reviews in Oncology/Hematology, 2020. **153**: p. 103037.

147. Janssens, E., et al., *Headspace Volatile Organic Compound Profiling of Pleural Mesothelioma and Lung Cancer Cell Lines as Translational Bridge for Breath Research.* Frontiers in Oncology, 2022. **12**.

148. Huang, J., et al., *Selected ion flow tube mass spectrometry analysis of volatile metabolites in urine headspace for the profiling of gastro-esophageal cancer.* Analytical Chemistry, 2013. **85**(6): p. 3409-3416.

149. He, J., et al., *Fingerprinting breast cancer vs. normal mammary cells by mass spectrometric analysis of volatiles.* Scientific reports, 2014. **4**(1): p. 1-6.

150. Lavra, L., et al., *Investigation of VOCs associated with different characteristics of breast cancer cells.* Scientific reports, 2015. **5**(1): p. 1-12.

151. Silva, C.L., et al., *Volatile metabolomic signature of human breast cancer cell lines.* Scientific reports, 2017. **7**(1): p. 1-8.

152. Tang, H., et al., *Determination of volatile organic compounds exhaled by cell lines derived from hematological malignancies.* Bioscience reports, 2017. **37**(3).

153. Forleo, A., et al. *Evaluation of the volatile organic compounds released from peripheral blood mononuclear cells and THP1 cells under normal and proinflammatory conditions*. in *AISEM Annual Conference on Sensors and Microsystems*. 2017. Springer.

154. Amal, H., et al., *The scent fingerprint of hepatocarcinoma: in-vitro metastasis prediction with volatile organic compounds (VOCs).* International journal of nanomedicine, 2012. **7**: p. 4135.

155. Mochalski, P., et al., *Release and uptake of volatile organic compounds by human hepatocellular carcinoma cells (HepG2) in vitro.* Cancer cell international, 2013. **13**(1): p. 1-9.

156. Lima, A.R., et al., *Discrimination between the human prostate normal and cancer cell exometabolome by GC-MS.* Scientific Reports, 2018. **8**(1): p. 1-12.

157. Phillips, M., et al., *Prediction of lung cancer using volatile biomarkers in breath.* Cancer biomarkers, 2007. **3**(2): p. 95-109.

158. Phillips, M., et al., *Detection of lung cancer with volatile markers in the breath.* Chest, 2003. **123**(6): p. 2115-2123.

159. Phillips, M., et al., *Blinded validation of breath biomarkers of lung cancer, a potential ancillary to chest CT screening.* PLoS One, 2015. **10**(12): p. e0142484.

160. McCunney, R.J. and J. Li, *Radiation risks in lung cancer screening programs.* Chest, 2014. **145**(3): p. 618-624.

161. Maziak, D.E., et al., *Positron emission tomography in staging early lung cancer: a randomized trial.* Annals of internal medicine, 2009. **151**(4): p. 221-228.

162. Vansteenkiste, J., et al., *Screening and early—detection of lung cancer.* Annals of Oncology, 2012. **23**: p. x320-x327.

163. van Klaveren, R.J., et al., *Management of lung nodules detected by volume CT scanning.* New England Journal of Medicine, 2009. **361**(23): p. 2221-2229.

164. Fang, M., et al., *Thermal degradation of small molecules: a global metabolomic investigation.* Analytical chemistry, 2015. **87**(21): p. 10935-10941.

165. Hauschild, A.-C., J.I. Baumbach, and J. Baumbach, *Integrated statistical learning of metabolic ion mobility spectrometry profiles for pulmonary disease identification.* Genet. Mol. Res, 2012. **11**(3): p. 2733-2744.

166. Westhoff, M., et al., *Differentiation of chronic obstructive pulmonary disease (COPD) including lung cancer from healthy control group by breath analysis using ion mobility spectrometry.* International Journal for Ion Mobility Spectrometry, 2010. **13**(3): p. 131-139.

167. Basanta, M., et al., *Non-invasive metabolomic analysis of breath using differential mobility spectrometry in patients with chronic obstructive pulmonary disease and healthy smokers.* Analyst, 2010. **135**(2): p. 315-320.

168. Borsdorf, H. and G.A. Eiceman, *Ion mobility spectrometry: principles and applications.* Applied Spectroscopy Reviews, 2006. **41**(4): p. 323-375.

169. Fernández-Maestre, R., *Ion mobility spectrometry: history, characteristics and applications.* Revista UDCA Actualidad & Divulgación Científica, 2012. **15**(2): p. 467-479.

170. Merenbloom, S.I., et al., *High-resolution ion cyclotron mobility spectrometry.* Analytical chemistry, 2009. **81**(4): p. 1482-1487.

171. Eiceman, G.A. and Z. Karpas, *Ion mobility spectrometry*. 2005: CRC press.

172. Cumeras, R., et al., *Review on ion mobility spectrometry. Part 1: current instrumentation.* Analyst, 2015. **140**(5): p. 1376-1390.

173. Covington, J., et al., *The application of FAIMS gas analysis in medical diagnostics.* Analyst, 2015. **140**(20): p. 6775-6781.

174. Kalkan, Y., et al., *Cluster ions in gas-based detectors.* Journal of Instrumentation, 2015. **10**(07): p. P07004.

175. Ruzsanyi, V., et al., *Detection of human metabolites using multi-capillary columns coupled to ion mobility spectrometers.* Journal of Chromatography A, 2005. **1084**(1-2): p. 145-151.

176. Fink, T., J.I. Baumbach, and S. Kreuer, *Ion mobility spectrometry in breath research.* Journal of breath research, 2014. **8**(2): p. 027104.

177. Westhoff, M., et al., *Ion mobility spectrometry: a new method for the detection of lung cancer and airway infection in exhaled air? First results of a pilot study.* Chest, 2005. **128**(4): p. 155S.

178. Baumbach, J. and M. Westhoff, *Ion mobility spectrometry to detect lung cancer and airway infections.* Spectroscopy Europe, 2006. **18**(6): p. 22-27.

179. Darwiche, K., et al., *Bronchoscopically obtained volatile biomarkers in lung cancer.* Lung, 2011. **189**(6): p. 445-452.

180. Baumbach, J., et al., *Significant different volatile biomarker during bronchoscopic ion mobility spectrometry investigation of patients suffering lung carcinoma.* International Journal for Ion Mobility Spectrometry, 2011. **14**(4): p. 159-166.

181. Bessa, V., et al., *Detection of volatile organic compounds (VOCs) in exhaled breath of patients with chronic obstructive pulmonary disease (COPD) by ion mobility spectrometry.* International Journal for Ion Mobility Spectrometry, 2011. **14**(1): p. 7-13.

182. Westhoff, M., et al., *Statistical and bioinformatical methods to differentiate chronic obstructive pulmonary disease (COPD) including lung cancer from healthy control by breath analysis using ion mobility spectrometry.* International Journal for Ion Mobility Spectrometry, 2011. **14**(4): p. 139-149.

183. Rabis, T., et al., *Detection of infectious agents in the airways by ion mobility spectrometry of exhaled breath.* International Journal for Ion Mobility Spectrometry, 2011. **14**(4): p. 187-195.

184. Maddula, S., et al., *Correlation analysis on data sets to detect infectious agents in the airways by ion mobility spectrometry of exhaled breath.* International Journal for Ion Mobility Spectrometry, 2011. **14**(4): p. 197-206.

185. Pagonas, N., et al., *Volatile organic compounds in uremia.* 2012.

186. Furtwängler, R., et al., *Signals of neutropenia in human breath?* International journal for ion mobility spectrometry, 2014. **17**(1): p. 19-23.

187. Bunkowski, A., et al., *MCC/IMS signals in human breath related to sarcoidosis—results of a feasibility study using an automated peak finding procedure.* Journal of Breath Research, 2009. **3**(4): p. 046001.

188. Koczulla, R., et al., *MCC/IMS as potential noninvasive technique in the diagnosis of patients with COPD with and without alpha 1-antitrypsin deficiency.* International Journal for Ion Mobility Spectrometry, 2011. **14**(4): p. 177-185.

189. Arasaradnam, R.P., et al., *Detection of colorectal cancer (CRC) by urinary volatile organic compound analysis.* PloS one, 2014. **9**(9): p. e108750.

190. Niemi, R.J., et al., *FAIMS analysis of urine gaseous headspace is capable of differentiating ovarian cancer.* Gynecologic Oncology, 2018. **151**(3): p. 519-524.

191. Arasaradnam, R.P., et al., *Noninvasive diagnosis of pancreatic cancer through detection of volatile organic compounds in urine.* Gastroenterology, 2018. **154**(3): p. 485-487. e1.

192. Westhoff, M., et al., *Ion mobility spectrometry for the detection of volatile organic compounds in exhaled breath of patients with lung cancer: results of a pilot study.* Thorax, 2009. **64**(9): p. 744-748.

193. Miekisch, W. and J.K. Schubert, *From highly sophisticated analytical techniques to life-saving diagnostics: Technical developments in breath analysis.* TrAC Trends in Analytical Chemistry, 2006. **25**(7): p. 665-673.

194. Costanzo, M.T., et al., *Portable FAIMS: Applications and future perspectives.* International journal of mass spectrometry, 2017. **422**: p. 188-196.

195. Vautz, W., et al., *Breath analysis—performance and potential of ion mobility spectrometry.* Journal of breath research, 2009. **3**(3): p. 036004.

196. Neri, G., et al., *Real-time monitoring of breath ammonia during haemodialysis: use of ion mobility spectrometry (IMS) and cavity ring-down spectroscopy (CRDS) techniques.* Nephrology Dialysis Transplantation, 2012. **27**(7): p. 2945-2952.

197. Vautz, W., et al., *On the potential of ion mobility spectrometry coupled to GC pre-separation–A tutorial.* Analytica chimica acta, 2018. **1024**: p. 52-64.

198. Vautz, W., S. Sielemann, and J.I. Baumbach, *Determination of terpenes in humid ambient air using ultraviolet ion mobility spectrometry.* Analytica Chimica Acta, 2004. **513**(2): p. 393-399.

199. Vautz, W., et al., *Sensitive ion mobility spectrometry of humid ambient air using 10.6 eV UV-IMS.* Int. J. Ion Mobility Spectrom, 2004. **7**(3).

200. Dummer, J., et al., *Analysis of biogenic volatile organic compounds in human health and disease.* TrAC Trends in Analytical Chemistry, 2011. **30**(7): p. 960-967.

201. Baumbach, J.I., *Ion mobility spectrometry coupled with multi-capillary columns for metabolic profiling of human breath.* Journal of breath research, 2009. **3**(3): p. 034001.

202. Kirk, A.T., et al., *Ultra-high-resolution ion mobility spectrometry—current instrumentation, limitations, and future developments.* Analytical and bioanalytical chemistry, 2019. **411**(24): p. 6229-6246.

203. Thaler, E.R. and C.W. Hanson, *Medical applications of electronic nose technology.* Expert review of medical devices, 2005. **2**(5): p. 559-566.

204. Turner, A.P. and N. Magan, *Electronic noses and disease diagnostics.* Nature Reviews Microbiology, 2004. **2**(2): p. 161-166.

205. Jia, Z., et al., *Critical review of volatile organic compound analysis in breath and in vitro cell culture for detection of lung cancer.* Metabolites, 2019. **9**(3): p. 52.

206. Amal, H. and H. Haick, *Point of care breath analysis systems*, in *Advanced Nanomaterials for Inexpensive Gas Microsensors*. 2020, Elsevier. p. 315-334.

207. Konvalina, G. and H. Haick, *Sensors for breath testing: from nanomaterials to comprehensive disease detection.* Accounts of chemical research, 2014. **47**(1): p. 66-76.

208. Guntner, A.T., et al., *Breath sensors for health monitoring.* ACS sensors, 2019. **4**(2): p. 268-280.

209. Cellini, A., et al., *Potential applications and limitations of electronic nose devices for plant disease diagnosis.* Sensors, 2017. **17**(11): p. 2596.

210. Persaud, K. and G. Dodd, *Analysis of discrimination mechanisms in the mammalian olfactory system using a model nose.* Nature, 1982. **299**(5881): p. 352-355.

211. Berna, A., *Metal oxide sensors for electronic noses and their application to food analysis.* Sensors, 2010. **10**(4): p. 3882-3910.

212. Kononov, A., et al., *Online breath analysis using metal oxide semiconductor sensors (electronic nose) for diagnosis of lung cancer.* Journal of breath research, 2019. **14**(1): p. 016004.

213. Blatt, R., et al. *Lung cancer identification by an electronic nose based on an array of MOS sensors*. in *2007 International joint conference on neural networks*. 2007. IEEE.

214. van Hooren, M.R., et al., *Differentiating head and neck carcinoma from lung carcinoma with an electronic nose: a proof of concept study.* European Archives of Oto-Rhino-Laryngology, 2016. **273**(11): p. 3897-3903.

215. Kort, S., et al., *Multi-centre prospective study on diagnosing subtypes of lung cancer by exhaled-breath analysis.* Lung Cancer, 2018. **125**: p. 223-229.

216. Van de Goor, R., et al., *Training and validating a portable electronic nose for lung cancer screening.* Journal of Thoracic Oncology, 2018. **13**(5): p. 676-681.

217. De Vries, R., et al., *Integration of electronic nose technology with spirometry: validation of a new approach for exhaled breath analysis.* Journal of breath research, 2015. **9**(4): p. 046001.

218. Marzorati, D., et al. *A Metal Oxide Gas Sensors Array for Lung Cancer Diagnosis Through Exhaled Breath Analysis*. in *2019 41st Annual International Conference of the IEEE Engineering in Medicine and Biology Society (EMBC)*. 2019. IEEE.

219. Leunis, N., et al., *Application of an electronic nose in the diagnosis of head and neck cancer.* The Laryngoscope, 2014. **124**(6): p. 1377-1381.

220. Van De Goor, R., et al., *Feasibility of electronic nose technology for discriminating between head and neck, bladder, and colon carcinomas.* European Archives of Oto-Rhino-Laryngology, 2017. **274**(2): p. 1053-1060.

221. van de Goor, R.M., et al., *Detecting recurrent head and neck cancer using electronic nose technology: a feasibility study.* Head & Neck, 2019. **41**(9): p. 2983-2990.

222. Schuermans, V.N., et al., *Pilot study: detection of gastric cancer from exhaled air analyzed with an electronic nose in Chinese patients.* Surgical innovation, 2018. **25**(5): p. 429-434.

223. Roine, A., et al., *Detection of prostate cancer by an electronic nose: a proof of principle study.* The Journal of urology, 2014. **192**(1): p. 230-235.

224. Waltman, C.G., T.A. Marcelissen, and J.G. van Roermund, *Exhaled-breath testing for prostate cancer based on volatile organic compound profiling using an electronic nose device (Aeonose™): a preliminary report.* European urology focus, 2020. **6**(6): p. 1220-1225.

225. Horvath, G., J. Chilo, and T. Lindblad, *Different volatile signals emitted by human ovarian carcinoma and healthy tissue.* Future Oncology, 2010. **6**(6): p. 1043-1049.

226. Weber, C.M., et al., *Evaluation of a gas sensor array and pattern recognition for the identification of bladder cancer from urine headspace.* Analyst, 2011. **136**(2): p. 359-364.

227. Horstmann, M., et al., *PD25-03 an electronic nose system detects bladder cancer in urine specimen: First results of a pilot study.* The Journal of Urology, 2015. **193**(4S): p. e560-e561.

228. Guo, D., et al., *A novel breath analysis system based on electronic olfaction.* IEEE transactions on biomedical engineering, 2010. **57**(11): p. 2753-2763.

229. Ping, W., et al., *A novel method for diabetes diagnosis based on electronic nose.* Biosensors and bioelectronics, 1997. **12**(9-10): p. 1031-1036.

230. Voss, A., et al., *Smelling renal dysfunction via electronic nose.* Annals of biomedical engineering, 2005. **33**(5): p. 656-660.

231. Baldini, C., et al., *Electronic nose as a novel method for diagnosing cancer: a systematic review.* Biosensors, 2020. **10**(8): p. 84.

232. Schaller, E., J.O. Bosset, and F. Escher, *'Electronic noses' and their application to food.* LWT-Food Science and Technology, 1998. **31**(4): p. 305-316.

233. Lewis, N.S., *Comparisons between mammalian and artificial olfaction based on arrays of carbon black− polymer composite vapor detectors.* Accounts of chemical research, 2004. **37**(9): p. 663-672.

234. Wilson, A.D. and M. Baietto, *Applications and advances in electronic-nose technologies.* Sensors, 2009. **9**(7): p. 5099-5148.

235. Machado, R.F., et al., *Detection of lung cancer by sensor array analyses of exhaled breath.* American journal of respiratory and critical care medicine, 2005. **171**(11): p. 1286-1291.

236. Tirzīte, M., et al., *Detection of lung cancer in exhaled breath with an electronic nose using support vector machine analysis.* Journal of breath research, 2017. **11**(3): p. 036009.

237. Tirzïte, M., et al., *Detection of lung cancer with electronic nose and logistic regression analysis.* Journal of breath research, 2018. **13**(1): p. 016006.

238. Dragonieri, S., et al., *An electronic nose in the discrimination of patients with non-small cell lung cancer and COPD.* Lung cancer, 2009. **64**(2): p. 166-170.

239. de Meij, T.G., et al., *Electronic nose can discriminate colorectal carcinoma and advanced adenomas by fecal volatile biomarker analysis: proof of principle study.* International journal of cancer, 2014. **134**(5): p. 1132-1138.

240. Chapman, E.A., et al., *A breath test for malignant mesothelioma using an electronic nose.* European Respiratory Journal, 2012. **40**(2): p. 448-454.

241. Dragonieri, S., et al., *An electronic nose distinguishes exhaled breath of patients with Malignant Pleural Mesothelioma from controls.* Lung cancer, 2012. **75**(3): p. 326-331.

242. Bikov, A., et al., *Expiratory flow rate, breath hold and anatomic dead space influence electronic nose ability to detect lung cancer.* BMC pulmonary medicine, 2014. **14**(1): p. 1-9.

243. Hubers, A.J., et al., *Combined sputum hypermethylation and eNose analysis for lung cancer diagnosis.* Journal of Clinical Pathology, 2014. **67**(8): p. 707-711.

244. McWilliams, A., et al., *Sex and smoking status effects on the early detection of early lung cancer in high-risk smokers using an electronic nose.* IEEE Transactions on Biomedical Engineering, 2015. **62**(8): p. 2044-2054.

245. Yu, J.-B., et al., *Analysis of diabetic patient's breath with conducting polymer sensor array.* Sensors and Actuators B: Chemical, 2005. **108**(1-2): p. 305-308.

246. Fend, R., et al., *Monitoring haemodialysis using electronic nose and chemometrics.* Biosensors and Bioelectronics, 2004. **19**(12): p. 1581-1590.

247. Fens, N., et al., *Exhaled breath profiling enables discrimination of chronic obstructive pulmonary disease and asthma.* American journal of respiratory and critical care medicine, 2009. **180**(11): p. 1076-1082.

248. Dragonieri, S., et al., *An electronic nose in the discrimination of patients with asthma and controls.* Journal of allergy and clinical immunology, 2007. **120**(4): p. 856-862.

249. Di Natale, C., et al., *Lung cancer identification by the analysis of breath by means of an array of non-selective gas sensors.* Biosensors and Bioelectronics, 2003. **18**(10): p. 1209-1218.

250. D'Amico, A., et al., *An investigation on electronic nose diagnosis of lung cancer.* Lung cancer, 2010. **68**(2): p. 170-176.

251. Santonico, M., et al., *In situ detection of lung cancer volatile fingerprints using bronchoscopic air-sampling.* Lung cancer, 2012. **77**(1): p. 46-50.

252. Gasparri, R., et al., *Volatile signature for the early diagnosis of lung cancer.* Journal of breath research, 2016. **10**(1): p. 016007.

253. Di Natale, C., R. Paolesse, and A. D'Amico, *Metalloporphyrins based artificial olfactory receptors.* Sensors and Actuators B: Chemical, 2007. **121**(1): p. 238-246.

254. Bernabei, M., et al., *A preliminary study on the possibility to diagnose urinary tract cancers by an electronic nose.* Sensors and Actuators B: Chemical, 2008. **131**(1): p. 1-4.

255. D'Amico, A., et al., *A novel approach for prostate cancer diagnosis using a gas sensor array.* Procedia Engineering, 2012. **47**: p. 1113-1116.

256. Asimakopoulos, A., et al., *Prostate cancer diagnosis through electronic nose in the urine headspace setting: a pilot study.* Prostate cancer and prostatic diseases, 2014. **17**(2): p. 206-211.

257. Santonico, M., et al., *Chemical sensors for prostate cancer detection oriented to non-invasive approach.* Procedia Engineering, 2014. **87**: p. 320-323.

258. D'amico, A., et al., *Identification of melanoma with a gas sensor array.* Skin Research and Technology, 2008. **14**(2): p. 226-236.

259. Lin, Y.-J., et al., *Application of the electronic nose for uremia diagnosis.* Sensors and Actuators B: Chemical, 2001. **76**(1-3): p. 177-180.

260. Di Natale, C., et al., *Electronic nose analysis of urine samples containing blood.* Physiological Measurement, 1999. **20**(4): p. 377.

261. Haick, H., *Chemical sensors based on molecularly modified metallic nanoparticles.* Journal of Physics D: Applied Physics, 2007. **40**(23): p. 7173.

262. Tisch, U. and H. Haick, *Nanomaterials for cross-reactive sensor arrays.* MRS bulletin, 2010. **35**(10): p. 797-803.

263. Peng, G., et al., *Diagnosing lung cancer in exhaled breath using gold nanoparticles.* Nature Nanotechnology, 2009. **4**(10): p. 669-673.

264. Hakim, M., et al., *Diagnosis of head-and-neck cancer from exhaled breath.* British journal of cancer, 2011. **104**(10): p. 1649-1655.

265. Peng, G., et al., *Detection of lung, breast, colorectal, and prostate cancers from exhaled breath using a single array of nanosensors.* British journal of cancer, 2010. **103**(4): p. 542-551.

266. Barash, O., et al., *Sniffing the Unique "Odor Print" of Non-Small-Cell Lung Cancer with Gold Nanoparticles.* Small, 2009. **5**(22): p. 2618-2624.

267. Shuster, G., et al., *Classification of breast cancer precursors through exhaled breath.* Breast cancer research and treatment, 2011. **126**(3): p. 791-796.

268. Wang, B., et al., *Artificial sensing intelligence with silicon nanowires for ultraselective detection in the gas phase.* Nano letters, 2014. **14**(2): p. 933-938.

269. Shehada, N., et al., *Ultrasensitive silicon nanowire for real-world gas sensing: noninvasive diagnosis of cancer from breath volatolome.* Nano letters, 2015. **15**(2): p. 1288-1295.

270. Zilberman, Y., et al., *Carbon nanotube/hexa-peri-hexabenzocoronene bilayers for discrimination between nonpolar volatile organic compounds of cancer and humid atmospheres.* Advanced Materials, 2010. **22**(38): p. 4317-4320.

271. Zilberman, Y., et al., *Nanoarray of polycyclic aromatic hydrocarbons and carbon nanotubes for accurate and predictive detection in real-world environmental humidity.* ACS nano, 2011. **5**(8): p. 6743-6753.

272. Peng, G., E. Trock, and H. Haick, *Detecting simulated patterns of lung cancer biomarkers by random network of single-walled carbon nanotubes coated with nonpolymeric organic materials.* Nano letters, 2008. **8**(11): p. 3631-3635.

273. Zhang, Y., et al., *Identification of volatile biomarkers of gastric cancer cells and ultrasensitive electrochemical detection based on sensing interface of Au-Ag alloy coated MWCNTs.* Theranostics, 2014. **4**(2): p. 154.

274. Marom, O., et al., *Gold nanoparticle sensors for detecting chronic kidney disease and disease progression.* Nanomedicine, 2012. **7**(5): p. 639-650.

275. Nakhleh, M.K., et al., *Detecting active pulmonary tuberculosis with a breath test using nanomaterial-based sensors.* European Respiratory Journal, 2014. **43**(5): p. 1522-1525.

276. Haick, H., et al., *Sniffing chronic renal failure in rat model by an array of random networks of single-walled carbon nanotubes.* ACS nano, 2009. **3**(5): p. 1258-1266.

277. Ionescu, R., et al., *Detection of multiple sclerosis from exhaled breath using bilayers of polycyclic aromatic hydrocarbons and single-wall carbon nanotubes.* ACS Chemical Neuroscience, 2011. **2**(12): p. 687-693.

278. Gardner, J., et al., *The prediction of bacteria type and culture growth phase by an electronic nose with a multi-layer perceptron network.* Measurement Science and Technology, 1998. **9**(1): p. 120.

279. Holmberg, M., et al., *Bacteria classification based on feature extraction from sensor data.* Biotechnology techniques, 1998. **12**(4): p. 319-324.

280. Pavlou, A.K., et al., *An intelligent rapid odour recognition model in discrimination of Helicobacter pylori and other gastroesophageal isolates in vitro.* Biosensors and Bioelectronics, 2000. **15**(7-8): p. 333-342.

281. Lai, S.Y., et al., *Identification of upper respiratory bacterial pathogens with the electronic nose.* The Laryngoscope, 2002. **112**(6): p. 975-979.

282. Pavlou, A., A. Turner, and N. Magan, *Recognition of anaerobic bacterial isolates in vitro using electronic nose technology.* Letters in applied microbiology, 2002. **35**(5): p. 366-369.

283. Pavlou, A.K., et al., *Detection of Mycobacterium tuberculosis (TB) in vitro and in situ using an electronic nose in combination with a neural network system.* Biosensors and Bioelectronics, 2004. **20**(3): p. 538-544.

284. Lykos, P., et al., *Rapid detection of bacteria from blood culture by an electronic nose.* Journal of Microbiology, 2001. **39**(3): p. 213-218.

285. Gibson, T., et al., *Detection and simultaneous identification of microorganisms from headspace samples using an electronic nose.* Sensors and Actuators B: Chemical, 1997. **44**(1-3): p. 413-422.

286. Fend, R., et al., *Prospects for clinical application of electronic-nose technology to early detection of Mycobacterium tuberculosis in culture and sputum.* Journal of Clinical Microbiology, 2006. **44**(6): p. 2039-2045.

287. Dutta, R., et al., *Bacteria classification using Cyranose 320 electronic nose.* Biomedical engineering online, 2002. **1**(1): p. 1-7.

288. Bruins, M., et al., *Device-independent, real-time identification of bacterial pathogens with a metal oxide-based olfactory sensor.* European journal of clinical microbiology & infectious diseases, 2009. **28**(7): p. 775-780.

289. Wilson, A.D., D. Lester, and C. Oberle, *Development of conductive polymer analysis for the rapid detection and identification of phytopathogenic microbes.* Phytopathology, 2004. **94**(5): p. 419-431.

290. Siripatrawan, U., *Rapid differentiation between E. coli and Salmonella typhimurium using metal oxide sensors integrated with pattern recognition.* Sensors and Actuators B: Chemical, 2008. **133**(2): p. 414-419.

291. Roine, A., et al., *Rapid and accurate detection of urinary pathogens by mobile IMS-based electronic nose: A proof-of-principle study.* PLoS One, 2014. **9**(12): p. e114279.

292. Parry, A., et al., *Leg ulcer odour detection identifies β-haemolytic streptococcal infection.* Journal of wound care, 1995. **4**(9): p. 404-406.

293. Shykhon, M., et al., *Clinical evaluation of the electronic nose in the diagnosis of ear, nose and throat infection: a preliminary study.* The Journal of Laryngology & Otology, 2004. **118**(9): p. 706-709.

294. Chandiok, S., et al., *Screening for bacterial vaginosis: a novel application of artificial nose technology.* Journal of clinical pathology, 1997. **50**(9): p. 790-791.

295. Hay, P., et al., *Evaluation of a novel diagnostic test for bacterial vaginosis:'the electronic nose'.* International journal of STD & AIDS, 2003. **14**(2): p. 114-118.

296. Chaudry, A.N., et al., *Analysis of vaginal acetic acid in patients undergoing treatment for bacterial vaginosis.* Journal of clinical microbiology, 2004. **42**(11): p. 5170-5175.

297. Persaud, K.C., et al., *Monitoring urinary tract infections and bacterial vaginosis.* Sensors and Actuators B: Chemical, 2006. **116**(1-2): p. 116-120.

298. Aathithan, S., et al., *Diagnosis of bacteriuria by detection of volatile organic compounds in urine using an automated headspace analyzer with multiple conducting polymer sensors.* Journal of clinical microbiology, 2001. **39**(7): p. 2590-2593.

299. Pavlou, A.K., et al., *Use of an electronic nose system for diagnoses of urinary tract infections.* Biosensors and Bioelectronics, 2002. **17**(10): p. 893-899.

300. Kodogiannis, V. and E. Wadge, *The use of gas-sensor arrays to diagnose urinary tract infections.* International journal of neural systems, 2005. **15**(05): p. 363-376.

301. Arasaradnam, R., et al., *Evaluation of gut bacterial populations using an electronic e-nose and field asymmetric ion mobility spectrometry: further insights into 'fermentonomics'.* Journal of medical engineering & technology, 2012. **36**(7): p. 333-337.

302. Kodogiannis, V.S., et al., *Artificial odor discrimination system using electronic nose and neural networks for the identification of urinary tract infection.* IEEE Transactions on information technology in biomedicine, 2008. **12**(6): p. 707-713.

303. Yates, J.W., et al., *Data reduction in headspace analysis of blood and urine samples for robust bacterial identification.* Computer methods and programs in biomedicine, 2005. **79**(3): p. 259-271.

304. Capelli, L., et al., *Application and uses of electronic noses for clinical diagnosis on urine samples: A review.* Sensors, 2016. **16**(10): p. 1708.

305. Hanson, C. and H. Steinberger. *The use of a novel'electronic nose'to diagnose the presence of intrapulmonary infection*. in *Anesthesiology*. 1997. LIPPINCOTT-RAVEN PUBL 227 EAST WASHINGTON SQ, PHILADELPHIA, PA 19106.

306. Hockstein, N.G., et al., *Diagnosis of pneumonia with an electronic nose: correlation of vapor signature with chest computed tomography scan findings.* The Laryngoscope, 2004. **114**(10): p. 1701-1705.

307. Hockstein, N.G., et al., *Correlation of pneumonia score with electronic nose signature: A prospective study.* Annals of Otology, Rhinology & Laryngology, 2005. **114**(7): p. 504-508.

308. Hanson, C.W. and E.R. Thaler, *Electronic nose prediction of a clinical pneumonia score: biosensors and microbes.* The Journal of the American Society of Anesthesiologists, 2005. **102**(1): p. 63-68.

309. Mohamed, E.I., et al. *A novel method for diagnosing chronic rhinosinusitis based on an electronic nose*. in *Anales otorrinolaringológicos ibero-americanos*. 2003.

310. Bruno, E., et al., *Can the electronic nose diagnose chronic rhinosinusitis? A new experimental study.* European archives of oto-rhino-laryngology, 2008. **265**(4): p. 425-428.

311. Saha, D., *Insect Olfaction in Chemical Sensing*, in *Canines*. 2022, Jenny Stanford Publishing. p. 151-177.

312. Röck, F., N. Barsan, and U. Weimar, *Electronic nose: current status and future trends.* Chemical reviews, 2008. **108**(2): p. 705-725.

313. Harper, W.J., *The strengths and weaknesses of the electronic nose.* Headspace analysis of foods and flavors, 2001: p. 59-71.

314. Rudnitskaya, A., *Calibration update and drift correction for electronic noses and tongues.* Frontiers in chemistry, 2018. **6**: p. 433.

315. Scheepers, M.H., et al., *Diagnostic Performance of Electronic Noses in Cancer Diagnoses Using Exhaled Breath: A Systematic Review and Meta-analysis.* JAMA Network Open, 2022. **5**(6): p. e2219372-e2219372.

316. Göpel, W., *From electronic to bioelectronic olfaction, or: from artificial "moses" to real noses.* Sensors and Actuators B: Chemical, 2000. **65**(1-3): p. 70-72.

317. Gaillard, I., S. Rouquier, and D. Giorgi, *Olfactory receptors.* Cellular and Molecular Life Sciences CMLS, 2004. **61**(4): p. 456-469.

318. Berna, A.Z., A.R. Anderson, and S.C. Trowell, *Bio-benchmarking of electronic nose sensors.* PloS one, 2009. **4**(7): p. e6406.

319. Janata, J., *Principles of chemical sensors*. 2010: Springer Science & Business Media.

320. Safran, M., et al., *Human gene-centric databases at the Weizmann Institute of Science: GeneCards, UDB, CroW 21 and HORDE.* Nucleic acids research, 2003. **31**(1): p. 142-146.

321. Pham-Delegue, M., et al., *Sunflower volatiles involved in honeybee discrimination among genotypes and flowering stages.* Journal of Chemical Ecology, 1989. **15**(1): p. 329-343.

322. Dobson, H.E., *Floral volatiles in insect biology.* Insect-plant interactions, 2017: p. 47-82.

323. Sandoz, J.-C., *Olfaction in honey bees: from molecules to behavior.* Honeybee neurobiology and behavior, 2012: p. 235-252.

324. Bruce, T.J. and J.A. Pickett, *Perception of plant volatile blends by herbivorous insects–finding the right mix.* Phytochemistry, 2011. **72**(13): p. 1605-1611.

325. Ache, B.W. and J.M. Young, *Olfaction: diverse species, conserved principles.* Neuron, 2005. **48**(3): p. 417-430.

326. Rouquier, S., A. Blancher, and D. Giorgi, *The olfactory receptor gene repertoire in primates and mouse: evidence for reduction of the functional fraction in primates.* Proceedings of the National Academy of Sciences, 2000. **97**(6): p. 2870-2874.

327. Malnic, B., P.A. Godfrey, and L.B. Buck, *The human olfactory receptor gene family.* Proceedings of the National Academy of Sciences, 2004. **101**(8): p. 2584-2589.

328. Bushdid, C., et al., *Humans can discriminate more than 1 trillion olfactory stimuli.* Science, 2014. **343**(6177): p. 1370-1372.

329. Niimura, Y. and M. Nei, *Evolution of olfactory receptor genes in the human genome.* Proceedings of the National Academy of Sciences, 2003. **100**(21): p. 12235-12240.

330. Ressler, K.J., S.L. Sullivan, and L.B. Buck, *Information coding in the olfactory system: evidence for a stereotyped and highly organized epitope map in the olfactory bulb.* Cell, 1994. **79**(7): p. 1245-1255.

331. Vassar, R., et al., *Topographic organization of sensory projections to the olfactory bulb.* Cell, 1994. **79**(6): p. 981-991.

332. Balu, R., R.T. Pressler, and B.W. Strowbridge, *Multiple modes of synaptic excitation of olfactory bulb granule cells.* Journal of Neuroscience, 2007. **27**(21): p. 5621-5632.

333. Buck, L.B. and C. Bargmann, *Smell and taste: The chemical senses.* Principles of neural science, 2000. **4**: p. 625-647.

334. Desmaisons, D., J.-D. Vincent, and P.-M. Lledo, *Control of action potential timing by intrinsic subthreshold oscillations in olfactory bulb output neurons.* Journal of Neuroscience, 1999. **19**(24): p. 10727-10737.

335. Schoppa, N.E. and G.L. Westbrook, *Glomerulus-specific synchronization of mitral cells in the olfactory bulb.* Neuron, 2001. **31**(4): p. 639-651.

336. Galán, R.F., et al., *Correlation-induced synchronization of oscillations in olfactory bulb neurons.* Journal of Neuroscience, 2006. **26**(14): p. 3646-3655.

337. Imamura, F., A. Ito, and B.J. LaFever, *Subpopulations of projection neurons in the olfactory bulb.* Frontiers in Neural Circuits, 2020. **14**: p. 561822.

338. Gilad, Y., et al., *Loss of olfactory receptor genes coincides with the acquisition of full trichromatic vision in primates.* PLoS biology, 2004. **2**(1): p. e5.

339. Elgar, M.A., et al., *Focus: ecology and evolution: insect antennal morphology: the evolution of diverse solutions to odorant perception.* The Yale journal of biology and medicine, 2018. **91**(4): p. 457.

340. Carraher, C., et al., *Towards an understanding of the structural basis for insect olfaction by odorant receptors.* Insect Biochemistry and Molecular Biology, 2015. **66**: p. 31-41.

341. Carey, A.F. and J.R. Carlson, *Insect olfaction from model systems to disease control.* Proceedings of the National Academy of Sciences, 2011. **108**(32): p. 12987-12995.

342. Ochieng, S.A., E. Hallberg, and B. Hansson, *Fine structure and distribution of antennal sensilla of the desert locust, Schistocerca gregaria (Orthoptera: Acrididae).* Cell and tissue research, 1998. **291**(3): p. 525-536.

343. Hallem, E.A. and J.R. Carlson, *Coding of odors by a receptor repertoire.* Cell, 2006. **125**(1): p. 143-160.

344. Masson, C. and H. Mustaparta, *Chemical information processing in the olfactory system of insects.* Physiological Reviews, 1990. **70**(1): p. 199-245.

345. Stocker, R.F., *The organization of the chemosensory system in Drosophila melanogaster: a rewiew.* Cell and tissue research, 1994. **275**: p. 3-26.

346. Sato, K., et al., *Insect olfactory receptors are heteromeric ligand-gated ion channels.* Nature, 2008. **452**(7190): p. 1002-1006.

347. Benton, R., et al., *Atypical membrane topology and heteromeric function of Drosophila odorant receptors in vivo.* PLoS biology, 2006. **4**(2): p. e20.

348. Buck, L. and R. Axel, *A novel multigene family may encode odorant receptors: a molecular basis for odor recognition.* Cell, 1991. **65**(1): p. 175-187.

349. Egea-Weiss, A., et al., *High precision of spike timing across olfactory receptor neurons allows rapid odor coding in Drosophila.* IScience, 2018. **4**: p. 76-83.

350. Wright, G.A., M. Carlton, and B.H. Smith, *A honeybee's ability to learn, recognize, and discriminate odors depends upon odor sampling time and concentration.* Behavioral neuroscience, 2009. **123**(1): p. 36.

351. Krofczik, S., R. Menzel, and M.P. Nawrot, *Rapid odor processing in the honeybee antennal lobe network.* Frontiers in computational neuroscience, 2009: p. 9.

352. Wicher, D., *Olfactory signaling in insects.* Progress in molecular biology and translational science, 2015. **130**: p. 37-54.

353. Vosshall, L.B., A.M. Wong, and R. Axel, *An olfactory sensory map in the fly brain.* Cell, 2000. **102**(2): p. 147-159.

354. Couto, A., M. Alenius, and B.J. Dickson, *Molecular, anatomical, and functional organization of the Drosophila olfactory system.* Current Biology, 2005. **15**(17): p. 1535-1547.

355. Hansson, B.S. and M.C. Stensmyr, *Evolution of insect olfaction.* Neuron, 2011. **72**(5): p. 698-711.

356. Hansson, B.S., et al., *Functional specialization of olfactory glomeruli in a moth.* Science, 1992. **256**(5061): p. 1313-1315.

357. Kelber, C., W. Rössler, and C.J. Kleineidam, *Multiple olfactory receptor neurons and their axonal projections in the antennal lobe of the honeybee Apis mellifera.* Journal of Comparative Neurology, 2006. **496**(3): p. 395-405.

358. Brockmann, A. and D. Brückner, *Projection pattern of poreplate sensory neurones in honey bee worker, Apis mellifera L.(Hymenoptera: Apidae).* International Journal of Insect Morphology and Embryology, 1995. **24**(4): p. 405-411.

359. Laurent, G. and M. Naraghi, *Odorant-induced oscillations in the mushroom bodies of the locust.* Journal of Neuroscience, 1994. **14**(5): p. 2993-3004.

360. Perez-Orive, J., et al., *Oscillations and sparsening of odor representations in the mushroom body.* Science, 2002. **297**(5580): p. 359-365.

361. Kay, L.M. and M. Stopfer. *Information processing in the olfactory systems of insects and vertebrates*. in *Seminars in cell & developmental biology*. 2006. Elsevier.

362. Bazhenov, M., et al., *Fast odor learning improves reliability of odor responses in the locust antennal lobe.* Neuron, 2005. **46**(3): p. 483-492.

363. Hosler, J.S., K.L. Buxton, and B.H. Smith, *Impairment of olfactory discrimination by blockade of GABA and nitric oxide activity in the honey bee antennal lobes.* Behavioral neuroscience, 2000. **114**(3): p. 514.

364. Stopfer, M., et al., *Impaired odour discrimination on desynchronization of odour-encoding neural assemblies.* Nature, 1997. **390**(6655): p. 70-74.

365. Szyszka, P., et al., *Sparsening and temporal sharpening of olfactory representations in the honeybee mushroom bodies.* Journal of neurophysiology, 2005. **94**(5): p. 3303-3313.

366. Wang, Y., et al., *Stereotyped odor-evoked activity in the mushroom body of Drosophila revealed by green fluorescent protein-based Ca2+ imaging.* Journal of Neuroscience, 2004. **24**(29): p. 6507-6514.

367. Szyszka, P., A. Galkin, and R. Menzel, *Associative and non-associative plasticity in Kenyon cells of the honeybee mushroom body.* Frontiers in systems neuroscience, 2008: p. 3.

368. Boeckh, J. and L.P. Tolbert, *Synaptic organization and development of the antennal lobe in insects.* Microscopy research and technique, 1993. **24**(3): p. 260-280.

369. Angioy, A.M., et al., *Extreme sensitivity in an olfactory system.* Chemical Senses, 2003. **28**(4): p. 279-284.

370. Kaissling, K.-E. and E. Priesner, *Die riechschwelle des seidenspinners.* Naturwissenschaften, 1970. **57**(1): p. 23-28.

371. Nei, M., Y. Niimura, and M. Nozawa, *The evolution of animal chemosensory receptor gene repertoires: roles of chance and necessity.* Nature Reviews Genetics, 2008. **9**(12): p. 951-963.

372. Pinching, A. and T. Powell, *The neuropil of the glomeruli of the olfactory bulb.* Journal of cell science, 1971. **9**(2): p. 347-377.

373. Gazit, I. and J. Terkel, *Explosives detection by sniffer dogs following strenuous physical activity.* Applied Animal Behaviour Science, 2003. **81**(2): p. 149-161.

374. Caygill, J.S., F. Davis, and S.P. Higson, *Current trends in explosive detection techniques.* Talanta, 2012. **88**: p. 14-29.

375. Browne, C., K. Stafford, and R. Fordham, *The use of scent-detection dogs.* Irish Veterinary Journal, 2006. **59**(2): p. 97.

376. Habib, M.K., *Controlled biological and biomimetic systems for landmine detection.* Biosensors and Bioelectronics, 2007. **23**(1): p. 1-18.

377. Lazarowski, L. and D.C. Dorman, *Explosives detection by military working dogs: Olfactory generalization from components to mixtures.* Applied Animal Behaviour Science, 2014. **151**: p. 84-93.

378. Lubow, R.E., *The war animals*. 1977: Doubleday Books.

379. Brown, S.W. and L.H. Goldstein, *Can seizure-alert dogs predict seizures?* Epilepsy research, 2011. **97**(3): p. 236-242.

380. Catala, A., et al., *Dogs demonstrate the existence of an epileptic seizure odour in humans.* Scientific reports, 2019. **9**(1): p. 1-7.

381. Wells, D.L., S.W. Lawson, and A.N. Siriwardena, *Canine responses to hypoglycemia in patients with type 1 diabetes.* The Journal of Alternative and Complementary Medicine, 2008. **14**(10): p. 1235-1241.

382. Weber, K.S., M. Roden, and K. Müssig, *Do dogs sense hypoglycaemia?* Diabetic Medicine, 2016. **33**(7): p. 934-938.

383. Reeve, C., et al., *An idiographic investigation of diabetic alert dogs' ability to learn from a small sample of breath samples from people with Type 1 diabetes.* Canadian journal of diabetes, 2020. **44**(1): p. 37-43. e1.

384. Guest, C., et al., *Trained dogs identify people with malaria parasites by their odour.* The Lancet Infectious Diseases, 2019. **19**(6): p. 578-580.

385. Kokocińska-Kusiak, A., et al., *Canine olfaction: physiology, behavior, and possibilities for practical applications.* Animals, 2021. **11**(8): p. 2463.

386. Angle, T.C., et al., *Real-time detection of a virus using detection dogs.* Frontiers in veterinary science, 2016: p. 79.

387. Williams, H. and A. Pembroke, *Sniffer dogs in the melanoma clinic?* The Lancet, 1989. **333**(8640): p. 734.

388. Church, J. and H. Williams, *Another sniffer dog for the clinic?* The Lancet, 2001. **358**(9285): p. 930.

389. Fraser, L., *Scientists put sniffer dogs on the scent of men with cancer.* Sunday Telegraph, 2002. **2**.

390. Dobson, R., *Dogs can sniff out first signs of men's cancer.* Sunday Times, 2003. **27**(5).

391. McCulloch, M., et al., *Diagnostic accuracy of canine scent detection in early-and late-stage lung and breast cancers.* Integrative cancer therapies, 2006. **5**(1): p. 30-39.

392. Ehmann, R., et al., *Canine scent detection in the diagnosis of lung cancer: revisiting a puzzling phenomenon.* European respiratory journal, 2012. **39**(3): p. 669-676.

393. Amundsen, T., et al., *Can dogs smell lung cancer? First study using exhaled breath and urine screening in unselected patients with suspected lung cancer.* Acta oncologica, 2014. **53**(3): p. 307-315.

394. Pickel, D., et al., *Evidence for canine olfactory detection of melanoma.* Applied Animal Behaviour Science, 2004. **89**(1-2): p. 107-116.

395. Cornu, J.-N., et al., *Olfactory detection of prostate cancer by dogs sniffing urine: a step forward in early diagnosis.* European urology, 2011. **59**(2): p. 197-201.

396. Sonoda, H., et al., *Colorectal cancer screening with odour material by canine scent detection.* Gut, 2011. **60**(6): p. 814-819.

397. Horvath, G., et al., *Human ovarian carcinomas detected by specific odor.* Integrative cancer therapies, 2008. **7**(2): p. 76-80.

398. Elliker, K.R., et al., *Key considerations for the experimental training and evaluation of cancer odour detection dogs: lessons learnt from a double-blind, controlled trial of prostate cancer detection.* BMC urology, 2014. **14**(1): p. 1-9.

399. Jezierski, T., et al., *Study of the art: canine olfaction used for cancer detection on the basis of breath odour. Perspectives and limitations.* Journal of breath research, 2015. **9**(2): p. 027001.

400. Willis, C.M., et al., *Olfactory detection of human bladder cancer by dogs: proof of principle study.* Bmj, 2004. **329**(7468): p. 712.

401. Gordon, R.T., et al., *The use of canines in the detection of human cancers.* The Journal of Alternative and Complementary Medicine, 2008. **14**(1): p. 61-67.

402. Taverna, G., et al., *Olfactory system of highly trained dogs detects prostate cancer in urine samples.* The Journal of urology, 2015. **193**(4): p. 1382-1387.

403. Taverna, G., et al., *Highly-trained dogs' olfactory system for detecting biochemical recurrence following radical prostatectomy.* Clinical Chemistry and Laboratory Medicine (CCLM), 2016. **54**(3): p. e67-e70.

404. Moser, E. and M. McCulloch, *Canine scent detection of human cancers: A review of methods and accuracy.* Journal of Veterinary Behavior, 2010. **5**(3): p. 145-152.

405. Boedeker, E., G. Friedel, and T. Walles, *Sniffer dogs as part of a bimodal bionic research approach to develop a lung cancer screening.* Interactive cardiovascular and thoracic surgery, 2012. **14**(5): p. 511-515.

406. Lippi, G. and G. Cervellin, *Canine olfactory detection of cancer versus laboratory testing: myth or opportunity?* Clinical chemistry and laboratory medicine, 2012. **50**(3): p. 435-439.

407. Manzini, I., D. Schild, and C. Di Natale, *Principles of odor coding in vertebrates and artificial chemosensory systems.* Physiological Reviews, 2022. **102**(1): p. 61-154.

408. Angle, C., et al., *Canine detection of the volatilome: a review of implications for pathogen and disease detection.* Frontiers in veterinary science, 2016. **3**: p. 47.

409. Concha, A.R., et al., *Canine olfactory thresholds to amyl acetate in a biomedical detection scenario.* Frontiers in Veterinary Science, 2019. **5**: p. 345.

410. Walker, D.B., et al., *Naturalistic quantification of canine olfactory sensitivity.* Applied Animal Behaviour Science, 2006. **97**(2-4): p. 241-254.

411. Craven, B.A., E.G. Paterson, and G.S. Settles, *The fluid dynamics of canine olfaction: unique nasal airflow patterns as an explanation of macrosmia.* Journal of the Royal Society Interface, 2010. **7**(47): p. 933-943.

412. Jenkins, E.K., M.T. DeChant, and E.B. Perry, *When the nose doesn't know: Canine olfactory function associated with health, management, and potential links to microbiota.* Frontiers in veterinary science, 2018: p. 56.

413. Walczak, M., et al., *Impact of individual training parameters and manner of taking breath odor samples on the reliability of canines as cancer screeners.* Journal of veterinary behavior, 2012. **7**(5): p. 283-294.

414. Edwards, T.L., et al., *Animal olfactory detection of human diseases: Guidelines and systematic review.* Journal of veterinary behavior, 2017. **20**: p. 59-73.

415. Weetjens, B., et al., *African pouched rats for the detection of pulmonary tuberculosis in sputum samples.* The International journal of tuberculosis and lung disease, 2009. **13**(6): p. 737-743.

416. Poling, A., et al., *Tuberculosis detection by giant African pouched rats.* The Behavior Analyst, 2011. **34**(1): p. 47-54.

417. Poling, A., et al., *Using giant African pouched rats to detect tuberculosis in human sputum samples: 2009 findings.* The American journal of tropical medicine and hygiene, 2010. **83**(6): p. 1308.

418. Mgode, G.F., et al., *Diagnosis of tuberculosis by trained African giant pouched rats and confounding impact of pathogens and microflora of the respiratory tract.* Journal of clinical microbiology, 2012. **50**(2): p. 274-280.

419. Mgode, G.F., et al., *Mycobacterium tuberculosis volatiles for diagnosis of tuberculosis by Cricetomys rats.* Tuberculosis, 2012. **92**(6): p. 535-542.

420. Rospars, J.-P., et al., *Heterogeneity and convergence of olfactory first-order neurons account for the high speed and sensitivity of second-order neurons.* PLoS computational biology, 2014. **10**(12): p. e1003975.

421. Liao, C., et al., *Behavioural and genetic evidence for C. elegans' ability to detect volatile chemicals associated with explosives.* PloS one, 2010. **5**(9): p. e12615.

422. Neto, M.F., et al., *The nematode Caenorhabditis elegans displays a chemotaxis behavior to tuberculosis-specific odorants.* Journal of clinical tuberculosis and other mycobacterial diseases, 2016. **4**: p. 44-49.

423. Hirotsu, T., et al., *A highly accurate inclusive cancer screening test using Caenorhabditis elegans scent detection.* PloS one, 2015. **10**(3): p. e0118699.

424. Ueda, Y., et al., *Application of C. elegans cancer screening test for the detection of pancreatic tumor in genetically engineered mice.* Oncotarget, 2019. **10**(52): p. 5412.

425. Kusumoto, H., et al., *Efficiency of gastrointestinal cancer detection by Nematode-NOSE (N-NOSE).* in vivo, 2020. **34**(1): p. 73-80.

426. Lanza, E., et al., *C. elegans-based chemosensation strategy for the early detection of cancer metabolites in urine samples.* Scientific reports, 2021. **11**(1): p. 1-16.

427. Thompson, M., et al., *A Caenorhabditis elegans behavioral assay distinguishes early stage prostate cancer patient urine from controls.* Biology open, 2021. **10**(3): p. bio057398.

428. di Luccio, E., M. Morishita, and T. Hirotsu, *C. elegans as a Powerful Tool for Cancer Screening.* Biomedicines, 2022. **10**(10): p. 2371.

429. Olson, D., et al., *Parasitic wasps learn and report diverse chemicals with unique conditionable behaviors.* Chemical senses, 2003. **28**(6): p. 545-549.

430. Tomberlin, J.K., et al., *Conditioned Microplitis croceipes Cresson (Hymenoptera: Braconidae) detect and respond to 2, 4-DNT: development of a biological sensor.* Journal of Forensic Science, 2005. **50**(5): p. JFS2005014-4.

431. Rains, G.C., S.L. Utley, and W.J. Lewis, *Behavioral monitoring of trained insects for chemical detection.* Biotechnology progress, 2006. **22**(1): p. 2-8.

432. Rains, G.C., et al., *Limits of volatile chemical detection of a parasitoid wasp, Microplitis croceipes, and an electronic nose: a comparative study.* Transactions of the ASAE, 2004. **47**(6): p. 2145.

433. Meiners, T., F. Wäckers, and W.J. Lewis, *The effect of molecular structure on olfactory discrimination by the parasitoid Microplitis croceipes.* Chemical senses, 2002. **27**(9): p. 811-816.

434. MacDonald, J., et al., *Alternatives for landmine detection*. 2003, RAND CORP SANTA MONICA CA.

435. Repasky, K.S., et al., *Optical detection of honeybees by use of wing-beat modulation of scattered laser light for locating explosives and land mines.* Applied optics, 2006. **45**(8): p. 1839-1843.

436. Taylor-mccabe, K.J., R.M. Wingo, and T.K. Haarmann, *Honey bees (Apis mellifera) as explosives detectors: exploring proboscis extension reflex conditioned response to trinitrotolulene (TNT)*. 2008, Los Alamos National Lab.(LANL), Los Alamos, NM (United States).

437. Leitch, O., et al., *Biological organisms as volatile compound detectors: A review.* Forensic science international, 2013. **232**(1-3): p. 92-103.

438. Suckling, D.M. and R.L. Sagar, *Honeybees Apis mellifera can detect the scent of Mycobacterium tuberculosis.* Tuberculosis, 2011. **91**(4): p. 327-328.

439. Davis, N., *How honey bees may one day help detect signs of cancers*, in *The Guardian*. 2013.

440. Bryant, R. *Honey bees can be trained to detect cancer "in ten minutes" says designer*. 2013 2022, November 20]; Available from: https://www.dezeen.com/2013/11/20/honey-bees-can-be-trained-to-detect-cancer-in-ten-minutes-says-designer-susana-soares/.

441. King, T.L., et al., *Explosives detection with hard-wired moths.* IEEE Transactions on Instrumentation and Measurement, 2004. **53**(4): p. 1113-1118.

442. Rains, G.C., J.K. Tomberlin, and D. Kulasiri, *Using insect sniffing devices for detection.* Trends in biotechnology, 2008. **26**(6): p. 288-294.

443. Roelofs, W.L., *Electroantennogram assays: rapid and convenient screening procedures for pheromones*, in *Techniques in pheromone research*. 1984, Springer. p. 131-159.

444. Schott, M., et al., *Insect antenna-based biosensors for in situ detection of volatiles.* Yellow Biotechnology II, 2013: p. 101-122.

445. Guo, M., et al., *Odorant receptors for detecting flowering plant cues are functionally conserved across moths and butterflies.* Molecular biology and evolution, 2021. **38**(4): p. 1413-1427.

446. Färbert, P., et al., *Measuring pheromone concentrations in cotton fields with the EAG method*, in *Insect Pheromone Research*. 1997, Springer. p. 347-358.

447. Van der Pers, J. and A. Minks, *A portable electroantennogram sensor for routine measurements of pheromone concentrations in greenhouses.* Entomologia experimentalis et applicata, 1998. **87**(2): p. 209-215.

448. Sauer, A.E., et al., *A portable EAG system for the measurement of pheromone concentrations in the field.* Chemical Senses, 1992. **17**(5): p. 543-553.

449. Schiestl, F. and F. Marion-Poll, *Detection of physiologically active flower volatiles using gas chromatography coupled with electroantennography*, in *Analysis of taste and aroma*. 2002, Springer. p. 173-198.

450. Moore, I., *Biological amplification for increasing electroantennogram discrimination between two female sex pheromones ofSpodoptera littoralis (Lepidoptera: Noctuidae).* Journal of Chemical Ecology, 1981. **7**(5): p. 791-798.

451. Park, K.C. and T.C. Baker, *Improvement of signal-to-noise ratio in electroantennogram responses using multiple insect antennae.* Journal of Insect Physiology, 2002. **48**(12): p. 1139-1145.

452. Park, K.C., et al., *Odor discrimination using insect electroantennogram responses from an insect antennal array.* Chemical senses, 2002. **27**(4): p. 343-352.

453. Cork, A., et al., *Gas chromatography linked to electroantennography: a versatile technique for identifying insect semiochemicals*, in *Chromatography and isolation of insect hormones and pheromones*. 1990, Springer. p. 271-279.

454. Moorhouse, J., et al., *Method for use in studies of insect chemical communication.* Nature, 1969. **223**(5211): p. 1174-1175.

455. Struble, D.L. and H. Arn, *Combined gas chromatography and electroantennogram recording of insect olfactory responses*, in *Techniques in pheromone research*. 1984, Springer. p. 161-178.

456. Sillam-Dusses, D., et al., *Identification by GC-EAD of the two-component trail-following pheromone of Prorhinotermes simplex (Isoptera, Rhinotermitidae, Prorhinotermitinae).* Journal of Insect Physiology, 2009. **55**(8): p. 751-757.

457. Kurtovic, A., A. Widmer, and B.J. Dickson, *A single class of olfactory neurons mediates behavioural responses to a Drosophila sex pheromone.* Nature, 2007. **446**(7135): p. 542-546.

458. Siderhurst, M.S. and E.B. Jang, *Female-biased attraction of oriental fruit fly, Bactrocera dorsalis (Hendel), to a blend of host fruit volatiles from Terminalia catappa L.* Journal of chemical ecology, 2006. **32**(11): p. 2513-2524.

459. Olsson, P.-O.C., et al., *Electrophysiological and behavioral responses to chocolate volatiles in both sexes of the pyralid moths Ephestia cautella and Plodia interpunctella.* Journal of chemical ecology, 2005. **31**(12): p. 2947-2961.

460. Zhang, Q.-H., N. Erbilgin, and S.J. Seybold, *GC-EAD responses to semiochemicals by eight beetles in the subcortical community associated with Monterey pine trees in coastal California: similarities and disparities across three trophic levels.* Chemoecology, 2008. **18**(4): p. 243-254.

461. Van Der Pers, J., *Comparison of electroantennogram response spectra to plant volatiles in seven species of Yponomeuta and in the tortricid Adoxophyes orana.* Entomologia experimentalis et applicata, 1981. **30**(2): p. 181-192.

462. Park, K.C., et al., *Electroantennogram responses of a parasitic wasp, Microplitis croceipes, to host-related volatile and anthropogenic compounds.* Physiological Entomology, 2001. **26**(1): p. 69-77.

463. Revadi, S., et al., *Olfactory responses of D rosophila suzukii females to host plant volatiles.* Physiological Entomology, 2015. **40**(1): p. 54-64.

464. Schroth, P., et al., *Extending the capabilities of an antenna/chip biosensor by employing various insect species.* Sensors and Actuators B: Chemical, 2001. **78**(1-3): p. 1-5.

465. Schöning, M.J., et al., *A BioFET on the basis of intact insect antennae.* Sensors and Actuators B: Chemical, 1998. **47**(1-3): p. 235-238.

466. Schroth, P., et al., *Insect-based BioFETs with improved signal characteristics.* Biosensors and Bioelectronics, 1999. **14**(3): p. 303-308.

467. Schütz, S., et al., *An insect-based BioFET as a bioelectronic nose.* Sensors and Actuators B: Chemical, 2000. **65**(1-3): p. 291-295.

468. Schöning, M.J., P. Schroth, and S. Schütz, *The use of insect chemoreceptors for the assembly of biosensors based on semiconductor field-effect transistors.* Electroanalysis: An International Journal Devoted to Fundamental and Practical Aspects of Electroanalysis, 2000. **12**(9): p. 645-652.

469. Wadhams, L.J., *Coupled gas chromatography—single cell recording: a new technique for use in the analysis of insect pheromones.* Zeitschrift für Naturforschung C, 1982. **37**(10): p. 947-952.

470. Wadhams, L., *The use of coupled gas chromatography: electrophysiological techniques in the identification of insect pheromones*, in *Chromatography and isolation of insect hormones and pheromones*. 1990, Springer. p. 289-298.

471. Blight, M., et al., *Antennal perception of oilseed rape, Brassica napus (Brassicaceae), volatiles by the cabbage seed weevilCeutorhynchus assimilis (Coleoptera, Curculionidae).* Journal of chemical ecology, 1995. **21**(11): p. 1649-1664.

472. Hansson, B., et al., *Correlation between dendrite diameter and action potential amplitude in sex pheromone specific receptor neurons in male Ostrinia nubilalis (Lepidoptera: Pyralidae).* Tissue and Cell, 1994. **26**(4): p. 503-512.

473. Olsson, S.B. and B.S. Hansson, *Electroantennogram and single sensillum recording in insect antennae*, in *Pheromone signaling*. 2013, Springer. p. 157-177.

474. De Bruyne, M., K. Foster, and J.R. Carlson, *Odor coding in the Drosophila antenna.* Neuron, 2001. **30**(2): p. 537-552.

475. Hallem, E.A., M.G. Ho, and J.R. Carlson, *The molecular basis of odor coding in the Drosophila antenna.* Cell, 2004. **117**(7): p. 965-979.

476. Dobritsa, A.A., et al., *Integrating the molecular and cellular basis of odor coding in the Drosophila antenna.* Neuron, 2003. **37**(5): p. 827-841.

477. Mustaparta, H., *Responses of single olfactory cells in the pine weevilHylobius abietis L.(Col.: Curculionidae).* Journal of Comparative Physiology, 1975. **97**(4): p. 271-290.

478. Ma, W.C. and J. Visser, *Single unit analysis of odour quality coding by the olfactory antennal receptor system of the Colorado beetle.* Entomologia Experimentalis et Applicata, 1978. **24**(3): p. 520-533.

479. Sass, H., *Olfactory receptors on the antenna ofPeriplaneta: Response constellations that encode food odors.* Journal of comparative physiology, 1978. **128**(3): p. 227-233.

480. Hansson, B., et al., *Physiological responses and central nervous projections of antennal olfactory receptor neurons in the adult desert locust, Schistocerca gregaria (Orthoptera: Acrididae).* Journal of Comparative Physiology A, 1996. **179**(2): p. 157-167.

481. Ignell, R., S. Anton, and B. Hansson, *Central nervous processing of behaviourally relevant odours in solitary and gregarious fifth instar locusts, Schistocerca gregaria.* Journal of Comparative Physiology A, 1998. **183**(4): p. 453-465.

482. MacLeod, K., A. Bäcker, and G. Laurent, *Who reads temporal information contained across synchronized and oscillatory spike trains?* Nature, 1998. **395**(6703): p. 693-698.

483. Marshall, B., C.G. Warr, and M. De Bruyne, *Detection of volatile indicators of illicit substances by the olfactory receptors of Drosophila melanogaster.* Chemical senses, 2010. **35**(7): p. 613-625.

484. Nowotny, T., et al., *Drosophila olfactory receptors as classifiers for volatiles from disparate real world applications.* Bioinspiration & Biomimetics, 2014. **9**(4): p. 046007.

485. Pelz, D., et al., *The molecular receptive range of an olfactory receptor in vivo (Drosophila melanogaster Or22a).* Journal of neurobiology, 2006. **66**(14): p. 1544-1563.

486. Silbering, A.F., et al., *Complementary function and integrated wiring of the evolutionarily distinct Drosophila olfactory subsystems.* Journal of Neuroscience, 2011. **31**(38): p. 13357-13375.

487. Cui, X., C. Wu, and L. Zhang, *Electrophysiological response patterns of 16 olfactory neurons from the trichoid sensilla to odorant from fecal volatiles in the locust, Locusta migratoria manilensis.* Archives of insect biochemistry and physiology, 2011. **77**(2): p. 45-57.

488. Strauch, M., et al., *More than apples and oranges-Detecting cancer with a fruit fly's antenna.* Scientific reports, 2014. **4**(1): p. 1-9.

489. Bhandawat, V., et al., *Sensory processing in the Drosophila antennal lobe increases reliability and separability of ensemble odor representations.* Nature neuroscience, 2007. **10**(11): p. 1474-1482.

490. Olsen, S.R. and R.I. Wilson, *Lateral presynaptic inhibition mediates gain control in an olfactory circuit.* Nature, 2008. **452**(7190): p. 956-960.

491. Wilson, R.I., G.C. Turner, and G. Laurent, *Transformation of olfactory representations in the Drosophila antennal lobe.* Science, 2004. **303**(5656): p. 366-370.

492. Olsen, S.R., V. Bhandawat, and R.I. Wilson, *Divisive normalization in olfactory population codes.* Neuron, 2010. **66**(2): p. 287-299.

493. Silbering, A.F. and C.G. Galizia, *Processing of odor mixtures in the Drosophila antennal lobe reveals both global inhibition and glomerulus-specific interactions.* Journal of Neuroscience, 2007. **27**(44): p. 11966-11977.

494. Kazama, H. and R.I. Wilson, *Origins of correlated activity in an olfactory circuit.* Nature neuroscience, 2009. **12**(9): p. 1136-1144.

495. Ng, M., et al., *Transmission of olfactory information between three populations of neurons in the antennal lobe of the fly.* Neuron, 2002. **36**(3): p. 463-474.

496. Hansson, B.S. and S. Anton, *Function and morphology of the antennal lobe: new developments.* Annual review of entomology, 2000. **45**(1): p. 203-231.

497. Moreaux, L.C. and G. Laurent, *Estimating firing rates from calcium signals in locust projection neurons in vivo.* Frontiers in neural circuits, 2007: p. 2.

498. Sachse, S. and C.G. Galizia, *Role of inhibition for temporal and spatial odor representation in olfactory output neurons: a calcium imaging study.* Journal of neurophysiology, 2002. **87**(2): p. 1106-1117.

499. Joerges, J., et al., *Representations of odours and odour mixtures visualized in the honeybee brain.* Nature, 1997. **387**(6630): p. 285-288.

500. Galizia, C.G., et al., *The glomerular code for odor representation is species specific in the honeybee Apis mellifera.* Nature neuroscience, 1999. **2**(5): p. 473-478.

501. Sachse, S., A. Rappert, and C.G. Galizia, *The spatial representation of chemical structures in the antennal lobe of honeybees: steps towards the olfactory code.* European Journal of Neuroscience, 1999. **11**(11): p. 3970-3982.

502. Galizia, C.G., et al., *Odour coding is bilaterally symmetrical in the antennal lobes of honeybees (Apis mellifera).* European Journal of Neuroscience, 1998. **10**(9): p. 2964-2974.

503. Galizia, C.G., et al., *A semi-in-vivo preparation for optical recording of the insect brain.* Journal of neuroscience methods, 1997. **76**(1): p. 61-69.

504. Mohamed, A.A., et al., *Odor mixtures of opposing valence unveil inter-glomerular crosstalk in the Drosophila antennal lobe.* Nature Communications, 2019. **10**(1): p. 1-17.

505. Ai, M., et al., *Acid sensing by the Drosophila olfactory system.* Nature, 2010. **468**(7324): p. 691-695.

506. Wang, J.W., et al., *Two-photon calcium imaging reveals an odor-evoked map of activity in the fly brain.* Cell, 2003. **112**(2): p. 271-282.

507. Carlsson, M.A., et al., *Spatio-temporal Ca2+ dynamics of moth olfactory projection neurones.* European Journal of Neuroscience, 2005. **22**(3): p. 647-657.

508. Moreaux, L.C., et al., *Integrated neurophotonics: toward dense volumetric interrogation of brain circuit activity—at depth and in real time.* Neuron, 2020. **108**(1): p. 66-92.

509. Ali, F. and A.C. Kwan, *Interpreting in vivo calcium signals from neuronal cell bodies, axons, and dendrites: a review.* Neurophotonics, 2019. **7**(1): p. 011402.

510. Grewe, B.F. and F. Helmchen, *Optical probing of neuronal ensemble activity.* Current opinion in neurobiology, 2009. **19**(5): p. 520-529.

511. Laurent, G. and H. Davidowitz, *Encoding of olfactory information with oscillating neural assemblies.* Science, 1994. **265**(5180): p. 1872-1875.

512. MacLeod, K. and G. Laurent, *Distinct mechanisms for synchronization and temporal patterning of odor-encoding neural assemblies.* Science, 1996. **274**(5289): p. 976-979.

513. Wehr, M. and G. Laurent, *Odour encoding by temporal sequences of firing in oscillating neural assemblies.* Nature, 1996. **384**(6605): p. 162-166.

514. Bazhenov, M., et al., *Model of cellular and network mechanisms for odor-evoked temporal patterning in the locust antennal lobe.* Neuron, 2001. **30**(2): p. 569-581.

515. Anton, S., R. Ignell, and B.S. Hansson, *Developmental changes in the structure and function of the central olfactory system in gregarious and solitary desert locusts.* Microscopy research and technique, 2002. **56**(4): p. 281-291.

516. Stopfer, M., V. Jayaraman, and G. Laurent, *Intensity versus identity coding in an olfactory system.* Neuron, 2003. **39**(6): p. 991-1004.

517. Brown, S.L., J. Joseph, and M. Stopfer, *Encoding a temporally structured stimulus with a temporally structured neural representation.* Nature Neuroscience, 2005. **8**(11): p. 1568-1576.

518. Mazor, O. and G. Laurent, *Transient dynamics versus fixed points in odor representations by locust antennal lobe projection neurons.* Neuron, 2005. **48**(4): p. 661-673.

519. Ito, I., et al., *Sparse odor representation and olfactory learning.* Nature neuroscience, 2008. **11**(10): p. 1177-1184.

520. Daly, K.C., G.A. Wright, and B.H. Smith, *Molecular features of odorants systematically influence slow temporal responses across clusters of coordinated antennal lobe units in the moth Manduca sexta.* Journal of neurophysiology, 2004. **92**(1): p. 236-254.

521. Wilson, R.I. and G. Laurent, *Role of GABAergic inhibition in shaping odor-evoked spatiotemporal patterns in the Drosophila antennal lobe.* Journal of Neuroscience, 2005. **25**(40): p. 9069-9079.

522. Masse, N.Y., G.C. Turner, and G.S. Jefferis, *Olfactory information processing in Drosophila.* Current Biology, 2009. **19**(16): p. R700-R713.

523. Saha, D., et al., *Explosive sensing with insect-based biorobots.* Biosensors and Bioelectronics: X, 2020. **6**: p. 100050.

524. Kuehn, M., et al., *Changes of pressure and humidity affect olfactory function.* European archives of oto-rhino-laryngology, 2008. **265**(3): p. 299-302.

525. Altundağ, A., et al., *The effect of high altitude on olfactory functions.* European Archives of Oto-Rhino-Laryngology, 2014. **271**(3): p. 615-618.

526. Martin, F., J. Riveron, and E. Alcorta, *Environmental temperature modulates olfactory reception in Drosophila melanogaster.* Journal of insect physiology, 2011. **57**(12): p. 1631-1642.

527. Stone, H., *Influence of temperature on olfactory sensitivity.* Journal of Applied Physiology, 1963. **18**(4): p. 746-751.

528. DeBerardinis, R.J. and C.B. Thompson, *Cellular metabolism and disease: what do metabolic outliers teach us?* Cell, 2012. **148**(6): p. 1132-1144.

529. Navale, A.M. and A.N. Paranjape, *Glucose transporters: physiological and pathological roles.* Biophysical reviews, 2016. **8**(1): p. 5-9.

530. Phypers, B. and J.T. Pierce, *Lactate physiology in health and disease.* Continuing Education in Anaesthesia, Critical Care and Pain, 2006. **6**(3): p. 128-132.

531. Rosenthal, M.D. and R.H. Glew, *Medical biochemistry: human metabolism in health and disease*. 2011: John Wiley & Sons.

532. Association, A.D., *Diagnosis and classification of diabetes mellitus.* Diabetes care, 2009. **32**(Supplement_1): p. S62-S67.

533. King, G.L. and M.R. Loeken, *Hyperglycemia-induced oxidative stress in diabetic complications.* Histochemistry and cell biology, 2004. **122**(4): p. 333-338.

534. Rolo, A.P. and C.M. Palmeira, *Diabetes and mitochondrial function: role of hyperglycemia and oxidative stress.* Toxicology and applied pharmacology, 2006. **212**(2): p. 167-178.

535. Vanessa Fiorentino, T., et al., *Hyperglycemia-induced oxidative stress and its role in diabetes mellitus related cardiovascular diseases.* Current pharmaceutical design, 2013. **19**(32): p. 5695-5703.

536. Fernández-Real, J.M., A. López-Bermejo, and W. Ricart, *Cross-talk between iron metabolism and diabetes.* Diabetes, 2002. **51**(8): p. 2348-2354.

537. Anderson, J.C., A.L. Babb, and M.P. Hlastala, *Modeling soluble gas exchange in the airways and alveoli.* Annals of biomedical engineering, 2003. **31**(11): p. 1402-1422.

538. Sulway, M. and J. Malins, *Acetone in diabetic ketoacidosis.* The lancet, 1970. **296**(7676): p. 736-740.

539. Reichard Jr, G., et al., *Acetone metabolism in humans during diabetic ketoacidosis.* Diabetes, 1986. **35**(6): p. 668-674.

540. Galassetti, P.R., et al., *Breath ethanol and acetone as indicators of serum glucose levels: an initial report.* Diabetes technology & therapeutics, 2005. **7**(1): p. 115-123.

541. Wang, W., et al., *Accuracy of breath test for diabetes mellitus diagnosis: a systematic review and meta-analysis.* BMJ Open Diabetes Research and Care, 2021. **9**(1): p. e002174.

542. Yatscoff, R.W., et al., *13C glucose breath test for the diagnosis of diabetic indications and monitoring glycemic control*. 2006, Google Patents.

543. Zhou, M.-G., et al., *Investigation and identification of breath acetone as a potential biomarker for type 2 diabetes diagnosis.* Chinese Science Bulletin, 2014. **59**(17): p. 1992-1998.

544. Yan, K., et al., *Design of a breath analysis system for diabetes screening and blood glucose level prediction.* IEEE transactions on biomedical engineering, 2014. **61**(11): p. 2787-2795.

545. Turner, C., et al., *Breath acetone concentration decreases with blood glucose concentration in type I diabetes mellitus patients during hypoglycaemic clamps.* Journal of breath research, 2009. **3**(4): p. 046004.

546. Righettoni, M. and A. Tricoli, *Toward portable breath acetone analysis for diabetes detection.* Journal of breath research, 2011. **5**(3): p. 037109.

547. Rydosz, A., *Sensors for enhanced detection of acetone as a potential tool for noninvasive diabetes monitoring.* Sensors, 2018. **18**(7): p. 2298.

548. Saasa, V., et al., *Sensing technologies for detection of acetone in human breath for diabetes diagnosis and monitoring.* Diagnostics, 2018. **8**(1): p. 12.

549. Minh, T.D.C., D.R. Blake, and P.R. Galassetti, *The clinical potential of exhaled breath analysis for diabetes mellitus.* Diabetes research and clinical practice, 2012. **97**(2): p. 195-205.

550. Warburg, O., *On the origin of cancer cells.* Science, 1956. **123**(3191): p. 309-314.

551. Chen Jr, Y., et al., *Lactate metabolism is associated with mammalian mitochondria.* Nature chemical biology, 2016. **12**(11): p. 937-943.

552. de la Cruz-López, K.G., et al., *Lactate in the regulation of tumor microenvironment and therapeutic approaches.* Frontiers in oncology, 2019. **9**: p. 1143.

553. DeBerardinis, R.J., et al., *The biology of cancer: metabolic reprogramming fuels cell growth and proliferation.* Cell metabolism, 2008. **7**(1): p. 11-20.

554. Hirayama, A., et al., *Quantitative metabolome profiling of colon and stomach cancer microenvironment by capillary electrophoresis time-of-flight mass spectrometry.* Cancer research, 2009. **69**(11): p. 4918-4925.

555. Gottfried, E., et al., *Tumor-derived lactic acid modulates dendritic cell activation and antigen expression.* Blood, 2006. **107**(5): p. 2013-2021.

556. Fischer, K., et al., *Inhibitory effect of tumor cell–derived lactic acid on human T cells.* Blood, 2007. **109**(9): p. 3812-3819.

557. Hanahan, D. and R.A. Weinberg, *Hallmarks of cancer: the next generation.* cell, 2011. **144**(5): p. 646-674.

558. Fuchs, P., et al., *Breath gas aldehydes as biomarkers of lung cancer.* International Journal of Cancer, 2010. **126**(11): p. 2663-2670.

559. Leitch, B. and G. Laurent, *GABAergic synapses in the antennal lobe and mushroom body of the locust olfactory system.* Journal of comparative Neurology, 1996. **372**(4): p. 487-514.

560. Laurent, G., *Olfactory network dynamics and the coding of multidimensional signals.* Nature reviews neuroscience, 2002. **3**(11): p. 884-895.

561. Bazhenov, M., et al., *Model of transient oscillatory synchronization in the locust antennal lobe.* Neuron, 2001. **30**(2): p. 553-567.

562. Sejnowski, T.J. and O. Paulsen, *Network oscillations: emerging computational principles.* Journal of Neuroscience, 2006. **26**(6): p. 1673-1676.

563. Turner, G.C., M. Bazhenov, and G. Laurent, *Olfactory representations by Drosophila mushroom body neurons.* Journal of neurophysiology, 2008. **99**(2): p. 734-746.

564. Ernst, K., J. Boeckh, and V. Boeckh, *A neuroanatomical study on the organization of the central antennal pathways in insects.* Cell and tissue research, 1977. **176**(3): p. 285-308.

565. Bergmann, G.A. and G. Bicker, *Cholinergic calcium responses in cultured antennal lobe neurons of the migratory locust.* Scientific reports, 2021. **11**(1): p. 1-15.

566. Stopfer, M., *Central processing in the mushroom bodies.* Current opinion in insect science, 2014. **6**: p. 99-103.

567. Jortner, R.A., S.S. Farivar, and G. Laurent, *A simple connectivity scheme for sparse coding in an olfactory system.* Journal of Neuroscience, 2007. **27**(7): p. 1659-1669.

568. Gupta, N. and M. Stopfer, *A temporal channel for information in sparse sensory coding.* Current Biology, 2014. **24**(19): p. 2247-2256.

569. Hanna, G.B., et al., *Accuracy and methodologic challenges of volatile organic compound–based exhaled breath tests for cancer diagnosis: a systematic review and meta-analysis.* JAMA oncology, 2019. **5**(1): p. e182815-e182815.

570. Raman, B., et al., *Temporally diverse firing patterns in olfactory receptor neurons underlie spatiotemporal neural codes for odors.* Journal of Neuroscience, 2010. **30**(6): p. 1994-2006.

571. Goodwin, M.L., et al., *Lactate and cancer: revisiting the Warburg effect in an era of lactate shuttling.* Frontiers in nutrition, 2015. **1**: p. 27.

572. Boland, M.L., A.H. Chourasia, and K.F. Macleod, *Mitochondrial dysfunction in cancer.* Frontiers in oncology, 2013. **3**: p. 292.

573. Sabharwal, S.S. and P.T. Schumacker, *Mitochondrial ROS in cancer: initiators, amplifiers or an Achilles' heel?* Nature Reviews Cancer, 2014. **14**(11): p. 709-721.

574. Denko, N.C., *Hypoxia, HIF1 and glucose metabolism in the solid tumour.* Nature Reviews Cancer, 2008. **8**(9): p. 705-713.

575. DeBerardinis, R.J., *Is cancer a disease of abnormal cellular metabolism? New angles on an old idea.* Genetics in Medicine, 2008. **10**(11): p. 767-777.

576. Levine, A.J. and A.M. Puzio-Kuter, *The control of the metabolic switch in cancers by oncogenes and tumor suppressor genes.* Science, 2010. **330**(6009): p. 1340-1344.

577. Pfeiffer, T., S. Schuster, and S. Bonhoeffer, *Cooperation and competition in the evolution of ATP-producing pathways.* Science, 2001. **292**(5516): p. 504-507.

578. Shestov, A.A., et al., *Quantitative determinants of aerobic glycolysis identify flux through the enzyme GAPDH as a limiting step.* elife, 2014. **3**: p. e03342.

579. Vaupel, P., H. Schmidberger, and A. Mayer, *The Warburg effect: essential part of metabolic reprogramming and central contributor to cancer progression.* International journal of radiation biology, 2019. **95**(7): p. 912-919.

580. Walenta, S., et al., *High lactate levels predict likelihood of metastases, tumor recurrence, and restricted patient survival in human cervical cancers.* Cancer research, 2000. **60**(4): p. 916-921.

581. Sonveaux, P., et al., *Targeting lactate-fueled respiration selectively kills hypoxic tumor cells in mice.* The Journal of clinical investigation, 2008. **118**(12): p. 3930-3942.

582. Zent, R. and A. Pozzi, *Cell-extracellular matrix interactions in cancer*. 2010: Springer.

583. Hakim, M., et al., *Volatile organic compounds of lung cancer and possible biochemical pathways.* Chemical reviews, 2012. **112**(11): p. 5949-5966.

584. Gessner, C., et al., *Detection of p53 gene mutations in exhaled breath condensate of non-small cell lung cancer patients.* Lung cancer, 2004. **43**(2): p. 215-222.

585. Brunner, C., et al., *Discrimination of cancerous and non-cancerous cell lines by headspace-analysis with PTR-MS.* Analytical and bioanalytical chemistry, 2010. **397**(6): p. 2315-2324.

586. Sulé-Suso, J., et al., *Quantification of acetaldehyde and carbon dioxide in the headspace of malignant and non-malignant lung cells in vitro by SIFT-MS.* Analyst, 2009. **134**(12): p. 2419-2425.

587. Smith, D., et al., *Quantification of acetaldehyde released by lung cancer cells in vitro using selected ion flow tube mass spectrometry.* Rapid communications in mass spectrometry, 2003. **17**(8): p. 845-850.

588. Elmassry, M.M. and M.A. Farag, *In vivo and in vitro volatile organic compounds (VOCs) analysis in bacterial diagnostics: case studies in agriculture and human diseases*, in *Bacterial Volatile Compounds as Mediators of Airborne Interactions*. 2020, Springer. p. 123-138.

589. Pereira, J., et al., *Breath analysis as a potential and non-invasive frontier in disease diagnosis: an overview.* Metabolites, 2015. **5**(1): p. 3-55.

590. Saha, D., et al., *A spatiotemporal coding mechanism for background-invariant odor recognition.* Nature Neuroscience, 2013. **16**(12): p. 1830-1839.

591. Pouzat, C., O. Mazor, and G. Laurent, *Using noise signature to optimize spike-sorting and to assess neuronal classification quality.* Journal of Neuroscience Methods, 2002. **122**(1): p. 43-57.

592. Nizampatnam, S., et al., *Dynamic contrast enhancement and flexible odor codes.* Nat Commun, 2018. **9**(1): p. 3062.

593. Stopfer, M. and G. Laurent, *Short-term memory in olfactory network dynamics.* Nature, 1999. **402**(6762): p. 664-8.

594. Perez-Orive, J., et al., *Oscillations and Sparsening of Odor Representations in the Mushroom Body.* Science, 2002. **297**(5580): p. 359.

595. Stopfer, M., et al., *Impaired odour discrimination on desynchronization of odour-encoding neural assemblies.* Nature, 1997. **390**: p. 70-74.

596. Saha, D., et al., *Behavioural correlates of combinatorial versus temporal features of odour codes.* Nature Communications, 2015. **6**(1): p. 6953.

597. Kaloumenou, M., et al., *Breath Analysis: A Promising Tool for Disease Diagnosis-The Role of Sensors.* Sensors (Basel), 2022. **22**(3).

598. Gouzerh, F., et al., *Odors and cancer: Current status and future directions.* Biochim Biophys Acta Rev Cancer, 2022. **1877**(1): p. 188644.

599. Brunner, C., et al., *Discrimination of cancerous and non-cancerous cell lines by headspace-analysis with PTR-MS.* Analytical and Bioanalytical Chemistry, 2010. **397**(6): p. 2315-2324.

600. Altomare, D.F., et al., *Exhaled volatile organic compounds identify patients with colorectal cancer.* British Journal of Surgery, 2013. **100**(1): p. 144-150.

601. Altomare, D.F., et al., *Chemical signature of colorectal cancer: case–control study for profiling the breath print.* BJS Open, 2020. **4**(6): p. 1189-1199.

602. Amal, H., et al., *Detection of precancerous gastric lesions and gastric cancer through exhaled breath.* Gut, 2016. **65**(3): p. 400.

603. Amal, H., et al., *Assessment of ovarian cancer conditions from exhaled breath.* International Journal of Cancer, 2015. **136**(6): p. E614-E622.

604. Gruber, M., et al., *Analysis of exhaled breath for diagnosing head and neck squamous cell carcinoma: a feasibility study.* British Journal of Cancer, 2014. **111**(4): p. 790-798.

605. Mochalski, P., et al., *<i>Ex vivo</i>emission of volatile organic compounds from gastric cancer and non-cancerous tissue.* Journal of Breath Research, 2018. **12**(4): p. 046005.

606. Nardi-Agmon, I. and N. Peled, *Exhaled breath analysis for the early detection of lung cancer: recent developments and future prospects.* Lung Cancer (Auckl), 2017. **8**: p. 31-38.

607. Phillips, M., et al., *Rapid Point-Of-Care Breath Test Predicts Breast Cancer And Abnormal Mammograms in Symptomatic Women.* medRxiv, 2020: p. 2020.04.07.20042895.

608. Saidi, T., et al., *Non-invasive prediction of lung cancer histological types through exhaled breath analysis by UV-irradiated electronic nose and GC/QTOF/MS.* Sensors and Actuators B: Chemical, 2020. **311**: p. 127932.

609. Wang, C., et al., *Volatile Organic Metabolites Identify Patients with Breast Cancer, Cyclomastopathy and Mammary Gland Fibroma.* Scientific Reports, 2014. **4**(1): p. 5383.

610. Španěl, P. and D. Smith, *Quantification of volatile metabolites in exhaled breath by selected ion flow tube mass spectrometry, SIFT-MS.* Clin Mass Spectrom, 2020. **16**: p. 18-24.

611. Chen, H., et al., *COVID-19 screening using breath-borne volatile organic compounds.* Journal of Breath Research, 2021.

612. Tiele, A., et al., *Breath-based non-invasive diagnosis of Alzheimer’s disease: a pilot study.* Journal of Breath Research, 2020. **14**(2): p. 026003.

613. Arasaradnam, R.P., et al., *Detection of Colorectal Cancer (CRC) by Urinary Volatile Organic Compound Analysis.* PLOS ONE, 2014. **9**(9): p. e108750.

614. Arasaradnam, R.P., et al., *Noninvasive Diagnosis of Pancreatic Cancer Through Detection of Volatile Organic Compounds in Urine.* Gastroenterology, 2018. **154**(3): p. 485-487.e1.

615. Koureas, M., et al., *Target Analysis of Volatile Organic Compounds in Exhaled Breath for Lung Cancer Discrimination from Other Pulmonary Diseases and Healthy Persons.* Metabolites, 2020. **10**(8).

616. Tiele, A., et al., *Breath Analysis Using eNose and Ion Mobility Technology to Diagnose Inflammatory Bowel Disease-A Pilot Study.* Biosensors (Basel), 2019. **9**(2).

617. Baldini, C., et al., *Electronic Nose as a Novel Method for Diagnosing Cancer: A Systematic Review.* Biosensors (Basel), 2020. **10**(8).

618. Röck, F., N. Barsan, and U. Weimar, *Electronic Nose: Current Status and Future Trends.* Chemical Reviews, 2008. **108**(2): p. 705-725.

619. Broza, Y.Y., et al., *Screening for gastric cancer using exhaled breath samples.* British Journal of Surgery, 2019. **106**(9): p. 1122-1125.

620. Chang, J.-E., et al., *Analysis of volatile organic compounds in exhaled breath for lung cancer diagnosis using a sensor system.* Sensors and Actuators B: Chemical, 2018. **255**: p. 800-807.

621. Díaz de León-Martínez, L., et al., *Identification of profiles of volatile organic compounds in exhaled breath by means of an electronic nose as a proposal for a screening method for breast cancer: a case-control study.* Journal of Breath Research, 2020. **14**(4): p. 046009.

622. Kononov, A., et al., *Online breath analysis using metal oxide semiconductor sensors (electronic nose) for diagnosis of lung cancer.* Journal of Breath Research, 2019. **14**(1): p. 016004.

623. Krauss, E., et al., *Recognition of breathprints of lung cancer and chronic obstructive pulmonary disease using the Aeonose® electronic nose.* Journal of Breath Research, 2020. **14**(4): p. 046004.

624. Roine, A., et al., *Detection of Prostate Cancer by an Electronic Nose: A Proof of Principle Study.* The Journal of Urology, 2014. **192**(1): p. 230-235.

625. van de Goor, R.M.G.E., et al., *Feasibility of electronic nose technology for discriminating between head and neck, bladder, and colon carcinomas.* European Archives of Oto-Rhino-Laryngology, 2017. **274**(2): p. 1053-1060.

626. van Keulen, K.E., et al., *Volatile organic compounds in breath can serve as a non-invasive diagnostic biomarker for the detection of advanced adenomas and colorectal cancer.* Alimentary Pharmacology & Therapeutics, 2020. **51**(3): p. 334-346.

627. Waltman, C.G., T.A.T. Marcelissen, and J.G.H. van Roermund, *Exhaled-breath Testing for Prostate Cancer Based on Volatile Organic Compound Profiling Using an Electronic Nose*

Device (Aeonose™): A Preliminary Report. European Urology Focus, 2020. **6**(6): p. 1220-1225.

628. Barash, O., et al., *Differentiation between genetic mutations of breast cancer by breath volatolomics.* Oncotarget, 2015. **6**(42): p. 44864-76.

629. Chen, Y., et al., *Breath Analysis Based on Surface-Enhanced Raman Scattering Sensors Distinguishes Early and Advanced Gastric Cancer Patients from Healthy Persons.* ACS Nano, 2016. **10**(9): p. 8169-8179.

630. Peng, G., et al., *Detection of lung, breast, colorectal, and prostate cancers from exhaled breath using a single array of nanosensors.* British Journal of Cancer, 2010. **103**(4): p. 542-551.

631. Raspagliesi, F., et al., *Detection of Ovarian Cancer through Exhaled Breath by Electronic Nose: A Prospective Study.* Cancers (Basel), 2020. **12**(9).

632. Karakaya, D., O. Ulucan, and M. Turkan, *Electronic Nose and Its Applications: A Survey.* International Journal of Automation and Computing, 2020. **17**(2): p. 179-209.

633. Covington, J., et al., *The application of FAIMS gas analysis in Medical Diagnostics.* Analyst, 2015. **140**.

634. Brooks, S.W., et al., *Canine olfaction and electronic nose detection of volatile organic compounds in the detection of cancer: a review.* Cancer investigation, 2015. **33**(9): p. 411-419.

635. Hurot, C., et al., *Bio-Inspired Strategies for Improving the Selectivity and Sensitivity of Artificial Noses: A Review.* Sensors, 2020. **20**(6).

636. Feng, X., et al., *A living cell-based biosensor utilizing G-protein coupled receptors: principles and detection methods.* Biosens Bioelectron, 2007. **22**(12): p. 3230-7.

637. Ko, H.J. and T.H. Park, *Bioelectronic nose and its application to smell visualization.* J Biol Eng, 2016. **10**: p. 17.

638. Lee, S.H., E.H. Oh, and T.H. Park, *Cell-based microfluidic platform for mimicking human olfactory system.* Biosens Bioelectron, 2015. **74**: p. 554-61.

639. Hwi Jin, K. and P. Tai Hyun, *Dual signal transduction mediated by a single type of olfactory receptor expressed in a heterologous system.* Biological Chemistry, 2006. **387**(1): p. 59-68.

640. Lee, S.H., et al., *Cell-based olfactory biosensor using microfabricated planar electrode.* Biosensors and Bioelectronics, 2009. **24**(8): p. 2659-2664.

641. Lee, S.H., et al., *Enhancement of cellular olfactory signal by electrical stimulation.* ELECTROPHORESIS, 2009. **30**(18): p. 3283-3288.

642. Misawa, N., et al., *Construction of a Biohybrid Odorant Sensor Using Biological Olfactory Receptors Embedded into Bilayer Lipid Membrane on a Chip.* ACS Sens, 2019. **4**(3): p. 711-716.

643. Mitsuno, H., et al., *Novel cell-based odorant sensor elements based on insect odorant receptors.* Biosens Bioelectron, 2015. **65**: p. 287-94.

644. Termtanasombat, M., et al., *Cell-Based Odorant Sensor Array for Odor Discrimination Based on Insect Odorant Receptors.* J Chem Ecol, 2016. **42**(7): p. 716-24.

645. Murugathas, T., et al., *Biosensing with Insect Odorant Receptor Nanodiscs and Carbon Nanotube Field-Effect Transistors.* ACS Appl Mater Interfaces, 2019. **11**(9): p. 9530-9538.

646. Sato, K. and S. Takeuchi, *Chemical Vapor Detection Using a Reconstituted Insect Olfactory Receptor Complex.* Angewandte Chemie International Edition, 2014. **53**(44): p. 11798-11802.

647. Gardner, E.P. and J.H. Martin, *Coding of sensory information.* Principles of neural science, 2000. **4**: p. 411-429.

648. Malnic, B., et al., *Combinatorial receptor codes for odors.* Cell, 1999. **96**(5): p. 713-723.

649. Kandel, E.R., et al., *Principles of neural science*. Vol. 4. 2000: McGraw-hill New York.

650. Moran, J.K., et al., *The scent of blood: a driver of human behavior?* PLoS One, 2015. **10**(9): p. e0137777.

651. Sarrafchi, A. and M. Laska, *Olfactory sensitivity for the mammalian blood odor component trans-4, 5-epoxy-(E)-2-decenal in CD-1 mice.* Perception, 2017. **46**(3-4): p. 333-342.

652. Giurfa, M. and J.-C. Sandoz, *Invertebrate learning and memory: fifty years of olfactory conditioning of the proboscis extension response in honeybees.* Learning & memory, 2012. **19**(2): p. 54-66.

653. Wenner, A.M., P.H. Wells, and D.L. Johnson, *Honey bee recruitment to food sources: olfaction or language?* Science, 1969. **164**(3875): p. 84-86.

654. Galizia, C.G., S.L. McIlwrath, and R. Menzel, *A digital three-dimensional atlas of the honeybee antennal lobe based on optical sections acquired by confocal microscopy.* Cell and tissue research, 1999. **295**(3): p. 383-394.

655. Flanagan, D. and A.R. Mercer, *An atlas and 3-D reconstruction of the antennal lobes in the worker honey bee, Apis mellifera L.(Hymenoptera: Apidae).* International Journal of Insect Morphology and Embryology, 1989. **18**(2-3): p. 145-159.

656. Brandt, R., et al., *Three-dimensional average-shape atlas of the honeybee brain and its applications.* Journal of Comparative Neurology, 2005. **492**(1): p. 1-19.

657. Rybak, J., *The digital honey bee brain atlas*, in *Honeybee neurobiology and behavior*. 2012, Springer. p. 125-140.

658. Sachse, S. and C.G. Galizia, *The coding of odour-intensity in the honeybee antennal lobe: local computation optimizes odour representation.* European journal of neuroscience, 2003. **18**(8): p. 2119-2132.

659. Galizia, C.G. and R. Menzel, *The role of glomeruli in the neural representation of odours: results from optical recording studies.* Journal of insect physiology, 2001. **47**(2): p. 115-130.

660. Fialho, M.d.C.Q., et al., *A comparative study of the antennal sensilla in corbiculate bees.* Journal of Apicultural Research, 2014. **53**(3): p. 392-403.

661. Esslen, J. and K.-E. Kaissling, *Zahl und Verteilung antennaler Sensillen bei der Honigbiene (Apis mellifera L.).* Zoomorphologie, 1976. **83**(3): p. 227-251.

662. Forêt, S. and R. Maleszka, *Function and evolution of a gene family encoding odorant binding-like proteins in a social insect, the honey bee (Apis mellifera).* Genome research, 2006. **16**(11): p. 1404-1413.

663. Robertson, H.M. and K.W. Wanner, *The chemoreceptor superfamily in the honey bee, Apis mellifera: expansion of the odorant, but not gustatory, receptor family.* Genome research, 2006. **16**(11): p. 1395-1403.

664. Akers, R.P. and W.M. Getz, *A test of identified response classes among olfactory receptor neurons in the honey-bee worker.* Chemical Senses, 1992. **17**(2): p. 191-209.

665. Suzuki, H., *Convergence of olfactory inputs from both antennae in the brain of the honeybee.* 1975.

666. Sinakevitch, I.T., et al., *Apis mellifera octopamine receptor 1 (AmOA1) expression in antennal lobe networks of the honey bee (Apis mellifera) and fruit fly (Drosophila melanogaster).* Frontiers in systems neuroscience, 2013. **7**: p. 70.

667. Galizia, C.G. and P. Szyszka, *Olfactory coding in the insect brain: molecular receptive ranges, spatial and temporal coding.* Entomologia experimentalis et applicata, 2008. **128**(1): p. 81-92.

668. Brodie, A. and N. Vasdev, *The future of robotic surgery.* The Annals of The Royal College of Surgeons of England, 2018. **100**(Supplement 7): p. 4-13.

669. Hanson, T.L., et al., *The "sewing machine" for minimally invasive neural recording.* bioRxiv, 2019: p. 578542.

670. Musk, E., *An Integrated Brain-Machine Interface Platform With Thousands of Channels.* J Med Internet Res, 2019. **21**(10): p. e16194.

671. Salatino, J.W., et al., *Glial responses to implanted electrodes in the brain.* Nature biomedical engineering, 2017. **1**(11): p. 862-877.

672. Steinmetz, N.A., et al., *Neuropixels 2.0: A miniaturized high-density probe for stable, long-term brain recordings.* Science, 2021. **372**(6539): p. eabf4588.

673. Obaid, A., et al., *Massively parallel microwire arrays integrated with CMOS chips for neural recording.* Science Advances. **6**(12): p. eaay2789.

674. Hashemi Noshahr, F., M. Nabavi, and M. Sawan, *Multi-Channel Neural Recording Implants: A Review.* Sensors (Basel), 2020. **20**(3).

675. Schmidt, K. and I. Podmore, *Current Challenges in Volatile Organic Compounds Analysis as Potential Biomarkers of Cancer.* Journal of Biomarkers, 2015. **2015**: p. 981458.

676. Jia, Z., et al., *Critical Review of Volatile Organic Compound Analysis in Breath and In Vitro Cell Culture for Detection of Lung Cancer.* Metabolites, 2019. **9**(3).